Assessing the synergistic anticancer effects of thymoquinone, β-lapachone, and β-lapachol in combination with irinotecan in colon cancer (HCT116) and breast cancer (MCF-7) cell lines

By

KRISTEN PRETORIUS

67721893

Submitted in accordance with the requirements for the degree of

MAGISTER SCIENTAE RESEARCH

in the subject

LIFE SCIENCES

Department of Life and Consumer Science

at the

UNIVERSITY OF SOUTH AFRICA

SUPERVISOR: DR. SELISHA SOOKLAL

CO-SUPERVISOR: MS. SABEEHA MAHOMED

2026

ABSTRACT

Colon and breast cancers remain major global health challenges, driving interest in plant-derived compounds as alternative or adjunct therapies. Thymoquinone, β-lapachone, and β-lapachol exhibit distinct anticancer mechanisms, including anti-proliferative activity, apoptosis induction, and cell cycle disruption. Despite their shared quinone-based structures, these compounds differ in functional properties, and comparative evaluation of their activity in combination with established chemotherapeutics such as irinotecan remains limited. This study aimed to investigate anticancer activities of thymoquinone, β-lapachone, and β-lapachol in combination with a well-established chemotherapeutic agent, irinotecan. Cell viability was assessed using the AlamarBlue assay, followed by IC_{50} determination and evaluation of drug interactions using the Chou–Talalay method. Apoptotic activity was examined with the EnzChek Caspase-3 assay to select optimal treatment concentrations, and flow cytometry using the Muse Cell Cycle Kit was employed to assess treatment-induced cell cycle arrest. Comparative analyses in MCF-7 and HCT116 cell lines provided insight into differential responses and the therapeutic potential of synergistic combination treatments. The AlamarBlue assay revealed distinct, cell line–specific responses to both single and combination treatments. In MCF-7 cells, β-lapachone exhibited the greatest single-agent potency (IC_{50} = 26.8 μM), followed by β-lapachol (IC_{50} = 61.7 μM) and Thymoquinone (IC_{50} = 72.9 μM), while irinotecan alone showed limited cytotoxicity (IC_{50} = 99.3 μM). In HCT116 cells, β-lapachone was extremely potent (IC_{50} = 0.36 μM), whereas β-Lapachol (IC_{50} = 24.2 μM), Irinotecan (IC_{50} = 61.9 μM), and thymoquinone (IC_{50} = 113.3 μM) demonstrated moderate activity. Combination analysis using the Chou–Talalay method identified thymoquinone + irinotecan and β-lapachol + irinotecan as the most synergistic pairs in MCF-7 cells, while β-lapachol + irinotecan emerged as the most effective synergistic combination in HCT116 cells; β-lapachone + irinotecan showed inconsistent synergy and was excluded from further mechanistic studies in HCT116. EnzChek Caspase-3 assays, normalized to protein content, confirmed significant, time-dependent increases in caspase-3 activity for the selected synergistic combinations, with the highest activity observed at the chosen optimal concentrations. Flow cytometric cell cycle analysis demonstrated that thymoquinone + irinotecan and β-lapachol + irinotecan predominantly induced G_0/G_1 phase arrest in both cell lines, while β-lapachone + Irinotecan caused rapid pre-G_1 cell death in MCF-7 cells. Collectively, these findings demonstrate that selected phytochemical–irinotecan combinations enhance anticancer activity through synergistic cytotoxicity, caspase-3–mediated apoptosis, and G_0/G_1 cell cycle arrest in breast and colon cancer cell models. In conclusion, the combination of irinotecan with thymoquinone and β-lapachol enhanced anticancer activity through synergistic cytotoxicity, apoptosis induction, and G_0/G_1 cell cycle arrest in breast and colorectal cancer models. These findings highlight the potential of phytochemical–chemotherapy combinations as promising adjuvant strategies for cancer treatment.

DECLARATION

Kristen Pretorius

67721893

Degree of MAGISTER SCIENTAE RESEARCH PROPOSAL in the subject LIFE SCIENCES Department of Life and Consumer Science at the UNIVERSITY OF SOUTH AFRICA.

Title: **Assessing the Synergistic Anticancer Effects of Thymoquinone, β-Lapachone, and β-Lapachol in Combination with Irinotecan in Colon Cancer (HCT116) and Breast Cancer (MCF-7) Cell Lines**

I declare that the above dissertation is my own work and that all the sources that I have used or quoted have been indicated and acknowledged by means of complete references.

I further declare that I submitted the dissertation to originality checking software and that it falls within the accepted requirements for originality.

I further declare that I have not previously submitted this work, or part of it, for examination at Unisa for another qualification or at any other higher education institution.



_____ _4 February 2026_

Kristen Pretorius **Date:**

ACKNOWLEDGEMENTS

To the Lord Jesus Christ for being by my side every step of the way. For being my strength, holding my hand through everything, for His hands in everything I do. Without Him I am nothing. All the glory to Him!

To Dr Selisha Sooklal, my supervisor, I do not know how to say thank you. But thank you for everything, your kindness, motivation, encouragement, care, and so much more. You are and inspiration to all, you are always there with an open hand. You are beautiful from the inside and the outside. I appreciate all your guidance, support, and time.

To Ms Sabeeha Mahomed, my co-supervisor, you have been there all the way, teaching me and guiding me. You have been kind from the moment we met until the end. You encouraged me greatly. Your kindness and perfectionism inspired me and helped me through so much, I appreciate you. Thank you for everything.

To Dr Itumeleng Setshedi, from the day we met, you made me feel comfortable and you made me smile. Thank you for being there in times of need. Thank you for being my supervisor in the Flow Cytometry Assay.

To Dr Adewale Oladipo also from the day we met, you were also there in times of need, guiding me, teaching me, and being there for encouragement and motivation. Thank you for your kindness.

To my family and partner, thank you for your persistent patience and support. You all are my everything and you mean the world to me.

RESEARCH OUTPUT

Publications:

1. Research Article:

Pretorius, K., Mahomed, S., Setshedi, I. and Sooklal, S.A. (2026) Synergistic anticancer effects of quinone-based phytochemicals combined with irinotecan in breast and colon cancer cells. **Scientific Reports**. *In preparation*.

2. Systematic Article/Review:

Pretorius, K., Mahomed, S. and Sooklal, S.A. (2026) The anticancer effects of thymoquinone in combination with antineoplastic agents in mammalian cells. **Expert review of Anticancer therapy**. *In preparation.*

Pretorius, K., Mahomed, S. and Sooklal, S.A. (2026) The anticancer effects of β-lapachone and β-lapachol in combination with antineoplastic agents in mammalian cells. **Expert review of Anticancer therapy**. *In preparation.*

TABLE OF CONTENTS

Abstract....2
Declaration....3
Acknowledgements....4
Research Output....5
Table of Contents....6
List of Abbreviations....9
List of Figures....11
List of Tables....13

Chapter 1: Literature View....14

1.1 Introduction....14
1.1.1 Cell Line Models and Therapeutic Rationale....15
1.2 Cancer....16
1.2.1 A General Overview on Colon Cancer....16
1.2.1.1 Current Treatment in Colon Cancer....17
1.2.1.2 Challenges and Future Directions....17
1.2.1.3 Comparative Overview of Colorectal and Breast Cancer....17

1.2.2 A General Overview on Breast Cancer....18
1.2.2.1 Current Treatment in Breast Cancer....18
1.2.2.2 Challenges and Future Directions....19

1.3 Remedies of Nature....19
1.3.1 Thymoquinone....19
1.3.1.1 Anticancer Effects of Thymoquinone....21
1.3.1.2 Anti-Inflammatory Properties of Thymoquinone....21
1.3.1.3 Antioxidant Activity of Thymoquinone....22
1.3.1.4 Mechanism of Action....22

1.3.2 β-Lapachone....23
1.3.2.1 Anticancer Effects of β-Lapachone....25
1.3.2.2 Anti-Inflammatory Properties of β-Lapachone....26
1.3.2.3 Anti-Microbial Properties of β-Lapachone....26
1.3.2.4 Mechanism of Action....26

1.3.3 β-Lapachol....27
1.3.3.1 Anticancer Effect of β-Lapachol....28
1.3.3.2 Anti-Microbial Properties of β-Lapachol....29
1.3.3.3 Mechanism of Action....29

1.2 Current Anticancer Therapies....30
1.4.1 Cisplatin....30
1.4.1.1 Treatment Side Effects....30
1.4.1.2 Treatment Mechanism....31
1.4.1.3 Drug Resistance....31

1.4.2 Irinotecan....31
1.4.2.1 Challenges in Treatment....32
1.4.2.2 Treatment Mechanism....33
1.4.2.3 Drug Resistance....34

1.5 Problem Statement....35

Chapter 2: Aims and Objectives 36

2.1 Aims..... 36
2.2 Objectives..... 36

Chapter 3: Methodology 37

3.1 Overview..... 37
3.2 Research Ethics Clearance..... 39

3.3 Cell Culture..... 39
3.3.1 Cell Lines..... 39
3.3.2 Cell Culture Conditions..... 39

3.4 Cell Counting..... 40
3.5 Drug Treatment..... 40

3.6 Alamar Blue Assay..... 41
3.6.1 Individual Drug Treatments on Cancer and Non-Cancerous Cell Lines..... 41

3.6.2 Combination Drug Treatments on Cancer and Non-Cancerous Cell Lines..... 42

3.7 EnzChek Assay..... 43
3.7.1 Combination Treatments..... 44
3.7.2.1 Qubit Assay..... 46
3.7.2.1.1 Caspase-3 Activity Correlation..... 46

3.8 Flow Cytometry: Muse Cell Cycle Kit..... 47
3.8.1 Combination Treatments..... 47

3.9 Statistical Analysis and Quantitative Evaluation of Drug Responses and Interactions..... 48

Chapter 4: Results..... 50

4.1 Cytotoxic Effects of β-Lapachone, β-Lapachol, and Thymoquinone, Both Individually and in Combination with the Chemotherapeutic Agent Irinotecan..... 50
4.1.1 Cytotoxic Effects of Individual Drug Treatments..... 50
4.1.1.1 MCF-7..... 51
4.1.1.2 HCT116..... 54
4.1.1.3 VERO..... 57
4.1.2 Cytotoxic Effects of Combination Drug Treatments..... 60
4.1.2.1 MCF-7 Combination Treatments..... 61
4.1.2.2 HCT116 Combination Treatments..... 75

4.2 Evaluation of Apoptotic Activity on the Analysis of Caspase-3 Activation by Using β-Lapachone, β-Lapachol, and Thymoquinone in Combination with the Chemotherapeutic Agent Irinotecan..... 88
4.2.1 Evaluation of Caspase-3 Apoptotic Activity following Combination Treatments..... 88
4.2.2 Quantification of Total Cellular Protein for Normalization of Caspase-3 Activity..... 94

4.3 Cell Cycle Distribution Analysis by Flow Cytometry Reveals Treatment-Induced Cell Cycle Arrest in MCF-7 and HCT116 Cells..... 103
4.3.1.1 Effects of Combination Treatments on Cell Cycle Distribution on MCF-7 Cells..... 103
4.3.1.2 Effects of Combination Treatments on Cell Cycle Distribution in HCT116 Cells..... 109

Chapter 5: Discussion..... 114

5.1 Overview..... 114

5.1.1 β-Lapachol and Irinotecan Demonstrate Greater Selectivity and Lower Cytotoxicity in VERO Cells than β-Lapachone and Cisplatin..... 115
5.1.2 Mechanism-Driven Synergy Reveals β-Lapachone as a Potent Cytotoxic Agent and β-Lapachol as a Chemosensitizer in MCF-7 Cells..... 118
5.1.3 β-Lapachol Emerges as the Most Potent Chemosensitizer While β-Lapachone Exhibits Limited Additional Synergy in HCT116 Cells.....121

5.2 Limitations.....124

5.3 Translational Relevance and Clinical Implications.....125

Chapter 6: Conclusion..... 126

6.1 Future Work..... 126

References.....127

Appendix..... 137

LIST OF ABBREVIATIONS

β	Beta
°C	Degree Celsius
%	Percentage
a.u	Arbitrary Units
AMC	7-Amino-4-methylcoumarin
BRCA1	Breast cancer gene 1
BRCA2	Breast cancer gene 2
C1	Concentration 1
C2	Concentration 2
Ca^{2+}	Calcium ion
CaCl	Calcium chloride
CI	Combination index
Cis	Cisplatin
CO_2	Carbon dioxide
Conc	Concentration
COX-2	Cyclooxygenase-2
CV	Cell viability
Dm	Median-Effect Dose
DMEM	Dulbecco's Modified Eagle Medium
DMSO	Dimethyl sulfoxide
DNA	Deoxyribonucleic acid
EDTA	Ethylenediaminetetraacetic
EGFR	Epidermal growth factor receptor
ER	Endoplasmic reticulum
Fa	Fraction Affected
FBS	Fetal bovine serum
G_0	Quiescent (resting) phase of the cell cycle
G_1	Gap 1 phase
G_2	Gap 2 phase
HCT116	Human colorectal carcinoma
HER2	Human epidermal growth factor receptor 2
IC_{50}	Half maximal inhibitory concentration
IRI	Irinotecan
KRAS	Kirsten rat sarcoma viral oncogene homolog
LAP	β-Lapachone
M	Mitotic phase
MAPK	Mitogen-activated protein kinases
MCF-7	Human breast cancer cell line

mL	Milliliter
NaCl	Sodium chloride
NAD(P)H	Nicotinamide-adenine dinucleotide phosphate
NF-kB	Nuclear factor kappa
NQO1	Quinone oxidoreductase
ns	Not significant
NSCLC	Non-small cell lung carcinoma
OL	β-Lapachol
p53	Tumor protein p53
PBS	Phosphate-buffered saline
PS	Phosphatidylserine
R^2	Coefficient of determination
ROS	Reactive oxygen species
RPMI	Roswell Park Memorial Institution
RTCA	Real-Time Cell Analysis
S	DNA synthesis phase
SERMs	Selective estrogen receptor modulators
SN-38	7-Ethyl-10-hydroxycamptothecin (the active metabolite of irinotecan)
TKI	Tyrosine kinase inhibitor
TQ	Thymoquinone
VEGF	Vascular endothelial growth factor
VERO	Kidney cell of the African green monkey
µL	micro-Liter
µM	micro-Molar
Z-DEVD-CHO	Benzyloxycarbonyl-Asp-Glu-Val-Asp-aldehyde

LIST OF FIGURES

Figure 1: The Chemical Structure of Thymoquinone..... 20
Figure 2: Thymoquinone Immune-Modulating and Anti-Inflammatory Effects..... 22
Figure 3: The Chemical Structure of β-Lapachone..... 24
Figure 4: NQO1-Dependent Lethal Redox Cycling and Cell Death Pathways Induced by β-Lapachone..... 25
Figure 5: The Chemical Structure of β-Lapachol..... 29
Figure 6: Schematic Overview of the Experimental Workflow Illustration the Rationale of Drug Selection and Downstream Analyses..... 38
Figure 7: Dose-Response Analysis Demonstrates Enhanced Cytotoxicity of β-Lapachone and Cisplatin Relative to Other Compounds in MCF-7 Cells..... 53
Figure 8: Dose-Dependent Reduction in HCT116 Cell Viability Reveals Superior Potency of β-Lapachone Compared to Other Treatments..... 56
Figure 9: Dose-Response Analysis Indicates Lower Cytotoxicity of Thymoquinone and Greater Toxicity of β-Lapachone and Cisplatin in VERO cells..... 59
Figure 10: Combination Index Analysis on the Synergistic Effects of Thymoquinone, β-Lapachone, and β-Lapachol with Irinotecan in MCF-7 Cells..... 64
Figure 11: Differential Potency and Activity of Thymoquinone, β-Lapachone, and β-Lapachol in Combination with Irinotecan in MCF-7 Cells..... 66
Figure 12: Differential Dose-Response Slopes of Thymoquinone, β-Lapachone, and β-Lapachol in Combination with Irinotecan in MCF-7 Cells..... 68
Figure 13: Differential Dose Reduction Effects of Thymoquinone, β-Lapachone, and β-Lapachol in Combination with Irinotecan in MCF-7 Cells..... 71
Figure 14: Isobologram Analysis of Irinotecan Combined with Thymoquinone, β-Lapachone, and β-Lapachol in MCF-7 Cells..... 74
Figure 15: Combination Index Analysis on the Synergistic Effects of Thymoquinone, β-Lapachone, and β-Lapachol with Irinotecan in HCT116 Cells..... 77
Figure 16: Differential Potency and Activity of Thymoquinone, β-Lapachone, and β-Lapachol in Combination with Irinotecan in HCT116 Cells..... 79
Figure 17: Differential Dose-Response Slopes of Thymoquinone, β-Lapachone, and β-Lapachol in Combination with Irinotecan in HCT116 Cells..... 81
Figure 18: Differential Dose Reduction Effects of Thymoquinone, β-Lapachone, and β-Lapachol in Combination with Irinotecan in HCT116 Cells..... 83
Figure 19: Isobologram Analysis of Irinotecan Combined with Thymoquinone, β-Lapachone, and β-Lapachol in HCT116 Cells..... 85
Figure 20: Caspase-Dependent Apoptosis Induced by Drug Combinations is Attenuated by Z-DEVD-CHO in MCF-7 Cells..... 90
Figure 21: Caspase-Dependent Apoptosis Induced by Drug Combinations is Attenuated by Z-DEVD-CHO in HCT116 Cells..... 93
Figure 22: Enhance Caspase-3 Activation by Drug Combinations, with Peak Activity in Thymoquinone-Irinotecan Treated MCF-7 Cells..... 97
Figure 23: Time-Dependent Caspase-3 Activation Reveals Superior Apoptotic Response to β-Lapachol-Irinotecan in HCT116 Cells..... 100

Figure 24: Flow-Cytometric Analysis Reveals Predominant G_1 Phase Arrest Following Thymoquinone and Irinotecan Combination Treatment in MCF-7 Cells..... 104
Figure 25: Flow-Cytometric Analysis Reveals Predominant G_1/G_0 Phase Arrest Following β-Lapachone and Irinotecan Combination Treatment in MCF-7 Cells..... 105
Figure 26: Flow-Cytometric Analysis Reveals Predominant G_1 Phase Arrest Following β-Lapachol and Irinotecan Combination Treatment in MCF-7 Cells..... 107
Figure 27: Baseline Cell Cycle Distribution in Untreated MCF-7 Cells Shows Active Proliferation Without Phase Arrest..... 108
Figure 28: Flow-Cytometric Analysis Reveals Predominant G_1/G_0 Phase Arrest Following Thymoquinone and Irinotecan Combination Treatment in HCT116 Cells..... 109
Figure 29: Flow-Cytometric Analysis Reveals Predominant G_1 Phase Arrest Following β-Lapachol and Irinotecan Combination Treatment in HCT116 Cells..... 111
Figure 30: Baseline Cell Cycle Distribution in Untreated HCT116 Cells Shows Active Proliferation Without Phase Arrest..... 112

Figure A 1: Limited Time-Dependent Cytotoxicity of Irinotecan in MCF-7 Cells Following 48-Hour Exposure..... 137
Figure A 2: β-Lapachone Exhibits the Highest Cytotoxic Potency Across Cell Lines with Greater Sensitivity Observed in VERO Cells..... 142
Figure A 3: AMC Standard Curves Demonstrate Strong Linearity and Time-Dependent Fluorescence Increase in MCF-7 Cells..... 143
Figure A 4: AMC Standard Curves Demonstrate Strong Linearity and Time-Dependent Fluorescence Increase in HCT116 Cells..... 144

LIST OF TABLES

Table 1: Differential Cytotoxic Potency of Single Treatments in MCF-7 Cells Based on IC_{50} Values.....54
Table 2: Differential Cytotoxic Potency of Single Treatments in HCT116 Cells Based on IC_{50} Values.....57
Table 3: Differential Cytotoxic Potency of Single Treatments in VERO Cells Based on IC_{50} Values.....60
Table 4: Predominant G_0/G_1 Phase Accumulation Indicates G_1 Cell Cycle Arrest in MCF-7 Cells Treated with Thymoquinone and Irinotecan Combination..... 104
Table 5: Predominant G_0/G_1 Phase Accumulation Indicates G_1 Cell Cycle Arrest in MCF-7 Cells Treated with β-Lapachone and Irinotecan Combination..... 106
Table 6: Flow Cytometric Analysis Reveals Predominant G_1 Phase Arrest Following β-Lapachol and Irinotecan Combination in MCF-7 Cells..... 107
Table 7: Balanced Cell Cycle Distribution Indicates Active Proliferation Without Phase Arrest in Untreated MCF-7 Cells.....108
Table 8: Predominant G_0/G_1 Phase Accumulation Indicates G_1 Cell Cycle Arrest in HCT116 Cells Treated with Thymoquinone and Irinotecan Combination..... 110
Table 9: Flow Cytometric Analysis Reveals Predominant G_1 Phase Arrest Following β-Lapachol and Irinotecan Combination in HCT116 Cells.....111
Table 10: Balanced Cell Cycle Distribution Indicates Active Proliferation Without Phase Arrest in Untreated HCT116 Cells..... 112

Table A 1: Drug Treatments and Stock Solution Preparation..... 137
Table A 2: Statistical Significance (P-Values) of Dose-Dependent Cytotoxic Effects of Thymoquinone (TQ), β-Lapachone (β-LAP), β-Lapachol (β-OL), Cisplatin (CIS), and Irinotecan (IRI) in MCF-7 Cells.....138
Table A 3: Statistical Significance (P-Values) of Dose-Dependent Cytotoxic Effects of Thymoquinone (TQ), β-Lapachone (β-LAP), β-Lapachol (β-OL), Cisplatin (CIS), and Irinotecan (IRI) in HCT116 Cells.....139
Table A 4: Statistical Significance (P-Values) Of Dose-Dependent Cytotoxic Effects of Thymoquinone (TQ), β-Lapachone (β-LAP), β-Lapachol (β-OL), Cisplatin (CIS), and Irinotecan (IRI) in VERO Cells.....140
Table A 5: Linear Regression Analysis of Dose–Response Relationships for Thymoquinone, B-Lapachone, B-Lapachol, Cisplatin, and Irinotecan Across Cancerous (MCF-7, HCT116) and Non-Cancerous (VERO) Cell Lines.....141
Table A 6: Ranking of Cytotoxic Potency Based on Linear Regression Slopes (M) for Thymoquinone, β-Lapachone, β-Lapachol, Cisplatin, and Irinotecan Across MCF-7, HCT116, and VERO Cell Lines.....141
Table A 7: EnzChek Assay Combination Treatment Statistical Analysis in MCF-7 Cell Line..... 145
Table A 8: EnzChek Assay Combination Treatment Statistical Analysis in HCT116 Cell Line.....146
Table A 9: Statistical Comparison of Control Versus Combination Treatments in the Enzchek Caspase-3 Assay Across Time Points in MCF-7 Cells..... 146
Table A 10: Statistical Comparison of Control Versus Combination Treatments in the Enzchek Caspase-3 Assay Across Time Points in HCT116 Cells..... 147
Table A 11: Total Protein Quantification in MCF-7 Cells Following Combination Treatment with Thymoquinone, β-Lapachol, and β-Lapachone with Irinotecan..... 148
Table A 12: Total Protein Quantification in MCF-7 Cells Following Combination Treatment with Thymoquinone, β-Lapachol, and β-Lapachone with Irinotecan..... 149

CHAPTER 1: LITERATURE REVIEW

1.1 Introduction

Colon cancer and breast cancer are leading causes of cancer-related mortality worldwide, underscoring the urgent need for innovative treatment strategies. Natural compounds have emerged as promising candidates for cancer therapy, including thymoquinone, a bioactive component of *Nigella sativa* (black seed), and β-lapachone, which is derived from the pink lapacho tree (*Tabebuia impetiginosa*) (Dajani *et al.,* 2016; Wuerzberger *et al.,* 1998). Thymoquinone has been demonstrated to exhibit anti-proliferative, pro-apoptotic, and anti-metastatic effects in various cancer models, including colon, prostate, and breast cancers (Majdalawieh *et al.,* 2017). Its mechanisms of action involve the modulation of various signaling pathways that regulate cell growth, survival, and metastasis (Khurshid *et al.,* 2020).

Similarly, β-lapachone has garnered attention for its ability to induce cancer cell death through multiple mechanisms. In particular, it generates reactive oxygen species (ROS) and inhibits topoisomerase activity, leading to DNA damage and apoptosis (Kung *et al.,* 2014). As a natural quinone compound, β-lapachone undergoes enzymatic reduction to form unstable hydroquinone intermediates, which can generate ROS within cancer cells. This build-up of oxidative stress is capable of causing DNA damage, triggering apoptotic pathways, and disrupting cellular redox balance, ultimately resulting in the selective death of cancer cells (Zhang *et al.,* 2021).

β-Lapachol, a related naphthoquinone derived from the same source as β-lapachone, has also been recognized for its anticancer properties. It shares a comparable mechanism of action with β-lapachone but exhibits some distinct features that could enhance its therapeutic potential. Research indicates that β-lapachol can induce apoptosis through ROS generation and has demonstrated cytotoxic effects across various cancer cell lines, including breast and lung cancers (Loredo-Carrillo *et al.,* 2024). In particular, β-lapachol has been shown to interfere with various signaling pathways involved in cancer cell proliferation and survival, such as the PI3K/Akt pathway, leading to cell cycle arrest and apoptosis in cancer cells (Lesgards *et al.,* 2014).

Furthermore, recent studies have highlighted the potential of β-lapachol in combination therapy, where its ability to sensitize cancer cells to conventional chemotherapeutics like cisplatin and irinotecan may overcome resistance mechanisms that limit treatment efficacy (De Angelis *et al.,* 2004). The generation of ROS by β-lapachol can enhance the therapeutic effects of DNA-damaging agents, positioning it as a valuable adjunct in cancer treatment regimens.

1.1.1 Cell Line Models and Therapeutic Rationale

The MCF-7 breast cancer cell line and HCT116 colon cancer cell line is widely used models in cancer research, offering insights into breast and colon cancers, respectively. MCF-7 cells are hormone receptor-positive and frequently examined for their response to anticancer agents targeting hormone-dependent breast cancer (Barnes *et al.,* 2005). In contrast, HCT116 cells, derived from human colorectal carcinoma, serve as a valuable model for studying colorectal cancer, which is one of the most prevalent types of cancer worldwide (Rajput *et al.,* 2008). This cell line is commonly used to investigate the activity of anticancer agents due to its well-characterized genetic background and sensitivity to various chemotherapeutics (De Angelis *et al.,* 2004). HCT116 cells provide a relevant platform for assessing the anticancer potential of novel compounds and their combinations, allowing researchers to explore treatment strategies not only for colorectal cancer but also for other cancers that share similar molecular characteristics.

Additionally, cisplatin and irinotecan are established chemotherapeutic agents used to treat a variety of cancers, including colon and breast cancers. Cisplatin exerts its anticancer effects by forming DNA adducts, which lead to DNA damage and subsequent cell death. Irinotecan targets topoisomerase I, inhibiting DNA replication and inducing apoptosis in cancer cells (Pabla and Dong, 2008; Pommier, 2006). However, the clinical activity of these agents is often hampered by the development of drug resistance and adverse effects, prompting ongoing efforts to enhance their effectiveness and safety through innovative approaches.

Given the promising anticancer activities of thymoquinone, β-lapachone, and β-lapachol, combined with the established efficacy of irinotecan, there is a compelling rationale to investigate the synergistic effects of these compounds in colon and breast cancer contexts. This study aims to compare the anticancer activities of thymoquinone, β-lapachone, and β-lapachol in combination with irinotecan, utilizing MCF-7 and HCT116 cell lines as representative models for breast and colon cancer, respectively. By including these cell lines, the study assessed the effects of combination therapies on distinct cancer types, contributing to a comprehensive evaluation of their combined efficacy.

This research represents a novel approach in cancer therapy by exploring drug combinations that have not been previously investigated. The specific interactions between the drug compounds in this study provided unique insights and could uncover valuable new avenues for cancer treatment, particularly in overcoming resistance and enhancing the efficacy of existing therapies.

1.2 CANCER

1.2.1 A GENERAL OVERVIEW OF COLON CANCER

Colorectal cancer (CRC) is a prevalent malignancy, ranking as the third most common cancer worldwide, with an estimated 1.9 million new cases diagnosed globally (Rajput *et al.,* 2008). Bray *et al.* (2024) reports and presents global cancer statistics for 2022 based on updated estimates from the International Agency for Research on Cancer. Nearly 20 million new cancer cases were reported worldwide, alongside approximately 9.7 million cancer-related deaths. The findings indicate that about one in five individuals will develop cancer during their lifetime, while cancer mortality affects roughly one in nine men and one in twelve women. Lung cancer was identified as both the most commonly diagnosed cancer and the leading cause of cancer-related deaths globally, followed by breast, colorectal, prostate, and stomach cancers. Considerable regional variation in cancer incidence was observed, with the highest rates in Australia and New Zealand and the lowest in parts of Africa and South-Central Asia, underscoring the need for strengthened global cancer prevention and control strategies. Among the critical genetic alterations associated with CRC, approximately 40% of cases harbor mutations in the KRAS gene.

The HCT116 cell line, characterized by a mutant KRAS G13D, serves as a vital model for investigating KRAS-driven cancers (Takeda *et al.,* 2025). While the 5-year relative survival rate for localized colorectal cancer stands at around 90%, the prognosis is significantly poorer for metastatic disease, with a mere 14% survival rate for patients diagnosed at stage IV (American Cancer Society, 2021). A study done by Arhin *et al.* (2022) investigated the epidemiology and age-standardized incidence of colorectal cancer in Africa through a systematic review and meta-analysis. The analysis included 14 studies with a total of 3,365 colorectal cancer cases and reported an overall age-standardized incidence rate of 5.25 per 100,000 population, with no significant difference between males and females. Higher incidence estimates were observed in North and Eastern Africa compared with Western and Southern regions, although these differences were not statistically significant, and incidence rates have remained relatively stable over the past six decades. The authors concluded that colorectal cancer incidence across Africa is heterogeneous and likely underestimated, emphasizing the need for improved population-based cancer registries to enable accurate incidence estimates and inform screening, early detection, and resource allocation strategies. Current chemotherapeutic regimens, such as FOLFOX and FOLFIRI, yield response rates of approximately 40% to 60% in metastatic cases; however, treatment resistance remains a significant hurdle, with 50% to 60% of patients experiencing disease progression during or after chemotherapy (Gmeiner, 2024).

Furthermore, for patients with KRAS wild-type tumors, targeted therapies such as cetuximab have demonstrated response rates of 20% to 30% (Graham *et al.,* 2020). The HCT116 cell line has been utilized in research studies focused on elucidating drug activity and resistance mechanisms, underscoring its importance as a tool in cancer research (Baygin, 2022). These statistical insights

highlight the complexities of CRC treatment and the critical role that HCT116 plays in advancing understanding and therapeutic approaches for this disease.

1.2.1.1 Current Treatments in Colon Cancer

Current standards for CRC treatment involve a multifaceted approach that includes surgery, chemotherapy, and targeted therapies. Among the primary chemotherapeutic regimens informed by research utilizing the HCT116 cell line are FOLFOX and FOLFIRI. FOLFOX is a combination of 5-fluorouracil (5-FU), leucovorin, and oxaliplatin, and its efficacy has been demonstrated in studies assessing drug response in HCT116 cells (Gmeiner, 2024). Similarly, FOLFIRI, which combines 5-FU, leucovorin, and irinotecan, is another regimen routinely evaluated in preclinical studies involving HCT116 (Zoetemelk *et al.,* 2020). In addition to chemotherapy, targeted therapies such as cetuximab and bevacizumab play a crucial role in CRC management. Cetuximab, an anti-EGFR monoclonal antibody, is primarily used for patients with KRAS wild-type tumors, while bevacizumab, an anti-VEGF monoclonal antibody, aims to inhibit angiogenesis and is often used in combination with chemotherapy (Yazdi *et al.,* 2015). Research employing HCT116 cells is vital for evaluating the responses to these therapies and for elucidating the underlying biological mechanisms that contribute to treatment efficacy.

1.2.1.2 Challenges and Future Directions

CRC treatment faces significant challenges, including drug resistance to therapies like 5-fluorouracil (5-FU) and oxaliplatin. HCT116 cells are instrumental in studying these resistance mechanisms. Tumor heterogeneity further complicates treatment activity, as genetic variability leads to varied responses among tumor cells (Dagogo-Jack and Shaw, 2020). Current treatments also result in side effects that negatively affect patients' quality of life (Yazdi *et al.,* 2015).

Future directions include personalized medicine, which uses genomic profiling to tailor treatments, potentially improving outcomes (Zoetemelk *et al.,* 2020). Research is focused on combination therapies that counter drug resistance (Takeda *et al.,* 2025) and developing new drugs targeting resistance pathways. Continued use of HCT116 models will enhance understanding of resistance and aid in discovering new therapies, underscoring the need for ongoing research in CRC treatment.

1.2.1.3 Comparative Overview of Colorectal and Breast Cancer

While CRC represents a major global health burden with well-characterized genetic mutations and treatment challenges, breast cancer differs significantly in its biological complexity, risk factors, and therapeutic approaches. Unlike CRC, which is primarily associated with mutations such as KRAS and often linked to gastrointestinal pathology, breast cancer is a highly heterogeneous disease influenced by hormonal, genetic, and environmental factors. Additionally, breast cancer demonstrates distinct molecular subtypes, including hormone receptor–positive, HER2-positive, and triple-negative forms,

each requiring tailored therapeutic strategies. Despite these differences, both cancers share common challenges, such as treatment resistance, disease progression, and the need for more effective combination therapies. Given the global impact and clinical complexity of breast cancer, it is essential to examine its epidemiology, treatment strategies, and ongoing challenges in greater detail.

1.2.2 A GENERAL OVERVIEW OF BREAST CANCER

Breast cancer is a significant global health concern, with a profound impact on women's health. The incidence of breast cancer continues to rise, with an estimated 2.3 million new cases diagnosed worldwide in 2020. This disease is not only prevalent but also a leading cause of cancer-related mortality among women, with over 685,000 deaths attributed to breast cancer in the same year (Arnold *et al.,* 2022). The 5-year survival rates for breast cancer vary widely depending on the stage at diagnosis, highlighting the importance of early detection and treatment. While localized breast cancer has a high 5-year survival rate of around 99%, metastatic breast cancer poses a greater challenge with a lower survival rate of approximately 27%. Understanding the risk factors associated with breast cancer, such as age, family history, genetic mutations (e.g., BRCA1 and BRCA2), hormonal influences, and lifestyle factors, is crucial for prevention and early intervention efforts (Bray *et al.,* 2018; American Cancer Society, 2021; World Cancer Research Fund/American Institute for Cancer Research, 2018). The ongoing research and public health initiatives aimed at raising awareness, promoting early screening, and advancing treatment options are essential in the fight against breast cancer and improving outcomes for those affected by disease. Women from sub-Saharan Africa were diagnosed with breast cancer at a younger median age compared with women in the United States, with median ages of 54 years reported in Botswana and South Africa versus 61 years in the US. Patients from Botswana and South Africa were also significantly more likely to present with late-stage disease at diagnosis than their US counterparts. The prevalence of triple-negative breast cancer was notably higher in Botswana compared with South Africa and the United States. While initial differences in hormone receptor status were observed across the three populations, these variations were no longer evident after adjusting for ethnicity. Among ethnic subgroups, Black and multiracial women in Botswana and the United States showed the highest likelihood of presenting with the aggressive triple-negative breast cancer subtype (Sinah *et al.,* 2022).

1.2.2.1 Current Treatments in Breast Cancer

Current breast cancer management relies on a multidisciplinary treatment approach tailored to tumor biology, disease stage, and patient-specific factors. Surgical intervention remains the cornerstone of treatment for localized disease and may involve breast-conserving surgery (lumpectomy) or mastectomy, often combined with sentinel lymph node biopsy or axillary lymph node dissection to assess metastatic spread (Sparavigna *et al.,* 2025). Chemotherapy is widely used in both early-stage and advanced breast cancer, either as neoadjuvant therapy to reduce tumor size before surgery or as

adjuvant therapy to eliminate residual microscopic disease. Common chemotherapeutic agents include anthracyclines (such as doxorubicin and epirubicin), taxanes (including paclitaxel and docetaxel), alkylating agents like cyclophosphamide, and antimetabolites such as 5-fluorouracil and capecitabine, which act through different mechanisms to inhibit cancer cell proliferation and induce apoptosis (Kashifa Fathima *et al.,* 2022). Radiation therapy is frequently administered following surgery to eradicate remaining cancer cells and reduce local recurrence risk by delivering targeted high-energy radiation to the breast or chest wall (Wand and Tepper*,* 2021). Hormonal therapy is indicated for hormone receptor–positive breast cancers and includes agents such as tamoxifen, aromatase inhibitors (letrozole, anastrozole, exemestane), and ovarian suppression therapies, all of which aim to block estrogen-driven tumor growth (Burciu *et al.,* 2025). Targeted therapies have significantly improved outcomes by selectively inhibiting specific molecular pathways, including HER2-directed agents such as trastuzumab and pertuzumab, as well as CDK4/6 inhibitors used in hormone receptor–positive disease. More recently, immunotherapy—particularly immune checkpoint inhibitors—has emerged as a promising option for selected patients, especially those with triple-negative breast cancer, by enhancing the host immune response against tumor cells. Together, these treatment modalities underscore the complexity of breast cancer therapy and highlight ongoing advances aimed at improving survival while minimizing treatment-related toxicity (Salem *et al.,* 2023; Iancopetta *et al.,* 2023).

1.2.2.2 Challenges and Future Directions

Despite the progress in breast cancer treatment, challenges persist, including drug resistance, treatment-related toxicities, and the need for more effective therapies for advanced or aggressive subtypes of breast cancer (Turner *et al.,* 2012). Ongoing research efforts are focused on exploring novel therapeutic targets, immunotherapies, and the development of early detection methods to further improve patient outcomes and reduce the global burden of breast cancer (Nanda *et al.,* 2016).

1.3 REMEDIES OF NATURE

1.3.1 THYMOQUINONE

Thymoquinone (TQ) is a bioactive compound derived from the seeds of Nigella sativa, a plant commonly known as black seed (Ahmad *et al.,* 2013). The concentration of TQ in the whole black seed is significantly lower than in the oil extracted from the seeds. Research indicates that the TQ content in the whole seeds typically ranges from about 0.5% to 2.5% by weight (Gharby *et al.,* 2015). Typically, TQ makes up about 30% to 48% of the oil extracted from black seeds (Forouzanfar *et al.,* 2014).

TQ has garnered significant attention in recent years due to its potential therapeutic properties, including anti-inflammatory, antioxidant, and anticancer properties (Woo *et al.,* 2012; Darakhshan *et al.,* 2015). Numerous preclinical studies have demonstrated the anti-proliferative, pro-apoptotic, and

anti-metastatic effects of TQ in various cancer types, including breast, lung, prostate, colon, and pancreatic cancers (Khan and Siveen, 2019; Woo *et al.,* 2012). The mechanisms underlying the anticancer effects of TQ involve modulation of multiple signaling pathways involved in cell growth, survival, angiogenesis, and metastasis (Darakhshan *et al.,* 2015; Woo *et al.,* 2012).

Figure 1 illustrates the chemical structure of TQ, a quinone compound characterized by a conjugated diketone system. This structural feature is critical to its biological activity, as it enables redox cycling and the generation of ROS, which contribute to its pro-apoptotic and anticancer effects (Bolton *et al.,* 2000; Woo *et al.,* 2012). The presence of the quinone moiety is therefore directly linked to its mechanism of action, including oxidative stress induction and modulation of key cellular signaling pathways (Bolton *et al.,* 2000).

In addition, TQ is prone to degradation after isolation, particularly when exposed to certain conditions. Factors like heat, light, oxygen, and moisture can contribute to its instability (Goyal *et al.,* 2017). To enhance stability and prolong shelf life, it is advisable to store TQ in opaque, airtight containers in a cool, dry place, minimizing exposure to light, heat, and air. When used in formulations, it may also be combined with stabilizers to help maintain its integrity (Goyal *et al.,* 2017).

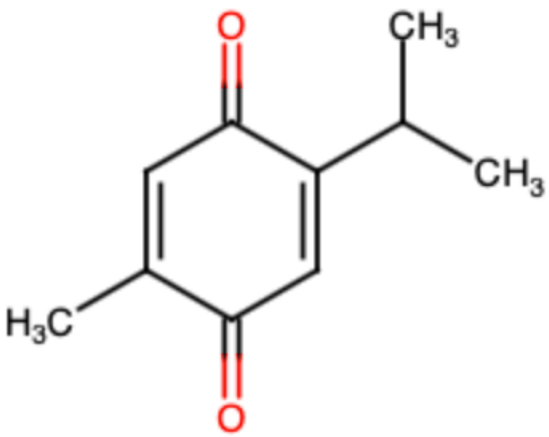


FIGURE 1: The Chemical Structure of Thymoquinone. Image created on RCSB PBD Protein Data Bank (Chemical Sketch Tool).

1.3.1.1 Anticancer Effects of Thymoquinone

Numerous studies have extensively investigated the anticancer potential of TQ across a wide range of malignancies, highlighting its multi-targeted mode of action. Gali-Muhtasib *et al*. (2004) demonstrated that TQ significantly inhibits breast cancer cell proliferation by inducing cell cycle arrest at key checkpoints and triggering apoptosis through the regulation of critical cell cycle and apoptotic proteins, including cyclins, cyclin-dependent kinases, and caspases. In colon cancer models, Badary *et al.* (1998) and Al-Damook *et al.* (2025) reported that TQ suppresses tumor growth by downregulating anti-apoptotic proteins such as Bcl-2, promoting mitochondrial-mediated apoptosis, and inhibiting angiogenesis, thereby limiting tumor vascularization and nutrient supply. Beyond its direct cytotoxic effects, TQ has been shown to modulate multiple oncogenic signaling pathways, including NF-κB, PI3K/Akt, MAPK, and p53 pathways, contributing to reduced cancer cell survival, invasion, and metastasis (Shaban, 2024). Importantly, preclinical studies have demonstrated that TQ enhances the activity of conventional chemotherapeutic and targeted agents, including camptothecin, doxorubicin, and paclitaxel, through synergistic interactions that increase cancer cell sensitivity to treatment and overcome drug resistance (Ravindran *et al.,* 2011; Sunoqrot *et al.,* 2023). These combination effects are often accompanied by reduced required drug doses, which may help mitigate the systemic toxicities commonly associated with standard chemotherapy. Collectively, these findings underscore the potential of TQ as a promising adjuvant therapeutic agent in cancer treatment, offering a multi-faceted approach that enhances anti-tumor activity while potentially improving tolerability and overall treatment outcomes.

1.3.1.2 Anti-Inflammatory Properties of Thymoquinone

In addition to its anticancer effects, TQ has been shown to possess potent anti-inflammatory properties. El Gazzar (2006) and Liu *et al.* (2022) investigated the anti-inflammatory effects of TQ in macrophages and found that TQ inhibits the production of pro-inflammatory cytokines, such as interleukin-6 and tumor necrosis factor-alpha, by suppressing the activation of NF-κB signaling pathway, as shown in **Figure 2**. Furthermore, Kotta-Loizou *et al.* (2012) demonstrated that TQ attenuates inflammation in a mouse model of colitis by modulating the expression of inflammatory mediators and reducing oxidative stress. Furthermore, TQ exhibits anti-inflammatory and immunomodulatory properties, which contribute to its anticancer effects. TQ has been shown to inhibit inflammatory mediators, such as NF-κB and COX-2, and modulate immune responses by enhancing natural killer cell activity and cytokine production (Khan and Siveen, 2019). These immunomodulatory effects of TQ may play a role in enhancing the anti-tumor immune response and inhibiting tumor growth and metastasis.

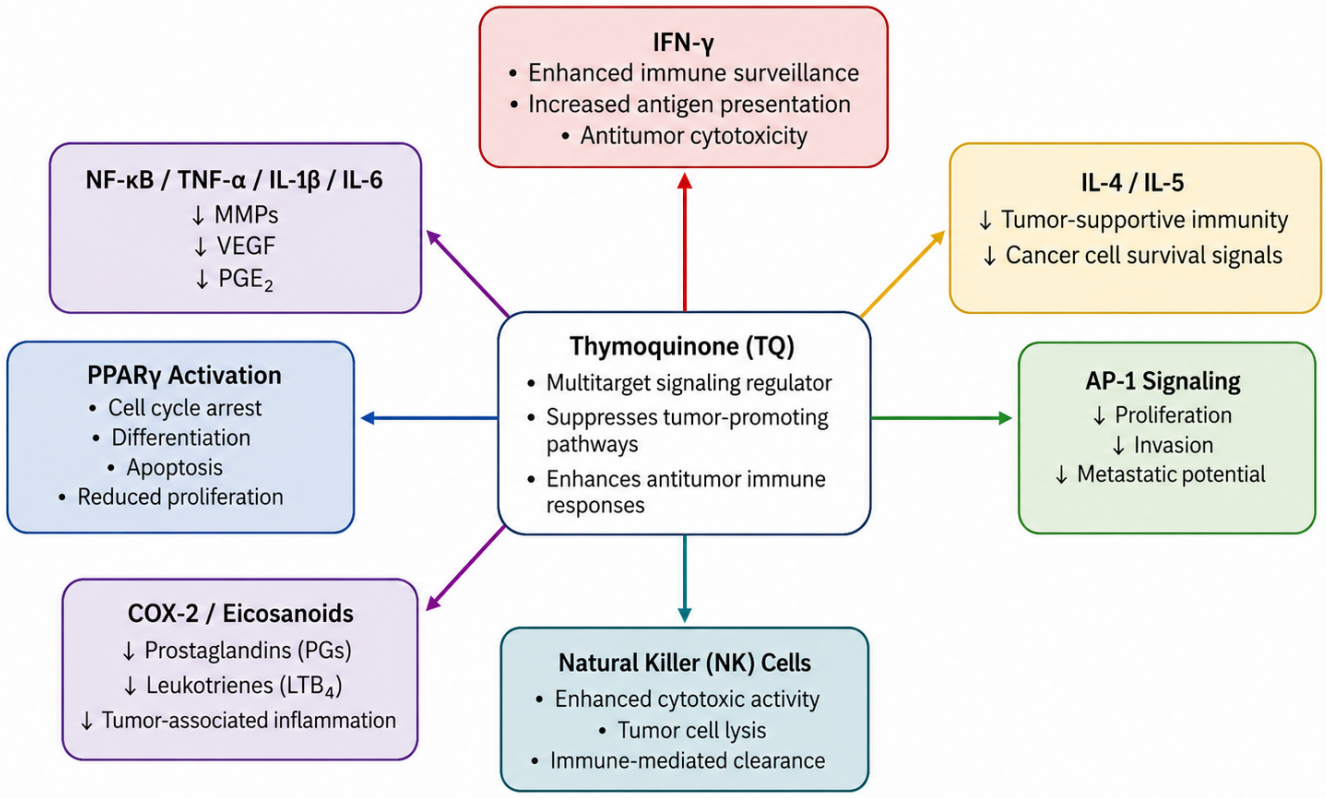


FIGURE 2: **Thymoquinone Immune-Modulating and Anti-Inflammatory Effects**. TQ targets various cytokines and signaling molecules in the body. It works by inactivating specific cytokines such as interleukin and interferon gamma (γ), as well as reducing the activity of regulatory factors like IRF and AP-1. Thymoquinone also decreases the production of inflammatory molecules like nitric oxide, TNF-α, and prostaglandins, while inhibiting the synthesis of leukotrienes. Additionally, it activates PPARγ, which helps to regulate immune responses and inflammation. Adapted from Mahmoud and Abdelrazek (2019).

1.3.1.3 Antioxidant Activity of Thymoquinone

TQ also exhibits significant antioxidant activity, which plays a crucial role in its cytoprotective effects. Nagi *et al*. (2011) conducted a study showing that TQ protects against oxidative stress-induced liver injury by enhancing the activity of antioxidant enzymes, such as superoxide dismutase and catalase, and reducing lipid peroxidation. Moreover, Sayed-Ahmed *et al*. (2010) investigated the antioxidant effects of TQ in a rat model of doxorubicin-induced cardiotoxicity and found that TQ mitigates oxidative damage by scavenging free radicals and restoring cellular redox balance.

1.3.1.4 Mechanisms of Action

One of the key mechanisms by which TQ exerts its anticancer effects is through the induction of apoptosis in cancer cells. TQ has been shown to activate intrinsic and extrinsic apoptotic pathways, leading to caspase activation, DNA fragmentation, and cell death in cancer cells (Gali-Muhtasib *et al.,*

2004). This pro-apoptotic effect is mediated through the modulation of various signaling molecules, including increasing the levels of pro-apoptotic proteins such as Bax while decreasing anti-apoptotic proteins like Bcl-2 (Mahmoud *et al.,* 2018).

Additionally, TQ has been reported to inhibit cell proliferation by regulating cell cycle progression, inducing cell cycle arrest, and suppressing oncogenic signaling pathways involved in cell growth and survival (Khan *et al.,* 2014). TQ has been shown to promote G_0/G_1 phase cell cycle arrest by upregulating cyclin-dependent kinase inhibitors such as p21 and p27, and downregulating cyclin D1, which plays a crucial role in the transition from the G_1 phase to the S phase of the cell cycle (Adinew *et al.,* 2022). TQ also exhibits anti-inflammatory properties by inhibiting the activation of the Nuclear Factor-kappa B (NF-κB) signaling pathway, which is known to play a significant role in inflammation and cancer progression. By blocking NF-κB, TQ reduces the production of pro-inflammatory cytokines and proteins associated with tumor progression (Akter *et al.,* 2021). Moreover, TQ can modulate the mitogen-activated protein kinase (MAPK) pathways, specifically p38 MAPK and ERK1/2, enhancing the apoptotic response in cancer cells (Sadeghi *et al.,* 2023).

In addition to its effects on apoptosis and cell proliferation, TQ has been shown to inhibit angiogenesis—the process by which new blood vessels form from existing ones—by downregulating the expression of vascular endothelial growth factor (VEGF), which is critical for angiogenesis (Yi *et al.,* 2008). This anti-angiogenic effect further contributes to its anticancer properties by limiting the nutrient supply to tumors. Furthermore, TQ possesses antioxidant properties, which can reduce oxidative stress in cells. This antioxidant activity not only helps in the protection of normal cells but also potently enhances the efficacy of other anticancer agents when used in combination therapies (Fatfat *et al.,* 2021).

Despite these insights into its mechanisms, the comprehensive action of TQ in cancer therapy remains unclear, indicating the necessity for further research to elucidate its multifaceted effects and potential therapeutic applications in oncology.

1.3.2 β-LAPACHONE

β-Lapachone is a naturally occurring naphthoquinone compound, **Figure 3** illustrates the chemical structure (quinone structure) of β-lapachone, that has gained attention for its potential therapeutic properties, including anticancer, anti-inflammatory, and antimicrobial effects (Bey *et al.,* 2013; Li *et al.,* 2000). Several studies have investigated the pharmacological activities and mechanisms of action of β-lapachone in various disease conditions (Bey *et al.,* 2013). β-lapachone is a bioactive compound derived from the bark of the lapacho tree (Tabebuia impetiginosa) with a wide range of pharmacological properties (da Silva *et al.,* 2002). One of the most studied effects of β-lapachone is its anticancer activity. Li *et al.* (2000) report that β-lapachone induces apoptosis and inhibits proliferation in various human cancer cell lines, including prostate cancer cells. The mechanism of action involves the generation of

ROS, leading to DNA damage, cell cycle arrest, and ultimately, cell death (Bey *et al.,* 2013). These findings highlight the potential of β-lapachone as a promising anticancer agent with selective cytotoxic effects on cancer cells. **Figure 4** illustrates the proposed mechanism of action of β-lapachone, highlighting its NQO1-dependent bioactivation, redox cycling, and subsequent induction of oxidative stress, DNA damage, and cell death pathways, including apoptosis and necroptosis (Bey *et al.,* 2013).

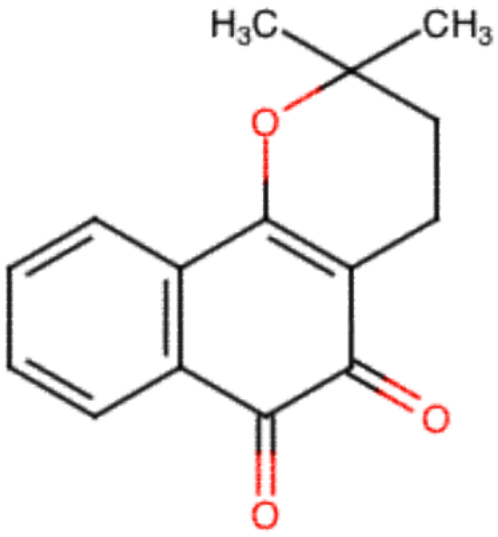


FIGURE 3: The Chemical Structure of β-Lapachone. Image created on RCSB PBD Protein Data Bank (Chemical Sketch Tool).

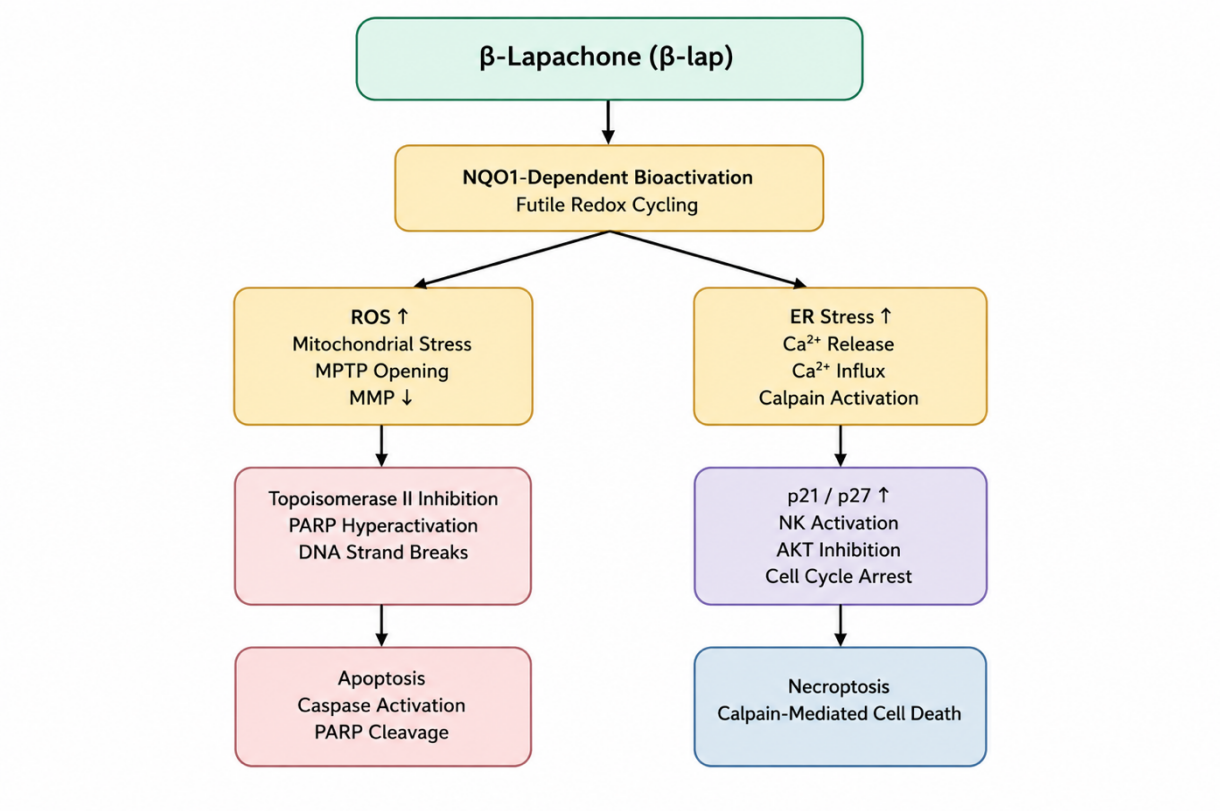


FIGURE 4: NQO1-Dependent Lethal Redox Cycling and Cell Death Pathways Induced by β-Lapachone. This diagram depicts the anticancer mechanisms of β-lapachone (β-lap) following bioactivation by NQO1, which initiates a futile redox cycle and excessive ROS generation. Elevated ROS induces mitochondrial dysfunction, endoplasmic reticulum stress with Ca^{2+} release, and DNA damage through topoisomerase inhibition and PARP hyperactivation, leading to cell cycle arrest. Sustained Ca^{2+} influx activates calpain, while cumulative cellular stress triggers caspase-dependent apoptosis and calpain-mediated necroptosis. Together, these pathways illustrate how β-lapachone selectively induces lethal cell death in NQO1-expressing cancer cells. Adapted from Kung *et al.* (2014).

1.3.2.1 Anticancer Effects of β-Lapachone

Don *et al.* (2001) report that β-lapachone exert potent anticancer activity by significantly inhibiting cell proliferation and inducing apoptosis in human colon cancer cell lines. The authors demonstrated that β-lapachone induces cell cycle arrest and programmed cell death primarily through the activation of ROS–dependent signaling pathways, resulting in marked suppression of tumor growth. A central mechanism underlying the anticancer action of β-lapachone is its capacity to generate excessive intracellular ROS, leading to severe oxidative stress that overwhelms cellular antioxidant defenses. This oxidative stress causes extensive DNA damage, including single- and double-strand breaks, which activates DNA damage response pathways and ultimately triggers both apoptotic and necrotic forms of cell death (Li *et al.,* 2011). Importantly, β-lapachone selectively targets cancer cells through its bioactivation by NAD(P)H:quinone oxidoreductase 1 (NQO1), an enzyme frequently overexpressed in many solid tumors, including colorectal cancer, breast cancer, prostate cancer, and pancreatic cancer (Silvers *et al.,* 2017). NQO1-mediated reduction of β-lapachone initiates a futile redox cycling process

that rapidly consumes NAD(P)H and generates high levels of ROS, leading to hyperactivation of poly(ADP-ribose) polymerase (PARP), depletion of cellular energy stores, and accumulation of irreparable DNA damage (Silvers *et al.,* 2017; Ross and Siegel, 2021). These events culminate in mitochondrial dysfunction, loss of membrane potential, activation of caspases, and, in cases of extreme stress, calpain-mediated necrotic cell death. Collectively, these findings highlight β-lapachone as a highly potent anticancer agent that exploits redox imbalance and DNA repair vulnerabilities in cancer cells, supporting its potential use as a targeted therapeutic strategy, particularly in NQO1-overexpressing tumors.

1.3.2.2 Anti-Inflammatory Properties of β-Lapachone

β-Lapachone has shown promise as an anti-inflammatory agent. Ferraz du Costa *et al.* (2019) and Yin *et al.* (2025) conducted a study in a murine model of colitis and found that β-lapachone attenuated inflammation by suppressing the production of pro-inflammatory cytokines and inhibiting the activity of key inflammatory mediators, such as NF-κB and COX-2. The anti-inflammatory effects of β-lapachone suggest its potential therapeutic use in the management of inflammatory bowel diseases and other inflammatory conditions. Furthermore, β-lapachone exhibits anti-inflammatory and anti-angiogenic properties, which contribute to its anticancer effects. β-Lapachone has been reported to inhibit inflammatory mediators, such as NF-κB and COX-2, and suppress angiogenesis by targeting vascular endothelial growth factor (VEGF) signaling pathways (Li *et al.,* 2018). These anti-inflammatory and anti-angiogenic effects of β-lapachone may play a role in inhibiting tumor growth, metastasis, and angiogenesis in cancer.

1.3.2.3 Anti-Microbial Properties of β-Lapachone

In addition to its anticancer and anti-inflammatory effects, β-lapachone has also been reported to possess anti-microbial activity. A study by Sousa *et al.* (2025) investigated the anti-microbial properties of β-lapachone against various bacterial strains and found that β-lapachone exhibited significant anti-bacterial effects by disrupting bacterial cell membranes and inhibiting bacterial growth.

1.3.2.4 Mechanism of Action

One of the primary mechanisms by which β-lapachone exerts its anticancer effects is through the induction of apoptosis in cancer cells. β-Lapachone activates the intrinsic apoptotic pathway by generating ROS, which lead to mitochondrial outer membrane permeabilization (MOMP) (Park *et al.,* 2011). The resultant increase in mitochondrial permeability allows pro-apoptotic factors like cytochrome c to be released into the cytosol, activating caspases that facilitate apoptotic cell death (Park *et al.,* 2011). Furthermore, β-lapachone has been shown to upregulate pro-apoptotic proteins such as Bax

while downregulating anti-apoptotic proteins like Bcl-2, further promoting apoptosis in cancer cells (Kee *et al.,* 2017).

β-Lapachone plays a significant role in modulating oxidative stress within cancer cells. It acts as a substrate for the enzyme NAD(P)H:quinone oxidoreductase 1 (NQO1), leading to the generation of ROS and subsequent oxidative damage to cellular macromolecules (Bai *et al.,* 2017). This oxidative stress can cause DNA damage, ultimately triggering cellular responses such as apoptosis or cell cycle arrest. Importantly, the effectiveness of β-lapachone is often correlated with the expression levels of NQO1, as cancer cells exhibiting high NQO1 activity are more susceptible to β-lapachone-induced cytotoxicity (Zada *et al.,* 2019). In addition to its pro-apoptotic effects, β-lapachone inhibits key oncogenic signaling pathways that are often hijacked by cancer cells. The compound has been shown to inhibit the NF-κB signaling pathway, which is known to promote cell survival, proliferation, and the expression of anti-apoptotic genes (Huang *et al.,* 2014). By downregulating this pathway, β-lapachone not only enhances apoptotic signaling but also reduces the invasiveness of cancer cells.

In addition, β-lapachone has been reported to inhibit the phosphorylation and activation of Akt, a critical component of the PI3K/Akt signaling pathway that promotes cell growth and survival (Han *et al.,* 2019). This inhibition results in the suppression of downstream targets that are essential for cancer cell proliferation and survival, leading to enhanced anti-tumor effects. The combination of β-lapachone with conventional chemotherapeutic agents or targeted therapies has shown synergistic effects in preclinical studies, suggesting the potential for β-lapachone to enhance the activity of standard cancer treatments (Planchon *et al.,* 1995). The use of β-lapachone as a sensitizer or adjuvant therapy in cancer management holds promise for overcoming drug resistance and improving treatment outcomes in cancer patients.

1.3.3 β-LAPACHOL

β-Lapachol is a naturally occurring naphthoquinone compound isolated from the bark of the pink lapacho tree (*Tabebuia impetiginosa*), a plant long used in traditional medicine for the treatment of a wide range of ailments (Dajani *et al.,* 2016; Wuerzberger *et al.,* 1998). Traditionally, the inner bark of the lapacho tree was prepared as decoctions or teas—commonly known as pau d'arco or taheebo tea—and used by indigenous populations in South and Central America to treat bacterial and fungal infections, gastrointestinal disorders, respiratory illnesses, fever, inflammatory conditions, and to promote wound healing (Castellanos *et al.,* 2009; Bussmann, 2018). These preparations were also employed as immune-supporting tonics and, in some ethnomedical practices, were used in the management of tumors and other abnormal growths (Castellanos *et al.,* 2009). Such traditional applications prompted scientific investigation into the bioactive constituents responsible for these therapeutic effects. More recently, β-lapachol has gained attention in biomedical research due to its

emerging anticancer potential across multiple cancer types. Experimental studies have demonstrated that β-lapachol exhibits cytotoxic effects against cancer cells by inhibiting cellular proliferation and inducing programmed cell death through mechanisms involving oxidative stress and disruption of intracellular redox balance (Castellanos *et al.,* 2009). As a quinone-containing compound, β-lapachol can undergo redox cycling, leading to the generation of ROS, which cause DNA damage and activate stress-response signaling pathways that culminate in apoptosis or other forms of cell death (Xiang *et al.,* 2025). In addition to its anticancer activity, β-lapachol has demonstrated broad-spectrum antimicrobial effects against various bacterial and fungal pathogens, further underscoring its biological relevance (Mohsenzadeh *et al.,* 2010). Collectively, its long-standing use in traditional medicine and its demonstrated biological activities highlight β-lapachol as a promising natural compound for further therapeutic investigation.

1.3.3.1 Anticancer Effects of β-Lapachol

β-Lapachol has garnered increasing attention in cancer research due to its pronounced anticancer effects across a variety of malignancies, including breast, lung, and prostate cancers (Castellanos *et al.,* 2009; Bussmann, 2018). Experimental studies have consistently demonstrated that β-lapachol significantly inhibits cancer cell proliferation and reduces overall tumor cell viability, thereby limiting tumor growth and progression (Mohsenzadeh *et al.,* 2010). In breast cancer models, β-lapachol treatment has been shown to markedly decrease cancer cell survival and clonogenic potential, indicating a sustained suppression of tumor cell growth beyond short-term cytotoxic effects (De Almeida, 2009). Notably, β-lapachol induces substantial levels of cancer cell death, contributing directly to its anti-tumor activity.

An important characteristic of β-lapachol is its reported selectivity toward malignant cells, with several studies indicating minimal cytotoxic effects in normal, non-transformed cells (Nepomuceno, 2014). This selective anticancer activity enhances its therapeutic appeal, as it suggests the potential for effective tumor targeting while reducing the risk of adverse effects commonly associated with conventional chemotherapy. Furthermore, the ability of β-lapachol to suppress tumor cell viability across multiple cancer types suggests that its anticancer activity is not limited to a single tissue or molecular subtype (Xiang *et al.,* 2025). Collectively, these findings underscore the therapeutic promise of β-lapachol as a naturally derived anticancer compound and support continued investigation into its potential application as a standalone treatment or as an adjuvant to existing cancer therapies. β-lapachol, is a related naphthoquinone derived from the same source as β-lapachone. **Figure 5** illustrates the chemical structure (quinone structure) of β-lapachol.

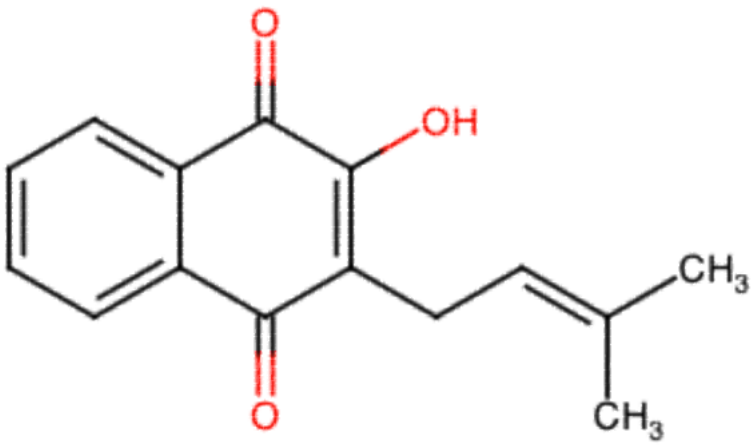


FIGURE 5: The Chemical Structure of β-Lapachol. Image created on RCSB PBD Protein Data Bank (Chemical Sketch Tool).

1.3.3.2 Anti-Microbial Properties of β-Lapachol

Apart from its anticancer effects, β-lapachol also exhibits significant anti-microbial properties. It has been evaluated against a variety of pathogens, including bacteria and fungi. For example, β-lapachol has shown inhibitory activity against Gram-positive bacteria, such as *Staphylococcus aureus* (Miyazawa *et al.,* 2019). The compound disrupts microbial cell membranes, leading to cell lysis and death (Hussain *et al.,* 2007).

In addition to its anti-bacterial properties, β-lapachol has also demonstrated anti-fungal activity, particularly against Candidiasis, which is caused by Candida species (Taleb *et al.,* 2018). The anti-fungal activity of β-lapachol can be attributed to its ability to interfere with the fungal cell wall synthesis, crucial for maintaining cell integrity (Hussain *et al.,* 2007).

1.3.3.3 Mechanisms of Action

The mechanisms by which β-lapachol exerts its anticancer effects are multifaceted. Research indicates that the compound can modulate various cellular pathways involved in cell proliferation and survival. For instance, β-lapachol has been reported to induce oxidative stress within cancer cells, leading to DNA damage and subsequent apoptosis (Loredo-Carrillo *et al.,* 2024). Additionally, it impacts key signaling pathways, such as the NF-kB pathway, which plays a significant role in regulating apoptosis and inflammation (Kim and Kim, 2021).

Another important mechanism is its ability to inhibit angiogenesis, the process through which tumors develop new blood vessels to sustain their growth. β-lapachol has been shown to reduce the expression of VEGF, which is crucial for angiogenesis (Kim and Kim, 2021). By inhibiting the formation of new blood vessels, β-lapachol can effectively starve tumors of necessary nutrients and oxygen, thereby decreasing their growth and metastatic potential.

1.4 CURRENT ANTICANCER THERAPIES

1.4.1 CISPLATIN

Cisplatin (cis-diammine-dichloroplatinum II) is a platinum-based chemotherapeutic agent that was initially identified for its ability to inhibit the growth of *Escherichia coli* and was subsequently recognized for its potent antineoplastic and cytotoxic effects against cancer cells (Rosenberg *et al.,* 1969). Administered intravenously, cisplatin has become a cornerstone of cancer chemotherapy and is widely used as a first-line treatment for a broad range of malignancies, including testicular, ovarian, bladder, lung, breast, head and neck, cervical cancers, leukemias, lymphomas, and sarcomas (Brown *et al.,* 2019; Dasari and Tchounwou, 2014). Following cellular uptake, cisplatin undergoes activation through the loss of chloride ligands, enabling it to bind covalently to DNA and form both intrastrand and interstrand DNA adducts (Siddik, 2003; Kelland, 2007). These lesions disrupt DNA replication and transcription, activate cell cycle checkpoints, and ultimately suppress tumor cell proliferation. The DNA damage induced by cisplatin triggers multiple signaling pathways involved in apoptosis, including p53- and MAPK-mediated responses, contributing to its effectiveness in targeting rapidly dividing cancer cells (Siddik, 2003; Kelland, 2007; Brown *et al.,* 2019). In parallel, cisplatin-induced DNA lesions activate cellular repair mechanisms, particularly the nucleotide excision repair pathway, as well as the ATM-dependent DNA damage response, which can limit cytotoxicity and contribute to treatment resistance (Kelland, 2007; Dasari and Tchounwou, 2014). Although cisplatin has demonstrated substantial clinical efficacy in both curative and palliative settings, the development of drug resistance and disease relapse remains a significant clinical challenge (Dasari and Tchounwou, 2014). Consequently, alternative platinum-based agents such as carboplatin and oxaliplatin have been developed and incorporated into clinical practice with varying degrees of success (Brown *et al.,* 2019; Kelland, 2007). Overall, cisplatin remains a foundational agent in oncology, with ongoing research aimed at enhancing its therapeutic efficacy and overcoming resistance in cancer treatment.

1.4.1.1 Treatment Side Effects

Despite its activity, cisplatin is associated with significant side effects, with nephrotoxicity being one of the most common and dose-limiting toxicities. Cisplatin-induced nephrotoxicity is characterized by acute kidney injury, renal tubular damage, and electrolyte disturbances, leading to impaired kidney

function (Miller *et al.,* 2010). Strategies to prevent or mitigate nephrotoxicity, such as hydration protocols, diuretics, and the use of nephroprotective agents like amifostine, have been explored to improve the tolerability of cisplatin therapy and reduce the risk of renal damage (Pabla and Dong, 2008). Despite its potent anticancer activity, cisplatin is associated with dose-limiting side effects, including nephrotoxicity and ototoxicity. Nephrotoxicity, characterized by renal tubular damage and impaired kidney function, is a major concern in cisplatin therapy (Miller *et al.,* 2010). Strategies to mitigate cisplatin-induced nephrotoxicity, such as hydration protocols and the use of nephroprotective agents like amifostine, have been explored to improve the tolerability of cisplatin treatment (Pabla and Dong, 2008).

1.4.1.2 Treatment Mechanism

In addition to its role in solid tumors, cisplatin has also shown activity in the treatment of hematologic malignancies, particularly in combination regimens with other chemotherapeutic agents. The combination of cisplatin with drugs such as etoposide, vinblastine, or bleomycin has been utilized in the treatment of various cancers, including non-small cell lung cancer and germ cell tumors (Peters *et al.,* 2012). These combination regimens have demonstrated synergistic effects, enhanced the antitumor activity of cisplatin and improved treatment outcomes in patients with advanced or metastatic disease. The combination of cisplatin with other agents, such as paclitaxel or gemcitabine, has shown synergistic effects in enhancing anti-tumor activity and overcoming drug resistance (Kartalou and Essigmann, 2001).

1.4.1.3 Drug Resistance

The development of resistance to cisplatin remains a significant challenge in cancer therapy. Mechanisms of cisplatin resistance include decreased drug accumulation, increased drug efflux, alterations in DNA repair pathways, and upregulation of anti-apoptotic proteins (Galluzzi *et al.,* 2012). Understanding the molecular mechanisms underlying cisplatin resistance is critical for the development of novel therapeutic strategies, such as combination therapies with targeted agents or immunotherapies, to overcome resistance and improve treatment responses in patients with refractory or recurrent disease.

1.4.2 IRINOTECAN

Irinotecan is a semisynthetic camptothecin derivative and a potent topoisomerase I inhibitor that is extensively used in the treatment of a variety of solid malignancies, most notably colorectal cancer, as well as lung and pancreatic cancers (Kamle *et al.,* 2024). Following administration, irinotecan is converted by carboxylesterases into its active metabolite, SN-38, which is primarily responsible for its antitumor activity. SN-38 exerts cytotoxic effects by stabilizing the transient DNA–topoisomerase I

cleavage complex, thereby preventing the re-ligation of single-strand DNA breaks that normally occur during DNA replication and transcription. As a result, the accumulation of unrepaired single-strand breaks leads to replication fork collapse and the formation of lethal double-strand DNA breaks during S-phase, ultimately triggering apoptosis in rapidly proliferating cancer cells (Pommier, 2006; Kamle *et al.,* 2024).

Clinically, irinotecan has demonstrated significant efficacy in both first-line and second-line treatment settings, either as a monotherapy or as part of combination regimens such as FOLFIRI, where it is combined with fluoropyrimidines and leucovorin (Zhang *et al.,* 2022). These combination strategies have been shown to improve response rates, progression-free survival, and overall survival in patients with advanced colorectal cancer. In addition to its role in colorectal cancer, irinotecan has shown therapeutic benefit in other solid tumors, including small-cell and non-small-cell lung cancers and pancreatic cancer, highlighting its broad anti-tumor activity. The effectiveness of irinotecan is further supported by its ability to target rapidly dividing tumor cells while exploiting defects in DNA repair pathways commonly present in cancer cells. Despite its clinical success, treatment with irinotecan can be limited by dose-limiting toxicities, such as severe diarrhea and myelosuppression, as well as the development of drug resistance (Díaz-Villamarín *et al.,* 2025). Ongoing research therefore focuses on optimizing dosing strategies, identifying predictive biomarkers of response, and exploring combination therapies to enhance efficacy while minimizing adverse effects. Collectively, these characteristics underscore the importance of irinotecan as a key chemotherapeutic agent in modern oncology and support its continued use and development in cancer treatment.

1.4.2.1 Challenges in Treatment

One of the major limitations of irinotecan-based chemotherapy is the development of dose-limiting toxicities, most notably severe diarrhea and myelosuppression, which can significantly impact treatment continuity and patient quality of life. Irinotecan-induced diarrhea is among the most frequent and clinically significant adverse effects and occurs in two distinct forms: an early-onset, acute diarrhea that develops during or shortly after infusion, and a delayed-onset diarrhea that can occur several days after treatment (Díaz-Villamarín *et al.,* 2025). Early-onset diarrhea is thought to be mediated by irinotecan's cholinergic properties, leading to increased intestinal motility and secretions, whereas delayed-onset diarrhea is primarily attributed to direct cytotoxic damage to the intestinal mucosa, resulting from inhibition of rapidly proliferating epithelial cells in the gastrointestinal tract (Rothenberg, 2001). This mucosal injury disrupts intestinal barrier function, promotes inflammation, and impairs fluid absorption, thereby exacerbating diarrheal symptoms.

In addition to gastrointestinal toxicity, irinotecan commonly causes myelosuppression, particularly neutropenia, which increases the risk of infection and may necessitate treatment delays or dose reductions (Díaz-Villamarín *et al.,* 2025). The severity of these toxicities is influenced by individual patient factors, including genetic variations affecting irinotecan metabolism, such as polymorphisms in

the UGT1A1 gene that impair the glucuronidation and clearance of the active metabolite SN-38. As a result, patients with reduced metabolic capacity may experience higher systemic exposure to SN-38 and an increased risk of severe toxicity (Faisal *et al.,* 2025). To manage irinotecan-associated diarrhea and improve treatment tolerability, several strategies have been implemented in clinical practice, including the prompt use of antidiarrheal agents such as loperamide, dose modification protocols, and supportive care measures such as hydration and electrolyte replacement. In severe cases, hospitalization and the use of additional pharmacological interventions may be required. Collectively, these toxicity management strategies are essential for maintaining patient adherence to irinotecan therapy, optimizing therapeutic outcomes, and minimizing treatment-related complications, while ongoing research continues to focus on improving the safety profile of irinotecan through personalized dosing and combination approaches.

1.4.2.2 Treatment Mechanism

In addition to its established use in solid tumors, irinotecan has demonstrated encouraging anti-tumor activity in several hematologic malignancies (Kciuk, *et al.,* 2020; Kamle *et al.,* 2024). Preclinical studies have shown that irinotecan and its active metabolite, SN-38, effectively inhibit the proliferation of leukemic and lymphoid cells by inducing DNA damage and promoting apoptosis in rapidly dividing hematopoietic malignancies (Kamle *et al.,* 2024). These findings have provided the rationale for evaluating irinotecan in clinical settings involving hematologic cancers, particularly in patients with relapsed or refractory disease who have limited treatment options.

Combination approaches incorporating irinotecan with other cytotoxic agents or targeted therapies have been extensively investigated to enhance its therapeutic efficacy in hematologic malignancies. Garcia-Manero (2005) reported that combining irinotecan with agents such as cytarabine, anthracyclines, or topoisomerase II inhibitors resulted in synergistic anti-tumor effects, characterized by increased leukemic cell death and improved suppression of malignant clones. Such synergism is thought to arise from the complementary mechanisms of DNA damage induced by these agents, which overwhelm cellular repair pathways and amplify apoptotic signaling. Additionally, irinotecan has been evaluated in combination with emerging targeted therapies that disrupt survival signaling pathways in colon cancer cells, further enhancing treatment responses (Chai *et al.,* 2025).

Clinically, these combination strategies have shown promise in improving response rates and disease control in patients with refractory or relapsed hematologic malignancies, where standard therapies often fail to achieve durable remission. By enhancing anti-tumor activity while potentially allowing for dose reductions of individual agents, combination regimens may also help mitigate treatment-related toxicity (Chai *et al.,* 2025). Collectively, these findings underscore the potential role of irinotecan as a valuable component of combination therapy strategies in hematologic cancers and support continued investigation into optimized regimens aimed at improving outcomes for patients with aggressive or treatment-resistant disease.

1.4.2.3 Drug Resistance

Furthermore, the emergence of resistance to irinotecan represents a major obstacle to its long-term effectiveness in cancer therapy and is a frequent cause of treatment failure and disease progression (Pommier, 2006; Kumar *et al.,* 2023). Resistance to irinotecan arises through multiple, often overlapping mechanisms that reduce drug efficacy at both the pharmacokinetic and cellular levels (Pommier, 2006; Kumar *et al.,* 2023). One well-characterized mechanism involves alterations in irinotecan metabolism, particularly changes in the activity of enzymes responsible for its activation and detoxification. Variations in carboxylesterase activity can reduce conversion of irinotecan to its active metabolite SN-38, while increased expression or activity of UDP-glucuronosyltransferases, such as UGT1A1, enhances SN-38 inactivation and clearance, thereby lowering intracellular drug exposure (Mathijssen *et al.,* 2001; de Jong *et al.,* 2006). In parallel, overexpression of efflux transporters belonging to the ATP-binding cassette (ABC) family, including ABCB1 (P-glycoprotein) and ABCG2, promotes the active export of irinotecan and SN-38 from cancer cells, further diminishing cytotoxic accumulation (Ozawa *et al.,* 2021; Li *et al.,* 2016).

At the cellular level, enhanced DNA repair capacity represents another critical mechanism of irinotecan resistance. Cancer cells may upregulate components of DNA damage response and repair pathways, enabling more efficient resolution of topoisomerase I–mediated DNA lesions and preventing the accumulation of lethal DNA strand breaks (Ozawa *et al.,* 2021). Additionally, alterations in apoptotic signaling cascades can impair the ability of cancer cells to undergo programmed cell death in response to irinotecan-induced DNA damage. Dysregulation of key apoptotic regulators, including p53, Bcl-2 family proteins, and caspases, allows resistant cells to survive despite extensive genomic stress (Fukuoka *et al.,* 1998). Changes in cell cycle checkpoint control may further contribute to resistance by allowing damaged cells to bypass arrest and continue proliferating.

Given the complexity and heterogeneity of these resistance mechanisms, a comprehensive understanding of the molecular basis of irinotecan resistance is essential for optimizing therapeutic strategies (Pommier, 2006; Mathijssen *et al.,* 2001). This knowledge has driven the development of personalized treatment approaches, including biomarker-guided patient stratification based on genetic variants, transporter expression profiles, or DNA repair capacity (Innocenti *et al.,* 2004; Hoskins *et al.,* 2007). Moreover, rational combination regimens incorporating irinotecan with targeted agents that inhibit efflux transporters, suppress DNA repair pathways, or restore apoptotic sensitivity are being actively explored as strategies to overcome resistance (Pommier, 2006). Collectively, these approaches hold significant promise for improving treatment efficacy and clinical outcomes in patients with irinotecan-resistant cancers (Mathijssen *et al.,* 2001; Pommier, 2006).

1.5 PROBLEM STATEMENT

In the realm of cancer therapeutics, the exploration of natural compounds such as thymoquinone, β-lapachol, and β-lapachone has garnered significant attention for their potential anticancer properties in colon cancer and breast cancer. These compounds, derived from natural sources, have shown promising effects in preclinical studies, exhibiting cytotoxicity towards cancer cells, inhibiting tumor growth, and inducing cell death through various mechanisms (Smith and Jones, 2018). Despite these encouraging findings, a substantial gap exists in our current understanding of the optimal dosing regimens, mechanisms of action, and effective rates for cancer cell apoptosis associated with thymoquinone, β-lapachol, and β-lapachone in the context of colon cancer and breast cancer.

Moreover, while conventional chemotherapeutic agents like irinotecan are mainstays in the treatment of colon cancer and breast cancer, the potential synergistic effects and interactions of comparing irinotecan with thymoquinone, β-lapachol, and β-lapachone remain relatively unexplored. Understanding the dynamic interplay between these natural compounds and conventional chemotherapies is essential for maximizing treatment activity and improving outcomes for colon cancer and breast cancer patients, as well as potentially mitigating the adverse effects associated with traditional chemotherapeutic regimens.

By addressing these critical knowledge gaps, we can advance the field of cancer therapeutics and pave the way for the development of more effective and personalized treatment approaches for colon cancer and breast cancer patients. Through comprehensive investigations into the individual effects of thymoquinone, β-lapachol, and β-lapachone in these cancer types, we can unlock the full therapeutic potential of these natural compounds, leading to the development of innovative strategies that harness their benefits to overcome therapeutic challenges and ultimately improve patient outcomes in the battle against colon cancer and breast cancer.

CHAPTER 2: AIMS AND OBJECTIVES

2.1 AIMS

The aim of the study is to compare the potential anticancer activities of β-lapachone, β-lapachol, and thymoquinone in combination with known anticancer drugs in colon cancer (HCT116) and breast cancer (MCF-7) cell lines. The study also seeks to elucidate the molecular targets of these compounds, with the ultimate goal of identifying novel and effective treatment strategies for these types of cancer.

2.2 OBJECTIVES

- To evaluate the individual effects of β-lapachone, β-lapachol, thymoquinone, cisplatin, and irinotecan on the viability of HCT116 and MCF-7 cell lines using the AlamarBlue® cell viability assay and to determine IC_{50} values through dose–response analysis.

- To determine the nature of drug–drug interactions (synergistic, additive, or antagonistic) between β-lapachone, β-lapachol, thymoquinone, and irinotecan using combination treatments, followed by Combination Index (CI) analysis based on the Chou–Talalay method (CompuSyn software).

- To assess cell cycle phase distribution changes induced by selected combination treatments using flow cytometry (Muse® Cell Analyzer) to quantify the proportion of cells in G_0/G_1, S, and G_2/M phases.

- To evaluate apoptosis induced by combination treatment regimens by measuring caspase-3 activity using the EnzChek® Caspase-3 assay, with fluorescence normalized to total protein concentration.

CHAPTER 3: METHODOLOGY

3.1 OVERVIEW

This study followed a stepwise experimental design to evaluate both the individual and combinational effects of selected compounds. Initially, single-agent dose–response experiments were performed using the AlamarBlue® assay to determine the cytotoxic potency (IC_{50} values) of β-lapachone, β-lapachol, thymoquinone, cisplatin, and irinotecan in MCF-7, HCT116, and VERO cell lines. Based on these results, irinotecan was selected as the primary combination partner due to its clinically established role as a topoisomerase I inhibitor and its moderate single-agent efficacy, making it suitable for detecting synergistic interactions. In contrast, cisplatin was excluded from combination studies due to its high intrinsic cytotoxicity and non-selective mechanism of action, which could mask potential synergistic effects.

Subsequently, combination treatments of β-lapachone, β-lapachol, and thymoquinone with irinotecan were evaluated using the Chou–Talalay method to determine synergistic, additive, or antagonistic interactions. The most relevant combinations were then further investigated using mechanistic assays, including caspase-3 activity (EnzChek® assay) to assess apoptosis and flow cytometry (Muse® Cell Analyzer) to evaluate cell cycle distribution. This structured approach, indicated a **Figure 6**, ensured that initial screening informed and guided subsequent mechanistic analyses.

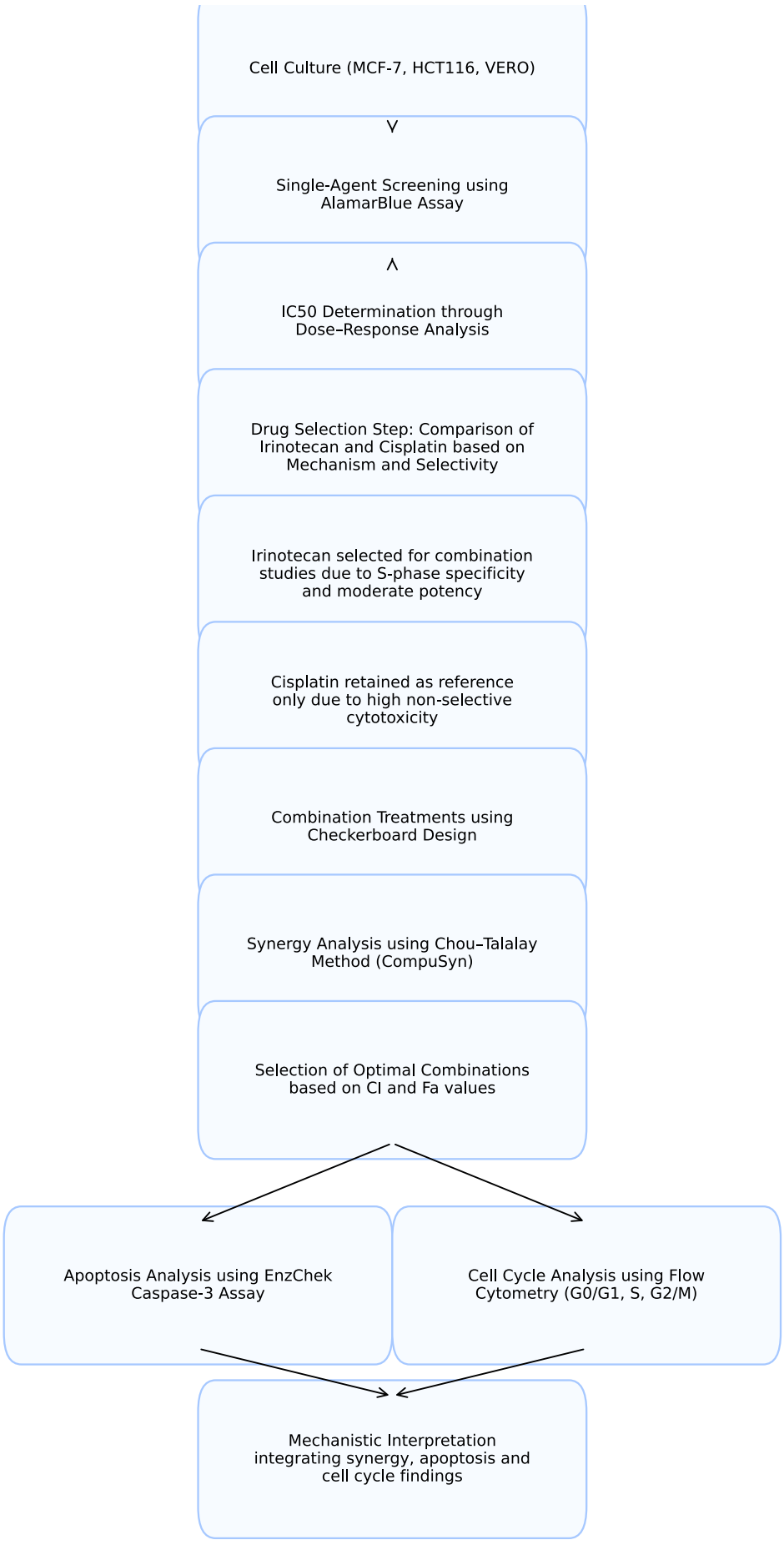

Cell Culture (MCF-7, HCT116, VERO)
Single-Agent Screening using AlamarBlue Assay
IC50 Determination through Dose–Response Analysis
Drug Selection Step: Comparison of Irinotecan and Cisplatin based on Mechanism and Selectivity
Irinotecan selected for combination studies due to S-phase specificity and moderate potency
Cisplatin retained as reference only due to high non-selective cytotoxicity
Combination Treatments using Checkerboard Design
Synergy Analysis using Chou–Talalay Method (CompuSyn)
Selection of Optimal Combinations based on CI and Fa values
Apoptosis Analysis using EnzChek Caspase-3 Assay
Cell Cycle Analysis using Flow Cytometry (G0/G1, S, G2/M)
Mechanistic Interpretation integrating synergy, apoptosis and cell cycle findings

Figure 6: Schematic Overview of the Experimental Workflow Illustrating the Rationale for Drug Selection and Downstream Analyses. Following single-agent screening and IC_{50} determination, irinotecan and cisplatin were compared based on mechanism of action and selectivity. Irinotecan was selected for combination studies due to its S-phase–specific activity and moderate cytotoxicity, while cisplatin was retained as a reference compound due to its high non-selective cytotoxicity. Combination treatments were evaluated using the Chou–Talalay method, and optimal combinations were further investigated through apoptosis (caspase-3 activity) and cell cycle analyses, culminating in integrated mechanistic interpretation.

3.2 RESEARCH ETHICS CLEARANCE

Ethical approval for the research was obtained in accordance with the UNISA-CAES Health Research Ethics Committee, with the NHREC Registration number: REC-170616-051and Reference number: 2024/CAES_HREC/5118

3.3 CELL CULTURE

3.3.1 Cell Lines: The human colon cancer cell line (HCT116 - CRL-3511), non-cancerous kidney cell from the African green monkey (VERO - CCL-81), and human breast cancer cell line (MCF-7 - HTB-22) were utilized in this study to investigate the effects of thymoquinone, β-lapachol, and β-lapachone, alone and in combination, with a conventional chemotherapeutic agent irinotecan. These cell lines were obtained from American Type Culture Collection, South Africa (ATCC) and were utilized from frozen stocks. The (VERO), non-cancerous kidney cell from the African green monkey cell line solely served as a control due to its non-cancerous nature.

3.3.2 Cell Culture Conditions: The frozen (-80 °C) cell lines were thawed at room temperature. Following this, the thawed cells was transferred to a T25 culture flask filled with 5 ml of recovery media, which consists of 20% fetal bovine serum (FBS), 1% penicillin-streptomycin, and 79% High glucose (4500 mg/L) Dulbecco's Modified Eagle Medium (DMEM) with L-Glutamine (4.00 mM). These cells were placed in an incubator set at 37 °C with 5% CO_2 and kept humid until 80-90% confluency was reached. Once required confluency was reached, the cells were regularly passaged for subsequent experiments.

To passage the cells, the media is the cell culture flask was discarded, and the flask was rinsed with 2-5 ml of phosphate-buffered saline (PBS) at a pH of 7.5. This rinsing step was repeated to ensure complete removal of the media before the trypsin-EDTA treatment. For the trypsin-EDTA treatment, 2-5 ml of 1 X trypsin-EDTA were added to the flask, and it was incubated at 37 °C for 5-10 minutes to aid in cell detachment. The time required for trypsinization varied depending on the cell line. Subsequently, 2-5 ml of pre-warmed maintenance media (consisting of 10% FBS, 1% penicillin-streptomycin, and 89% High Glucose Dulbecco's Modified Eagle Medium with L-Glutamine) was introduced to the flask to stop the trypsin-EDTA reaction. The cell solution was transferred to a sterile 15 ml tube and centrifuged at

100 x *g* for 3 minutes. The supernatant was then removed, and the cell pellet was suspended in 1-2 ml of fresh pre-warmed maintenance media. This resuspended cell solution was then distributed into a new T75 culture flask containing 8 ml of maintenance media for further sub-culturing. Subsequently, the cells were incubated in a humidified incubator at 37 °C with 5 % CO_2.

3.4 CELL COUNTING

The cell counting process involved the use of a hemocytometer. Initially, the resuspended cell solution was diluted with maintenance media that had been pre-warmed. Following this, a 10 µl aliquot of the diluted cell suspension was mixed with 10 µl of 0.4% trypan blue solution in an Eppendorf tube. The mixture was thoroughly combined and allowed to incubate for 5 minutes. Afterward, a coverslip was placed on the hemocytometer, and the mixture of cells and trypan blue was loaded into the hemocytometer chambers with a pipette. Counting was performed in the four corner squares, each measuring 1 mm. Cells that were touching the top and left borders of the squares were counted, whereas those in contact with the bottom and right borders were excluded from the count. The trypan blue dye-stained non-viable cells blue, making it easier to differentiate them from viable cells. The concentration of cells per milliliter was calculated based on the counts obtained using the following calculation:

Number of cells per ml: average count per square x 10^4 x dilution factor / number of squares counted

The average cell count was determined by calculating the number of cells counted in the four squares examined. Each square had a volume of 0.1 mm^3, equivalent to 10^{-4} cm^3. A dilution factor of 2 was applied because the cell suspension was diluted two-fold with trypan blue, effectively halving the original concentration. A total of four squares were analyzed. Only the counts of viable cells were utilized to calculate the concentration of cells per milliliter.

3.5 DRUG TREATMENT

The drug treatment of the cell lines MCF-7, HCT116, and VEROS was conducted uniformly. The drug agents, β-lapachone (A stock solution (10mM) of β-lapachone was made by dissolving in DMSO), β-lapachol (A stock solution (10mM) of β-lapachol was made by dissolving in DMSO), thymoquinone (A stock solution (10mM) of TQ was made by dissolving in ethanol), cisplatin (A stock solution (3mM) of cisplatin was made by dissolving in PBS), and irinotecan (A stock solution (10mM) of irinotecan was made by dissolving in DMSO), was applied to the cell lines at various concentrations to evaluate its effects on human breast cancer cells (MCF-7), human colon cancer cells (HCT116), and kidney cell line of the African green monkey (VERO). All the compounds were acquired from Merck, South Africa.

The cell lines were cultured as previously mentioned. After collecting the cell pellet, it was resuspended in 1 ml of fresh pre-warmed maintenance media, and the cells were counted according to the method described in **Section 3.4**. The cells were then seeded based on the experimental requirements and incubated for 24 hours to allow attachment in the maintenance media. Once the cells adhered, the maintenance media was removed and replaced with fresh DMEM containing different concentrations of β-lapachone (0.5 µM to 55 µM), β-lapachol (25 µM to 175 µM), thymoquinone (25 µM to 175 µM), cisplatin (25 µM to 175 µM), and irinotecan (25 µM to 175 µM). The cells were incubated for 24 hours at 37 °C with 5% CO_2 in a humidified incubator.

After the 24-hour incubation with the drug, floating cells were collected by decanting the media into a sterile 15 ml tube and centrifuging at 100 x *g* for 5 minutes. Remaining attached cells were harvested through trypsinization. The dead floating cells and the live trypsinized cells from each plate were combined, and the cell mixture was pelleted by centrifugation at 1000 x *g* for 5 minutes. Both the floating and attached cells were collected for experimentation to ensure unbiased results.

Controls included untreated cells, where the β-lapachone, β-lapachol, thymoquinone, cisplatin, and irinotecan was replaced with DMEM. These untreated controls served as a reference for comparison against the treated samples. Vehicle controls included cells treated with ethanol, DMSO, and PBS which was the solvent used to dilute the powdered β-lapachone, β-lapachol, thymoquinone, cisplatin, and irinotecan. The vehicle controls with ethanol, DMSO, and PBS were subjected to a concentration of 75 µM. This setup helped determine any potential effects of the vehicle on the cells that could influence the results of the β-lapachone, β-lapachol, thymoquinone, cisplatin, and irinotecan treatment.

3.6 ALAMAR BLUE ASSAY

3.6.1 INDIVIDUAL DRUG TREATMENTS ON CANCER AND NON-CANCEROUS CELL LINES

The Alamar Blue assay was used to evaluate the cytotoxicity of various concentrations of the compounds and cell lines mentioned in **Section 3.3.1**. This assay is a colorimetric method that measures cell viability based on the reduction of resazurin, a blue non-fluorescent compound, to the pink fluorescent resorufin in metabolically active cells. The observable color change reflects the viability of the cells in response to the different β-lapachone, β-lapachol, thymoquinone, cisplatin, and irinotecan concentrations.

For each cell line, the cells were harvested and counted as previously described in **Section 3.4** and then 10 000 cells were seeded to each well of a black 96-well plate. The cells were then incubated for 24 hours at 37 °C with 5% CO_2 in a humidified incubator to facilitate cell attachment. After the attachment period, 50 µL of different concentrations of β-lapachone, β-lapachol, thymoquinone,

cisplatin, and irinotecan, was added to the wells. The cells treated with the drugs continued to incubate for 24 hours at 37 °C with 5% CO_2.

Following the drug treatment, 20 µL of Alamar Blue reagent was added to each well, and the cells were incubated for an additional 2 to 6 hours at 37 °C with 5% CO_2. This allowed sufficient time for the reduction of resazurin to occur in viable cells. After incubation, the fluorescence intensity of the solution was subsequently measured using a Varioskan microplate reader, typically set to an excitation wavelength of 560 nm and an emission wavelength of 590 nm.

The results obtained from the Alamar Blue assay provided quantitative data on cellular viability, allowing for a comprehensive assessment of the impact of β-lapachone, β-lapachol, thymoquinone, cisplatin, and irinotecan on the tested cell lines. In addition, this assay was performed using technical replicates, with cells seeded in triplicate wells for each concentration and control in a 96-well plate to minimize intra-assay variability. Cells were expanded from three independent flasks, pooled, and plated under identical conditions to ensure consistency. Fluorescence readings were averaged per condition and used for dose–response analysis and IC_{50} determination in GraphPad Prism 9 software.

3.6.2 COMBINATION DRUG TREATMENTS ON CANCER AND NON-CANCEROUS CELL LINES

The Alamar Blue assay was utilized to evaluate the cytotoxicity of various drug combinations, including β-lapachone, β-lapachol, thymoquinone, and irinotecan, on human breast cancer cells (MCF-7), human colon cancer cells (HCT116), and the kidney cell line of the African green monkey (VERO).

For each cell line, the cells were harvested and counted as previously described in **Section 3.4** and then 10 000 cells were seeded to each well of a black 96-well plate. The cells were incubated for 24 hours at 37 °C with 5% CO_2 in a humidified incubator to facilitate cell attachment. After this attachment period, 50 µL of various drug combinations were added to the wells according to the checkerboard method. The concentrations were now used in combinations where the IC_{50} values were used. For thymoquinone, β-lapachone, and β-lapachol the IC_{50} values were multiplied by 0.1, 0.25, 0.5, 1.0, 1.5, and 2.0. For irinotecan the IC_{50} values were multiplied by, 0.5, 1.0, 1.5, and 2.0. The cells continued to incubate for another 24 hours at 37 °C with 5% CO_2.

Following the drug treatment, 20 µL of Alamar Blue reagent was added to each well, and the cells were incubated for an additional 2 to 6 hours at 37 °C with 5% CO_2. This incubation allowed enough time for the reduction of resazurin to occur in viable cells. After the incubation period, the fluorescence intensity of the solution was measured using a Varioskan microplate reader, typically set to an excitation wavelength of 560 nm and an emission wavelength of 590 nm.

The results obtained from the Alamar Blue assay provided quantitative data on cellular viability, enabling a comprehensive evaluation of the effects of the drug combinations on the tested cell lines. To analyze the interactions between the drugs, the Chou-Talalay method was employed. This method

allows for the assessment of drug synergy, additivity, or antagonism by calculating the combination index (CI) values (Chou, 2010). The Compusyn software was used to facilitate this analysis, providing a user-friendly platform for evaluating the efficacy of the drug combinations based on the dose-response data obtained from the assay (Chou and Martin, 2006).

It is important to note that cisplatin has been excluded from these combination treatments due to the cytotoxic and adverse effects observed during the single-agent treatments. In previous studies, cisplatin has been associated with significant nephrotoxicity and other severe side effects, which can limit its clinical utility (Jiang *et al.,* 2018). The results from the single treatments confirmed that cisplatin not only exhibited high cytotoxicity but also led to detrimental effects on cell viability across the tested cell lines. These findings align with existing literature, which highlights the challenges of using cisplatin in combination therapies due to its toxicity profile (Kelland, 2007).

Given these considerations, the focus then shifted towards exploring alternative agents that may offer similar therapeutic benefits without the associated risks of cisplatin. Overall, this study offers valuable insights into the potential of these drug combinations in cancer treatment, highlighting their effects on cell viability and the importance of utilizing appropriate analytical methods to determine their interactions.

In addition, the AlamarBlue combination-treatment experiments were performed using technical replicates, with cells seeded in triplicate wells for each drug combination, concentration, untreated control, and single-agent control in a 96-well plate to minimize intra-assay variability. Cells were expanded from three independent culture flasks, pooled, and plated under identical conditions to ensure consistency and reduce variability related to passage number and confluency. Fluorescence readings were averaged per condition and used for checkerboard analysis, dose–response evaluation, and synergy assessment using the Chou–Talalay method in CompuSyn software.

3.7 ENZCHEK ASSAY

The EnzChek Caspase-3 Activity Assay (Thermo Fisher Scientific) is a sensitive, fluorescence-based biochemical assay designed to specifically measure the enzymatic activity of caspase-3, a key executioner protease involved in the apoptotic pathway. The assay is based on the use of a synthetic fluorogenic peptide substrate, Z-DEVD-AMC, which contains the canonical caspase-3 recognition sequence Asp-Glu-Val-Asp (DEVD) conjugated to the reporter fluorophore 7-amino-4-methylcoumarin (AMC). In its intact form, AMC remains non-fluorescent due to quenching by the peptide moiety. Upon cleavage of the DEVD sequence by active caspase-3, free AMC is released, resulting in a measurable fluorescent signal.

The fluorescence generated by liberated AMC is detected using a microplate reader at specific excitation and emission wavelengths appropriate for AMC, and the intensity of the signal is directly

proportional to the amount of caspase-3 activity present in the sample. Because the DEVD peptide sequence is selectively recognized by caspase-3 (and closely related effector caspases), the assay provides a high degree of specificity for apoptosis-associated proteolytic activity. To further ensure assay specificity, the EnzChek system allows for the inclusion of a caspase-3–specific inhibitor (Z-DEVD-CHO), which competitively binds to the enzyme's active site and prevents substrate cleavage, serving as a biochemical control for non-specific fluorescence.

Prior to fluorescence measurement, cells are lysed under controlled conditions to release intracellular proteins, ensuring that enzymatic activity is measured independently of membrane integrity or uptake variability. The assay is typically conducted under optimized buffer conditions that preserve enzyme activity and support consistent substrate cleavage kinetics. Fluorescence can be measured at defined time intervals, enabling assessment of enzyme activity as a function of time and allowing calculation of reaction rates if required.

Overall, the EnzChek Caspase-3 assay provides a quantitative, enzyme-specific approach to measuring apoptotic protease activity at the biochemical level. By directly assessing caspase-3–mediated substrate cleavage, the assay enables precise evaluation of apoptosis-associated enzymatic processes independently of morphological or viability-based readouts.

3.7.1 Combination Treatments

For this assay, 600,000 HCT116 cells and 500,000 MCF-7 cells were seeded per well in a 6-well plate. The difference in seeding density was implemented to account for inherent biological differences between the two cell lines, including variations in cell size, morphology, and proliferation rate. HCT116 cells are generally smaller and exhibit a higher proliferative capacity compared to the larger, more epithelial-like MCF-7 cells. Consequently, a higher number of HCT116 cells was required to achieve comparable surface coverage and confluency within the same incubation period. Standardizing confluency at the time of treatment is critical, as cell density can influence cellular metabolism, cell cycle distribution, and drug sensitivity. By adjusting the initial seeding densities, both cell lines were maintained under comparable physiological conditions, ensuring that observed treatment effects were attributable to the drug interventions rather than differences in growth characteristics or cell density.

Cells were incubated overnight (24 hours) to allow for proper attachment. Following this, various drug concentrations were prepared in Dulbecco's Modified Eagle Medium (DMEM) without fetal bovine serum (FBS). After gently removing the media, 500 µL of each drug concentration was added to the respective wells. Control wells received media only (no drugs), while vehicle control wells contained 500 µL of media with ethanol and/or DMSO to ensure consistent volumes across all conditions. The cells were then incubated for an additional 24 hours. After exactly 24 hours, the cells were harvested by scraping and transferring the contents of each well into Eppendorf tubes.

The samples were centrifuged to discard the media, followed by a wash with 200 µL of PBS, and after the PBS wash, another centrifugation step was done to remove the PBS. Subsequently, 50 µL of 1X cell lysis buffer was added to each sample in the Eppendorf tubes, which were then frozen at -80 °C. After freezing, the tubes were thawed and incubated on ice for 30 minutes. For the fourth Eppendorf tube of each cell type, 1 µL of Ac-DEVD-CHO (a synthetic, cell-permeable peptide inhibitor of caspase-3) stock solution was added, mixed well, and incubated for 10 minutes at room temperature, while the other samples continued to incubate on ice for the full 30 minutes, covered in foil. Following incubation, the samples were centrifuged at 5000 rpm for 5 minutes to pellet the cellular debris. A volume of 50 µL of supernatant from each sample was transferred to a black 96-well plate. A no-enzyme control was set up by adding 50 µL of 1X cell lysis buffer to one well to determine the background fluorescence of the substrate. Each sample and control then received an additional 50 µL of the 2x substrate working solution. Standard dilutions of AMC (a reporter fluorophore 7-amino-4-methylcoumarin) stock (0, 7, 14, 21, 28, 35, 42, and 49) were prepared, with 100 µL or 90 µL added to empty wells as needed. The black 96-well plates were covered with foil and incubated at room temperature for 30 minutes, after which fluorescence was measured, followed by an additional 30-minute incubation and a second reading. Fluorescence intensity was assessed using a Varioskan microplate reader with excitation set at 342 nm and emission at 441 nm.

For the combination treatments, cell lines were treated with the following concentrations of thymoquinone in combination with irinotecan (MCF-7: concentration 1: 72.9 µM with 49.67 µM, concentration 2: 72.9 µM with 99.34 µM. HCT116: concentration 1: 94.2 µM with 123.8 µM, concentration 2: 141.3 µM with 61.9 µM), β-lapachone in combination with irinotecan (MCF-7: concentration 1: 6.71 µM with 49.67 µM, concentration 2: 13.41 µM with 49.67 µM), and β-lapachol in combination with irinotecan (MCF-7: concentration 1: 30.85 µM with 149.01 µM, concertation 2: 61.7 µM with 149.01 µM. HCT116: concentration 1: 6.05 µM with 30.95 µM, concentration 2: 12.1 µM with 30.95 µM) to target distinct pathways in cancer cell proliferation and survival. The rationale for these combination therapies stemmed from the hypothesis that concurrent targeting of multiple pathways could lead to more effective induction of apoptosis.

The fluorescence data obtained were then analyzed to determine the combined effects on caspase activity. By assessing the fluorescence intensity from the EnzChek assay, it was possible to discern whether the combined treatments resulted in a significantly heightened caspase activity compared to either drug used alone. This data was critical in identifying effective drug combinations that could improve therapeutic outcomes.

In addition, The EnzChek Caspase-3 activity assay for combination treatments was performed using technical replicates, with cells seeded in triplicate wells for each treatment, including untreated and inhibitor controls, within the same microplate to minimize intra-assay variability. Fluorescence readings were averaged per condition at each time point and used for normalization to total protein content and calculation of caspase-3 activity. Data analysis and graphical presentation were performed using Microsoft Excel and GraphPad Prism 9 software.

3.7.2.1 QUBIT ASSAY

The Qubit assay was adapted to measure protein concentrations in the same samples as for the Enzchek assay. The protein quantification was performed using a specific Qubit Protein Assay kit, which utilized a different fluorescent dye that selectively binds to proteins. For the protein assay, a volume of 20 µL of the protein sample was mixed with the Qubit protein reagent and incubated briefly to facilitate the binding of the dye to the proteins. The fluorescence was measured using the Qubit fluorometer 2.0, yielding the concentration of protein in each sample.

The concentration values of the proteins obtained from the Qubit assay were essential for further experimental validation. Notably, these protein concentrations were critical for correlating the caspase-3 activity data generated from the EnzChek assay, which measures the activity of caspases involved in apoptotic processes. By knowing the protein concentration for each sample, researchers could standardize the caspase-3 activity results based on protein content, allowing for more accurate and informative comparisons across different treatment groups.

3.7.2.1.1 Caspase-3 Activity Correlation

To construct the caspase-3 activity graph for the EnzChek assay, the caspase-3 activity in the treated samples using the EnzChek assay method was first assessed, which employs fluorogenic substrates specific to caspase-3. Following the assay, the fluorescence intensity from caspase-3 activity was recorded. The enzyme activity data obtained was then normalized to the protein concentrations measured by the Qubit assay.

Normalization involved calculating caspase-3 activity per microgram of protein, ensuring that each data point on the graph accurately represented the specific activity of caspase-3 relative to the total protein present in the sample. This normalization was crucial as it allowed for fair comparisons between groups with varying protein concentrations, providing a clearer understanding of how the treatments influenced caspase-3 activity. Calculations used was (AMC) / min x µg and caspase – 3 activity x µL.

Protein quantification was performed in technical replicates using the Qubit™ Protein Assay Kit, with each sample measured in triplicate to ensure accuracy and consistency. The triplicate readings were averaged to obtain a single mean protein concentration (µg/µL) for each condition, which was used to normalize EnzChek Caspase-3 fluorescence data and express enzyme activity as (AMC fluorescence units/min)/µg protein.

3.8 FLOW CYTOMETRY: MUSE CELL CYCLE KIT

3.8.1 Combination Treatments

The Muse® Cell Cycle Kit was used to assess the effects of single and combination treatments on cell cycle progression in human breast cancer (MCF-7) and human colon cancer (HCT116) cell lines. This assay is a flow cytometry–based method that quantifies cellular DNA content following propidium iodide (PI) staining, thereby allowing for determination of the proportion of cells in the G_0/G_1, S, and G_2/M phases of the cell cycle. The Muse Cell Cycle reagent contains PI and RNase, enabling selective staining of double-stranded DNA while eliminating RNA interference.

Cells were treated with the combination of thymoquinone, β-lapachone, and β-lapachol, with irinotecan, and their combination at concentrations were determined from the EnzChek Caspase-3 assay and the Qubit protein quantification assay.

In the flow cytometry protocol, 600,000 MCF-7 cells were seeded into 4 T75 flasks, each containing 8 mL of media. Meanwhile, 600,000 HCT116 cells were seeded into 3 T75 flasks, also with 8 mL of media. The experimental groups for MCF-7 included one untreated flask, one flask treated with TQ and IRI (72.9 µM TQ and 99.34 µM IRI), one flask treated with β-OL and IRI (61.7 µM β-OL and 149.01 µM IRI), and one flask treated with β-LAP and IRI (13.41 µM β-LAP and 49.67 µM IRI). For HCT116, the groups included one untreated flask, one flask treated with TQ and IRI (141.3 µM TQ and 61.9 µM IRI), and one treated flask with β-OL and IRI (12.1 µM β-OL and 30.95 µM IRI). After a 24-hour incubation period, the combination drug concentrations were prepared in normal clean media, with 27 500 µL (27.5 mL) of each concentration created. The media was then removed from all flasks, and 9 mL of each drug concentration was added to the respective flasks, with 9 mL of DMEM added to the untreated wells. Following another 24-hour incubation, fresh 70% ethanol was prepared by mixing cold 100% ethanol with autoclaved water (70 mL ethanol and 30 mL water), and stored at -20°C. It was noted to always use the prepared ethanol on ice. After the second incubation, all cells were scraped off from the media and transferred to 4 labeled 15 mL tubes for MCF-7 and 3 labeled 15 mL tubes for HCT116. The tubes were centrifuged at 300 x *g* for 5 minutes, and the supernatant was discarded. Each pellet received 1 mL (1000 µL) of PBS and was mixed gently by pipetting or vortexing, before being transferred to 2 mL labeled Eppendorf tubes. The cells were then centrifuged again at 300 x *g* for 5 minutes, with the PBS supernatant removed. A fresh 75 µL of PBS was added to each tube, and the contents were mixed once more. Subsequently, 1000 µL of prepared ice-cold ethanol was added to the treated Eppendorf tubes containing the cell pellets while swirling gently. All tubes were then frozen at -20°C for at least 3 hours, preferably overnight. After thawing on ice, the cells were centrifuged at 300 x *g* for 5 minutes at room temperature, and the supernatant was removed. Each pellet received 0.5 mL (500 µL) of PBS, followed by another centrifugation at 300 x *g* for 5 minutes at room temperature, after which the supernatant was discarded. Lastly, 200 µL of Muse Cell Cycle Reagent was added to each tube, and the cells were incubated at room temperature in foil for 30 minutes. The contents were then transferred

into 4 labeled 1.5 mL Eppendorf tubes for MCF-7 and 3 labeled 1.5 mL Eppendorf tubes for HCT116, ready for flow cytometry analysis.

Data acquisition was performed on the Muse Cell Analyzer using the dedicated Cell Cycle software module, which generated histograms and automatically quantified the percentages of cells in G_0/G_1, S, and G_2/M phases. This approach enabled mechanistic evaluation of whether the treatments induced specific phase arrest.

Flow cytometry cell cycle analysis was conducted as a population-based assay, with each sample comprising thousands of individual cell events to provide statistically robust data in a single run. Cells were prepared and analyzed per treatment condition without replicate wells, as statistical confidence was derived from the large number of single-cell measurements recorded by the cytometer. Cell cycle phase distributions (G_0/G_1, S, and G_2/M) were therefore considered representative of each treatment condition.

3.9 Statistical Analysis and Quantitative Evaluation of Drug Responses and Interactions

All statistical analyses were performed using GraphPad Prism 9 software. Data are presented as mean ± standard deviation (SD) from technical replicates (triplicate wells), while error bars represent the standard error of the mean (SEM) across biological replicates where applicable. Statistical significance was set at $p < 0.05$ (*), with $p \leq 0.01$ (**) and $p \leq 0.001$ (***) indicating increasing levels of significance, and $p \geq 0.05$ considered not significant (ns).

For the AlamarBlue assay, dose–response curves were generated from averaged fluorescence values, and half-maximal inhibitory concentration (IC_{50}) values were determined using linear regression analysis of cell viability versus drug concentration. These values were used to assess drug potency and to guide concentration selection for subsequent experiments.

Drug–drug interactions were evaluated using the Chou–Talalay method implemented in CompuSyn software. Dose–response data were used to generate median-effect plots, from which the median-effect dose (Dm, equivalent to IC_{50}), slope (m), and correlation coefficient (r) were derived. The fraction affected (Fa) was calculated for each concentration, and Combination Index (CI) values were determined to classify interactions as synergistic (CI < 1), additive (CI = 1), or antagonistic (CI > 1). Dose–effect, median-effect, Fa–CI, and dose reduction index (DRI) plots were generated to comprehensively assess interaction profiles and identify optimal combination conditions.

For the EnzChek caspase-3 assay, fluorescence-based measurements were used to quantify caspase-3 activity, with results analyzed using the same statistical parameters described above to evaluate treatment effects on apoptosis.

Cell cycle analysis was performed using the Muse® Cell Analyzer software, which automatically calculates the percentage of cells in G_0/G_1, S, and G_2/M phases based on DNA content. The software applies an internal curve-fitting algorithm to determine phase distribution, and results are reported as percentages derived from total cell counts.

CHAPTER 4: RESULTS

4.1 CYTOTOXIC EFFECTS OF B-LAPACHONE, B-LAPACHOL, AND THYMOQUINONE, BOTH INDIVIDUALLY AND IN COMBINATION WITH THE CHEMOTHERAPEUTIC AGENT IRINOTECAN

4.1.1 Cytotoxic Effects of Individual Drug Treatments

To ensure consistent interpretation of cytotoxic effects, IC_{50} values were classified according to commonly applied thresholds used in anticancer drug screening studies. Compounds with IC_{50} values < 10 µM were considered highly potent, values between 10–50 µM moderately cytotoxic, values between 50–100 µM weak to moderate, and values > 100 µM weakly cytotoxic under the experimental conditions. These thresholds are widely used to contextualize biological relevance in *in vitro* assays, as potency alone does not necessarily reflect therapeutic activity (Fallahi-Sichani et al., 2013; Xu et al., 2020). Accordingly, IC_{50} values in this study were interpreted within this framework to distinguish biologically meaningful cytotoxic effects from statistically significant but limited reductions in cell viability.

Single-compound treatments produced concentration-dependent decreases in viability across the cancer cell lines, with notable differences in potency and selectivity. β-lapachone exhibited the strongest cytotoxic effect among the natural compounds, significantly reducing viability even at lower concentrations in both HCT116 and MCF-7 cells. Thymoquinone also caused a clear dose-dependent reduction, though with a more gradual slope, while β-lapachol showed moderate cytotoxicity apparent mainly at higher concentrations. Irinotecan, as a single agent, produced only a modest reduction in metabolic activity at 24 hours, resulting in a relatively high IC_{50}, as shown in appendix **Figure A 1**. Extending the incubation to 48 hours did not substantially reduce its IC_{50}, indicating that longer exposure alone was insufficient to increase its cytotoxic effect under these experimental conditions. Overall, the concentration-dependent decrease in viability varied between compounds, reflecting differences in their cytotoxic potency and efficacy.

In the VERO cell line, the three natural compounds showed markedly lower cytotoxicity, demonstrating a degree of cancer-selective activity. Irinotecan also caused only mild effects in VERO cells at 24 hours, whereas cisplatin displayed strong cytotoxicity across all cell lines, including VERO. Due to its high and non-selective toxicity, cisplatin was excluded from subsequent combination studies, as it would obscure potential interactions with irinotecan and the natural compounds. A summary interpretation of the cytotoxicity comparison across all three cell lines (MCF-7, HCT116, and VERO) with their slope and R^2 values are shown in appendix **Tables A 4 and A 5**, and in appendix **Figure A 2**. The statistical analysis is shown in appendix **Tables A 1 – A 3**.

4.1.1.1 MCF-7

Linear regression analysis confirmed a dose-dependent cytotoxic response for all tested compounds, as evidenced by the consistent negative correlation between concentration and cell viability. Among the natural compounds, thymoquinone and β-lapachone exhibited the steepest regression slopes, indicating rapid and pronounced loss of viability with increasing dose. β-Lapachone demonstrated an early onset of cytotoxicity at low micromolar concentrations, consistent with its bar-graph profile and the low IC_{50} observed in MCF-7 cells.

In contrast, β-lapachol showed a markedly shallower regression slope, reflecting a more gradual and moderate cytotoxic response. This reduced potency aligns with its less reactive naphthoquinone structure and supports its classification as the weakest of the natural compounds tested. For the chemotherapeutic agents, cisplatin displayed a strong negative slope indicative of robust cytotoxic activity across the tested concentration range. Irinotecan, however, exhibited a milder slope, confirming its comparatively weaker short-term cytotoxicity. This finding is consistent with irinotecan's dependence on intracellular conversion to its active metabolite, SN-38, and its S-phase-specific mechanism of action, both of which limit its apparent efficacy in 24-hour *in vitro* assays.

Overall, the linear regression analysis, as presented in **Figure 7**, underscores a clear dose-dependent decline in viability across all treatments, with the steepest slopes corresponding to the most potent cytotoxic agents. The ranking of cytotoxic potency, based on slope magnitude, was as follows: Thymoquinone > β-lapachone > cisplatin > irinotecan > β-lapachol. These findings confirm that both thymoquinone and β-lapachone exhibit strong concentration-dependent anticancer activity in MCF-7 cells and are thus the most promising candidates for subsequent combination and mechanistic analyses.

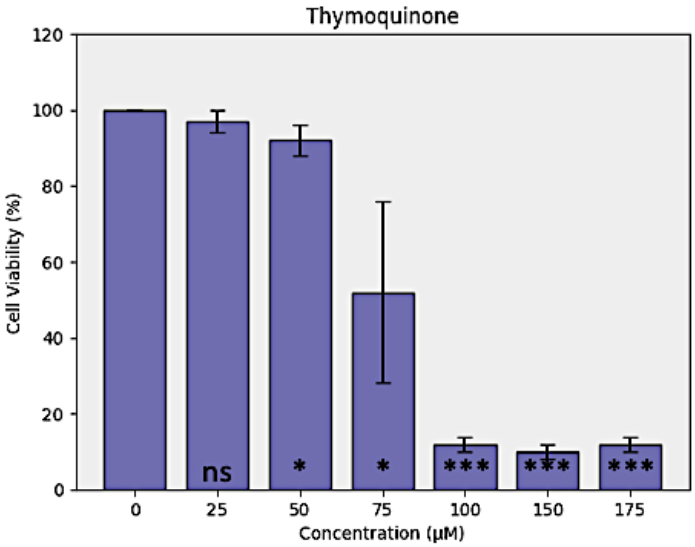
Thymoquinone (IC_{50} = 72.9 µM) and β-lapachol (IC_{50} = 61.7 µM) were classified as weak to moderate, indicating that higher concentrations are required to induce cytotoxicity. This is consistent with previous findings showing that thymoquinone primarily exerts anticancer effects through modulation of oxidative stress and apoptosis-related pathways such as PI3K/Akt, often requiring higher intracellular accumulation for significant activity (Woo et al., 2012). Similarly, β-lapachol exhibits reduced redox cycling compared to β-lapachone, resulting in lower cytotoxic potency (Hussain et al., 2007).

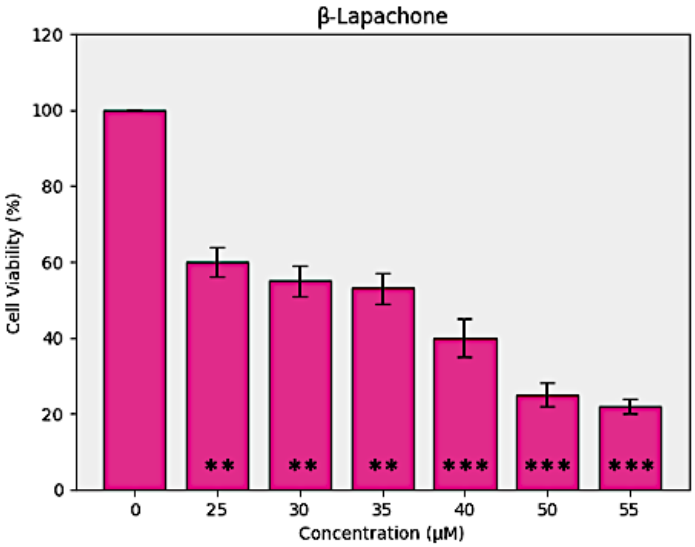
In contrast, β-lapachone exhibited an IC_{50} value of 26.8 µM, classifying it as moderately cytotoxic. This relatively strong activity is consistent with previous studies demonstrating that β-lapachone induces rapid cancer cell death through NAD(P)H:quinone oxidoreductase 1 (NQO1)-dependent redox cycling, leading to excessive ROS generation and DNA damage (Bey et al., 2013). The moderate IC_{50} observed in MCF-7 cells likely reflects variable NQO1 expression levels, which influence β-lapachone sensitivity.

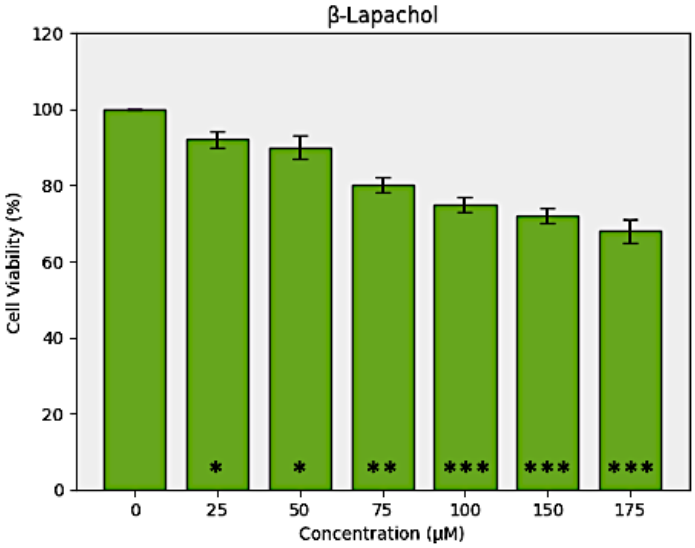
Cisplatin (IC_{50} = 26.6 μM) also fell within the moderately cytotoxic range, consistent with its well-established mechanism of DNA crosslinking and apoptosis induction. Its similar potency to β-lapachone aligns with reports showing that platinum-based agents produce substantial cytotoxicity in breast cancer cells regardless of hormone receptor status (Dasari and Tchounwou, 2014). However, due to its pronounced toxicity in both cancerous and non-cancerous cells (including VERO cells), cisplatin was excluded from subsequent combination experiments to avoid masking potential synergistic interactions.

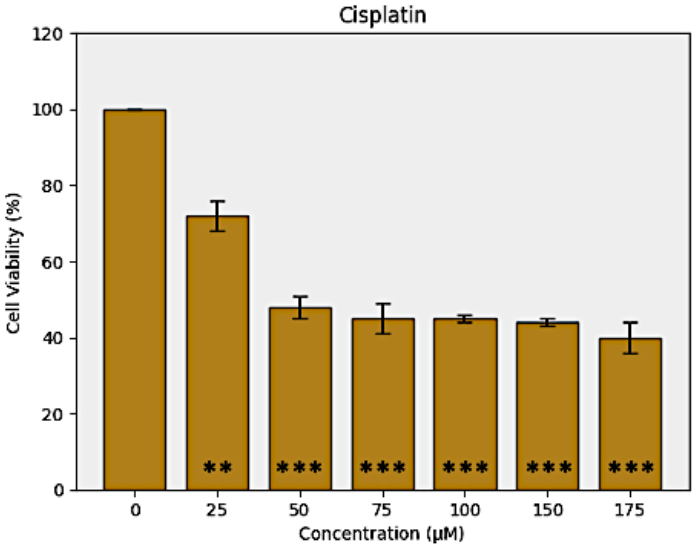
Irinotecan displayed the lowest potency (IC_{50} = 99.3 μM), placing it at the upper limit of the weak to moderate category. This reduced activity is consistent with its dependence on intracellular conversion to the active metabolite SN-38 and its S-phase-specific mechanism of action, which limits cytotoxic effects in short-term (24-hour) in vitro assays (Pommier, 2006).

Collectively, these findings in **Figure 7 and Table 1**, demonstrate that β-lapachone and thymoquinone are the most potent cytotoxic agents against MCF-7 cells, showing strong concentration-dependent declines in metabolic activity, while β-lapachol and irinotecan exhibit comparatively moderate effects. The statistical significance and steep slope of β-lapachone and thymoquinone justify their selection for subsequent combination assays and mechanistic analyses of apoptosis and cell-cycle modulation.


Thymoquinone
Cell Viability (%)
Concentration (μM)
0
25
50
75
100
150
175
ns
*
*
***
***
***


β-Lapachone
Cell Viability (%)
Concentration (μM)
0
25
30
35
40
50
55
**
**
**
***
***
***


β-Lapachol
Cell Viability (%)
Concentration (μM)
0
25
50
75
100
150
175
*
*
**
***
***
***


Cisplatin
Cell Viability (%)
Concentration (μM)
0
25
50
75
100
150
175
**
***
***
***
***
***

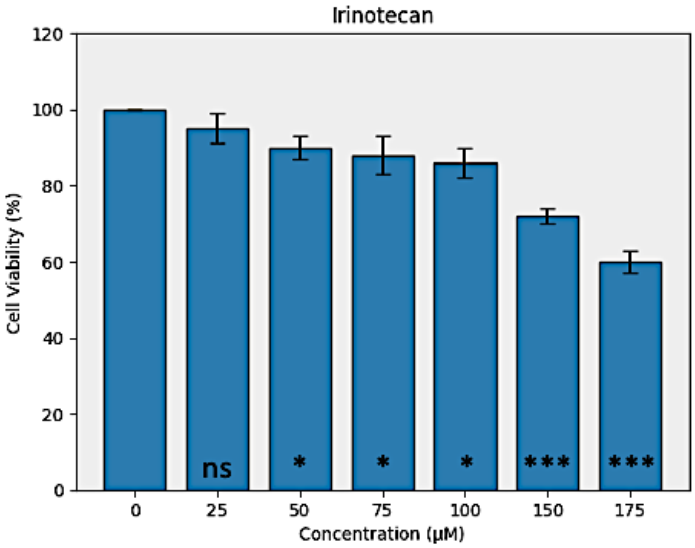

Irinotecan
Cell Viability (%)
Concentration (μM)
0
25
50
75
100
150
175
ns
*
*
*
***
***

Figure 7: **Dose–Response Analysis Demonstrates Enhanced Cytotoxicity of β-Lapachone and Cisplatin Relative to Other Compounds in MCF-7 Cells. A:** Thymoquinone induced a dose-dependent reduction in cell viability, with minimal effects at 25–50 μM and a marked decline beyond 75 μM. Viability decreased from approximately 97 % at 25 μM to ~10 % at concentrations ≥ 100 μM (*** $p < 0.001$). **B:** β-Lapachone caused a pronounced decrease in viability at low concentrations, declining from ~60 % at 25 μM to below 25 % at 50–55 μM (** $p < 0.01$–*** $p < 0.001$). **C:** β-Lapachol produced a gradual, moderate reduction in viability, decreasing from ~92 % at 25 μM to ~68 % at 175 μM (* $p < 0.05$–** $p < 0.01$). **D:** Cisplatin significantly reduced cell viability across all concentrations tested, with viability decreasing from ~73 % at 25 μM to below 45 % at ≥ 75 μM (** $p < 0.01$–*** $p < 0.001$). **E:** Irinotecan resulted in a shallow dose-dependent decrease in viability, from ~96 % at 25 μM to ~60 % at 175 μM, with significant effects observed only at the highest concentrations (*** $p < 0.001$). Regression lines represent best-fit linear trends derived from viability data across increasing concentrations. All compounds exhibited a negative linear correlation between concentration and cell viability. Thymoquinone and β-lapachone showed steep negative slopes ($y = -0.686x + 100$ and $y = -1.866x + 100$, respectively), while β-lapachol displayed a shallower slope ($y = -0.810x + 100$). Cisplatin and irinotecan produced regression slopes of −1.880 and −0.503, respectively.

Table 1: Differential Cytotoxic Potency of Single Treatments in MCF-7 Cells Based on IC_{50} Values

DRUG	IC_{50} VALUE (μM)
TQ	72.9 μM
β-LAP	26.8 μM
β-OL	61.7 μM
CIS	26.6 μM
IRI	99.34 μM

4.1.1.2 HCT116

Regression analysis, **Figure 8**, confirmed concentration-dependent cytotoxicity for all compounds tested in HCT116 cells. β-Lapachone and cisplatin produced the steepest regression slopes, reflecting strong and rapid reductions in cell viability that closely matched the sharp declines observed in the corresponding bar-graph data. β-Lapachone was particularly potent, achieving near-complete inhibition of viability at sub-micromolar concentrations, underscoring its exceptional activity in this cell line.

Irinotecan also demonstrated a steep negative slope, indicating greater cytotoxic potency in HCT116 cells than observed in MCF-7 cells. This enhanced activity may be attributed to higher carboxylesterase expression, facilitating more efficient conversion of irinotecan to its active metabolite, SN-38, or to increased topoisomerase I activity in HCT116 cells.

In contrast, β-lapachol displayed a more moderate regression slope, consistent with a steady but less pronounced reduction in viability. Thymoquinone exhibited the shallowest slope, indicating minimal

cytotoxic activity across the tested concentration range and corroborating its weak effect observed in the bar-graph analysis.

Overall, the linear regression analysis confirms a consistent dose-dependent response across all treatments, with the order of cytotoxic potency based on slope magnitude being: Cisplatin > irinotecan > β-lapachone > β-lapachol > thymoquinone. These results align with the observed Alamar Blue viability data and further support that β-lapachone and irinotecan are highly effective against HCT116 cells, whereas thymoquinone shows minimal cytotoxic influence in this colon cancer model.

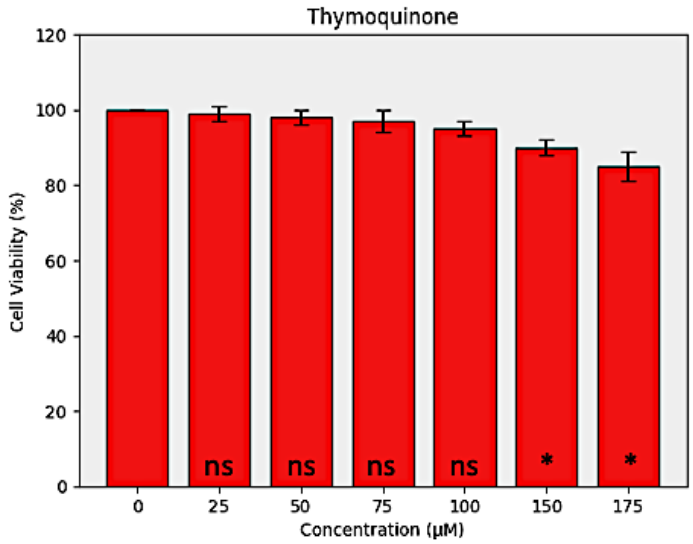
Thymoquinone exhibited the lowest potency (IC_{50} = 113.3 μM), classifying it as weakly cytotoxic, suggesting limited biological activity in this cell line. This reduced sensitivity may be linked to differences in redox balance and survival signaling pathways between colon and breast cancer cells (Woo et al., 2012).

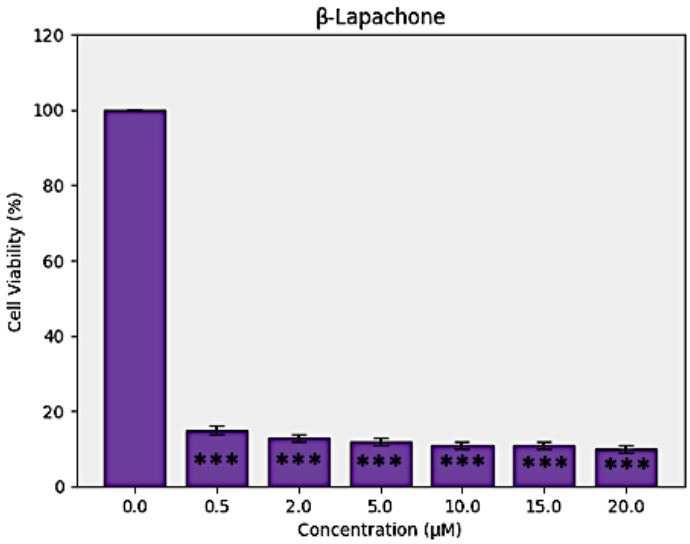
HCT116 cells exhibited marked sensitivity to β-lapachone, with an IC_{50} value of 0.36 μM, classifying it as highly potent. This exceptional sensitivity is consistent with reports indicating that colorectal cancer cells, including HCT116, often express elevated levels of NQO1, which enhances β-lapachone-mediated redox cycling and ROS-induced cell death (Bey et al., 2013). This mechanism explains the dramatic difference in potency compared to MCF-7 cells. β-Lapachol (IC_{50} = 24.2 μM) was classified as moderately cytotoxic, demonstrating improved efficacy in HCT116 cells relative to MCF-7 cells. This may reflect increased susceptibility of colorectal cancer cells to quinone-based compounds and oxidative stress-mediated apoptosis.

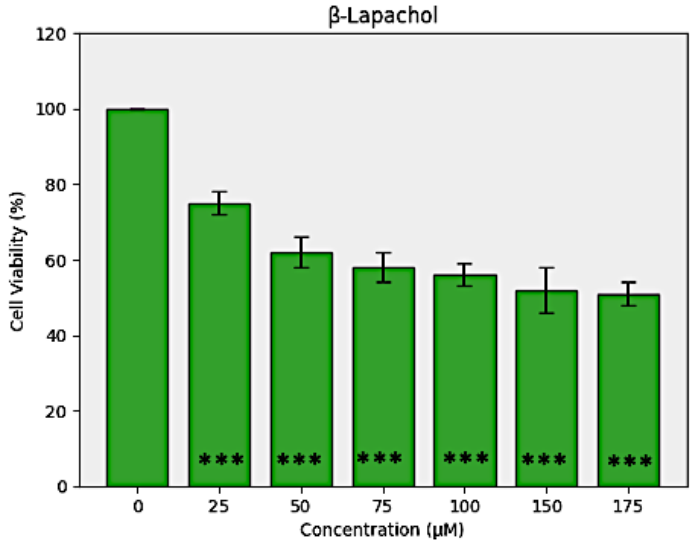
Cisplatin (IC_{50} = 37.1 μM) also fell within the moderately cytotoxic range, consistent with its broad-spectrum DNA-damaging activity. Irinotecan (IC_{50} = 61.9 μM) was categorized as weak to moderate but showed greater potency than in MCF-7 cells. This is likely due to higher expression of carboxylesterases and topoisomerase I in HCT116 cells, facilitating more efficient conversion to SN-38 and increased DNA damage (Pommier, 2006).

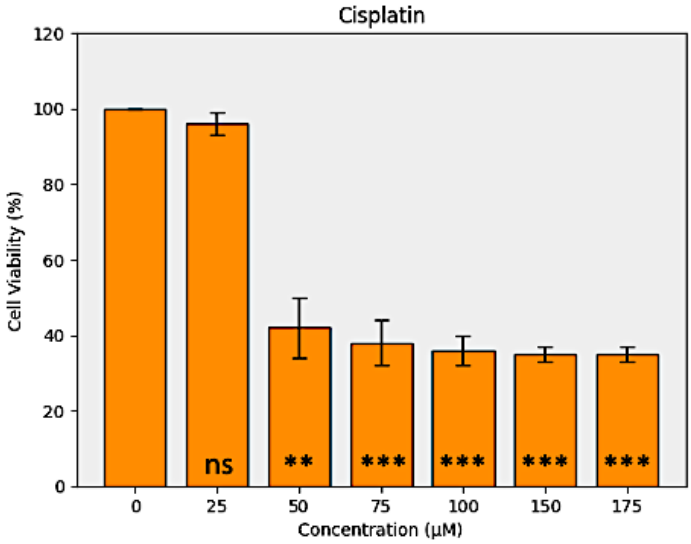
The response was more pronounced than that seen in MCF-7 cells, indicating that HCT116 cells may possess greater irinotecan sensitivity, possibly due to differences in carboxylesterase activity or topoisomerase I expression. Nevertheless, the relatively shallow decline and high IC_{50} values remain consistent with irinotecan's need for metabolic activation to SN-38.

Overall, these results in **Figure 8 and Table 2**, demonstrate that β-lapachone is exceptionally potent in HCT116 cells, causing near-complete loss of viability at sub-micromolar levels, while cisplatin and irinotecan display strong but less selective cytotoxic effects. β-lapachol produces a consistent moderate reduction, and thymoquinone exhibits minimal activity in this colon cancer model. These findings suggest that β-lapachone has the greatest potential as a lead compound for further mechanistic and combination analyses in HCT116 cells.


Thymoquinone
Cell Viability (%)
Concentration (μM)
0
25
50
75
100
150
175
ns
ns
ns
ns
*
*


β-Lapachone
Cell Viability (%)
Concentration (μM)
0.0
0.5
2.0
5.0
10.0
15.0
20.0
***
***
***
***
***
***


β-Lapachol
Cell Viability (%)
Concentration (μM)
0
25
50
75
100
150
175
***
***
***
***
***
***


Cisplatin
Cell Viability (%)
Concentration (μM)
0
25
50
75
100
150
175
ns
**
***
***
***
***

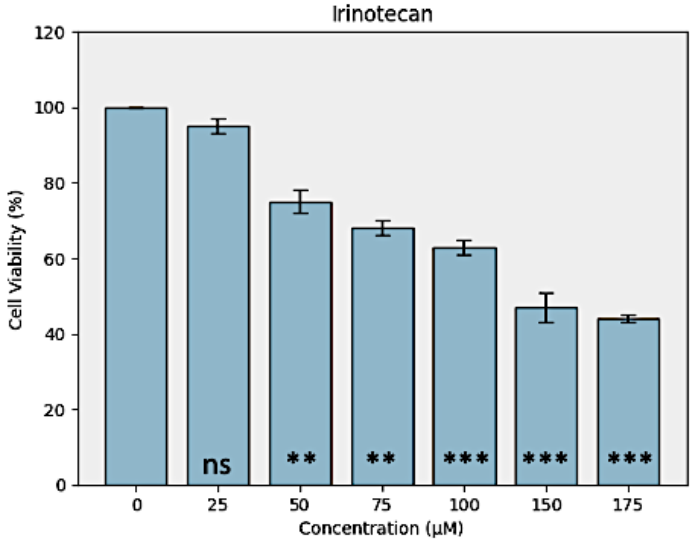

Irinotecan
Cell Viability (%)
Concentration (μM)
0
25
50
75
100
150
175
ns
**
**
***
***
***

Figure 8: **Dose-Dependent Reduction in HCT116 Cell Viability Reveals Superior Potency of β-Lapachone Compared to Other Treatments. A**: Thymoquinone produced minimal changes in viability at 25–100 μM, with viability remaining above 90%. A small but significant reduction was observed at 150 and 175 μM (* $p < 0.05$), where viability decreased to ~85%. **B:** β-Lapachone induced a pronounced decrease in viability at low concentrations, with viability falling from 100% in controls to below 15% at 0.5 μM and remaining low across 2–20 μM (*** $p < 0.001$). **C:** β-Lapachol caused a moderate, concentration-dependent reduction in viability, decreasing from 100% in controls to ~55% at 75 μM and stabilizing around 50% at 175 μM (*** $p < 0.001$ for concentrations ≥ 25 μM). **D:** Cisplatin significantly reduced viability at concentrations ≥ 25 μM (*** $p < 0.001$), with viability declining from ~95% at 25 μM to <40% at ≥ 75 μM. **E:** Irinotecan produced a dose-dependent decrease in viability, from ~96% at 25 μM to ~45% at 175 μM, with significant effects at higher concentrations (*** $p < 0.001$). All compounds exhibited negative linear correlations between concentration and cell viability. β-Lapachone and cisplatin displayed steep regression slopes ($y = -138.889x + 100$ and $y = -1.348x + 100$, respectively). Irinotecan also showed a pronounced negative slope ($y = -0.808x + 100$). β-Lapachol exhibited a moderate slope ($y = -2.066x + 100$), while thymoquinone showed the shallowest slope ($y = -0.441x + 100$).

Table 2: Differential Cytotoxic Potency of Single Treatments in HCT116 Cells Based on IC_{50} Values

DRUG	IC_{50} VALUE (μM)
TQ	113.3 μM
β-LAP	0.36 μM
β-OL	24.2 μM
CIS	37.1 μM
IRI	61.9 μM

4.1.1.3 VERO

Regression analysis confirmed concentration-dependent cytotoxic effects for all compounds in VERO cells, although marked differences in magnitude were observed. Thymoquinone exhibited a steep negative slope, indicating substantial loss of viability at higher concentrations. While this confirms its cytotoxic potential, it also suggests reduced selectivity at doses above 100 μM, where measurable toxicity toward non-cancerous cells became evident.

β-Lapachone demonstrated a strong negative correlation between concentration and viability, consistent with its high intrinsic potency. However, the pronounced cytotoxicity observed in VERO cells underscores its narrow therapeutic window and limited selectivity, as normal cells were affected at moderate concentrations.

In contrast, β-lapachol showed a more gradual decline in viability, reflecting lower overall toxicity. This comparatively shallow slope supports an improved safety profile and suggests greater selectivity for

malignant cells relative to β-lapachone and cisplatin. Cisplatin produced a steep regression slope in VERO cells that closely mirrored its effects in cancer cell lines, reinforcing its well-established non-selective cytotoxic mechanism. Irinotecan exhibited the shallowest slope among the compounds tested, indicating minimal cytotoxic impact on non-cancerous cells. This limited effect is consistent with irinotecan's dependence on metabolic activation to SN-38, which occurs predominantly in actively proliferating cancer cells rather than normal epithelial cells.

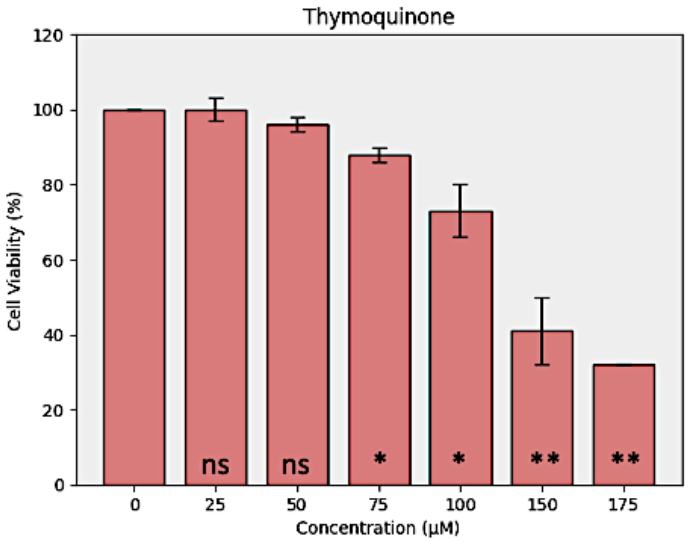
Collectively, in **Figure 9**, these linear regressions reveal a clear pattern of cytotoxic selectivity. Compounds such as β-lapachol and irinotecan produced mild slopes, indicating lower toxicity in normal cells, whereas thymoquinone, β-lapachone, and cisplatin demonstrated steeper negative trends, reflecting higher non-selective cytotoxicity. When compared to HCT116 and MCF-7 cells, the reduced slope magnitudes in VERO cells confirm that certain agents — notably β-lapachol and irinotecan — exhibit preferential activity toward cancerous cell lines, underscoring their potential value for further development as selective anticancer candidates.

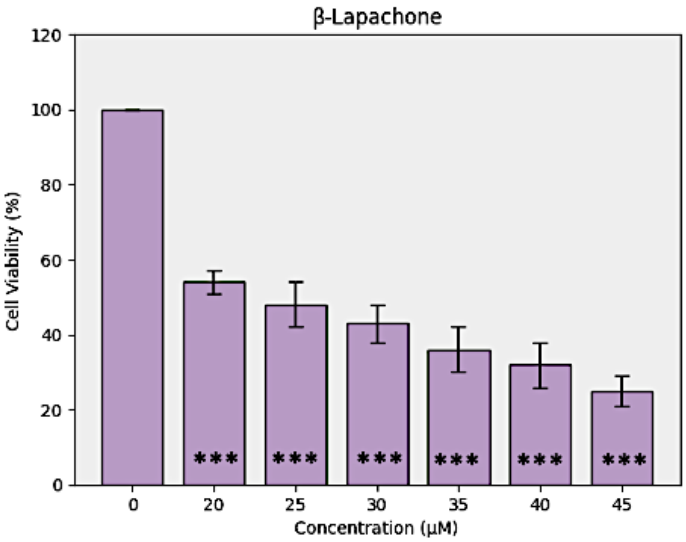
In non-malignant VERO cells, β-lapachone exhibited an IC_{50} value of 17.8 μM, classifying it as moderately cytotoxic, indicating substantial toxicity toward normal cells. This lack of selectivity is consistent with studies showing that β-lapachone can induce ROS-mediated damage in both malignant and non-malignant cells when NQO1-independent pathways are activated (Bey et al., 2013).

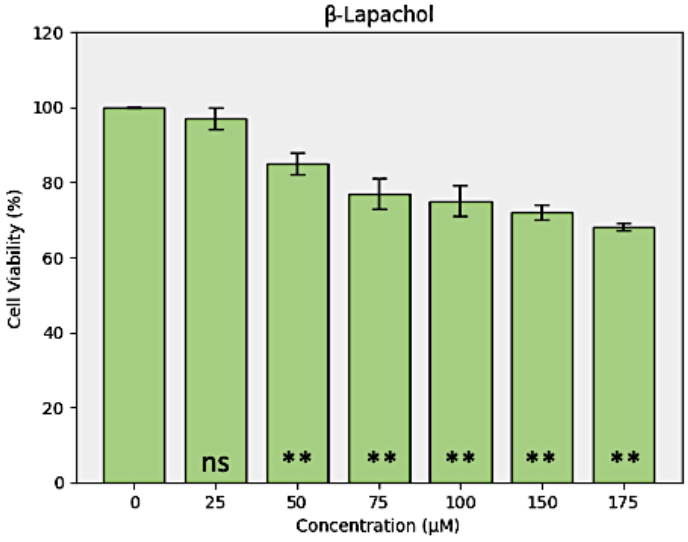
β-Lapachol (IC_{50} = 53.6 μM) was classified as weak to moderate, while thymoquinone (IC_{50} = 105.3 μM) was weakly cytotoxic, indicating reduced toxicity toward normal cells. This aligns with studies suggesting that both compounds exert cytotoxic effects through regulated oxidative stress and apoptosis pathways that are more active in cancer cells than in normal cells (Woo et al., 2012).

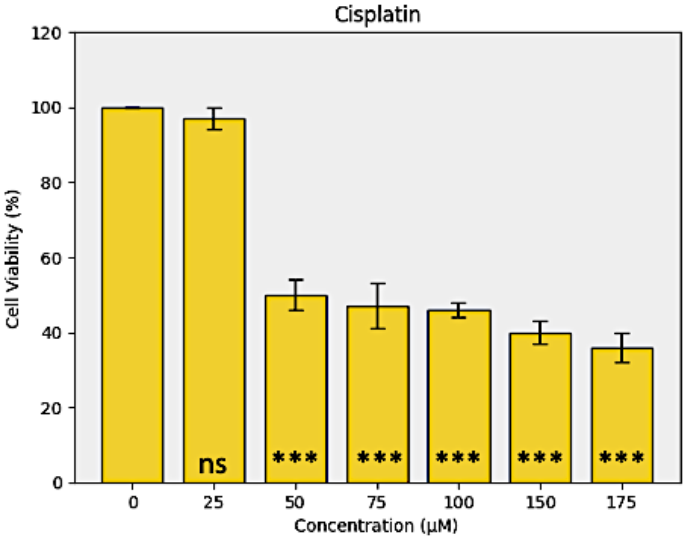
Cisplatin (IC_{50} = 41.0 μM) and irinotecan (IC_{50} = 37.0 μM) also fell within the moderately cytotoxic range. Cisplatin's non-selective DNA crosslinking mechanism explains its toxicity in normal cells (Dasari and Tchounwou, 2014). In contrast, irinotecan's moderate toxicity likely reflects basal levels of metabolic activation even in non-cancerous cells, although reduced proliferation limits its full cytotoxic potential (Pommier, 2006). The magnitude of reduction was smaller than in HCT116 or MCF-7 cells, suggesting relatively lower toxicity in non-cancerous cells. This result supports irinotecan's favorable selectivity, likely due to its requirement for metabolic activation (conversion to SN-38), which is limited in non-proliferative or metabolically quiescent cells such as VERO.

Overall, the VERO cell results, **Figure 9 and Table 3**, indicate that β-lapachol and irinotecan exhibit lower cytotoxicity and greater selectivity toward non-cancerous cells, whereas β-lapachone and cisplatin display high non-selective toxicity, and thymoquinone shows intermediate effects. These findings highlight β-lapachone's strong anticancer potency but limited safety margin, while β-lapachol and irinotecan demonstrate the most promising therapeutic selectivity for further consideration in combination strategies.


Thymoquinone
Cell Viability (%)
Concentration (μM)
0
25
50
75
100
150
175
ns
ns
*
*
**
**


β-Lapachone
Cell Viability (%)
Concentration (μM)
0
20
25
30
35
40
45
***
***
***
***
***
***


β-Lapachol
Cell Viability (%)
Concentration (μM)
0
25
50
75
100
150
175
ns
**
**
**
**
**


Cisplatin
Cell Viability (%)
Concentration (μM)
0
25
50
75
100
150
175
ns
***
***
***
***
***

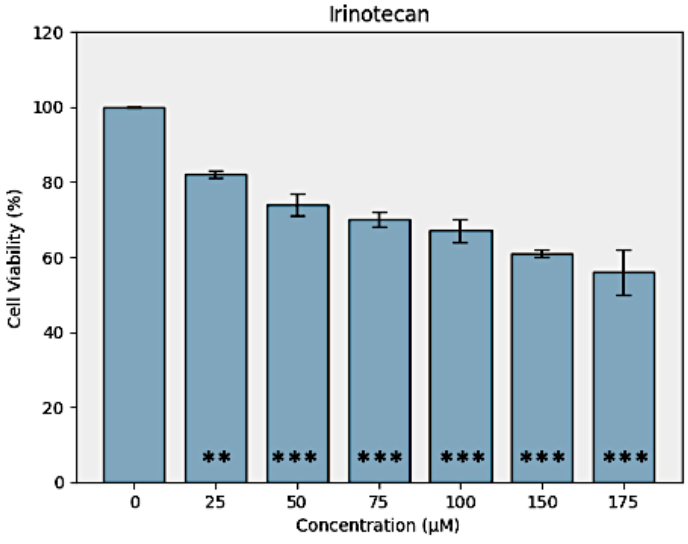

Irinotecan
Cell Viability (%)
Concentration (μM)
0
25
50
75
100
150
175
**
***
***
***
***
***

Figure 9: **Dose–Response Analysis Indicates Lower Cytotoxicity of Thymoquinone and Greater Toxicity of β-Lapachone and Cisplatin in VERO Cells. A**: Thymoquinone induced a concentration-dependent decrease in viability. Viability remained above 85% at 25–75 μM, declined to ~74% at 100 μM (* $p < 0.05$), and further decreased to ~41% and ~33% at 150 μM and 175 μM, respectively (** $p < 0.01$). **B:** β-Lapachone caused a marked reduction in viability, decreasing from 100% in controls to ~53% at 20 μM and stabilizing between ~43–24% at 25–45 μM (*** $p < 0.001$ at all concentrations). **C:** β-Lapachol produced a gradual reduction in viability, decreasing from ~97% at 25 μM to ~68% at 175 μM (** $p < 0.01$ at higher concentrations). **D:** Cisplatin significantly reduced viability at concentrations ≥ 25 μM (*** $p < 0.001$), with viability declining from ~97% at 25 μM to ~47% at 75–100 μM and ~36% at 175 μM. **E:** Irinotecan induced a dose-dependent decrease in viability, from ~82% at 25 μM to ~55% at 175 μM, with significant effects at higher concentrations (*** $p < 0.001$). All compounds exhibited negative regression slopes, indicating concentration-dependent decreases in cell viability. Thymoquinone showed a steep slope ($y = -0.475x + 100$), while β-lapachone displayed a strong negative correlation ($y = -2.809x + 100$). β-Lapachol exhibited a more gradual slope ($y = -0.933x + 100$). Cisplatin produced a steep regression line ($y = -1.220x + 100$), whereas irinotecan showed a moderate slope ($y = -1.351x + 100$).

Table 3: Differential Cytotoxic Potency of Single Treatments in VERO Cells Based on IC_{50} Values

DRUG	IC_{50} VALUE (μM)
TQ	105.3 μM
β-LAP	17.8 μM
β-OL	53.6 μM
CIS	41.0 μM
IRI	37.0 μM

4.1.2 Cytotoxic Effects of Combination Drug Treatments

Following the single-treatment cytotoxicity assays, combination studies were performed to evaluate the potential synergistic or additive effects between the natural compounds — thymoquinone (TQ), β-lapachone (B-LAP), and β-lapachol (B-OL) — and the chemotherapeutic agent irinotecan (IRI) in MCF-7 and HCT116 cells. Combination concentrations were derived from each compound's IC_{50} value, as discussed in **Section 3.6.2**, obtained in single-agent Alamar Blue assays, ensuring inclusion of sub-lethal, equi-effective, and supra-lethal doses. The experimental layout followed a checkerboard design, and the resulting cell viability data were analyzed using the Chou–Talalay method in CompuSyn software to calculate the Combination Index (CI), where $CI < 1$ indicates synergy, $CI = 1$ indicates additivity, and $CI > 1$ indicates antagonism (Chou, 2010; Chou and Martin, 2006).

4.1.2.1 MCF-7 Combination Treatments

The β-lapachone–irinotecan combination exhibited the most pronounced Fa-dependent interaction shift. The regression slope was steep (m = 2.40907 ± 0.40703), with a strong positive correlation (r = 0.78374), indicating that CI values increased significantly as Fa increased. At lower fractional effects, several CI values fell below 1, demonstrating synergistic interaction when partial growth inhibition was achieved. However, as Fa approached higher levels, CI values increased sharply above unity, indicating a transition toward antagonism at high cytotoxic intensities. The magnitude of the slope suggests that the interaction is highly sensitive to effect level, implying that cooperative cytotoxic mechanisms dominate at modest levels of growth inhibition but become progressively offset at higher levels of cell kill. This pattern may reflect saturation of topoisomerase I–mediated DNA damage or overlapping oxidative stress pathways, where excessive damage activates compensatory survival signaling or limits further synergistic enhancement. The logarithmic CI representation reinforces this observation, showing a clear upward divergence from log(CI)=0 with increasing Fa, highlighting the instability of synergy at maximal effect levels.

In contrast, the β-lapachol–irinotecan combination demonstrated a more moderate slope (m = 0.80814 ± 0.14977) with a comparably strong correlation coefficient (r = 0.75472), indicating a consistent and proportional relationship between CI and Fa. CI values clustered around 1 across much of the Fa range, with mild synergy observed at lower to intermediate effect levels. Importantly, the shallower slope indicates that the interaction profile remains relatively stable as cytotoxic intensity increases, without the dramatic synergism-to-antagonism transition observed with β-lapachone. The logarithmic CI plot confirms this relative stability, with most values oscillating closely around log(CI)=0. This suggests that β-lapachol does not induce strong Fa-dependent shifts in irinotecan responsiveness but instead maintains a largely additive interaction across escalating drug effects. Mechanistically, this may indicate partial mechanistic overlap without complete pathway redundancy, allowing cooperative effects without triggering compensatory antagonistic mechanisms at higher damage thresholds.

The thymoquinone–irinotecan combination displayed the weakest correlation (r = 0.38778) and a comparatively imprecise slope estimate (m = 0.75404 ± 0.38213), reflecting greater dispersion of CI values and reduced predictability of interaction dynamics. CI values fluctuated above and below 1 across the Fa spectrum, indicating variable shifts between synergism and antagonism. The broader confidence interval of the slope further suggests heterogeneity in interaction strength, potentially reflecting context-dependent modulation of oxidative stress, mitochondrial dysfunction, or apoptotic signaling pathways. Unlike β-lapachone, the Fa-dependent increase in CI was less steep, but unlike β-lapachol, the interaction lacked stability. The logarithmic transformation reveals wide dispersion around the additivity line, supporting the conclusion that the TQ–IRI interaction is inconsistent and strongly influenced by effect magnitude.

Comparatively, the magnitude of the slope (m) serves as an indicator of how rapidly interaction dynamics change with increasing cytotoxic effect. β-lapachone demonstrated the highest slope and strongest Fa-dependent modulation, β-lapachol exhibited moderate and stable interaction behavior, and thymoquinone showed variable, weakly correlated interaction patterns. The correlation coefficient further underscores that β-lapachone and β-lapachol combinations produce more predictable interaction trends than thymoquinone.

The inclusion of both linear and logarithmic CI representations strengthens interpretative accuracy, as the logarithmic transformation enhances sensitivity around the additivity threshold and clarifies subtle synergistic or antagonistic deviations that may not be immediately apparent on the linear scale. Together, these analyses provide quantitative evidence that drug–drug interactions in this system are not static but dynamically influenced by effect magnitude, underscoring the importance of evaluating combination therapies across a full range of fractional responses rather than relying on single-point CI determinations (Chou, 2010; Chou and Martin, 2006).

The combination index (CI) plot and the logarithmic combination index (log CI) plot are complementary tools used to evaluate drug–drug interactions across increasing levels of effect. The CI plot presents the CI values directly as a function of the fraction affected (Fa), which represents the proportion of cell death or growth inhibition. This plot allows direct classification of interactions as synergistic (CI < 1), additive (CI = 1), or antagonistic (CI > 1) and illustrates how the nature of the interaction changes across different levels of cytotoxicity. As such, the CI plot is particularly useful for identifying whether synergy occurs predominantly at low, intermediate, or high effect levels and for assessing the overall biological relevance and consistency of the interaction across the dose–response range.

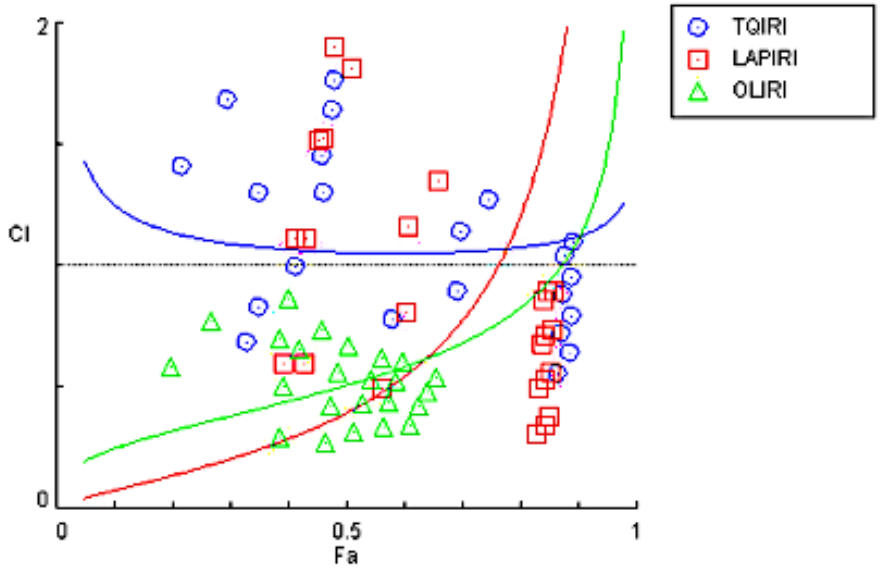
The logarithmic CI plot represents the same interaction data following logarithmic transformation of the CI values, plotting $\log_{10}(CI)$ against Fa. This transformation enhances resolution around the additivity threshold by expanding small deviations near CI = 1 while compressing extreme synergistic or antagonistic values. In this representation, negative log(CI) values indicate synergy, values close to zero indicate additivity, and positive values indicate antagonism. The log CI plot is therefore particularly informative for detecting subtle or borderline interactions that may not be readily apparent on a linear CI plot, as well as for evaluating the stability and reproducibility of drug interactions across effect levels.

Together, these analyses provide a comprehensive assessment of drug interaction behavior. The CI plot offers an intuitive and biologically meaningful overview of interaction trends, while the logarithmic CI plot refines interpretation by highlighting subtle deviations from additivity. When interpreted in combination, these plots strengthen confidence in conclusions regarding synergistic, additive, or antagonistic interactions and support robust evaluation of combination treatment efficacy in the experimental system.

Collectively, these data indicate that β-lapachone exerts the most potent modulatory influence on irinotecan efficacy, but this enhancement is conditional and diminishes at higher effect levels. β-lapachol maintains the most stable interaction profile, largely additive with limited antagonistic deviation, suggesting greater translational robustness across dosing intensities. Thymoquinone demonstrates heterogeneous interaction behavior, implying that its combinatorial efficacy may be highly context-dependent and influenced by cellular stress thresholds, as shown in **Figure 10**.

A

Combination Index Plot



B

Logarithmic Combination Index Plot

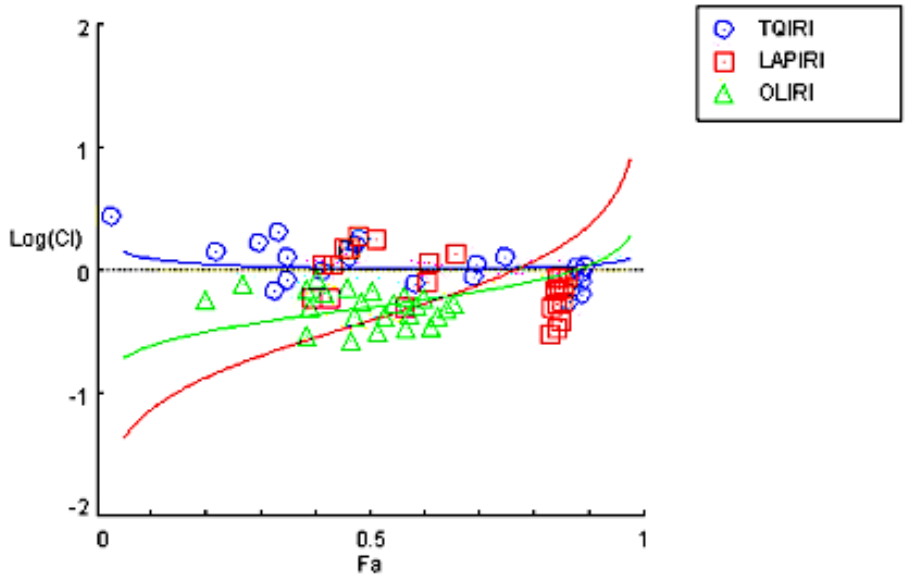


Figure 10: Combination Index Analysis on the Synergistic Effects of Thymoquinone, β-Lapachone and β-Lapachol with Irinotecan in MCF-7 Cells. A: B-Lap+IRI exhibits synergistic interactions at lower Fa values (CI < 1), but shifts progressively toward antagonism as Fa increases, with multiple data points exceeding CI = 1 at higher effect levels. B-OL+IRI shows predominantly additive interactions across most Fa values, with several data points falling slightly below CI = 1 at low-to-intermediate Fa, indicating mild synergy and minimal antagonistic deviation. In contrast, TQ+IRI displays greater variability, with CI values fluctuating above and below 1 across the Fa range, reflecting alternating regions of weak synergy and antagonism without a consistent directional trend. **B**: The logarithmic transformation [log(CI) vs Fa] further illustrates these interaction patterns relative to the additivity threshold (log(CI)=0). Downward deviation below zero confirms synergism, while upward deviation indicates antagonism. Consistent with panel A, B-Lap+IRI shows negative log(CI) values at lower Fa transitioning to positive values at higher Fa; B-OL+IRI remains clustered near zero, supporting primarily additive effects; and TQ+IRI demonstrates dispersed values on both sides of the threshold, indicating heterogeneous interaction behavior across effect levels.

The dose–effect curves illustrate the relationship between increasing combined drug dose and the resulting fractional effect (Fa) for irinotecan combined with thymoquinone (TQIRI), β-lapachone (LAPIRI), and β-lapachol (OLIRI) in MCF-7 cells. Fa represents the fraction of cells affected (growth inhibition), ranging from 0 (no effect) to 1 (complete inhibition). The sigmoidal nature of the fitted curves reflects the median-effect principle, where increasing dose produces a non-linear increase in cytotoxic response. Clear differences in potency, slope, and maximal achievable effect are observed among the three combinations (Chou, 2010; Chou and Martin, 2006).

The TQIRI curve (blue) displays a steep sigmoidal trajectory with a pronounced upward inflection, indicating strong dose responsiveness once a threshold concentration is reached. At lower doses, Fa values remain modest, but beyond mid-range concentrations the curve rises sharply, approaching high fractional inhibition (Fa ≈ 0.9–1). The steepness of this curve suggests a higher slope parameter (m), indicative of cooperative or threshold-driven cytotoxic mechanisms. Biologically, this may reflect amplification of apoptotic signaling once a critical level of DNA damage or oxidative stress is surpassed.

In contrast, the LAPIRI curve (red) demonstrates a rapid early rise in Fa at relatively low doses, suggesting strong initial potency. However, the curve begins to plateau at intermediate Fa values and does not reach the same maximal effect as TQIRI within the tested dose range. This profile indicates that although LAPIRI may exert substantial cytotoxicity at lower concentrations, its incremental efficacy diminishes as dose increases. Such plateauing behavior may reflect early engagement of its primary mechanism followed by saturation or compensatory cellular adaptation limiting further response escalation.

The OLIRI curve (green) exhibits the most gradual slope and the lowest overall maximal Fa within the evaluated dose range. The incremental increase in effect is steady but modest, and high-dose exposure does not achieve the same degree of growth inhibition observed with TQIRI. This shallower slope suggests reduced cooperative interaction between the two agents or a more limited ability to amplify

irinotecan-induced cytotoxic stress. The comparatively lower maximal effect may reflect partial pathway overlap or suboptimal potentiation of topoisomerase I–mediated DNA damage.

Comparatively, TQIRI demonstrates the greatest dynamic range and highest achievable cytotoxic effect, LAPIRI shows strong early potency with mid-range plateauing, and OLIRI exhibits the most moderate and gradual dose–response relationship. These distinctions align with the previously observed combination index trends, where interaction strength varied according to effect magnitude. The steepness and curvature of the dose–effect relationships provide mechanistic insight into how each phytochemical modulates irinotecan responsiveness across escalating concentrations.

Importantly, the dispersion of experimental data points around each fitted curve indicates biological variability but overall supports strong conformity to median-effect modeling, particularly for TQIRI and LAPIRI. The shape and inflection of these curves further suggest that combination efficacy is not solely dependent on absolute dose but is critically influenced by interaction kinetics and pathway engagement thresholds, as shown in **Figure 11**.

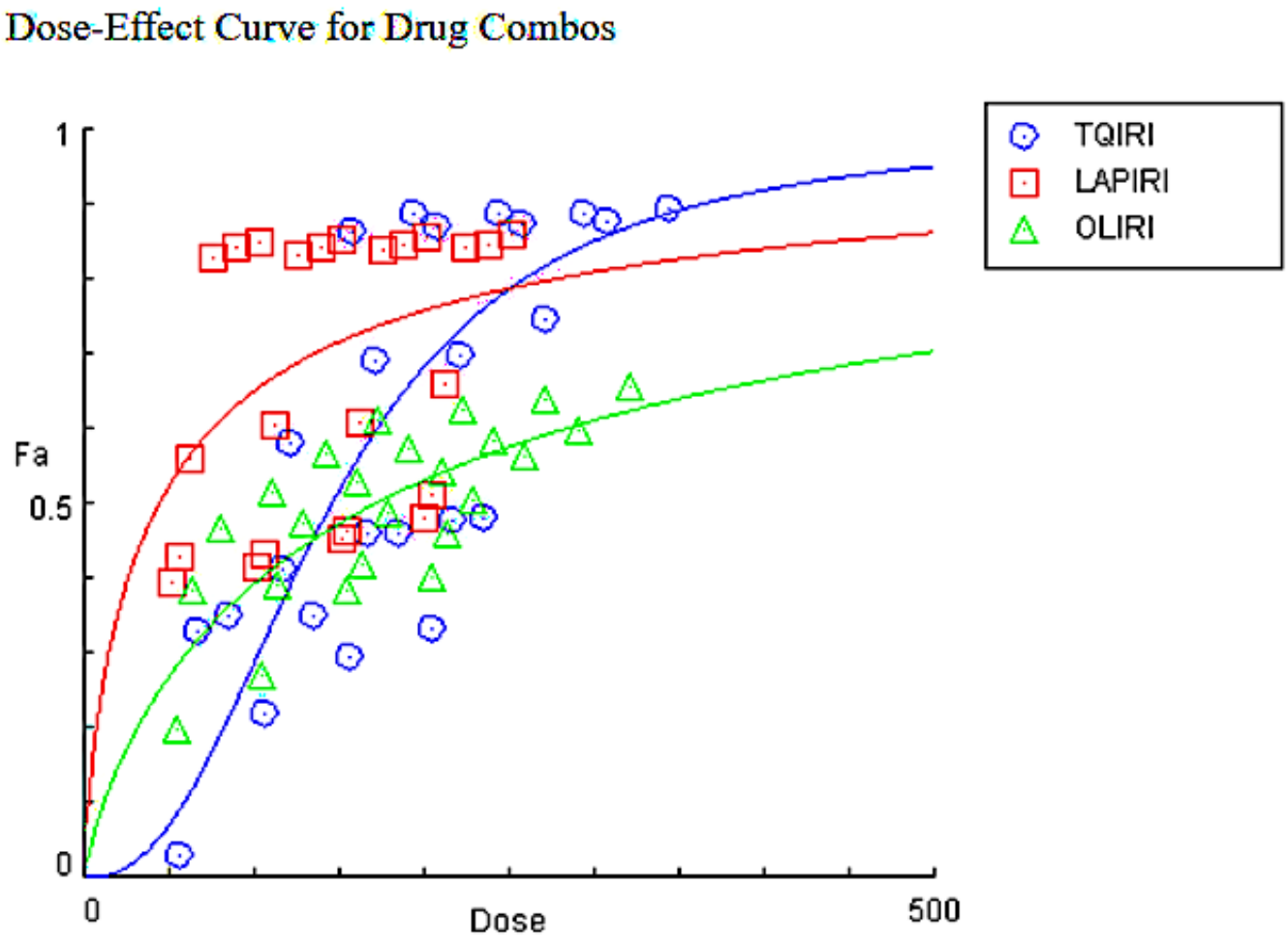


Figure 11: **Differential Potency and Activity of Thymoquinone, β-Lapachone, and β-Lapachol in Combination with Irinotecan in MCF-7 Cells**. Fractional effect (Fa) is plotted against increasing combination dose. Symbols represent individual experimental data points, and solid lines indicate fitted median-effect curves. TQIRI (blue) exhibits a steep sigmoidal response with high maximal Fa, LAPIRI (red) demonstrates strong early dose responsiveness with partial plateauing at higher doses, and OLIRI (green) shows a more gradual increase in Fa with lower maximal effect. The differences in curve steepness and maximal response reflect variation in potency, dose responsiveness, and the extent of cytotoxic amplification among the combinations.

The median-effect plot provides a linearized transformation of the dose–response data according to the Chou–Talalay median-effect equation, where log(Fa/Fu) is plotted against log(D). Fa represents the fraction affected, Fu = 1 − Fa the fraction unaffected, and D the combination dose. Linearization of the data allows direct extraction of the slope (m), reflecting the sigmoidicity of the dose–effect curve, and the x-intercept, corresponding to the median-effect dose (Dm), analogous to IC_{50} under combination conditions. The strength of linearity further reflects conformity to mass-action law principles (Chou, 2010; Chou and Martin, 2006).

All three combinations demonstrate reasonably linear distributions, confirming that the experimental data conform to median-effect modeling. However, clear differences in slope, line positioning, and dispersion are evident, reflecting distinct pharmacodynamic behaviors.

The TQIRI combination (blue) exhibits the steepest regression line among the three treatments. This indicates a higher slope (m), corresponding to greater sigmoidicity in the dose–effect relationship. A steep slope implies that small increases in dose beyond a threshold produce disproportionately large increases in effect, consistent with cooperative or amplification-driven cytotoxic mechanisms. The relative rightward positioning of the line suggests a higher median-effect dose compared to LAPIRI, indicating that higher combination doses are required to achieve Fa = 0.5. However, once this threshold is surpassed, effect escalates rapidly. The broader vertical spread of data points suggests some biological variability, but overall linearity remains strong.

The LAPIRI combination (red) demonstrates a more moderate slope with a left-shifted regression line relative to the other treatments. This leftward displacement indicates a lower Dm, meaning that 50% effect is achieved at a comparatively lower dose. Thus, LAPIRI appears more potent at mid-range effect levels. The moderate slope suggests less pronounced cooperativity than TQIRI but a more efficient initial dose–response relationship. The clustering of data points along the regression line indicates strong conformity to median-effect kinetics and consistent pharmacodynamic behavior.

The OLIRI combination (green) presents an intermediate profile. Its slope is shallower than TQIRI and comparable or slightly lower than LAPIRI, indicating reduced sigmoidicity. The line is positioned rightward of LAPIRI but slightly left of or overlapping TQIRI depending on Fa range, suggesting moderate median-effect dose requirements. The shallower gradient implies a more gradual increase in

effect with dose escalation, reflecting less abrupt cytotoxic amplification. Data dispersion appears modest, supporting acceptable adherence to median-effect assumptions.

Comparatively, the slope (m) values visually reflect the hierarchy of sigmoidicity: TQIRI > LAPIRI ≥ OLIRI. In median-effect theory, a slope greater than 1 indicates sigmoidal kinetics with cooperative behavior, m = 1 reflects hyperbolic kinetics, and m < 1 suggests flatter dose responsiveness. The steeper TQIRI line supports the previously observed steep dose–effect curve and pronounced Fa-dependent CI shifts. Conversely, LAPIRI's leftward position aligns with its strong early potency and relatively stable CI profile, while OLIRI's more moderate slope corresponds with its gradual dose–effect curve and largely additive interaction behavior.

The linearity of all three regression lines confirms that the combination responses obey the mass-action law framework, validating subsequent CI calculations derived from these parameters. Importantly, differences in slope and intercept collectively explain the distinct interaction dynamics observed in the CI plots: steeper slopes contribute to stronger Fa-dependent shifts in interaction, while lower Dm values indicate enhanced potency at mid-effect levels, as shown in **Figure 12**.

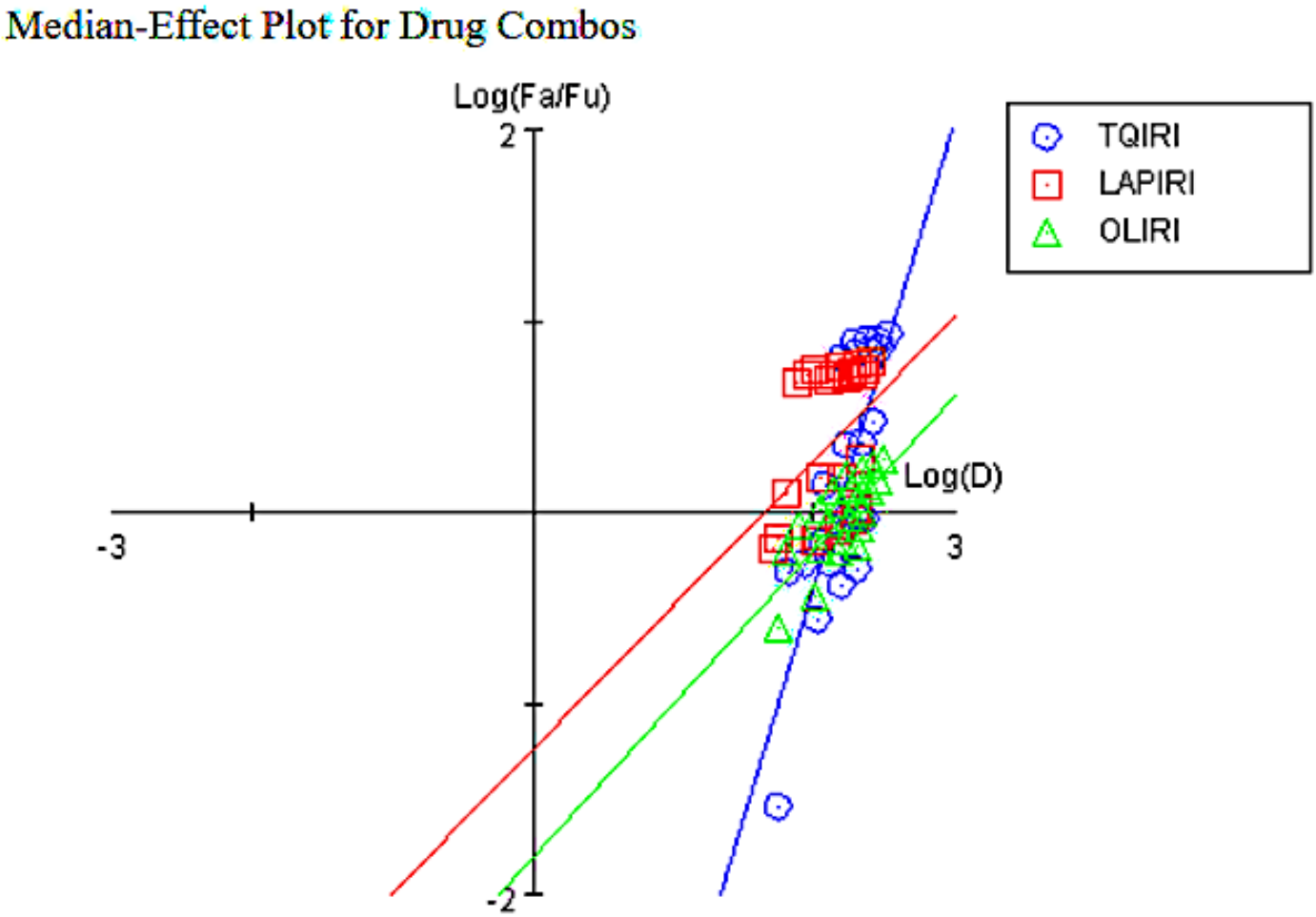


Figure 12: Differential Dose–Response Slopes of Thymoquinone, β-Lapachone, and β-Lapachol in Combination with Irinotecan in MCF-7 Cells. Log(Fa/Fu) is plotted against log(D) according to the Chou–Talalay median-effect equation. Symbols represent experimental data points, and solid lines indicate linear regression fits used to derive slope (m) and median-effect dose (Dm). TQIRI (blue) displays the steepest slope, indicating high sigmoidicity and strong dose-dependent amplification of effect. LAPIRI (red) is left-shifted, reflecting a lower median-effect dose and greater potency at intermediate effect levels. OLIRI (green) demonstrates a more gradual slope, consistent with a moderate and steady increase in cytotoxic response. Linearity of the plots confirms conformity to median-effect modeling and supports the validity of combination index calculations derived from these parameters.

The Dose Reduction Index (DRI) analysis quantifies the extent to which the dose of each individual drug within a combination can be reduced to achieve a given fractional effect (Fa) compared to the dose required when the drug is administered alone. A DRI > 1 indicates a favorable dose reduction (synergistic benefit), DRI = 1 indicates no dose reduction (additivity), and DRI < 1 indicates an unfavorable interaction. Distinct dose-reduction dynamics were observed among the three combinations in MCF-7 cells (Chou, 2010; Chou and Martin, 2006).

In **Figure 13 A**, irinotecan (red squares) exhibits DRI values consistently above 1 across the Fa range, with DRI increasing progressively as Fa rises. At intermediate-to-high effect levels, DRI values for IRI exceed 3–4, indicating substantial dose reduction potential when combined with thymoquinone. This suggests that TQ meaningfully potentiates irinotecan cytotoxicity, particularly at higher growth inhibition levels. In contrast, thymoquinone (blue circles) shows DRI values clustered around 1, with a slight downward trend at higher Fa values. This indicates minimal dose reduction benefit for TQ itself and suggests that the dominant benefit of this combination is preferentially conferred to irinotecan rather than reciprocally shared. Thus, the TQIRI combination appears to primarily enhance irinotecan efficiency rather than producing symmetrical mutual potentiation.

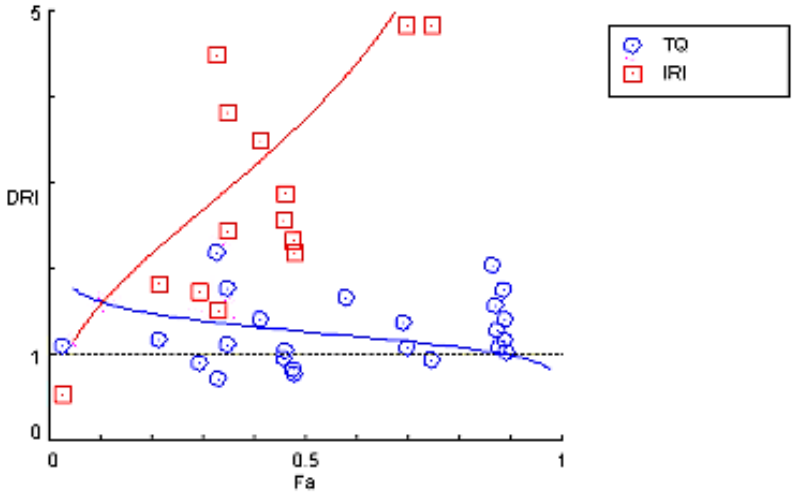
Figure 13 B demonstrates a divergent pattern between the two agents. β-lapachone (blue circles) shows DRI values above 1 at lower Fa values, but these values decline progressively toward or below 1 as Fa approaches higher levels. This downward trajectory indicates diminishing dose-reduction benefit at increased cytotoxic intensity, consistent with the previously observed antagonistic shift in the CI plot at high Fa. Irinotecan (red squares), however, maintains DRI values modestly above 1 across much of the Fa spectrum, though with less dramatic elevation compared to TQIRI. The declining DRI for β-lapachone at higher Fa levels reflects reduced cooperative advantage and supports the observation that this combination loses synergistic efficiency as effect magnitude increases.

Figure 13 C reveals the most favorable and balanced DRI profile among the three combinations. Both β-lapachol (blue circles) and irinotecan (red squares) display DRI values consistently above 1 across

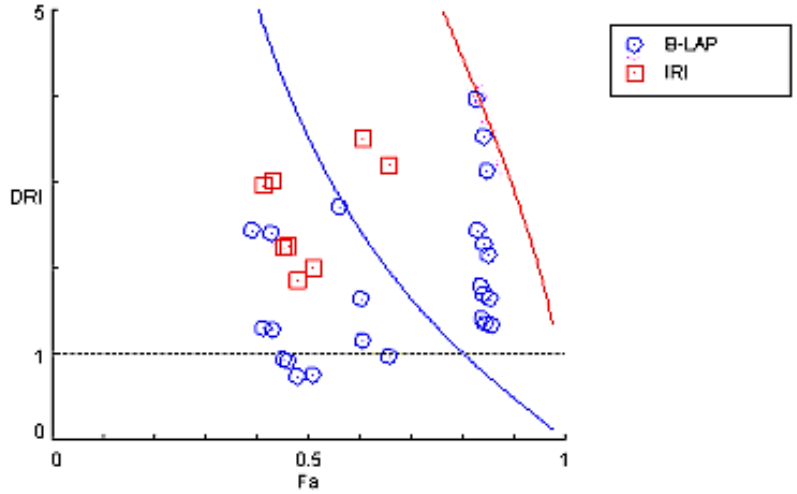
most of the Fa range. Although some downward curvature is visible at very high Fa values, DRI values remain substantially above unity, particularly within intermediate effect levels.

This indicates mutual dose-reduction benefit for both agents, consistent with sustained synergy observed in the CI analysis. The magnitude of DRI values (often between 2 and 4) suggests that significant dose reductions of both drugs could theoretically achieve equivalent cytotoxic effects when administered in combination.

A DRI Plot for Combo: TQIRI (TQ+IRI [1:1.36])



B DRI Plot for Combo: LAPIRI (B-LAP+IRI [1:3.71])



C DRI Plot for Combo: OLIRI (B-OL+IRI [1:1.61])

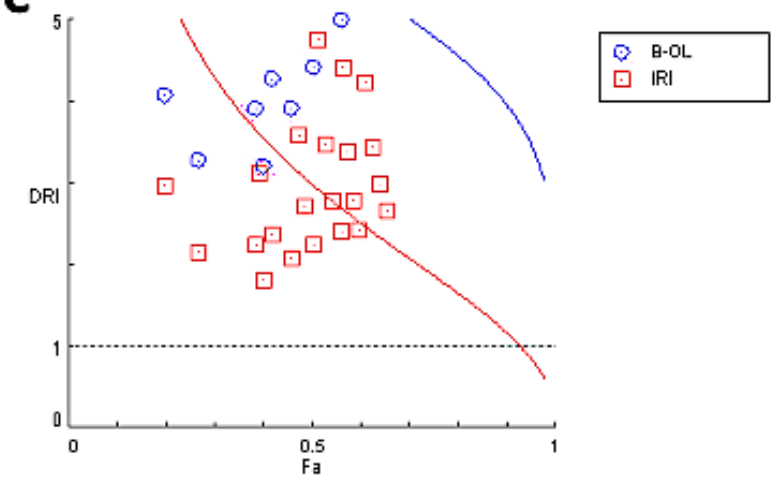


Figure 13: **Differential Dose Reduction Effects of Thymoquinone, β-Lapachone, and β-Lapachol in Combination with Irinotecan in MCF-7 Cells.** DRI values are plotted against fractional effect (Fa). The dashed horizontal line at DRI = 1 indicates no dose reduction benefit; DRI > 1 indicates favorable dose reduction, and DRI < 1 indicates unfavorable interaction. **A**: TQIRI (1:1.36) shows increasing DRI values for irinotecan (red squares), indicating substantial dose reduction benefit at higher Fa levels, while thymoquinone (blue circles) remains near unity. **B**: LAPIRI (1:3.71) demonstrates modest DRI benefit at lower Fa values with declining dose-reduction efficiency at higher Fa, particularly for β-lapachone. **C**: OLIRI (1:1.61) exhibits sustained DRI > 1 for both β-lapachol (blue circles) and irinotecan (red squares), indicating reciprocal and consistent dose-reduction advantage across effect levels.

An isobologram is a geometric representation of drug interaction based on Loewe additivity principles. For a given fractional effect, the dose of Drug A required to achieve that effect when used alone is plotted on the y-axis, and the corresponding dose of Drug B is plotted on the x-axis. The straight line connecting these single-agent intercepts represents the theoretical line of additivity (Chou, 2010; Chou and Martin, 2006).

Combination dose pairs that fall:

- Below the line indicate synergy (less drug required than predicted by additivity),
- On the line indicate additivity,
- Above the line indicate antagonism (greater drug required than predicted).

Thus, the distance of combination points from the additivity line reflects the magnitude of interaction, while comparison across increasing Fa levels reveals whether interaction strength is effect-dependent. Isobologram analysis was performed to visually assess the nature of interaction between irinotecan and each phytochemical at defined fractional effects (Fa = 0.5, 0.75, and 0.9). In these plots, the x- and y-axes represent the doses of Drug B and Drug A required to achieve a given Fa when administered alone. The straight line connecting these intercepts represents the line of additivity. Combination data points falling below this line indicate synergy (reduced doses required relative to additivity), points on the line indicate additivity, and points above the line indicate antagonism.

In **Figure 14 A**, the combination data points at Fa = 0.5 (blue) and Fa = 0.75 (red) predominantly fall below the corresponding additivity lines, indicating synergistic interaction at moderate effect levels. The displacement below the line is more pronounced at Fa = 0.5, suggesting stronger synergy at mid-range inhibition. At Fa = 0.9 (green), the combination point remains slightly below or near the additivity line, indicating that synergy is maintained, although less dramatically than at Fa = 0.5. The overall pattern suggests consistent cooperative interaction between TQ and irinotecan across increasing cytotoxic intensity, without clear evidence of antagonistic deviation at higher effect levels.

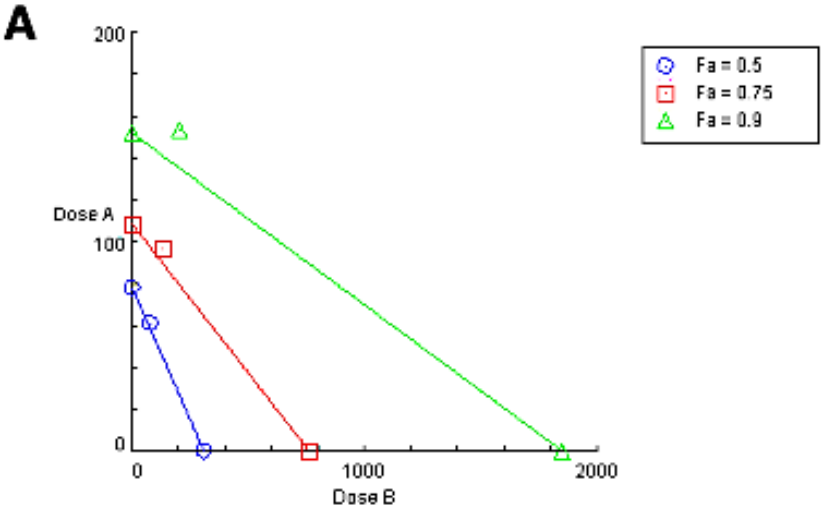
Figure 14 B demonstrates a more effect-dependent interaction profile. At Fa = 0.5 (blue), the combination point lies below the additivity line, indicating synergy at moderate inhibition. At Fa = 0.75 (red), the point approaches the line of additivity, suggesting reduced synergistic strength. At Fa = 0.9 (green), the combination point lies close to or slightly above the additivity line, indicating a shift toward

additivity or mild antagonism at high effect levels. This pattern mirrors the CI data, where β-lapachone demonstrated diminishing cooperative benefit and a tendency toward antagonism as Fa increased. Thus, the isobologram confirms that LAPIRI synergy is most pronounced at lower-to-intermediate effect levels and weakens at higher cytotoxic intensities.

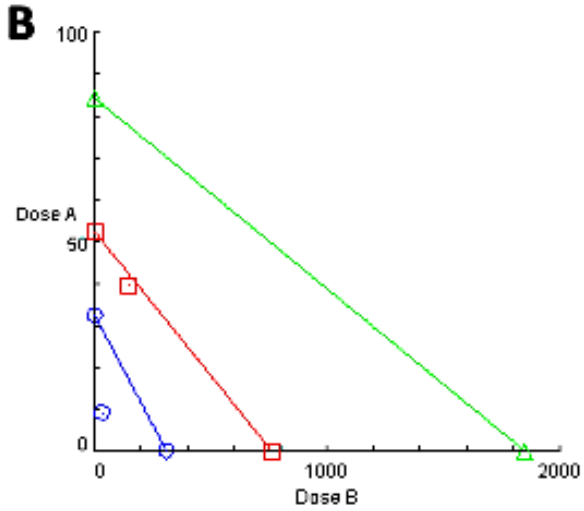
Figure 14 C displays a distinct pattern. At Fa = 0.5 (blue), combination points fall below the additivity line, indicating synergy at moderate effect levels. At Fa = 0.75 (red), the points remain below the line, confirming sustained cooperative interaction.

However, at Fa = 0.9 (green), the combination points shift closer to the line of additivity, suggesting reduced but still present synergistic interaction at high effect levels. Notably, the separation below the additivity line at Fa = 0.75 is appreciable, supporting robust synergy at therapeutically relevant mid-to-high inhibition levels.

Isobologram for Combo: TQIRI (TQ+IRI [1:1.36])



Isobologram for Combo: LAPIRI (B-LAP+IRI [1:3.71])



Isobologram for Combo: OLIRI (B-OL+IRI [1:1.61])

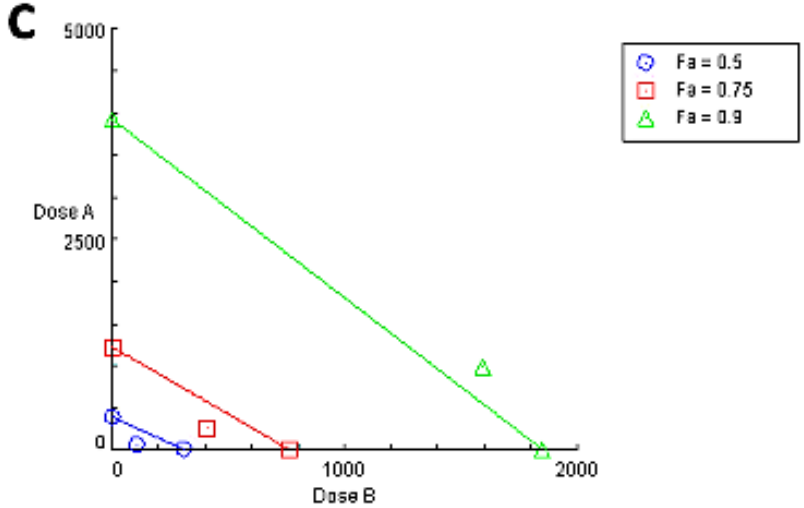


Figure 14: Isobologram Analysis of Irinotecan Combined with Thymoquinone (TQIRI), β-lapachone (LAPIRI), and β-lapachol (OLIRI) in MCF-7 Cells. Isobolograms were generated at fractional effects Fa = 0.5 (blue circles), Fa = 0.75 (red squares), and Fa = 0.9 (green triangles). The x-axis represents the dose of irinotecan (Drug B) required to achieve the indicated Fa when used alone, and the y-axis represents the dose of the partner compound (Drug A) required alone. The straight line connecting the single-agent intercepts represents the theoretical line of additivity. Combination data points falling below this line indicate synergism, points on the line indicate additivity, and points above the line indicate antagonism. **A**: Combination dose pairs fall below the line of additivity at Fa = 0.5 and 0.75, indicating synergistic interaction at moderate effect levels. At Fa = 0.9, the point remains at or slightly below the line, demonstrating maintained cooperative interaction at high cytotoxic intensity. **B**: Synergy is observed at Fa = 0.5, with combination points below the additivity line. At Fa = 0.75, points approach the line, indicating reduced interaction strength. At Fa = 0.9, the combination lies on or slightly above the line, reflecting a shift toward additivity or mild antagonism at higher effect levels. **C**: Combination points fall below the additivity line at Fa = 0.5 and 0.75, indicating sustained synergy at intermediate inhibition levels. At Fa = 0.9, the point lies closer to the additivity line, suggesting attenuation of synergy at maximal effect without clear antagonistic deviation.

4.1.2.2 HCT116 Combination Treatments

The LAPIRI combination (blue) demonstrated a progressive Fa-dependent increase in CI values. At lower Fa levels (~0.2–0.4), CI values approached or slightly fell below 1, suggesting borderline synergy or additivity. However, as Fa increased beyond ~0.5, CI values consistently rose above 1, with the regression curve steeply diverging upward. This pattern is quantitatively supported by a moderate slope ($m = 0.20639 \pm 0.05299$) and correlation coefficient ($r = 0.63883$). Although the slope appears numerically modest, the upward curvature of the fitted CI line at higher Fa values indicates increasing antagonism at elevated cytotoxic intensities. The median-effect dose ($Dm = 169.158$) further suggests that relatively high combined doses are required to achieve Fa = 0.5 in HCT116 cells. Thus, β-lapachone appears to confer limited cooperative enhancement with irinotecan in this cell line, particularly at higher effect levels where antagonistic behavior predominates.

In contrast, the OLIRI combination (green) exhibited a distinctly synergistic profile across much of the Fa spectrum. CI values remained well below 1 from low to high Fa levels, and at Fa approaching 0.9–1.0, CI values declined dramatically toward near-zero values, indicating strong synergy at high cytotoxic intensities. The regression parameters support this observation, with a slope of $m = 1.30513 \pm 0.47168$ and $Dm = 30.9304$. The relatively low Dm indicates that 50% effect is achieved at substantially lower doses compared to the other combinations, reflecting enhanced potency. Although the correlation coefficient ($r = 0.50810$) suggests moderate dispersion, the consistent placement of CI values below unity confirms a predominantly synergistic interaction profile. The logarithmic CI plot (Panel B) reinforces this, showing sustained negative log(CI) values across Fa levels, particularly pronounced at high Fa.

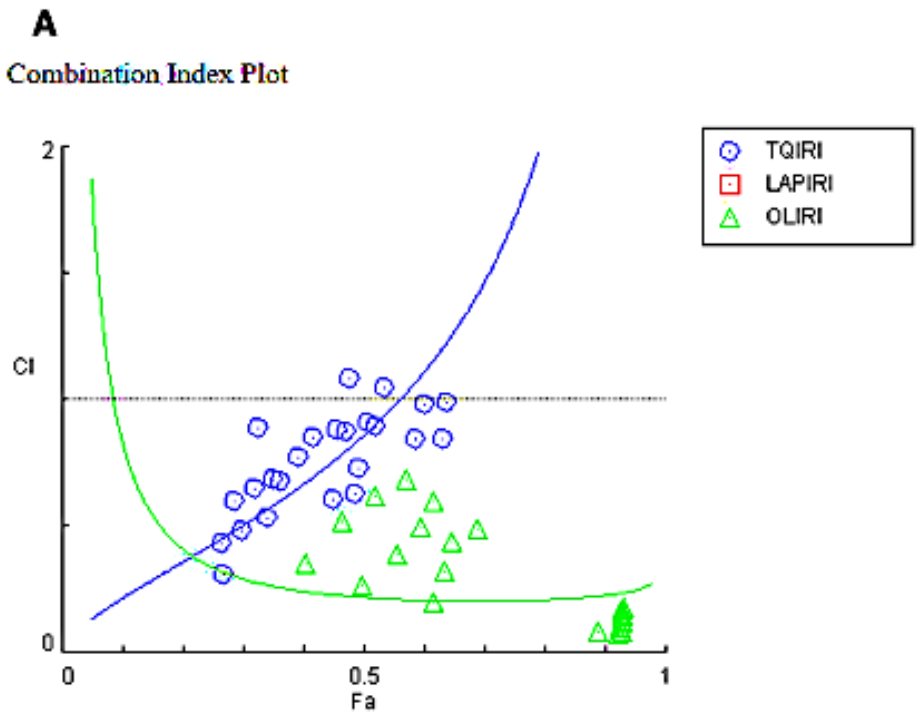
The TQIRI combination (red) demonstrated the most statistically robust linear conformity ($r = 0.92888$), indicating strong adherence to median-effect modeling. CI values were consistently below 1 across the tested Fa range, particularly within mid-to-high effect levels (Fa ~0.4–0.8), demonstrating sustained

synergism. The slope (m = 0.80960 ± 0.06883) indicates moderate Fa-dependence, without the dramatic antagonistic escalation observed with LAPIRI. The Dm value (217.449) suggests a higher dose requirement for achieving 50% effect relative to OLIRI; however, once effect is induced, the interaction remains synergistic rather than shifting toward antagonism. The tight clustering of points around the regression line in both linear and logarithmic plots indicates strong predictive consistency of the interaction.

Comparatively, the hierarchy of interaction strength in HCT116 cells differs markedly from that observed in MCF-7 cells. In HCT116, OLIRI and TQIRI display sustained synergism across increasing effect levels, whereas LAPIRI transitions toward antagonism at higher Fa. The pronounced downward curvature of the OLIRI CI curve at high Fa indicates enhanced cooperative cytotoxicity under conditions of substantial growth inhibition, suggesting that β-lapachol may potentiate irinotecan-induced DNA damage or apoptotic signaling more effectively in this colorectal carcinoma model.

The logarithmic transformation (Panel B) enhances interpretation by centering additivity at log(CI) = 0. Here, OLIRI and TQIRI remain predominantly below zero across the Fa range, confirming synergy, while LAPIRI progressively rises above zero at higher Fa, confirming antagonistic deviation. The divergence patterns emphasize that interaction behavior is strongly effect-dependent and cell-line specific.

Collectively, these findings in **Figure 15 A and B** indicate that in HCT116 cells, β-lapachol and thymoquinone enhance irinotecan cytotoxicity in a sustained and Fa-consistent manner, whereas β-lapachone demonstrates diminishing cooperative interaction at higher effect levels. These differences likely reflect cell-type-specific modulation of DNA damage response pathways, oxidative stress handling, and apoptotic threshold activation.


A
Combination Index Plot
CI
Fa
TQIRI
LAPIRI
OLIRI
0
0.5
1
2

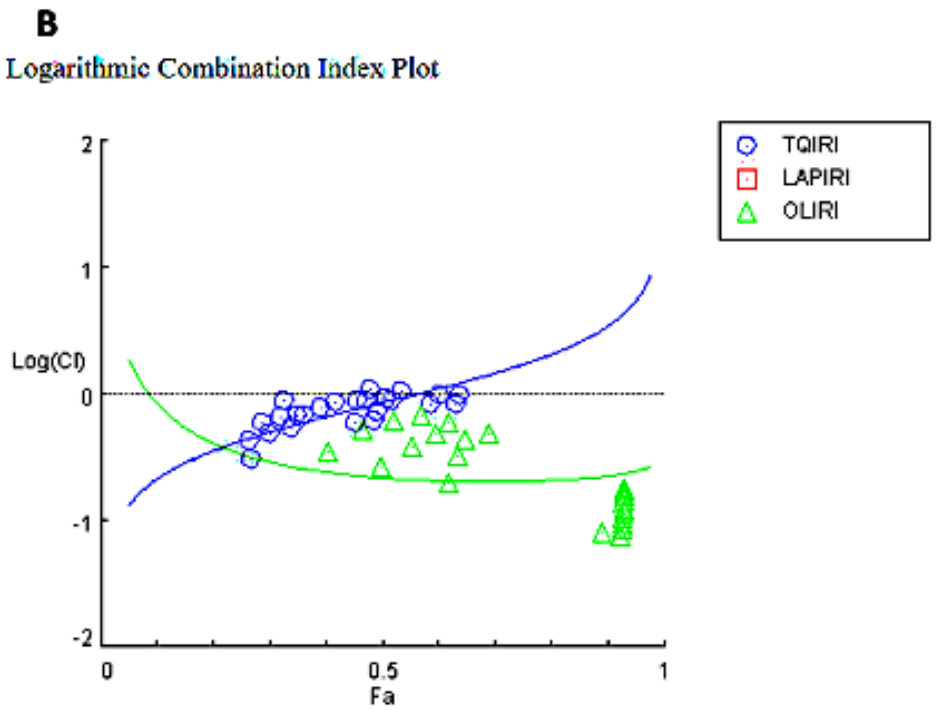

B
Logarithmic Combination Index Plot
Log(CI)
Fa
TQIRI
LAPIRI
OLIRI
2
1
0
-1
-2
0.5
1

Figure 15: **Combination Index Analysis on the Synergistic Effects of Thymoquinone, β-Lapachone and β-Lapachol with Irinotecan in HCT116 Cells. A**: CI values are plotted against fractional effect (Fa), with the dashed horizontal line indicating additivity (CI = 1). Values below this line represent synergism and values above represent antagonism. LAPIRI (blue circles) demonstrates CI values that increase above 1 as Fa rises, indicating a shift toward antagonism at higher cytotoxic effect levels. OLIRI (green triangles) remains consistently below CI = 1 across the Fa range, with marked CI reduction at high Fa, reflecting strong synergy. TQIRI (red squares) also shows CI values predominantly below 1, indicating sustained synergistic interaction without transition to antagonism. Solid curves represent fitted regression lines derived from median-effect modeling (n = 24 data points per combination). **B**: Logarithmic transformation of CI values [log(CI) vs Fa] centers additivity at log(CI) = 0. Downward deviation confirms synergism, while upward deviation indicates antagonism. OLIRI and TQIRI remain below zero across most Fa levels, whereas LAPIRI crosses above zero at higher Fa, confirming its antagonistic shift. Regression parameters (slope m, median-effect dose Dm, and correlation coefficient r) quantify the magnitude and Fa-dependence of each interaction.

The dose–effect curves for HCT116 cells illustrate the relationship between increasing combination dose and fractional effect (Fa) for irinotecan combined with thymoquinone (TQIRI), β-lapachone (LAPIRI), and β-lapachol (OLIRI). Fa reflects the proportion of growth inhibition (0–1), and the fitted curves represent median-effect modeling derived from the mass-action law. Marked differences in potency, maximal efficacy, and slope dynamics are evident among the three combinations.

The OLIRI combination (green) demonstrates the most striking pharmacodynamic profile. The curve rises sharply at very low doses, rapidly achieving high fractional effects (Fa ≈ 0.85–0.95) within a relatively narrow dose window. This steep early ascent indicates high potency and strong dose responsiveness. The rapid approach to maximal effect suggests that β-lapachol markedly potentiates irinotecan-induced cytotoxicity in HCT116 cells. The curve then plateaus near Fa ≈ 1, indicating near-complete growth inhibition without evidence of declining efficacy at higher doses. This profile is consistent with the previously observed strong synergistic CI behavior and the low median-effect dose (Dm ≈ 30.9), confirming that 50% inhibition is achieved at comparatively low combination doses.

In contrast, the TQIRI curve (blue) shows a gradual, sigmoidal increase in Fa across the dose range. The slope is moderate, and maximal effect remains below that achieved by OLIRI within the tested concentration range (Fa ≈ 0.65–0.7 at the highest doses). This indicates that although thymoquinone enhances irinotecan activity, the magnitude of potentiation is less pronounced than β-lapachol in this cell line. The rightward displacement of the curve reflects a higher Dm (≈217.4), indicating that greater doses are required to achieve equivalent cytotoxicity. Nevertheless, the steady upward trajectory without plateau at low Fa suggests sustained pharmacodynamic engagement without early saturation.

The LAPIRI curve (red) demonstrates the most limited efficacy profile. Although an initial increase in Fa is observed at low doses, the curve rapidly plateaus around Fa ≈ 0.5–0.55, indicating restricted maximal effect even at higher combination doses. This early plateau suggests that β-lapachone does not effectively amplify irinotecan-induced cytotoxic mechanisms in HCT116 cells and may encounter early pathway saturation or compensatory resistance mechanisms. The relatively flat upper segment of the curve is consistent with the antagonistic shift observed in the CI analysis at higher Fa levels.

Comparatively, the hierarchy of maximal cytotoxic efficacy in HCT116 cells is:
OLIRI > TQIRI > LAPIRI

In terms of potency (dose required to achieve mid-level effect), OLIRI exhibits the greatest potency (lowest Dm), followed by LAPIRI, while TQIRI requires substantially higher doses for equivalent effect. However, potency must be interpreted alongside maximal achievable efficacy: despite moderate early potency, LAPIRI fails to escalate cytotoxic response at higher doses. The separation of the curves across the entire dose spectrum indicates fundamentally distinct interaction kinetics between irinotecan and each phytochemical. The steepness and early inflection of the OLIRI curve reflect cooperative amplification of cytotoxic signaling, whereas the gradual slope of TQIRI suggests moderate synergy without strong amplification. The constrained profile of LAPIRI indicates limited pharmacodynamic synergy and aligns with the antagonistic CI behavior observed at higher Fa values.
Collectively, these dose–effect relationships, presented in **Figure 16**, confirm that in HCT116 cells, β-lapachol most effectively enhances irinotecan-mediated cytotoxicity, thymoquinone produces moderate enhancement, and β-lapachone demonstrates comparatively limited combinatorial benefit.

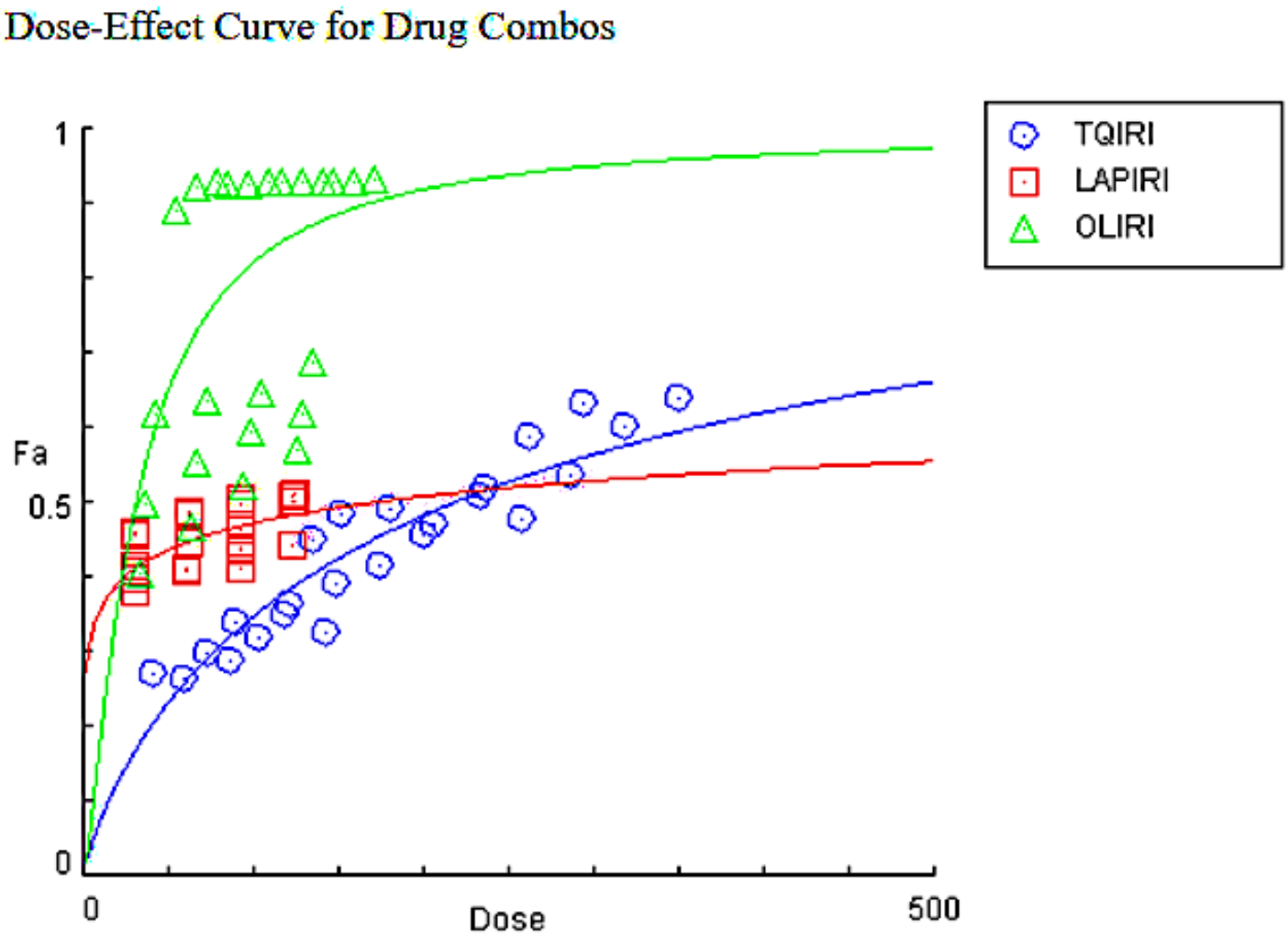


Figure 16: Differential Potency and Activity of Thymoquinone, β-Lapachone, and β-Lapachol in Combination with Irinotecan in HCT116 Cells. Fractional effect (Fa) is plotted against increasing combination dose. Symbols represent experimental data points, and solid lines indicate fitted median-effect curves. OLIRI (green triangles) exhibits a steep early rise and reaches near-maximal Fa, indicating high potency and strong enhancement of irinotecan cytotoxicity. TQIRI (blue circles) shows a gradual sigmoidal increase with moderate maximal effect. LAPIRI (red squares) displays early plateauing at intermediate Fa, indicating limited maximal efficacy. Differences in curve steepness, horizontal displacement, and plateau levels reflect variation in potency (Dm), sigmoidicity (m), and maximal cytotoxic amplification among the combinations.

The median-effect plot linearizes the dose–response relationship according to the Chou–Talalay equation, where log(Fa/Fu) is plotted against log(D). This transformation enables direct evaluation of the slope (m), which reflects the sigmoidicity and cooperativity of the response, and the x-intercept, corresponding to the median-effect dose (Dm), the combination dose required to produce 50% inhibition (Fa = 0.5). The linearity of each regression confirms adherence to mass-action law kinetics and validates subsequent CI calculations. Distinct pharmacodynamic behaviors are evident among the three combinations.

The OLIRI combination (green) displays the steepest regression line, consistent with a slope (m) greater than 1. This indicates strong sigmoidicity and cooperative dose–response behavior. A steep slope implies that once a threshold dose is reached, small incremental increases in dose produce disproportionately large increases in cytotoxic effect. The relative leftward positioning of the OLIRI line compared to TQIRI suggests a lower Dm, indicating greater potency and reduced dose requirement to achieve median effect. The tight upward trajectory at higher log(Fa/Fu) values reflects strong amplification of cytotoxic response at higher effect levels, aligning with the pronounced synergism observed in the CI analysis.

The TQIRI combination (blue) demonstrates a moderately steep regression line, indicating a slope close to but slightly below that of OLIRI. The line is positioned rightward relative to OLIRI, consistent with a higher Dm and therefore reduced potency in achieving Fa = 0.5. However, the linear conformity of the data points to the regression line indicates consistent pharmacodynamic behavior and strong adherence to median-effect modeling. The moderate slope suggests controlled but sustained dose-dependent enhancement of effect without extreme cooperativity.

In contrast, the LAPIRI combination (red) exhibits the shallowest slope, indicative of reduced sigmoidicity and diminished cooperative kinetics. The flatter trajectory suggests that increases in dose produce relatively modest increments in effect. Although the regression line intersects the mid-range of log(Fa/Fu), its shallow gradient indicates limited capacity for cytotoxic amplification at higher doses. This kinetic behavior corresponds with the plateau observed in the dose–effect curve and the antagonistic shift seen in the CI plot at higher fractional effects. The broader dispersion of data points

around the LAPIRI regression line suggests comparatively weaker conformity to median-effect assumptions relative to OLIRI and TQIRI.

Comparatively, the hierarchy of slope magnitude in HCT116 cells is:
OLIRI > TQIRI > LAPIRI

This ranking mirrors the observed degree of cytotoxic amplification and synergistic behavior. A higher slope (m > 1) for OLIRI indicates cooperative pharmacodynamics and strong enhancement of irinotecan activity. A moderate slope for TQIRI indicates stable, predictable dose-dependent response. A shallow slope for LAPIRI suggests limited cooperative interaction and reduced dynamic responsiveness.
The linearity of all regression plots confirms that the combination responses obey the mass-action principle; however, differences in slope and intercept demonstrate that potency and cooperative dynamics vary substantially between phytochemical partners. These distinctions mechanistically underpin the divergent CI behaviors observed in HCT116 cells, as shown in **Figure 17**.

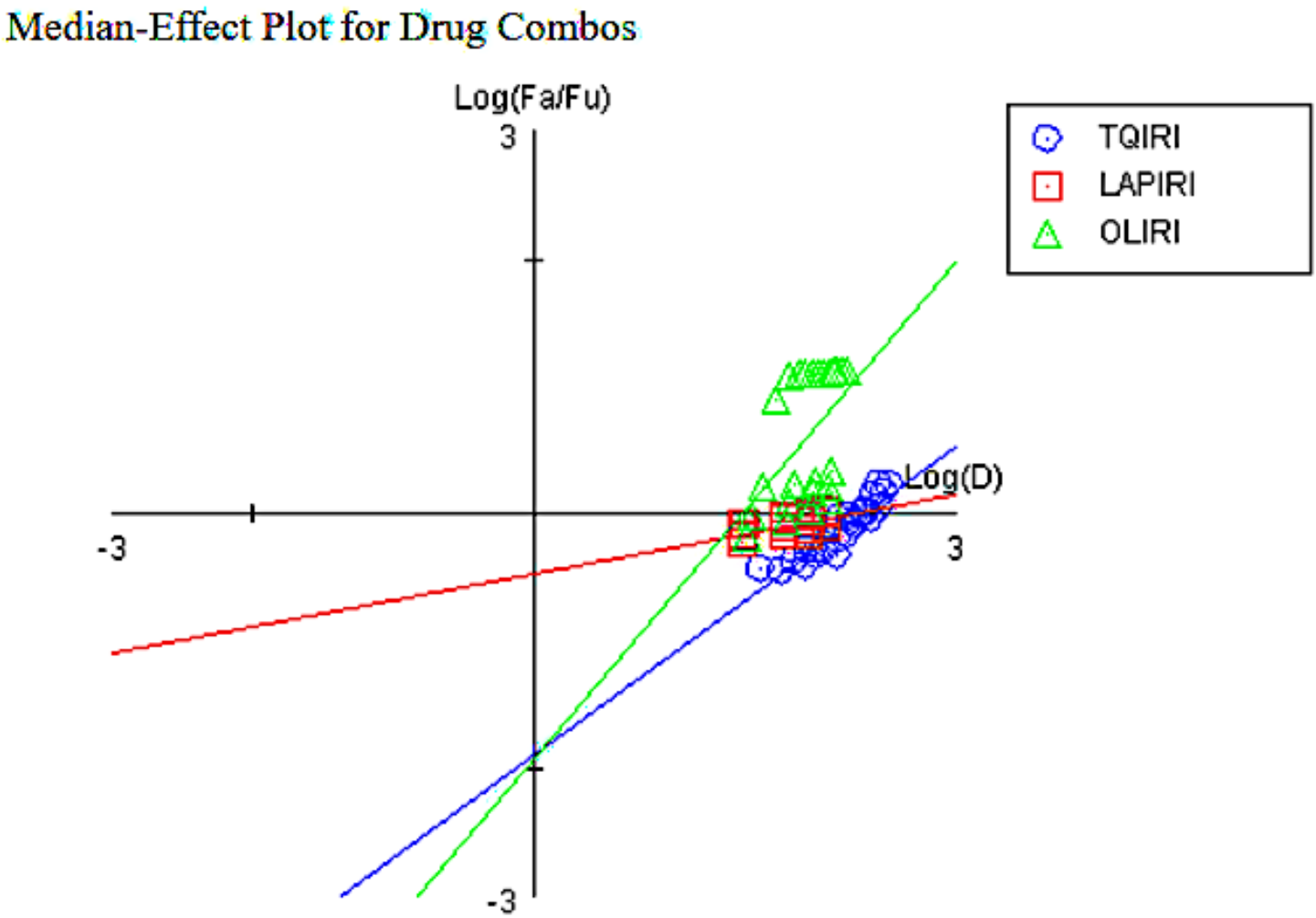


Figure 17: Differential Dose–Response Slopes of Thymoquinone, β-Lapachone, and β-Lapachol in Combination with Irinotecan in HCT116 Cells. Log(Fa/Fu) is plotted against log(D) according to the Chou–Talalay median-effect equation. Symbols represent experimental data points and solid lines represent linear regression fits used to determine slope (m) and median-effect dose (Dm). OLIRI (green triangles) exhibits the steepest slope and leftward positioning, indicating strong cooperativity and high potency. TQIRI (blue circles) demonstrates moderate slope and rightward displacement, reflecting stable but less potent dose responsiveness. LAPIRI (red squares) shows a shallow slope, indicating limited sigmoidicity and reduced amplification of effect. Linearity confirms conformity to median-effect modeling and supports the validity of combination index analysis derived from these parameters.

For **Figure 18 A**, in the TQIRI combination, both drugs demonstrate DRI values greater than 1 across much of the intermediate Fa range, indicating reciprocal dose-reduction benefit. Thymoquinone (blue circles) shows particularly elevated DRI values at lower-to-mid Fa (≈3–5), suggesting that its effective dose can be markedly reduced when combined with irinotecan. However, as Fa increases, DRI values for both agents trend downward toward 1, indicating diminishing dose-sparing advantage at higher cytotoxic intensities. Irinotecan (red squares) also maintains DRI values predominantly above 1 within moderate Fa levels, though with lower magnitude compared to TQ. The convergence of both curves toward unity at higher Fa suggests that while synergy is present at moderate inhibition levels, the cooperative dose-reduction effect is attenuated as near-maximal growth inhibition is approached.

For **Figure 18 B**, the LAPIRI combination demonstrates a markedly asymmetric DRI profile. β-lapachone (blue circles) exhibits DRI values consistently below 1 across nearly the entire Fa range, clustering close to zero at mid-to-high Fa levels. This indicates an unfavorable dose-reduction profile for β-lapachone, suggesting that higher, rather than lower, doses are required in combination to achieve comparable effects. This observation aligns with previously identified antagonistic tendencies in HCT116 CI analysis. In contrast, irinotecan (red squares) demonstrates DRI values above 1 at lower Fa levels, but these values decrease sharply as Fa increases, approaching or falling below unity. The steep downward regression of the irinotecan curve indicates rapidly diminishing dose-sparing benefit at higher effect levels. Collectively, this panel confirms limited pharmacodynamic compatibility between β-lapachone and irinotecan in HCT116 cells.

For **Figure 18 C**, the OLIRI combination exhibits the most favorable and consistent DRI profile in HCT116 cells. Irinotecan (red squares) demonstrates DRI values consistently above 1 across the evaluated Fa range, indicating meaningful dose reduction potential at moderate inhibition levels. β-Lapachol (blue circles) shows increasing DRI values as Fa increases, with a steep upward trajectory at lower Fa values. This suggests strong cooperative enhancement, particularly at early-to-intermediate cytotoxic thresholds. Unlike LAPIRI, neither drug demonstrates sustained DRI values below 1, and no pronounced collapse toward unity is observed within the primary Fa window evaluated. This balanced and sustained dose-sparing effect supports the previously observed strong synergistic CI profile and low median-effect dose (Dm) for OLIRI in HCT116 cells.

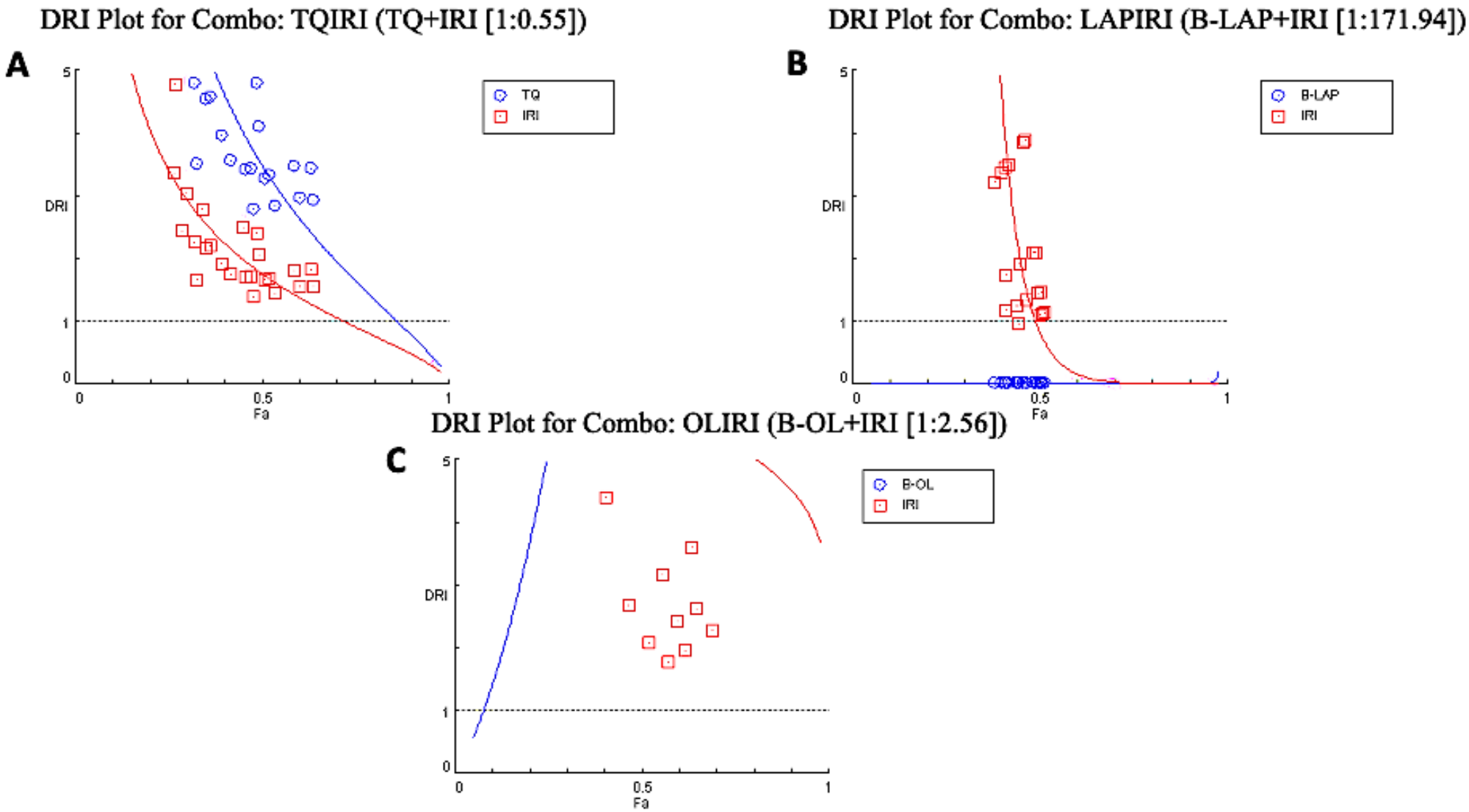

DRI Plot for Combo: TQIRI (TQ+IRI [1:0.55])
A
DRI
Fa
TQ
IRI
DRI Plot for Combo: LAPIRI (B-LAP+IRI [1:171.94])
B
B-LAP
IRI
DRI Plot for Combo: OLIRI (B-OL+IRI [1:2.56])
C
B-OL
IRI

Figure 18: Differential Dose Reduction Effects of Thymoquinone, β-Lapachone, and β-Lapachol in Combination with Irinotecan in HCT116 Cells. DRI values are plotted against fractional effect (Fa). The dashed horizontal line at DRI = 1 represents additivity. DRI > 1 indicates favorable dose reduction relative to single-agent treatment, while DRI < 1 indicates an unfavorable interaction. **A**: Both thymoquinone (blue circles) and irinotecan (red squares) demonstrate DRI values above 1 at intermediate Fa levels, indicating reciprocal dose-reduction benefit. DRI values decline toward unity at higher Fa, reflecting attenuation of dose-sparing at maximal inhibition. **B**: β-lapachone (blue circles) shows DRI values below 1 across most Fa levels, indicating unfavorable dose reduction. Irinotecan (red squares) exhibits modest DRI > 1 at lower Fa with sharp decline toward unity or below at higher Fa, reflecting limited cooperative benefit. **C**: Both β-lapachol (blue circles) and irinotecan (red squares) display sustained DRI > 1 across the Fa range, indicating consistent and reciprocal dose-reduction advantage in HCT116 cells.

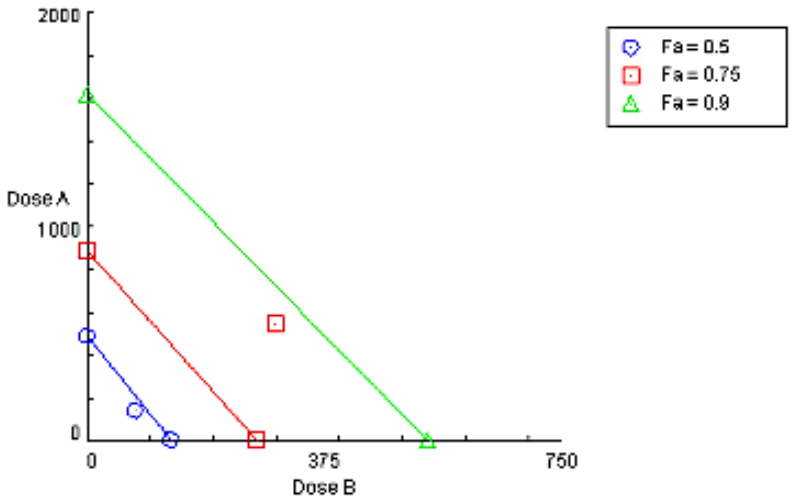
For **Figure 19 A**, at Fa = 0.5 (blue), combination dose pairs lie clearly below the additivity line, indicating synergistic interaction at moderate inhibition levels. At Fa = 0.75 (red), the combination point remains below the line, confirming maintained synergy at higher effect levels. At Fa = 0.9 (green), the point approaches but does not clearly exceed the additivity boundary, suggesting sustained cooperative interaction even at high cytotoxic intensity. The progressive positioning of the combination points consistently below the theoretical line across Fa levels confirms that thymoquinone enhances irinotecan efficacy in HCT116 cells without evidence of antagonistic deviation. The magnitude of downward displacement is most pronounced at intermediate Fa levels, indicating strongest synergy within this biologically relevant inhibition range.

For **Figure 19 B**, the LAPIRI isobologram displays a distinctly different interaction pattern. At Fa = 0.5 (blue), combination points lie near or slightly above the additivity line, suggesting limited synergy or early antagonistic tendency. At Fa = 0.75 (red), the combination aligns closely with the additivity line, indicating predominantly additive interaction. At Fa = 0.9 (green), the combination points approach or exceeds the line of additivity, consistent with antagonistic interaction at high cytotoxic effect levels. The minimal downward displacement across all Fa levels indicates weak cooperative interaction between β-lapachone and irinotecan in HCT116 cells. This geometric behavior directly corresponds to the unfavorable DRI profile and CI trend previously observed.

For **Figure 19 C**, the OLIRI combination demonstrates the most pronounced synergistic profile among the three. At Fa = 0.5 (blue), the combination point lies well below the additivity line, indicating strong synergy at moderate inhibition levels. At Fa = 0.75 (red), synergy remains evident, with combination doses substantially lower than predicted by additivity. At Fa = 0.9 (green), the combination point remains below the additivity line, demonstrating preserved synergistic interaction even at high levels of growth inhibition. The consistent downward displacement across all Fa levels confirms robust cooperative pharmacodynamics between β-lapachol and irinotecan in HCT116 cells.

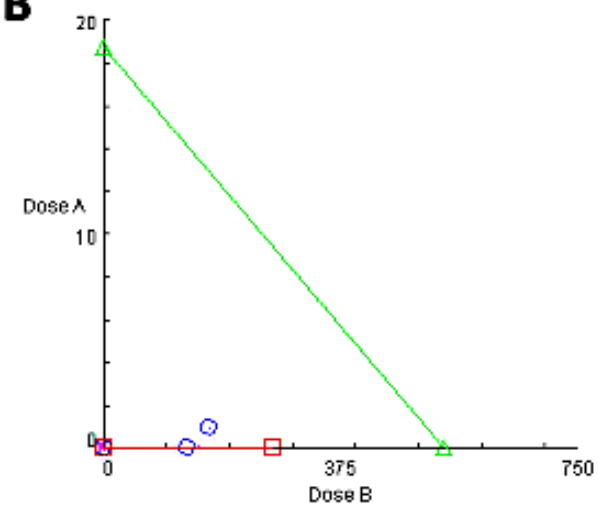
Isobologram for Combo: TOIRI (TO+IRI [1:0.55])

A



Isobologram for Combo: LAPIRI (B-LAP+IRI [1:171.94])

B



Isobologram for Combo: OLIRI (B-OL+IRI [1:2.56])

C

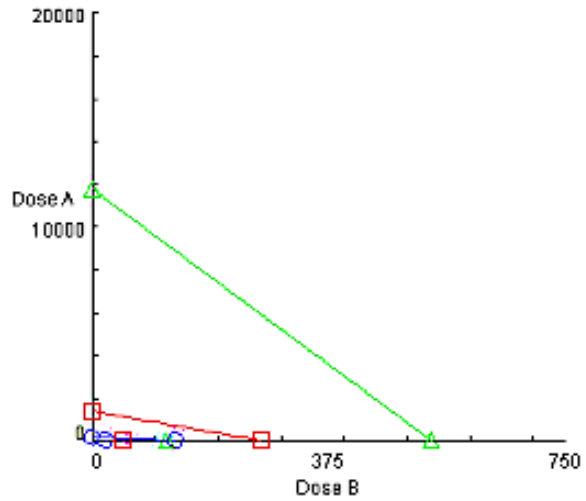


Figure 19: Isobologram Analysis of Irinotecan Combinations in HCT116 Cells. Isobolograms are shown for Fa = 0.5 (blue circles), Fa = 0.75 (red squares), and Fa = 0.9 (green triangles). The x-axis represents the dose of irinotecan required to achieve the specified Fa when used alone, and the y-axis represents the dose of the partner compound required alone. The straight-line connecting intercepts represents theoretical additivity; points below the line indicate synergism, on the line indicate additivity, and above the line indicate antagonism. **A**: Combination dose pairs fall below the additivity line across Fa levels, indicating sustained synergistic interaction. **B**: Combination points lie near or above the additivity line, particularly at Fa = 0.9, indicating reduced synergy and a shift toward antagonism at higher effect levels. **C**: Combination dose pairs consistently fall below the additivity line at Fa = 0.5, 0.75, and 0.9, demonstrating strong and sustained synergy in HCT116 cells.

Selection of drug combinations and concentrations for progression to the EnzChek caspase-3 assay was based on an integrated evaluation of median-effect modeling, Combination Index (CI) analysis, Dose Reduction Index (DRI) assessment, and isobologram geometry in both MCF-7 and HCT116 cell lines. The objective was to advance combinations that demonstrated reproducible and biologically meaningful synergistic cytotoxicity while excluding combinations that showed antagonistic interaction, pharmacodynamic instability, or limited dose-reduction benefit. Importantly, concentrations were selected within the mid-effect range (approximately Fa 0.4–0.7) rather than at extreme levels of growth inhibition. This approach ensured that subsequent caspase-3 measurements would reflect regulated apoptotic signaling rather than nonspecific late-stage cytotoxic collapse associated with near-complete cell death.

In MCF-7 cells, all three combinations demonstrated measurable interaction dynamics and were therefore considered for further mechanistic evaluation. The TQ+IRI combination consistently exhibited CI values below 1 within the moderate effect range, with isobologram points falling below the additivity line at Fa 0.5 and 0.75, and DRI analysis showing substantial dose-reduction benefit for irinotecan. Although synergy was attenuated at very high Fa levels, no clear antagonistic shift was observed, and concentrations corresponding to the mid-effect synergistic window were selected.

The LAPIRI combination displayed effect-dependent behavior, with synergy at lower fractional effects but increasing CI values at higher Fa, indicating a transition toward antagonism. Isobologram analysis similarly showed reduced interaction strength at Fa 0.9. Despite this attenuation, synergy was reproducible within the Fa ≈ 0.5 region, and concentrations within this window were selected to evaluate whether early cooperative cytotoxicity translated into apoptotic activation.

The OLIRI combination demonstrated stable CI values at or below 1 across intermediate effect levels, sustained DRI values above 1 for both agents, and consistent displacement below the additivity line on isobologram analysis. This profile indicated maintained cooperative interaction without pronounced antagonistic deviation, and mid-range synergistic concentrations were therefore advanced to apoptosis assessment. Thus, in MCF-7 cells, all combinations were retained, but concentration selection was restricted to the effect window where synergy was strongest, and interaction stability was preserved.

In HCT116 cells, interaction patterns diverged more clearly, permitting stricter prioritization. The TQIRI combination demonstrated sustained CI values below 1 at moderate effect levels, reciprocal dose-reduction benefit in DRI analysis, and consistent isobologram displacement below the additivity line. Although DRI values declined at extreme Fa, no antagonistic shift was observed within the biologically relevant inhibition range, and concentrations corresponding to synergistic mid-level effects were selected.

The OLIRI combination exhibited the most robust interaction profile in this cell line, with CI values consistently below 1, strong and reciprocal DRI benefit, pronounced displacement below the additivity line even at higher Fa, and favorable median-effect parameters indicating cooperative dose–response amplification. This sustained synergistic behavior supported its prioritization for caspase-3 analysis at concentrations reflecting Fa ≈ 0.5–0.7.

In contrast, the LAPIRI combination in HCT116 cells demonstrated limited or unfavorable interaction. CI values increased with Fa and approached or exceeded 1 at higher effect levels, indicating additivity or antagonism. DRI analysis revealed values below 1 for β-lapachone across much of the Fa range, indicating an absence of dose-reduction benefit, while irinotecan showed only transient improvement at low Fa that diminished rapidly. Isobologram analysis confirmed minimal displacement below the additivity line and, at higher effect levels, positioning consistent with antagonism. The dose–effect curve further showed early plateauing, suggesting restricted cytotoxic amplification. Because the EnzChek caspase-3 assay was intended to investigate apoptotic mechanisms underlying synergistic drug interaction, advancing a combination that demonstrated antagonistic pharmacodynamic behavior would not provide mechanistically meaningful insight. For this reason, the β-Lap + IRI combination was excluded from further evaluation in HCT116 cells.

Overall, progression to apoptosis analysis was guided by sustained CI values below unity within moderate effect ranges, favorable DRI profiles, geometric confirmation of synergy on isobologram analysis, and strong conformity to median-effect modeling. This multi-parameter selection strategy ensured that caspase-3 activation would be examined under conditions of genuine cooperative cytotoxic interaction rather than nonspecific toxicity or pharmacodynamic interference.

4.2 EVALUATION OF APOPTOTIC ACTIVITY ON THE ANALYSIS OF CASPASE-3 ACTIVATION BY USING B-LAPACHONE, B-LAPACHOL, AND THYMOQUINONE IN COMBINATION WITH THE CHEMOTHERAPEUTIC AGENT IRINOTECAN

4.2.1 Evaluation of Caspase-3–Mediated Apoptotic Activity Following Combination Treatments

Caspase-3 activity in MCF-7 cells showed clear variation across treatment groups, concentrations, and time points. At all measured time points (30, 60, and 90 minutes), all combination treatments exhibited higher caspase-3 activity than the untreated control. These increases were statistically significant across most treatment conditions, as indicated by the significance markers.

At 30 minutes, caspase-3 activity was elevated in all treatment groups relative to the control. Among the combinations, TQ+IRI produced the highest activity, followed by β-OL+IRI, while β-LAP+IRI showed comparatively lower values. Both concentration levels (C1 and C2) demonstrated increased activity relative to control, with the higher concentration (C2) consistently yielding greater caspase activity than the corresponding lower concentration (C1). Statistically significant differences were observed between treated and control groups, as well as between concentration levels within the same treatment.

At 60 minutes, caspase-3 activity increased further across all treatment conditions. The same relative pattern between treatments was maintained, with TQ+IRI and β-OL+IRI exhibiting higher activity than β-LAP+IRI. The magnitude of increase from 30 to 60 minutes was evident across all combinations, and statistical significance was maintained for most comparisons relative to control. Differences between C1 and C2 concentrations remained apparent, with higher concentrations producing significantly greater caspase activity.

By 90 minutes, caspase-3 activity reached its highest levels across all treatment groups. TQ+IRI and β-OL+IRI continued to show the greatest activity, while β-LAP+IRI remained comparatively lower, although still significantly elevated relative to the control. The increase over time was consistent across all treatments, demonstrating a time-dependent rise in caspase activity. Differences between concentrations remained evident, with C2 conditions consistently exceeding C1 values. Statistical significance was observed both in comparison to the control and between concentration levels within the same treatment group.

The inclusion of the caspase inhibitor (Z-DEVD-CHO) resulted in a substantial reduction in caspase-3 activity across all treatments and time points. Inhibitor-treated samples consistently displayed significantly lower activity compared to their corresponding untreated combination groups. Despite this reduction, some inhibitor-treated groups showed slightly elevated activity relative to the untreated control, although these differences were less pronounced and, in some cases, not statistically significant.

Across all time points, statistically significant differences were observed, **Figure 20**, not only between treated and control groups but also among the different combination treatments. TQ+IRI and β-OL+IRI consistently produced higher caspase-3 activity compared to β-LAP+IRI. Additionally, both time-dependent and dose-dependent increases were evident, with caspase activity progressively increasing from 30 to 90 minutes and with increasing concentration. These trends were consistently supported by statistical significance indicators across the dataset.

The statistical analysis of MCF-7 and HCT116 are presented in appendix **Tables A 6 – A 9**. AMC standard curves were generated for each incubation time (30, 60, and 90 minutes), as shown in appendix **Figures A 3 and A 4**, to determine the relationship between AMC concentration and fluorescence intensity. The standard curves displayed strong linearity, confirming the reliability and sensitivity of the assay. These calibration curves were then used to convert fluorescence values obtained from treated samples into AMC concentration, expressed as micro moles of AMC released per minute.

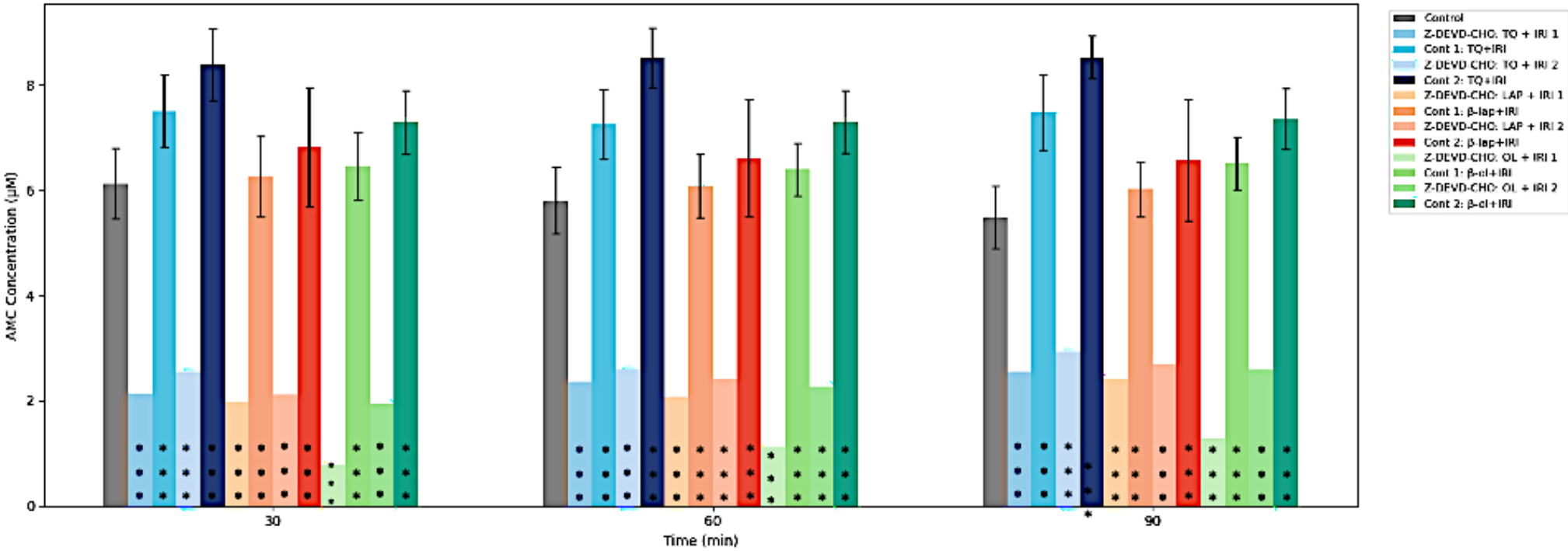

AMC Concentration (μM)
0
2
4
6
8
30
60
90
Time (min)
Control
Z-DEVD-CHO: TQ + IRI 1
Cont 1: TQ+IRI
Z-DEVD-CHO: TQ + IRI 2
Cont 2: TQ+IRI
Z-DEVD-CHO: LAP + IRI 1
Cont 1: β-lap+IRI
Z-DEVD-CHO: LAP + IRI 2
Cont 2: β-lap+IRI
Z-DEVD-CHO: OL + IRI 1
Cont 1: β-ol+IRI
Z-DEVD-CHO: OL + IRI 2
Cont 2: β-ol+IRI

Figure 20: **Caspase-Dependent Apoptosis Induced by Drug Combinations Is Attenuated by Z-DEVD-CHO in MCF-7 Cells.** Across all time points, the combination treatments produced markedly higher AMC concentrations compared to the untreated controls, indicating significant activation of caspase-3 in MCF-7 cells. The inclusion of Z-DEVD-CHO notably reduced fluorescence in all treated samples, confirming that the observed signal resulted primarily from caspase-3 enzymatic activity. Among the tested combinations, TQ+IRI (Conc 2: 72.9 μM + 99.34 μM) and LAP+IRI (Conc 2: 13.41 μM + 49.67 μM) induced the highest fluorescence intensities at 90 minutes, suggesting enhanced caspase-3 activation at higher combination concentrations and prolonged incubation. The OL+IRI combination also demonstrated a consistent increase in caspase-3 activity across all time points, though to a slightly lesser extent compared to the other two combinations. The overall trend indicates a time-dependent and concentration-dependent increase in caspase-3 activity across all treatments, supporting the induction of apoptosis by the combination therapies. Statistical analysis revealed that all treatment groups were significantly different from the control ($p < 0.001$), as indicated by the triple asterisks (***).

Caspase-3 activity in HCT116 cells varied significantly across treatment groups, concentrations, and time points (30, 60, and 90 minutes). At all time points, combination treatments resulted in higher caspase activity compared to the untreated control, with multiple conditions showing statistical significance as indicated by the presence of significance markers.

At 30 minutes, all treatment groups exhibited increased caspase-3 activity relative to the control. Among the combinations, β-OL+IRI demonstrated the highest activity, followed by TQ+IRI, while β-LAP+IRI showed comparatively lower levels. These increases were statistically significant for most treatment groups. A clear difference between concentrations was observed, with C2 treatments producing significantly higher caspase activity than their corresponding C1 treatments across all combinations.

At 60 minutes, caspase-3 activity increased further across all treatment groups. The relative trend between treatments remained consistent, with β-OL+IRI maintaining the highest activity, followed by TQ+IRI, while β-LAP+IRI remained comparatively lower. Statistical significance relative to the control was maintained across most conditions. Differences between concentration levels (C1 vs C2) remained evident and statistically significant, with higher concentrations consistently yielding greater caspase activity.

By 90 minutes, caspase-3 activity reached its highest levels across all treatment groups. β-OL+IRI showed the greatest increase, followed by TQ+IRI, while β-LAP+IRI remained the lowest among the combinations, although still significantly elevated relative to the control. The increase in caspase activity over time was consistent across all treatments, demonstrating a clear time-dependent effect. Concentration-dependent differences were also maintained, with C2 treatments significantly exceeding C1 across all combinations.

The inclusion of the caspase inhibitor (Z-DEVD-CHO) resulted in a substantial reduction in caspase-3 activity across all treatment groups at every time point. Inhibitor-treated samples consistently showed significantly lower activity compared to their respective untreated counterparts. While some inhibitor-

treated groups exhibited slight increases relative to the control, these differences were minimal and, in several cases, not statistically significant.

Overall, statistically significant differences were observed, **Figure 21**, between treatment groups, concentrations, and time points. β-OL+IRI consistently produced the highest caspase-3 activity, followed by TQ+IRI, while β-LAP+IRI showed comparatively lower responses. Additionally, caspase activity increased significantly over time and with increasing concentration, indicating both time-dependent and dose-dependent effects across all treatment conditions.

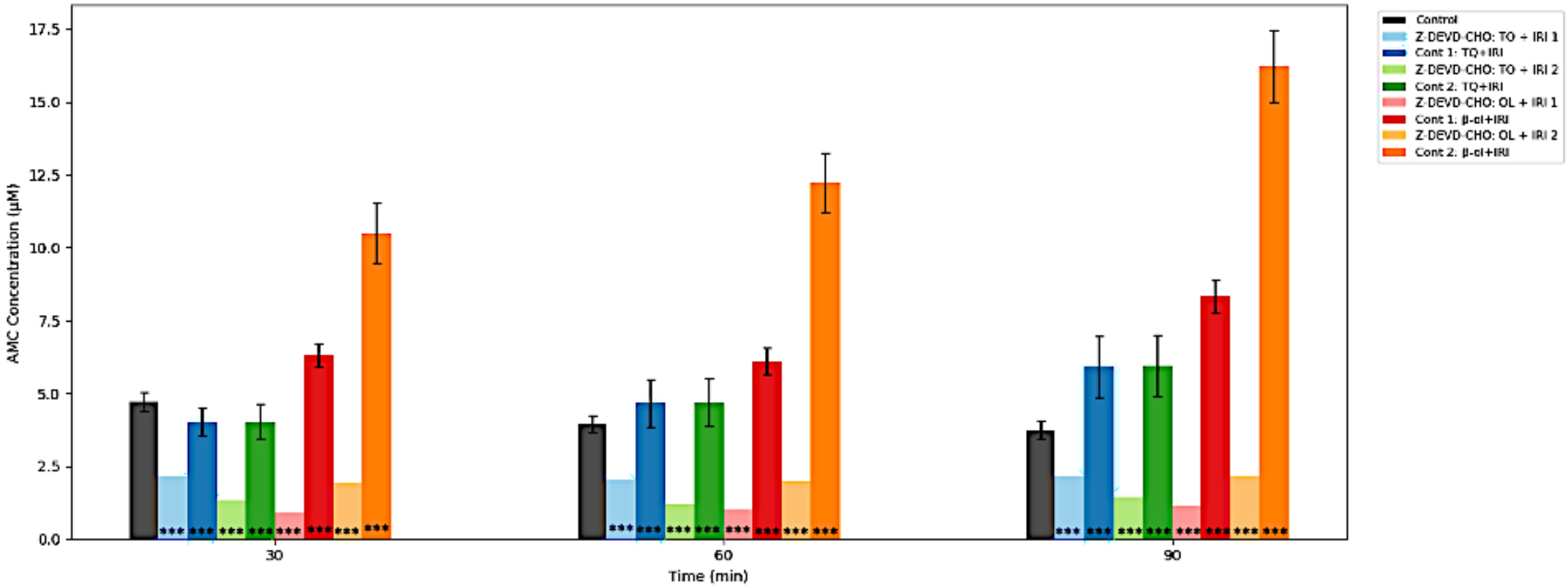

AMC Concentration (μM)
17.5
15.0
12.5
10.0
7.5
5.0
2.5
0.0
30
60
90
Time (min)
Control
Z-DEVD-CHO: TQ + IRI 1
Cont 1: TQ+IRI
Z-DEVD-CHO: TQ + IRI 2
Cont 2: TQ+IRI
Z-DEVD-CHO: OL + IRI 1
Cont 1: β-cl+IRI
Z-DEVD-CHO: OL + IRI 2
Cont 2: β-cl+IRI

Figure 21: **Caspase-Dependent Apoptosis Induced by Drug Combinations Is Attenuated by Z-DEVD-CHO in HCT116 Cells.** Across all time points (30, 60, and 90 minutes), a substantial increase in AMC concentrations was observed in all combination-treated groups compared to the untreated control, indicating enhanced caspase-3 activation. The addition of Z-DEVD-CHO markedly suppressed fluorescence, confirming that the observed activity resulted specifically from caspase-3 enzymatic cleavage rather than non-specific fluorescence or background signal. Among the treatments, the β-lapachol + Irinotecan (OL+IRI) combinations exhibited the highest fluorescence intensities, particularly at 90 minutes, suggesting strong and sustained activation of caspase-3. The Thymoquinone + Irinotecan (TQ+IRI) combination induced moderate but consistent fluorescence increases over time, indicating a comparatively lower level of caspase-3 activity in HCT116 cells. The overall pattern demonstrates a time-dependent elevation in caspase-3 activity across all treatments, with fluorescence values peaking at 90 minutes. Statistical analysis revealed significant differences between all treated groups and the control ($p < 0.001$), as denoted by triple asterisks (***).

When comparing caspase-3 activity between MCF-7 and HCT116 cells, distinct differences in apoptotic response patterns were observed. In MCF-7 cells, TQ+IRI and β-OL+IRI produced the highest caspase activity, with both treatments showing comparable and sustained increases over time. In contrast, HCT116 cells exhibited a more pronounced response to β-OL+IRI, which consistently produced the highest caspase activity across all time points and concentrations.

Furthermore, the overall magnitude of caspase-3 activity was higher in HCT116 cells compared to MCF-7 cells, indicating a stronger apoptotic response in HCT116. While both cell lines demonstrated clear time-dependent and dose-dependent increases, these effects were more pronounced in HCT116 cells, particularly at higher concentrations (C2). β-LAP+IRI consistently showed lower caspase-3 activity compared to the other combinations in both cell lines; however, this difference was more marked in HCT116 cells, where the disparity between β-LAP+IRI and the other treatments was greater.

The inhibitory effect of Z-DEVD-CHO was consistent across both cell lines, resulting in significantly reduced caspase activity in all treatment groups, confirming a similar pattern of caspase suppression. Overall, while both cell lines exhibited statistically significant increases in caspase-3 activity in response to combination treatments, HCT116 cells demonstrated a stronger and more pronounced apoptotic response, particularly for the β-OL+IRI combination, whereas MCF-7 cells showed a more balanced response between TQ+IRI and β-OL+IRI.

4.2.2 Quantification of Total Cellular Protein for Normalization of Caspase-3 Activity

To ensure accurate normalization of caspase-3 enzymatic activity, total protein concentration was quantified using the Qubit Protein Assay, presented in appendix **Tables A 10 and A 11** for MCF-7 and HCT116.

The results of the Qubit assay provided insight into variations in total protein content following exposure to the combination treatments, which may reflect treatment-induced cytotoxic effects and differences in cellular integrity or protein synthesis. These protein concentration values were then integrated into the

caspase activity calculations to express the data as activity per microgram of total protein (μM/min/μg), ensuring precise and biologically meaningful comparisons.

For the MCF-7 cell line, **Figure 22** illustrates time-dependent caspase-3 enzymatic activity (μM/min/μg protein) in MCF-7 cells treated with irinotecan in combination with thymoquinone (TQ), β-lapachone (β-LAP), or β-lapachol (β-OL). Unlike AMC accumulation graphs that reflect cumulative product formation, these data represent normalized reaction velocities and therefore provide a direct measure of active caspase-3 catalytic turnover at each time point. Across all treatment groups, caspase-3 activity was highest at 30 minutes and declined progressively at 60 and 90 minutes, indicating an early peak in executioner caspase activation followed by a gradual reduction in enzymatic rate. This kinetic profile is consistent with rapid activation of the apoptotic execution phase after drug exposure, followed by attenuation as substrate availability decreases or as cells progress further into apoptosis.

The control group demonstrated measurable basal caspase-3 activity at 30 minutes, which decreased over time. This reduction likely reflects natural decay in reaction velocity rather than a biological reversal of apoptosis and confirms that time-dependent decline is intrinsic to the assay system. Importantly, all combination treatments exceeded control activity at the early time point, demonstrating drug-induced enhancement of executioner caspase function.

Among the tested combinations, TQ+IRI produced the most pronounced early activation of caspase-3, with both concentrations exhibiting higher enzymatic rates than control at 30 minutes. Although activity declined at later time points, TQ-treated groups remained elevated relative to control throughout the time course. This suggests that thymoquinone potentiates irinotecan-mediated apoptotic signaling, leading to enhanced activation of the execution phase. The consistency between concentration replicates further supports the robustness of this effect.

The β-LAP+IRI groups displayed moderate caspase-3 activation at 30 minutes, with activity levels lower than those observed for TQ combinations but comparable to or slightly above control. The subsequent decline at 60 and 90 minutes followed a similar pattern to other treatments, indicating comparable kinetic behavior. These findings suggest that β-lapachone enhances apoptotic signaling, though to a lesser magnitude than thymoquinone under these experimental conditions.

β-OL+IRI treatment resulted in strong early caspase-3 activation, approaching levels observed in the TQ groups at 30 minutes. Notably, while activity decreased over time, β-OL groups maintained higher enzymatic rates than control at both 60 and 90 minutes. This sustained relative elevation suggests that β-OL effectively augments irinotecan-induced apoptotic execution and may exhibit prolonged catalytic engagement compared to β-lap.

Overall, in **Figure 22**, the temporal pattern observed across all groups demonstrates that combination treatments enhance early caspase-3 activation in MCF-7 cells, with peak enzymatic activity occurring

at 30 minutes. The subsequent decline likely reflects kinetic characteristics of the assay and progression through the apoptotic cascade rather than reduced apoptotic signaling. These findings support a caspase-3-dependent execution mechanism underlying the cytotoxic effects of irinotecan when combined with quinone derivatives.

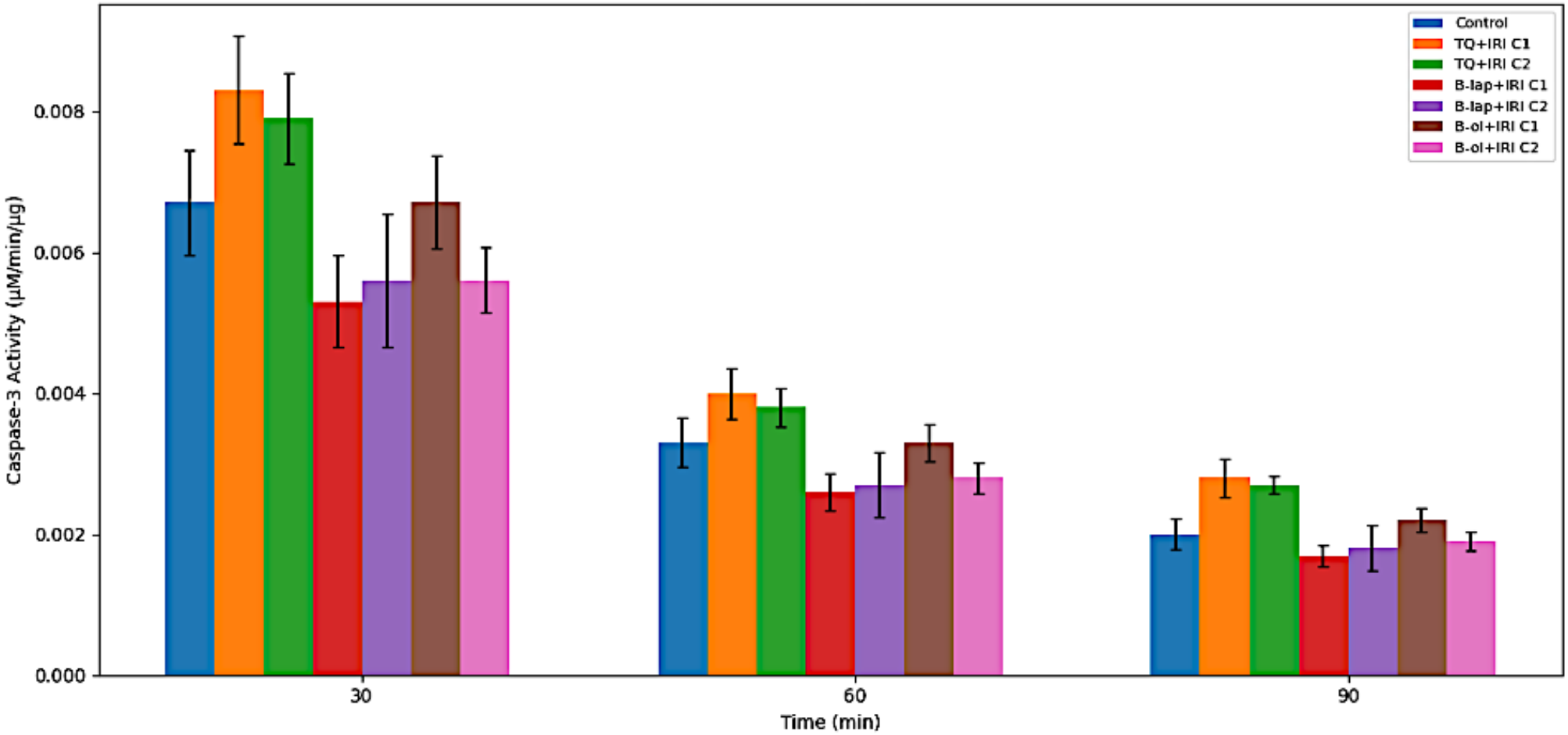

Control
TQ+IRI C1
TQ+IRI C2
B-lap+IRI C1
B-lap+IRI C2
B-ol+IRI C1
B-ol+IRI C2
Caspase-3 Activity (µM/min/µg)
0.000
0.002
0.004
0.006
0.008
30
60
90
Time (min)

Figure 22: **Enhanced Caspase-3 Activation by Drug Combinations, with Peak Activity in Thymoquinone–Irinotecan-Treated MCF-7 Cells**. Caspase-3 activity (μM/min/μg protein) was quantified at 30, 60, and 90 minutes and represents normalized reaction velocity of AMC substrate cleavage. Combination treatments with TQ, β-lapachone, or β-lapachol in the presence of irinotecan enhanced early caspase-3 catalytic activity relative to control, with peak activation observed at 30 minutes and a gradual decline at later time points.

Figure 23 illustrates time-dependent caspase-3 enzymatic activity (μM/min/μg protein) in HCT116 cells treated with irinotecan in combination with thymoquinone (TQ) or β-lapachol (β-OL). The values represent normalized reaction velocities of AMC substrate cleavage and therefore reflect the instantaneous catalytic activity of executioner caspase-3 rather than cumulative product formation. Across all treatment groups, enzymatic activity was highest at 30 minutes and declined progressively at 60 and 90 minutes, indicating an early peak in execution-phase activation followed by a gradual reduction in catalytic rate. This temporal decline is characteristic of apoptotic kinetics, where caspase activation occurs rapidly after treatment and subsequently decreases as substrate is consumed or as cells advance through later stages of apoptosis.

The control group demonstrated measurable basal caspase-3 activity at 30 minutes (~0.0046 μM/min/μg), with a marked reduction at later time points. This decrease reflects the time-dependent kinetics of the enzymatic assay rather than enhanced apoptosis in untreated cells. Importantly, combination treatments showed distinct patterns relative to control, indicating drug-induced modulation of caspase-3 activity.

In contrast to the MCF-7 dataset, TQ+IRI treatment in HCT116 cells did not enhance early caspase-3 activity above control levels at 30 minutes; rather, activity in both TQ+IRI concentrations was slightly lower than control. At 60 and 90 minutes, TQ-treated groups remained comparable to control, suggesting that thymoquinone does not strongly potentiate irinotecan-induced caspase-3 activation in HCT116 cells under these conditions. This observation highlights potential cell-line-specific differences in apoptotic signaling responsiveness.

By contrast, β-OL+IRI treatment produced a pronounced increase in caspase-3 activity at all time points. At 30 minutes, β-OL+IRI Concentration 1 (C1) and concentration 2 (C2) exhibited substantially higher enzymatic rates than both control and TQ-treated groups, with C2 demonstrating the greatest magnitude of activation. Although activity declined at 60 and 90 minutes, β-OL+IRI groups remained markedly elevated relative to all other treatments throughout the time course. This sustained elevation indicates strong and persistent executioner caspase activation, suggesting that β-ol robustly enhances irinotecan-induced apoptotic signaling in HCT116 cells.

The divergence between TQ and β-OL responses suggests mechanistic heterogeneity in quinone-mediated modulation of apoptosis. While TQ appears less effective at promoting caspase-3 catalytic activity in this cell line, β-OL induces substantial activation of the execution phase, indicating a

potentially stronger synergistic interaction with irinotecan in HCT116 cells. The consistency between concentration replicates further supports the reproducibility and biological validity of these findings.

Overall, in **Figure 23**, these results demonstrate that β-OL in combination with irinotecan markedly enhances caspase-3 enzymatic activity in HCT116 cells, whereas TQ shows minimal augmentation relative to control. The temporal decline across all groups reflects kinetic characteristics of enzymatic turnover and progression through apoptosis rather than attenuation of apoptotic signaling. These findings underscore cell-line-specific differences in caspase-3 activation profiles and suggest that β-OL may represent a more potent apoptotic sensitizer in HCT116 cells.

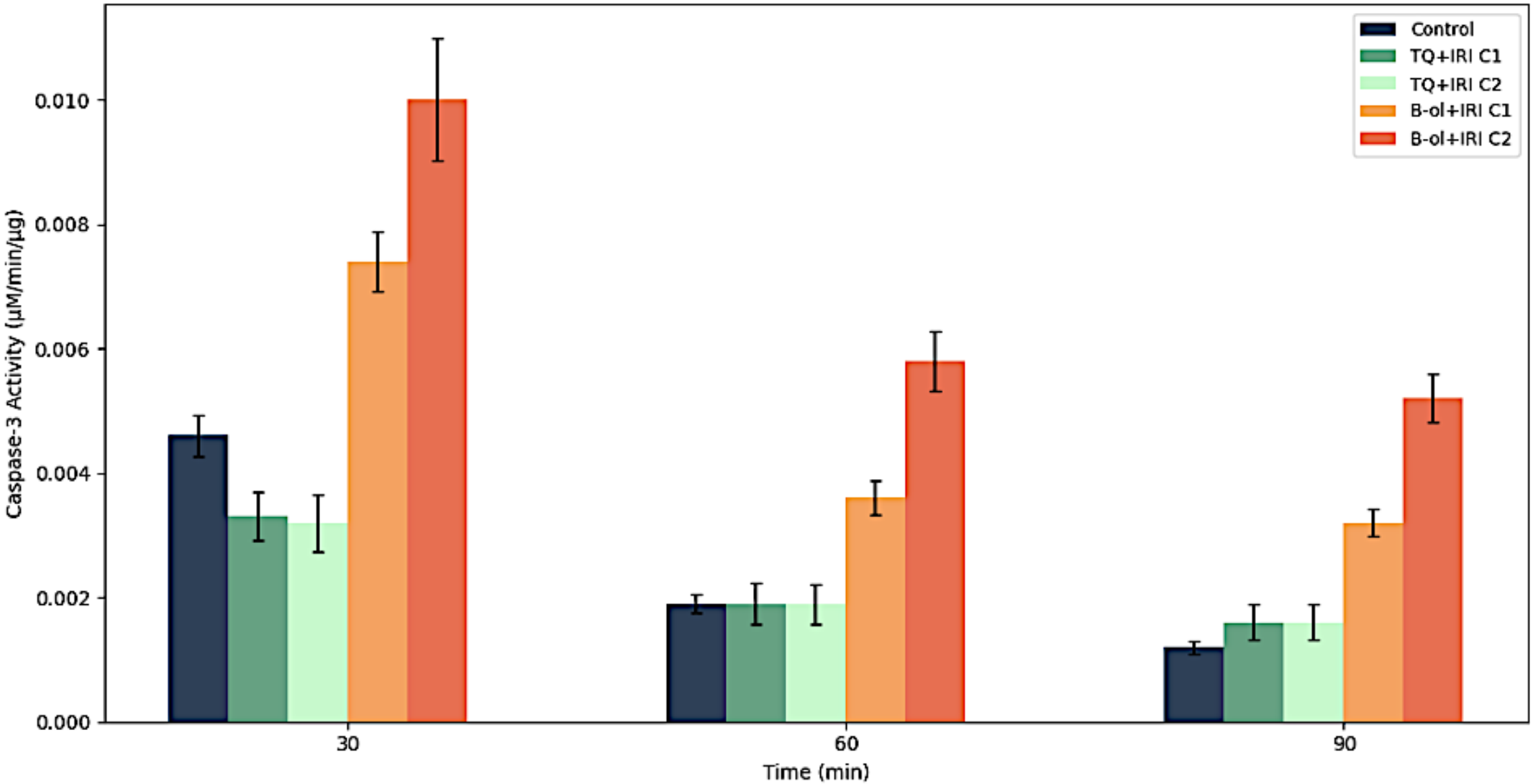

Control
TQ+IRI C1
TQ+IRI C2
B-ol+IRI C1
B-ol+IRI C2
Caspase-3 Activity (µM/min/µg)
0.000
0.002
0.004
0.006
0.008
0.010
30
60
90
Time (min)

Figure 23: **Time-Dependent Caspase-3 Activation Reveals Superior Apoptotic Response to β-Lapachol–Irinotecan in HCT116 Cells**. Caspase-3 activity (μM/min/μg protein) was measured at 30, 60, and 90 minutes and represents normalized reaction velocity of AMC substrate cleavage. β-lapachol combined with irinotecan produced marked early activation of caspase-3 that remained elevated relative to control at later time points, whereas thymoquinone combinations showed minimal enhancement.

In MCF-7 cells, both cumulative AMC concentration data and normalized caspase-3 enzymatic activity (μM/min/μg) were used to determine the most appropriate concentration of each drug combination for progression to subsequent mechanistic assays. The integration of these two datasets allowed assessment of both sustained substrate cleavage (AMC accumulation) and instantaneous catalytic activation (reaction velocity), providing a comprehensive evaluation of execution-phase apoptosis.

For the TQ+IRI combinations, both concentrations enhanced AMC accumulation relative to control at all time points. However, concentration 1 (C1) demonstrated strong early catalytic activation at 30 minutes while maintaining consistent kinetic decline and lower proportional variability across 60 and 90 minutes. Although concentration 2 (C2) occasionally showed similar cumulative AMC levels, it did not produce proportionally greater catalytic activity relative to variability. Importantly, C1 achieved robust apoptotic activation without suggesting excessive enzymatic amplification that could reflect acute cytotoxic stress rather than regulated apoptosis. Therefore, TQ+IRI concentration 1 (C1) was selected for subsequent assays in MCF-7 cells as the optimal concentration representing strong, reproducible, and biologically controlled caspase-3 activation.

For the β-LAP+IRI combinations, both AMC accumulation and caspase-3 activity data demonstrated moderate enhancement relative to control. Concentration 2 (C2) produced consistent increases in both cumulative and kinetic measures with comparatively stable variability. Concentration 1 did not demonstrate a clearly superior catalytic advantage and exhibited slightly higher variability. Since the goal is to evaluate mechanistically informative yet regulated apoptotic signaling, β-LAP+IRI concentration 2 (C2) was selected as the representative concentration for downstream assays in MCF-7 cells.

For the β-OL+IRI combinations, both concentrations elevated AMC accumulation over time, with sustained caspase-3 catalytic activity at early time points. However, concentration 1 (C1) demonstrated stable and reproducible activation without disproportionate variability. Although concentration 2 showed similar cumulative AMC trends, it did not provide a substantial kinetic advantage relative to reproducibility. Thus, β-OL+IRI concentration 1 (C1) was selected for subsequent analysis in MCF-7 cells.

Collectively, in MCF-7 cells, the lower effective concentration (C1) of each drug combination (TQ, β-LAP, and β-OL) was selected. This approach ensures robust but controlled apoptotic activation while maintaining translational relevance by avoiding unnecessary dose escalation. Importantly, selection

was guided by concordance between AMC accumulation and catalytic activity kinetics, confirming sustained caspase-3 engagement rather than transient or non-specific enzymatic activation.

In HCT116 cells, concentration selection was similarly based on integrated interpretation of cumulative AMC concentration and caspase-3 enzymatic activity data. However, the response hierarchy differed markedly from that observed in MCF-7 cells, reflecting cell-line-specific apoptotic sensitivity.

For the TQ+IRI combinations, both concentrations produced only modest increases in AMC accumulation and did not significantly elevate caspase-3 catalytic activity above control levels. Between the two, concentration 1 (C1) demonstrated slightly more stable variability and comparable cumulative trends relative to C2. Given the absence of clear catalytic superiority at higher concentration and the importance of reproducibility for downstream mechanistic studies, TQ+IRI concentration 1 (C1) was selected for further investigation in HCT116 cells.

In contrast, the β-OL+IRI combinations produced substantial and sustained increases in both AMC accumulation and caspase-3 catalytic activity. Concentration 2 (C2) consistently demonstrated the highest catalytic rate at 30 minutes and the greatest cumulative AMC levels at later time points. Importantly, the enhanced early reaction velocity translated directly into superior product accumulation, indicating strong and persistent execution-phase engagement. Variability remained acceptable relative to magnitude of effect, and the separation from control and TQ-treated groups was pronounced across all time points. Therefore, β-OL+IRI concentration 2 (C2) was selected for subsequent assays in HCT116 cells as it represents the most biologically robust apoptotic sensitization condition in this model.

These selections were not based solely on maximal absolute activity but rather on an integrated evaluation of:

1. Magnitude of caspase-3 catalytic activation
2. Sustained AMC accumulation over time
3. Kinetic stability across the assay window
4. Reproducibility (standard deviation relative to mean)
5. Biological regulation versus potential cytotoxic overload
6. Translational relevance

The divergence in optimal concentrations between cell lines underscores tumor-type-specific responsiveness to quinone-mediated sensitization of irinotecan-induced apoptosis. In MCF-7 cells, all three quinone combinations achieved controlled and reproducible activation at lower concentrations, whereas in HCT116 cells, β-OL required the higher concentration to achieve robust execution-phase engagement.

This integrative and systematic selection strategy ensures that all subsequent assays—such as mitochondrial integrity analysis, apoptotic protein expression profiling, DNA fragmentation studies, and

pathway interrogation—are performed under conditions that most effectively and reproducibly engage caspase-3-dependent apoptosis while maintaining mechanistic clarity and translational relevance.

4.3 CELL CYCLE DISTRIBUTION ANALYSIS BY FLOW CYTOMETRY REVEALS TREATMENT-INDUCED CELL CYCLE ARREST IN MCF-7 AND HCT116 CELLS

4.3.1.1 Effects of Combination Treatments on Cell Cycle Distribution in MCF-7 Cells

Treatment with TQ+IRI resulted in a marked increase in the proportion of cells in the G_0/G_1 phase, with 90.5% of the remaining cell population located within this phase. This represents a substantial shift from the untreated control, where only 24.1% of cells were in G_0/G_1, and indicates that the majority of cells were retained at the earliest stage of the cell cycle. Concurrently, the proportions of cells in the S phase (6.0%) and G_2/M phase (3.0%) were markedly reduced, demonstrating that only a small fraction of cells progressed into DNA synthesis or mitosis.

The G_0/G_1 phase represents the point at which cells either remain in a non-proliferative state or prepare for entry into S phase. Under normal conditions, a large proportion of cells transitions from G_0/G_1 into S phase, as reflected in the untreated control. In contrast, the strong predominance of cells in G_0/G_1 following TQ+IRI treatment indicates that progression beyond this point was substantially limited. The reduced representation of cells in S and G_2/M phases reflects a decreased number of cells undergoing DNA replication and division.

This pattern is significant because it shows that the treatment effectively limited the number of cells capable of advancing through the cell cycle. The high proportion of cells remaining in G_0/G_1 indicates that the treatment prevented further progression, thereby reducing the pool of actively dividing cells. At the same time, the reduced proportions of cells in later phases indicate that fewer cells were able to sustain proliferation. Together, these observations, **Figure 24 and Table 4**, demonstrate that TQ+IRI effectively restricted cell cycle progression at the earliest stage, resulting in a reduced presence of cells in phases associated with active replication and division.

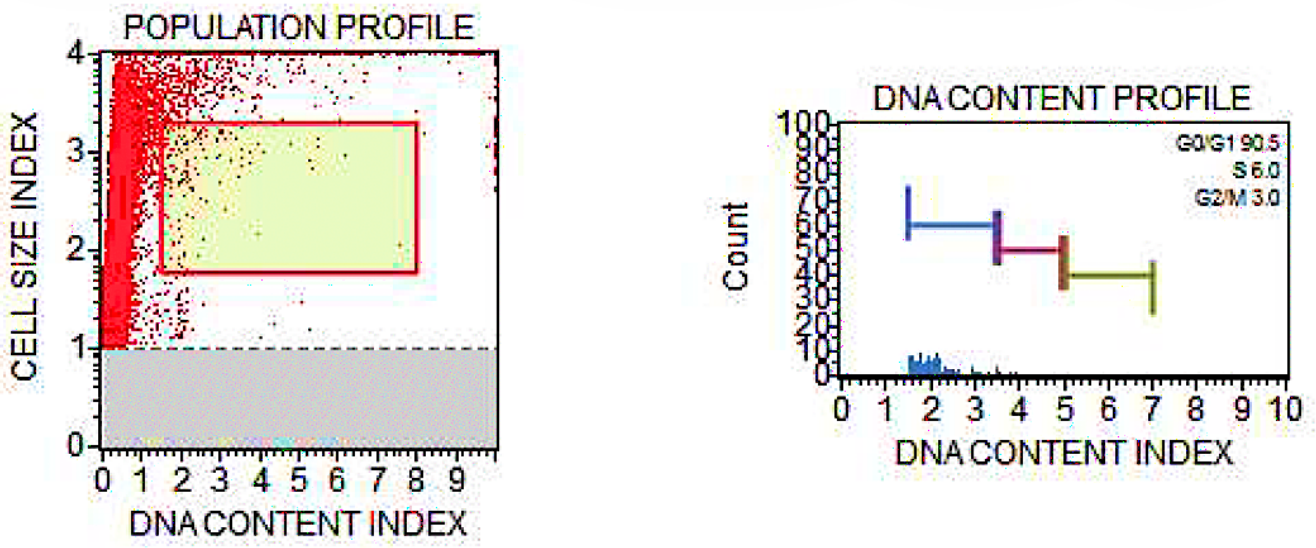


Figure 24: **Flow Cytometric Analysis Reveals Predominant G_1 Phase Arrest Following Thymoquinone and Irinotecan Combination Treatment in MCF-7 Cells.** The left panel (Population Profile) shows a bivariate dot plot of DNA content index versus cell size index, used to gate intact, single cells while excluding debris, apoptotic fragments, and cell aggregates. The gated population was subsequently analyzed for DNA content. The right panel (DNA Content Profile) displays the DNA content histogram derived from the gated cells, illustrating the distribution of cells across the G_0/G_1, S, and G_2/M phases of the cell cycle, as well as the sub-G_1 population representing cells with fragmented DNA.

Table 4: Predominant G0/G1 Phase Accumulation Indicates G_1 Cell Cycle Arrest in MCF-7 Cells Treated with Thymoquinone and Irinotecan Combination

Phase	G_0/G_1	S	G_2/M	Debris
% Gated	90.5	6.0	3.0	99.9
Mean	2085.6	3842.2	5551.9	271.9
% CV	21.7	10.5	6.4	157.8

Treatment with β-LAP+IRI resulted in a comparatively lower proportion of cells in the G_0/G_1 phase, with only 35.7% of the population retained within this phase. This value was substantially lower than that observed in both TQ+IRI and β-OL+IRI treatments. The proportions of cells in S phase (7.4%) and G_2/M phase (4.3%) remained low, similar to other treatments, but the overall distribution across all phases was reduced compared to the other combinations.

The relatively low proportion of cells in G_0/G_1 indicates that fewer cells were retained at the initial stage of the cell cycle. In contrast to treatments where cells accumulate in G_0/G_1, this distribution reflects a reduced number of cells remaining within the structured progression of the cell cycle. The consistently low proportions across all phases indicate that a smaller fraction of the total cell population was present within any defined phase.

Compared to TQ+IRI and β-OL+IRI, which showed strong accumulation of cells in G_0/G_1, β-LAP+IRI did not result in a dominant retention of cells at this early stage. Instead, the reduced proportion of cells in G_0/G_1, together with low representation in S and G_2/M phases, indicates that fewer cells remained within the active cell cycle distribution overall. This pattern, **Figure 25 and Table 5**, reflects a reduced retention of cells within proliferative phases rather than a concentration of cells at a specific checkpoint.

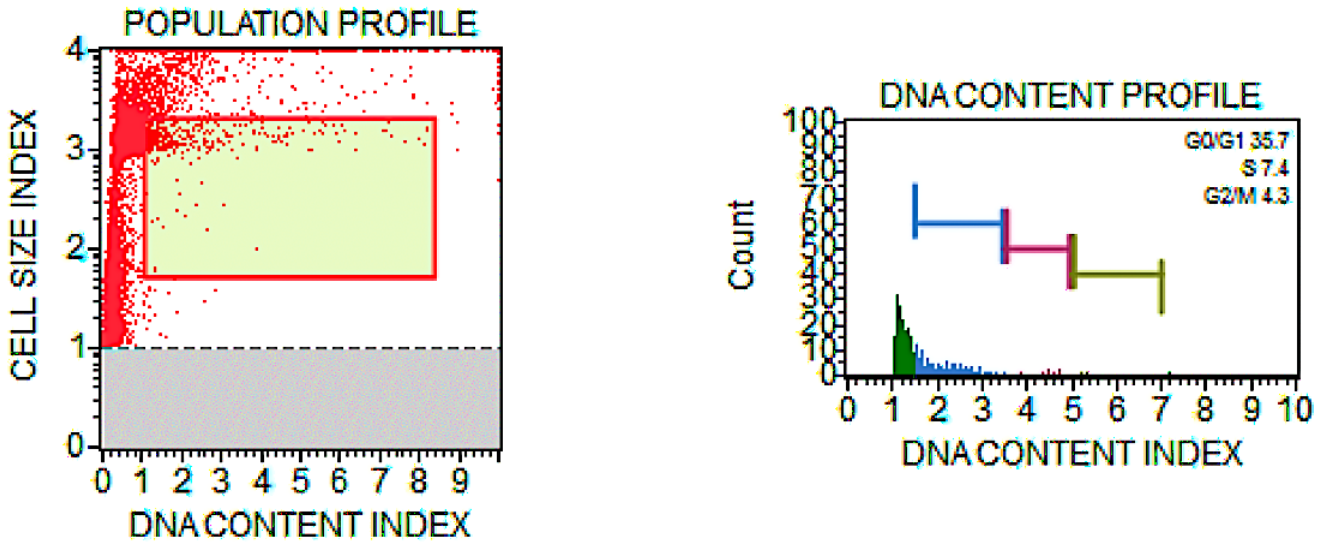


Figure 25: **Flow Cytometric Analysis Reveals Predominant G_0/G_1 Phase Arrest Following β-Lapachone and Irinotecan Combination Treatment in MCF-7 Cells**. The left panel (Population Profile) presents a bivariate dot plot of DNA content index versus cell size index, used to gate intact, single cells and exclude debris, apoptotic fragments, and cell aggregates. The gated population was subsequently analyzed for DNA content. The right panel (DNA Content Profile) shows the DNA content histogram of gated cells, illustrating the distribution of cells across the G_0/G_1, S, and G_2/M phases of the cell cycle, as well as the sub-G_1 population indicative of apoptotic DNA fragmentation. Percentage values for each phase are indicated.

Table 5: Predominant G_0/G_1 Phase Accumulation Indicates G1 Cell Cycle Arrest in MCF-7 Cells Treated with β-Lapachone and Irinotecan Combination

Phase	G_0/G_1	S	G_2/M	Debris
% Gated	35.7	7.4	4.3	97.5
Mean	2171.0	4211.2	5725.6	577.3
% CV	23.9	8.9	8.6	214.7

Treatment with β-OL+IRI resulted in a high proportion of cells in the G_0/G_1 phase, with 83.8% of the population located within this phase. This represents a substantial increase compared to the untreated control and is slightly lower than the accumulation observed in TQ+IRI-treated cells. In contrast, the S phase accounted for 11.0% of cells, while the G_2/M phase remained low at 3.7%.

The high proportion of cells in G_0/G_1 indicates that the majority of the remaining cell population was retained at the earliest stage of the cell cycle, limiting progression into DNA synthesis. However, compared to TQ+IRI, β-OL+IRI maintained a higher proportion of cells in the S phase, indicating that a greater fraction of cells continued into DNA replication. This suggests that while progression beyond G_0/G_1 was reduced, it was not as extensively limited as in TQ+IRI-treated cells.

The distribution observed in β-OL+IRI, **Figure 26 and Table 6**, reflects a strong retention of cells in G_0/G_1, combined with a measurable proportion of cells progressing into S phase. This indicates that although the treatment effectively reduced the number of cells advancing through the cell cycle, a subset of cells remained capable of entering DNA synthesis. Compared to β-LAP+IRI, β-OL+IRI retained a substantially larger proportion of cells within defined phases, particularly within G_0/G_1, indicating a more pronounced effect on limiting early cell cycle progression.

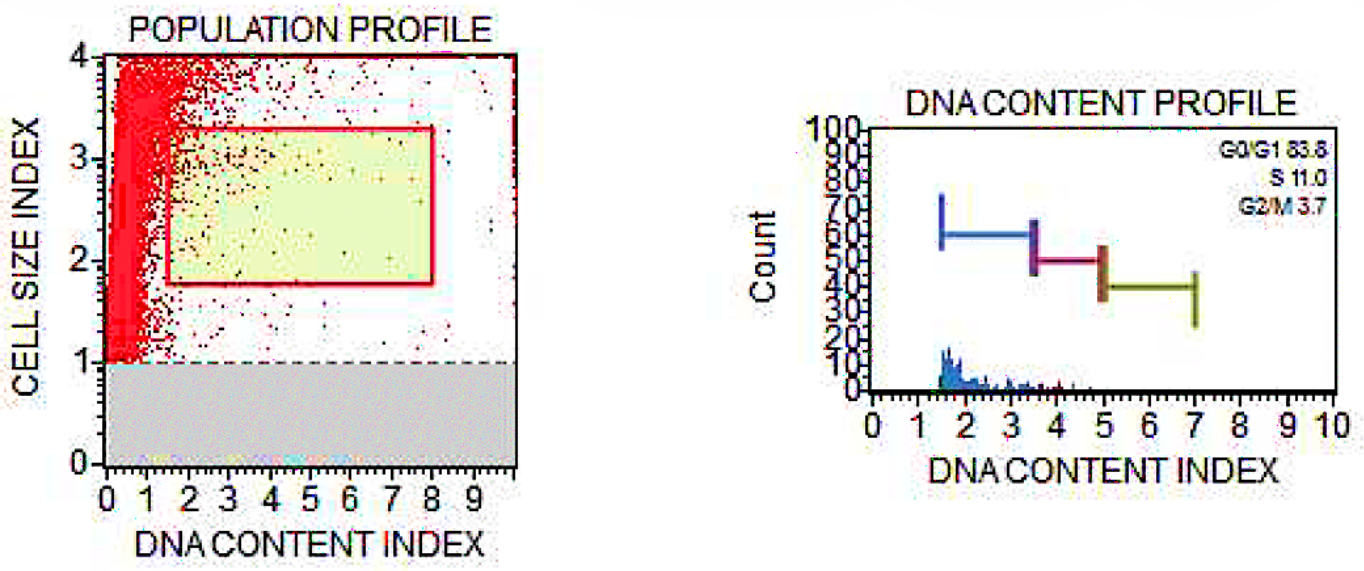


Figure 26: **Flow Cytometric Analysis Reveals Predominant G_1 Phase Arrest Following β-Lapachol and Irinotecan Combination Treatment in MCF-7 Cells**. The left panel (Population Profile) shows a bivariate dot plot of DNA content index versus cell size index used to gate intact, single cells and exclude debris, apoptotic fragments, and cell aggregates. The selected gated population was used for subsequent analysis. The right panel (DNA Content Profile) displays the DNA content histogram of gated cells, illustrating the distribution of cells across the G_0/G_1, S, and G_2/M phases of the cell cycle, as well as the sub-G_1 population indicative of apoptotic DNA fragmentation. Percentage values for each phase are indicated.

Table 6: Flow Cytometric Analysis Reveals Predominant G_1 Phase Arrest Following β-Lapachol and Irinotecan Combination Treatment in MCF-7 Cells

Phase	G_0/G_1	S	G_2/M	Debris
% Gated	83.8	11.0	3.7	99.9
Mean	2093.3	4015.3	6006.8	280.1
% CV	26.7	9.4	12.3	155.3

The untreated MCF-7 cell population exhibited a relatively even distribution across all phases of the cell cycle, with 24.1% of cells in G_0/G_1, 20.5% in S phase, and 28.8% in G_2/M. This distribution indicates that a substantial proportion of cells were actively progressing through the cell cycle, with a large fraction engaged in DNA synthesis and mitotic preparation. The presence of considerable populations in both S and G_2/M phases reflects ongoing proliferation, as cells are continuously transitioning from the preparatory phase (G_1) into DNA replication and subsequently into division.

In this context, the untreated condition. **Figure 27 and Table 7**, represents a population with sustained and uninterrupted cell cycle progression, where no single phase predominates and a continuous flow of cells is maintained across all stages of the cycle.

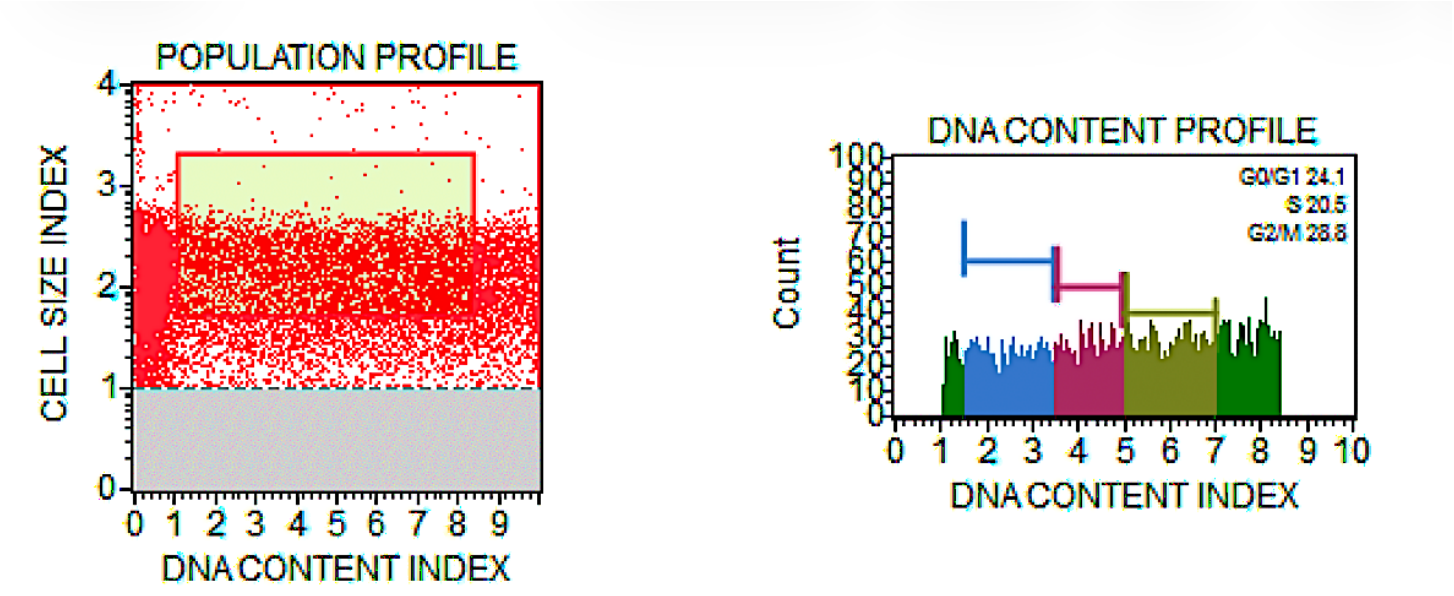


Figure 27: **Baseline Cell Cycle Distribution in Untreated MCF-7 Cells Shows Active Proliferation Without Phase Arrest**. The left panel (Population Profile) displays a bivariate dot plot of DNA content index versus cell size index, used to gate intact, single cells and exclude debris and cell aggregates. The gated population was used for subsequent analysis. The right panel (DNA Content Profile) shows the DNA content histogram of gated cells, illustrating the baseline distribution of cells across the G_0/G_1, S, and G_2/M phases of the cell cycle. Phase percentages are indicated.

Table 7: Balanced Cell Cycle Distribution Indicates Active Proliferation Without Phase Arrest in Untreated MCF-7 Cells

Phase	G_0/G_1	S	G_2/M	Debris
% Gated	24.1	20.5	28.8	91.8
Mean	2497.1	4259.8	6007.1	7625.7
% CV	23.7	10.2	9.7	53.3

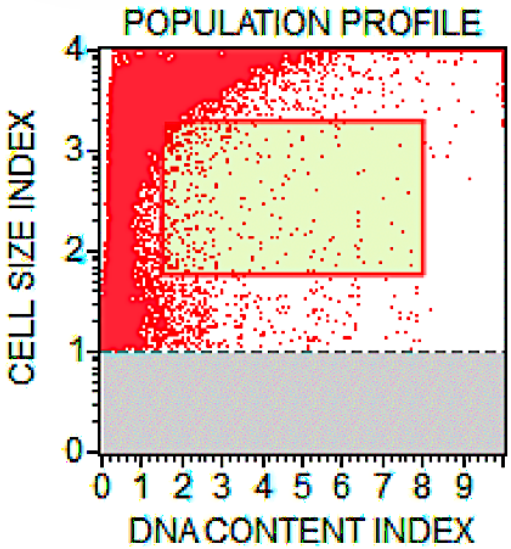
Overall, comparison across all conditions demonstrates that the untreated control maintained active cell cycle progression, with substantial populations in S and G_2/M phases reflecting ongoing proliferation. In contrast, all combination treatments reduced the proportion of cells progressing beyond G_0/G_1, indicating a limitation on entry into DNA synthesis and mitosis. TQ+IRI produced the most pronounced accumulation of cells in G_0/G_1, indicating the strongest restriction of progression beyond the initial stage of the cycle. β-OL+IRI also demonstrated substantial G_0/G_1 retention, although with a

greater proportion of cells continuing into S phase. In contrast, β-LAP+IRI showed a reduced proportion of cells across all phases, with no strong accumulation at G_0/G_1. These differences highlight distinct patterns in how each treatment influenced the distribution of cells within the cell cycle, particularly in terms of limiting progression beyond the initial phase and reducing the proportion of actively proliferating cells.

4.3.1.2 Effects of Combination Treatments on Cell Cycle Distribution in HCT116 Cells

Treatment with the TQ+IRI combination, a redistribution of the cell population was observed, with 82.0% of cells located in the G_0/G_1 phase. This represents an increase relative to the untreated control and indicates that a greater proportion of cells was retained at the earliest stage of the cell cycle. In parallel, the S phase population was reduced to 8.7%, and the G_2/M phase to 7.5%, reflecting a decrease in the proportion of cells progressing into DNA synthesis and mitosis. The G_0/G_1 phase represents the point at which cells prepare to enter DNA replication, and under normal conditions, a proportion of cells transitions into S phase.

The increased accumulation of cells in G_0/G_1 indicates that progression beyond this point was limited, resulting in fewer cells entering replication. The reduction in S phase reflects decreased DNA synthesis activity, while the reduced G_2/M population indicates fewer cells advancing to mitotic stages. Overall, this distribution, **Figure 28 and Table 8**, reflects a reduction in the number of cells progressing through the cell cycle, with a greater proportion retained at the initial stage.



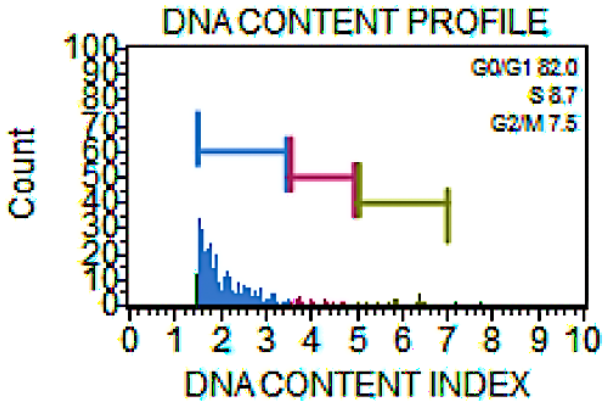


Figure 28: **Flow Cytometric Analysis Reveals Predominant G_0/G_1 Phase Arrest Following Thymoquinone and Irinotecan Combination Treatment in HCT116 Cells**. The left panel (Population Profile) presents a bivariate dot plot of DNA content index versus cell size index, used to gate intact, single cells and exclude cellular debris, apoptotic fragments, and cell aggregates. The gated population was subsequently used for DNA content analysis. The right panel (DNA Content Profile) displays the DNA content histogram of gated cells, illustrating the distribution of cells across the G_0/G_1, S, and G_2/M phases of the cell cycle, as well as the sub-G_1 population indicative of apoptotic DNA fragmentation. Percentage values for each phase are shown.

Table 8: Predominant G_0/G_1 Phase Accumulation Indicates G1 Cell Cycle Arrest in HCT116 Cells Treated with Thymoquinone and Irinotecan Combination

Phase	G_0/G_1	S	G_2/M	Debris
% Gated	82.0	8.7	7.5	99.2
Mean	2041.2	4144.4	5841.0	1315.9
% CV	24.7	10.3	9.7	169.5

Treatment with the β-OL+IRI combination resulted in 81.8% of cells accumulating in the G_0/G_1 phase, closely resembling the distribution observed with TQ+IRI. The S phase accounted for 10.6% of cells, while the G_2/M phase remained at 7.5%. The high proportion of cells in G_0/G_1 indicates that a substantial fraction of the population was retained at the earliest stage of the cell cycle. However, the S-phase proportion remained relatively similar to that observed in the untreated control, indicating that a measurable fraction of cells continued into DNA replication. The presence of cells in G_2/M further indicates that a portion of the population progressed through replication and entered mitosis. This distribution, **Figure 29 and Table 9**, therefore reflects a reduction in progression through the cell cycle, while still maintaining a subset of cells actively transitioning through DNA synthesis and division.

Overall, comparison within the HCT116 cell line shows that untreated cells maintained active progression through all phases of the cell cycle, with measurable populations in S and G_2/M phases. Following treatment, both TQ+IRI and β-OL+IRI resulted in increased retention of cells in the G_0/G_1 phase and a reduction in the proportion of cells progressing into later phases. These shifts indicate a limitation in cell cycle progression beyond the initial stage, reflected by reduced representation of cells undergoing DNA synthesis and mitosis.

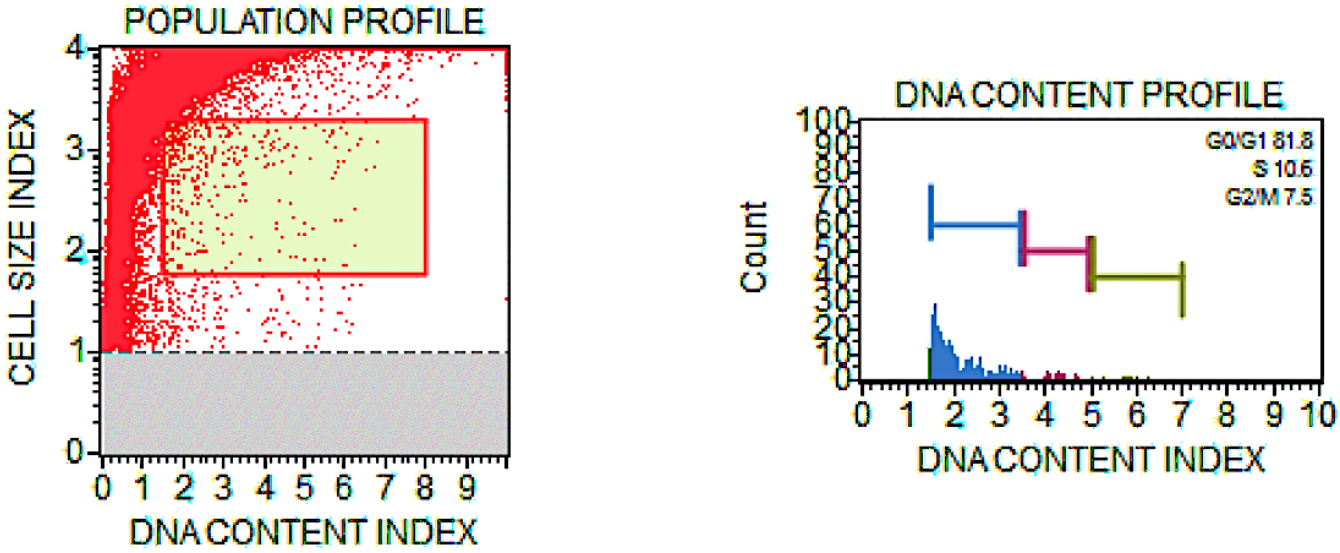


Figure 29: **Flow Cytometric Analysis Reveals Predominant G_1 Phase Arrest Following β-Lapachol and Irinotecan Combination Treatment in HCT116 Cells.** The left panel (Population Profile) shows a bivariate dot plot of DNA content index versus cell size index used to gate intact, single cells while excluding cellular debris, apoptotic fragments, and aggregates. The gated population was used for downstream analysis. The right panel (DNA Content Profile) presents the DNA content histogram of gated cells, illustrating the distribution across the G_0/G_1, S, and G_2/M phases of the cell cycle, as well as the sub-G_1 population indicative of apoptotic DNA fragmentation. Phase percentages are indicated.

Table 9: Flow Cytometric Analysis Reveals Predominant G_1 Phase Arrest Following β-Lapachol and Irinotecan Combination Treatment in HCT116 Cells

Phase	G_0/G_1	S	G_2/M	Debris
% Gated	81.8	10.6	7.5	99.2
Mean	2087.1	4214.9	5809.7	3708.7
% CV	25.6	9.1	8.3	95.5

The untreated HCT116 cell population exhibited a distribution characteristic of an actively proliferating cell line, with 77.8% of cells in the G_0/G_1 phase, 10.0% in S phase, and 8.9% in G_2/M. This distribution indicates that while the majority of cells were located in the G_0/G_1 phase, a measurable proportion of the population was actively progressing into DNA synthesis and mitosis. The presence of cells in the S phase reflects ongoing DNA replication, while the G_2/M population represents cells that had completed replication and were preparing for or undergoing division. Together, this distribution, **Figure 30 and Table 10**, reflects continuous cell cycle progression, with cells transitioning from G_0/G_1 into S phase and subsequently into G_2/M, maintaining an actively proliferating population.

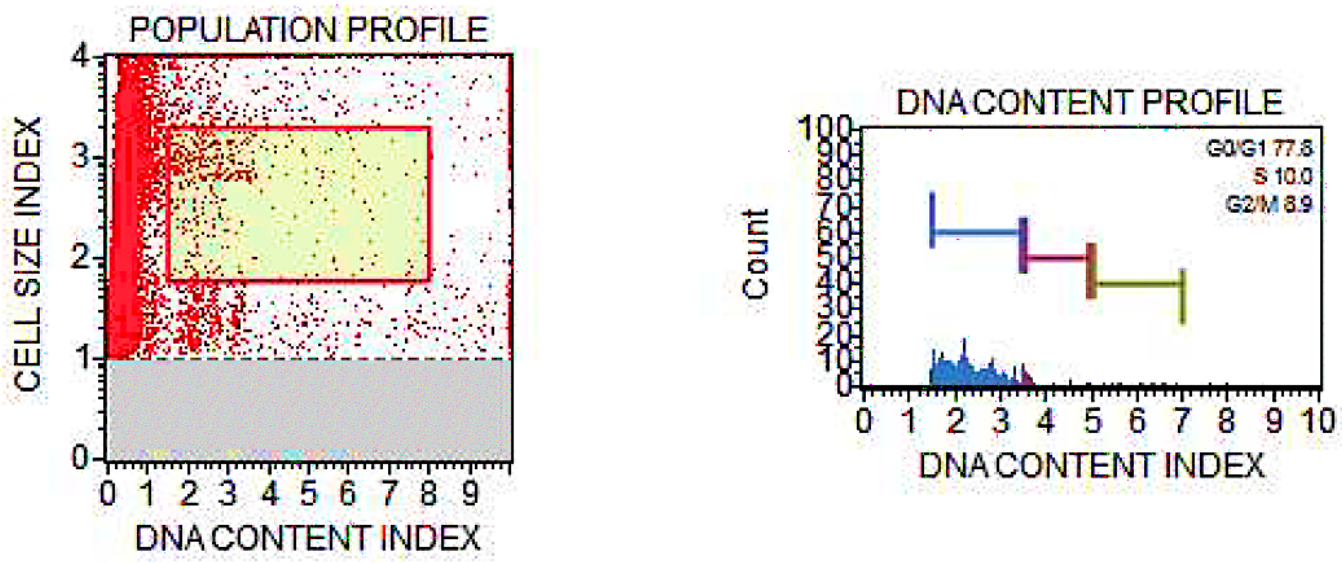


Figure 30: **Baseline Cell Cycle Distribution in Untreated HCT116 Cells Shows Active Proliferation Without Phase Arrest**. The left panel (Population Profile) shows a bivariate dot plot of DNA content index versus cell size index used to gate intact, single cells while excluding cellular debris and aggregates. The gated population was used for subsequent analysis. The right panel (DNA Content Profile) presents the DNA content histogram of gated cells, illustrating the baseline distribution of cells across the G_0/G_1, S, and G_2/M phases of the cell cycle. Phase percentages are indicated.

Table 10: Balanced Cell Cycle Distribution Indicates Active Proliferation Without Phase Arrest in Untreated HCT116 Cells

Phase	G0/G1	S	G2/M	Debris
% Gated	77.8	10.0	8.9	99.8
Mean	2302.7	4005.5	5966.2	276.9
% CV	23.3	12.4	9.0	184.4

Comparison of the cell cycle responses between MCF-7 and HCT116 cells revealed clear differences in the extent to which progression beyond the G_0/G_1 phase was reduced following treatment. In MCF-7 cells, combination treatments resulted in a pronounced accumulation of cells in G_0/G_1, accompanied by a substantial reduction in S and G_2/M phase populations, indicating a strong limitation on progression into DNA synthesis and mitosis. In contrast, although HCT116 cells also demonstrated increased G_0/G_1 accumulation following treatment, the reduction in S and G_2/M populations was less pronounced, with a measurable proportion of cells continuing to progress through these phases.

These observations indicate that, while both cell lines exhibited reduced progression beyond the initial stage of the cell cycle, the extent of this effect differed between them. MCF-7 cells showed a greater

shift toward retention in G_0/G_1 with minimal progression into later phases, whereas HCT116 cells retained a higher proportion of cells undergoing DNA synthesis and mitosis. Overall, this indicates that the reduction in proliferative progression was more pronounced in MCF-7 cells than in HCT116 cells under the same treatment conditions.

CHAPTER 5: DISCUSSION

5.1 OVERVIEW

The primary objective of this study was to determine whether combining these natural compounds with irinotecan could enhance cytotoxic efficacy through synergistic interactions, while simultaneously promoting apoptosis and disrupting cell cycle progression in cancer cells. The AlamarBlue assays provided quantitative insight into dose-dependent cytotoxicity and enabled the identification of effective concentration ranges for both single and combination treatments. Building on these findings, CompuSyn analyses allowed rigorous evaluation of drug–drug interactions, revealing concentration-dependent patterns of synergy, additivity, or antagonism that informed subsequent mechanistic investigations. Apoptotic mechanisms underlying the observed cytotoxic effects were explored through caspase-3 activity analysis, with protein normalization ensuring accurate interpretation of enzymatic activation across treatment conditions. These data provided direct biochemical evidence linking reduced cell viability to execution-phase apoptosis. Flow cytometric cell cycle analysis further complemented these findings by revealing treatment-induced alterations in cell cycle distribution, including phase-specific arrest and the accumulation of sub-G_1 populations indicative of DNA fragmentation and apoptotic progression.

Importantly, comparative analyses between MCF-7 and HCT116 cells revealed distinct patterns of sensitivity, synergistic behavior, and mechanistic response, underscoring the influence of tumor type and cellular context on treatment efficacy. Differences in apoptotic induction, cell cycle perturbation, and combination responsiveness highlight the complexity of phytochemical–chemotherapy interactions and emphasize the necessity of cell line–specific evaluation. Collectively, the findings discussed in this chapter provide a comprehensive assessment of the cytotoxic potency, synergistic potential, apoptotic induction, and cell cycle effects of TQ, β-LAP, and β-OL in combination with IRI. These results identify particularly promising combination strategies and offer mechanistic insight that supports further preclinical investigation of selected phytochemical–chemotherapy regimens as potential adjuncts to conventional cancer treatment.

To ensure objective interpretation of cytotoxicity, IC_{50} values were evaluated according to established in vitro classification thresholds, where compounds with IC_{50} values <10 μM are considered highly potent, 10–50 μM moderately cytotoxic, 50–100 μM weak–moderately cytotoxic, and >100 μM weakly cytotoxic. This distinction is critical, as statistical significance alone does not necessarily reflect biological relevance. In several cases, statistically significant reductions in cell viability were observed at higher concentrations; however, the corresponding IC_{50} values remained within the weak cytotoxic range, indicating limited therapeutic relevance. Therefore, conclusions regarding compound efficacy were based on both IC_{50} magnitude and overall dose–response behavior, rather than statistical significance alone.

5.1.1 β-Lapachol and Irinotecan Demonstrate Greater Selectivity and Lower Cytotoxicity in VERO Cells than β-Lapachone and Cisplatin

The use of VERO cells as a non-malignant epithelial model provides an essential benchmark for evaluating the selectivity and potential toxicity of anticancer agents. n evaluating toxicity in VERO cells, it is important to consider selectivity toward malignant cells as a key determinant of therapeutic potential. The selectivity index (SI), defined as the ratio of IC_{50} in non-cancerous cells to that in cancer cells, is commonly used to quantify this property, with values ≥3 considered indicative of high selectivity for anticancer agents (Prayong et al., 2008). Although SI values were not explicitly calculated in this study, comparative analysis of IC_{50} values across cancer and VERO cell lines provided a functional approximation of selectivity, enabling assessment of whether cytotoxic effects were preferentially directed toward malignant cells. Unlike transformed cancer cell lines, VERO cells lack oncogenic driver mutations, display relatively low proliferative activity, maintain intact redox buffering systems, and possess fully functional DNA repair and apoptotic regulatory pathways. Consequently, cytotoxic effects observed in VERO cells are more likely to reflect off-target or non-selective toxicity rather than therapeutic anticancer activity. In this context, the present findings demonstrate that β-lapachol and irinotecan exhibit superior safety profiles compared to β-lapachone and cisplatin, highlighting clear differences in selectivity that are consistent with their underlying mechanisms of action (Sunassee *et al.,* 2013; Crea *et al.,* 2009; Pabla and Dong, 2008).

β-Lapachone has been widely described in the literature as a tumor-selective agent due to its reliance on NAD(P)H:quinone oxidoreductase 1 (NQO1) for bioactivation, an enzyme frequently overexpressed in malignant cells. However, several studies have also cautioned that β-lapachone can induce substantial cytotoxicity in normal cells expressing basal levels of NQO1, particularly at moderate to high concentrations (Bey *et al.,* 2013; Zhao *et al.,* 2021). In agreement with these reports, the present study demonstrated pronounced β-lapachone-induced cytotoxicity in VERO cells, with significant reductions in metabolic activity observed across the tested concentration range. Whereas earlier cancer-focused studies emphasized β-lapachones exceptional potency in malignant cells, the current findings indicate that this potency is not strictly tumor-restricted. The relatively low IC_{50} observed in VERO cells suggests that β-lapachone readily overwhelms normal cellular redox homeostasis, leading to oxidative stress, DNA damage, and energetic collapse even in non-malignant epithelial cells. These findings confirm that β-lapachone exhibits limited selectivity, as its potent redox cycling mechanism can induce cytotoxicity in both malignant and non-malignant cells, consistent with previous reports describing its narrow therapeutic window (Bey *et al.,* 2013; Zhao *et al.,* 2021). This observation reinforces concerns raised in the literature regarding β-lapachones narrow therapeutic window and highlights the necessity for targeted delivery strategies to minimize damage to normal tissues. Quantitatively, the relatively low IC_{50} observed for β-lapachone in VERO cells compared to its activity in cancer cell lines indicates a limited differential between malignant and non-malignant toxicity. This suggests a low selectivity index and reinforces the conclusion that β-lapachone exhibits a narrow therapeutic window, as its potent redox cycling mechanism is not sufficiently restricted to cancer cells.

β-Lapachol, a structurally related analogue of β-lapachone, has consistently been reported to exhibit reduced cytotoxicity due to its weaker redox cycling capacity and diminished ability to generate reactive oxygen species (Sunassee *et al.,* 2013; Hussain *et al.,* 2007). Prior studies have suggested that β-lapachol induces sublethal oxidative stress that is insufficient to trigger widespread apoptosis in normal cells. The present findings strongly support this distinction. In VERO cells, β-lapachol produced only moderate, concentration-dependent reductions in viability, with metabolic activity remaining relatively preserved even at higher concentrations. Compared with β-lapachone, the shallower dose–response slope observed for β-lapachol indicates a more gradual impact on cellular metabolism, suggesting that endogenous antioxidant and repair mechanisms in VERO cells can counteract β-lapachol-induced stress. These results reinforce that β-lapachol possesses a more favorable safety profile than β-lapachone, consistent with its reduced redox cycling capacity and lower ROS generation, which allows normal cells to maintain redox balance and avoid extensive oxidative damage (Sunassee *et al.,* 2013; Hussain *et al.,* 2007). This differential response supports the conclusion that β-lapachol possesses a more favorable safety profile and greater selectivity than β-lapachone. In contrast, the higher IC_{50} observed in VERO cells relative to cancer cells indicates a greater differential in cytotoxic response, suggesting improved selectivity. This supports the interpretation that β-lapachol exerts preferential effects on malignant cells while sparing normal epithelial cells to a greater extent than β-lapachone.

Thymoquinone has been extensively investigated for its reported cancer-selective properties, with numerous studies indicating that it preferentially induces apoptosis in malignant cells while sparing normal cells at lower concentrations. Mechanistically, thymoquinone is thought to act primarily as a redox modulator and signaling regulator, suppressing oncogenic pathways such as NF-κB and PI3K/Akt while exerting comparatively mild effects on non-transformed cells with intact antioxidant defenses (Gali-Muhtasib *et al.,* 2011; Woo *et al.,* 2012). The present study largely corroborates these findings. In VERO cells, thymoquinone produced minimal cytotoxicity at low and intermediate concentrations, with more pronounced reductions in viability occurring only at higher doses. Compared with its marked cytotoxic effects in MCF-7 cells, this attenuated response in VERO cells supports a degree of cancer selectivity. However, the steep decline in viability observed at concentrations exceeding 100 μM demonstrates that thymoquinones safety is dose-dependent and that excessive exposure can compromise normal epithelial viability. This observation refines existing literature by confirming that thymoquinone is relatively well tolerated by normal cells only within a defined concentration range. This pattern further supports a degree of selective cytotoxicity at lower concentrations, although the convergence of cytotoxic effects at higher doses indicates that selectivity is concentration-dependent and may be lost under conditions of excessive exposure.

Irinotecan has been reported to exhibit limited cytotoxicity in non-malignant cells due to its requirement for metabolic activation to SN-38 and its preferential action on rapidly dividing cells. Previous studies have shown that normal epithelial cells display relative resistance to irinotecan-induced cytotoxicity under short-term exposure conditions because of reduced carboxylesterase activity and slower proliferation rates (Crea *et al.,* 2009; Kumar *et al.,* 2023). The present findings are consistent with this

literature, as irinotecan induced only mild to moderate reductions in VERO cell viability, with significant effects occurring primarily at higher concentrations. The comparatively shallow regression slope observed further supports irinotecans favorable selectivity profile and contrasts with its more pronounced cytotoxicity in HCT116 cells. This supports the conclusion that irinotecan exhibits greater selectivity toward rapidly proliferating cancer cells while exerting comparatively limited toxicity in non-malignant cells, a characteristic that contributes to its more favorable safety profile (Crea *et al.,* 2009; Kumar *et al.,* 2023). The higher IC_{50} values observed in VERO cells relative to cancer cells are consistent with a proliferation-dependent mechanism of action and suggest a favorable selectivity profile, as cytotoxic effects are more pronounced in rapidly dividing malignant cells than in non-proliferative epithelial cells.

Cisplatin was included as a reference compound to benchmark non-selective cytotoxicity and to contextualize the safety profiles of the phytochemicals tested. Extensive literature has documented cisplatins lack of tumor specificity and its propensity to damage normal epithelial tissues through indiscriminate DNA crosslinking and oxidative stress, resulting in severe dose-limiting toxicities such as nephrotoxicity (Pabla and Dong, 2008; Dasari and Tchounwou, 2014). In agreement with these reports, cisplatin produced strong and concentration-dependent cytotoxicity in VERO cells, closely mirroring its effects in cancer cell lines. The absence of differential toxicity indicates a lack of cancer selectivity and suggests that any enhancement observed in combination settings would be confounded by intrinsic cisplatin-induced cell death rather than true mechanistic synergy. Similar conclusions have been drawn in numerous *in vitro* and clinical studies, which highlight cisplatin's narrow therapeutic index and its inability to discriminate between malignant and normal proliferative tissues (Arany and Safirstein, 2003). Consequently, cisplatin was deliberately excluded from subsequent combination studies to avoid masking selective interactions, to preserve biological relevance, and to align with established experimental strategies that prioritize agents with differential toxicity when assessing combination-based anticancer therapies (Chou, 2010). These observations further confirm that cisplatin lacks selectivity, as its mechanism of indiscriminate DNA crosslinking results in comparable cytotoxic effects in both cancerous and non-cancerous cells (Pabla and Dong, 2008; Dasari and Tchounwou, 2014).

Collectively, the present findings clearly demonstrate that β-lapachol and irinotecan exhibit superior safety profiles compared to β-lapachone and cisplatin in VERO cells. While β-lapachone and cisplatin induced pronounced, non-selective cytotoxicity consistent with their aggressive mechanisms of action (Bey *et al.,* 2013; Pabla and Dong, 2008), β-lapachol and irinotecan produced comparatively mild effects on non-malignant epithelial cells. This improved safety profile can be attributed to reduced redox stress induction in the case of β-lapachol and the proliferation-dependent mechanism of irinotecan (Sunassee *et al.,* 2013; Crea *et al.,* 2009). These findings underscore the importance of selectivity in anticancer drug development and highlight β-lapachol and irinotecan as the most promising candidates for further investigation due to their ability to balance anticancer efficacy with reduced off-target toxicity.

5.1.2 Mechanism-Driven Synergy Reveals β-Lapachone as a Potent Cytotoxic Agent and β-Lapachol as a Chemosensitizer in MCF-7 Cells

Cellular response to anticancer agents is governed not only by compound potency but by the mechanistic compatibility between drug action and tumor genotype. In this study, a clear hierarchy of mechanism-driven effects was identified in MCF-7 cells. β-Lapachone functioned as a highly potent cytotoxic agent, driving rapid and irreversible cell death through oxidative DNA damage (Bey *et al.,* 2013; Zhao *et al.,* 2021). In contrast, β-lapachol, despite weak single-agent activity, emerged as a novel chemosensitizer that significantly enhanced irinotecan efficacy by prolonging DNA damage and stabilizing checkpoint arrest (Sunassee *et al.,* 2013; Hussain *et al.,* 2007). Thymoquinone, however, primarily induced cytostatic effects that limited synergistic interaction with irinotecan (Gali-Muhtasib *et al.*, 2011; *Woo et al.,* 2012). These findings demonstrate that synergy in MCF-7 cells is mechanism-dependent and governed by the interaction between drug action and tumor genotype.

The IC_{50} values obtained in this study are consistent with previously reported data, supporting the validity of the experimental approach. β-Lapachone exhibited high potency in MCF-7 cells, consistent with reported IC_{50} values in the low micromolar range for NQO1-expressing breast cancer models (Bey et al., 2013). Thymoquinone demonstrated moderate to weak cytotoxicity, aligning with literature values typically ranging between 20–100 μM (Woo et al., 2012). β-Lapachol displayed moderate cytotoxicity, consistent with previous reports describing it as less potent than β-lapachone but capable of inducing growth inhibition at higher concentrations (Hussain et al., 2007). Irinotecan exhibited relatively weak cytotoxicity under short-term exposure conditions, in agreement with studies indicating limited *in vitro* activity due to its requirement for metabolic activation to SN-38 (Pommier, 2006).

Previous investigations into phytochemical-induced cytotoxicity in breast cancer cells have repeatedly emphasized that cellular response is highly dependent on tumor genotype, redox status, and checkpoint integrity rather than compound class alone. The present study builds on this foundation by directly comparing thymoquinone, β-lapachone, and β-lapachol—both as single agents and in combination with irinotecan—within the same ER-positive breast cancer model, allowing mechanistic distinctions to be resolved with greater clarity than is typically possible across disparate studies. Importantly, MCF-7 cells possess wild-type p53, intact G_1/S and G_2/M checkpoints, estrogen receptor signaling dependency, and a well-documented deficiency in caspase-3, all of which critically shape drug response outcomes and must be considered when interpreting cytotoxic and apoptotic responses.

β-Lapachone has been extensively characterized in the literature as a potent cytotoxic agent in NQO1-overexpressing cancers, including ER-positive breast cancer. Studies by Bey *et al.* (2013) and Zhao *et al.* (2021) demonstrated that β-lapachone induces rapid cell death in MCF-7 cells via NQO1-mediated futile redox cycling, resulting in excessive reactive oxygen species production, widespread DNA single-strand breaks, and hyperactivation of PARP-1. These studies described rapid depletion of NAD^+ and ATP pools, leading to energetic collapse and cell death that often bypasses classical apoptotic

checkpoints. The present study strongly corroborates these findings, as β-lapachone was observed to be the most potent single agent in MCF-7 cells, producing pronounced loss of viability at relatively low concentrations. However, the current data extend previous observations by demonstrating that when β-lapachone is combined with irinotecan, cytotoxicity is further amplified to a degree that results in near-complete pre-G_1 cell loss. While earlier studies primarily evaluated β-lapachone as a monotherapy, the present work reveals that topoisomerase I inhibition acts as a synergistic amplifier of β-lapachone–induced oxidative DNA damage, overwhelming even the robust DNA repair machinery of p53-competent MCF-7 cells. This finding suggests that β-lapachone does not merely act independently of cell cycle control but can actively convert repairable irinotecan-induced lesions into lethal damage when redox stress exceeds cellular tolerance. Collectively, these findings confirm that β-lapachone is not only the most potent cytotoxic agent in MCF-7 cells but also the primary driver of synergistic cell death when combined with irinotecan, consistent with its established role in inducing NQO1-dependent ROS generation, PARP-1 hyperactivation, and energetic collapse (Bey *et al.,* 2013; Zhao *et al.,* 2013).

In contrast, β-lapachol has consistently been reported to exhibit weaker cytotoxic activity than β-lapachone in breast cancer models. Sunassee *et al.* (2013) and Hussain *et al.* (2007) demonstrated that β-lapachol generates significantly lower levels of reactive oxygen species and lacks the sustained redox cycling capacity required to trigger metabolic catastrophe. Consequently, earlier studies described β-lapachol as inducing moderate growth inhibition and transient oxidative stress rather than rapid apoptotic cell death. The present study aligns with these reports, as β-lapachol alone displayed limited cytotoxicity in MCF-7 cells. However, whereas previous work largely concluded that β-lapachol has inferior anticancer potential, the current findings challenge this assumption by showing that β-lapachol becomes highly effective when combined with irinotecan. Unlike β-lapachone, which induces immediate apoptotic collapse, β-lapachol–irinotecan treatment produced pronounced G_0/G_1 arrest followed by extensive apoptotic debris, indicating a fundamentally different mechanism of synergy. This suggests that β-lapachol functions primarily as a chemosensitizer rather than a direct cytotoxic agent, stabilizing checkpoint arrest and prolonging irinotecan-induced DNA damage beyond repair thresholds. Such a role has not been clearly established in previous breast cancer studies and represents a significant mechanistic contribution of the present work. Importantly, this identifies β-lapachol as a novel chemosensitizer in MCF-7 cells, shifting its role from a weak cytotoxic compound to a mechanistically complementary agent. Previous studies have shown that β-lapachol induces sublethal oxidative stress and limited ROS generation (Sunassee *et al.,* 2013; Hussain *et al.,* 2007), supporting its potential to enhance chemotherapeutic efficacy without inducing direct cytotoxic collapse.

Thymoquinone has been widely reported to exert anticancer effects through modulation of intracellular signaling pathways rather than direct genotoxic stress. Numerous studies in MCF-7 cells have shown that thymoquinone suppresses PI3K/Akt signaling, inhibits NF-κB activation, downregulates cyclin D1, and induces p21 and p27 expression in a p53-dependent manner, resulting in G_1 phase arrest (Gali-Muhtasib *et al.,* 2011; Woo *et al.,* 2012). These studies consistently describe thymoquinone as producing cytostasis at lower concentrations, with apoptosis occurring only after prolonged exposure

or at higher doses. The present findings strongly corroborate this pattern, as thymoquinone induced a threshold-dependent reduction in viability accompanied by pronounced G_0/G_1 accumulation. However, whereas some reports suggest that thymoquinone synergizes strongly with DNA-damaging agents, the present study demonstrates that thymoquinone combined with irinotecan produces predominantly additive effects in MCF-7 cells. This apparent discrepancy can be mechanistically explained by the S-phase specificity of irinotecan. Enforced G_1 arrest by thymoquinone may initially limit irinotecan's ability to induce replication-associated DNA damage, thereby reducing synergistic cytotoxicity. Thus, while thymoquinone effectively primes apoptotic pathways through mitochondrial and transcriptional mechanisms, it may simultaneously confer transient protection against S-phase–targeted agents in ER-positive breast cancer cells, a nuance not fully addressed in earlier studies. This reinforces that thymoquinones cytostatic mechanism limits its capacity to generate strong synergistic interactions with S-phase–dependent chemotherapeutics such as irinotecan, consistent with its known role in inducing G_1 arrest through modulation of p53, p21, and PI3K/Akt signaling pathways (Gali-Muhtasib *et al.,* 2011; Woo *et al.,* 2012).

Irinotecan alone has repeatedly been shown to exhibit limited cytotoxicity in MCF-7 cells under short-term *in vitro* conditions. Crea *et al*. (2009) and Kumar *et al.* (2023) and subsequent studies reported that ER-positive breast cancer cells often display relative resistance to irinotecan due to inefficient conversion to its active metabolite SN-38 and slower proliferation rates compared with colorectal cancer models. The present study is consistent with these observations, as irinotecan alone produced only modest reductions in viability even at higher concentrations. However, the current data extend this understanding by demonstrating that irinotecan resistance in MCF-7 cells is not absolute but can be overcome through mechanistically complementary combination strategies. Specifically, compounds that either overwhelm DNA repair capacity through oxidative stress (β-lapachone) or prolong checkpoint arrest and DNA damage persistence (β-lapachol) significantly enhance irinotecan efficacy, whereas compounds that primarily induce cytostasis (thymoquinone) yield only additive effects.

The apoptotic data generated in this study provide further mechanistic resolution. MCF-7 cells are well known to be deficient in caspase-3 due to a functional gene deletion, and numerous studies have shown that apoptosis in this cell line proceeds via caspase-7–dependent pathways (Janicke *et al.,* 1998). Previous work has therefore reported delayed or attenuated caspase activation in MCF-7 cells compared with caspase-3–competent models. The present study is consistent with these findings, as caspase activation was time-dependent rather than immediate. However, the current work adds significant depth by demonstrating robust DEVD-cleaving activity across all combination treatments that was significantly reduced by Z-DEVD-CHO. This confirms that apoptosis was caspase-dependent despite the absence of caspase-3. Importantly, thymoquinone–irinotecan combinations produced higher sustained caspase activity than β-lapachone–irinotecan, suggesting prolonged mitochondrial apoptotic signaling rather than acute energetic collapse. This distinction aligns with the observed cell cycle profiles and reinforces the concept that different phytochemicals drive apoptosis through fundamentally distinct temporal and mechanistic pathways.

Integration of the cell cycle data further highlights these differences. Previous studies have consistently reported that thymoquinone and β-lapachol induce G_1 arrest in MCF-7 cells, whereas β-lapachone induces apoptosis with minimal checkpoint accumulation (Gali-Muhtasib *et al.,* 2011; Sunassee *et al.,* 2013; Hussain *et al.,* 2007). The present study not only confirms these findings but directly compares all three compounds under identical conditions, demonstrating that combination treatment with irinotecan accentuates these mechanistic distinctions. β-Lapachone–irinotecan treatment resulted in extensive pre-G_1 cell loss, indicating rapid apoptotic execution. β-Lapachol–irinotecan treatment enforced prolonged G_1 arrest followed by apoptosis, consistent with checkpoint-mediated sensitization. Thymoquinone–irinotecan treatment primarily induced cytostasis, with apoptosis emerging only at higher concentrations. This direct side-by-side comparison within a single genetic background represents a significant advancement over prior studies that examined these compounds in isolation.

Collectively, these findings demonstrate that cytotoxic synergy in MCF-7 cells is fundamentally mechanism-driven rather than solely dependent on intrinsic drug potency. β-Lapachone acts as a potent cytotoxic agent that amplifies oxidative DNA damage beyond repair thresholds (Bey *et al.,* 2013; Zhao *et al.,* 2021), while β-lapachol functions as a novel chemosensitizer that enhances irinotecan-induced cytotoxicity through checkpoint stabilization and sustained DNA damage (Sunassee *et al.,* 2013; Hussain *et al.,* 2007). In contrast, thymoquinone primarily induces cytostasis, limiting its synergistic potential (Gali-Muhtasib *et al.,* 2011; Woo *et al.,* 2012). These results highlight the critical role of tumor genotype and mechanistic compatibility in determining therapeutic outcomes and provide strong justification for mechanism-based design of combination therapies in ER-positive breast cancer.

5.1.3 β-Lapachol Emerges as the Most Potent Chemosensitizer While β-Lapachone Exhibits Limited Additional Synergy in HCT116 Cells

The response of HCT116 colon cancer cells to β-lapachone, β-lapachol, thymoquinone, and their combinations with irinotecan reflects a fundamentally different biological context from that observed in breast cancer models and must be interpreted considering the distinctive genetic and metabolic features of this cell line. HCT116 cells are characterized by microsatellite instability (MSI-H), high proliferative capacity, robust topoisomerase I activity, and functionally intact p53-dependent DNA damage checkpoints, together with efficient executioner caspase machinery. These attributes collectively predispose HCT116 cells to heightened sensitivity toward agents that induce replication stress, DNA strand breaks, or oxidative damage, and they provide a mechanistic basis for the markedly stronger cytotoxic and apoptotic responses observed in this study compared with those reported in ER-positive breast cancer cells. The cytotoxic responses observed in HCT116 cells are consistent with previously reported literature, which describes this cell line as highly sensitive to DNA-damaging agents and oxidative stress. β-Lapachone exhibited sub-micromolar potency in HCT116 cells, aligning with reported IC_{50} values of approximately 0.1–1 μM in NQO1-expressing colorectal cancer models (Bey et

al., 2013). Irinotecan demonstrated greater cytotoxicity in HCT116 cells compared to MCF-7 cells, consistent with literature indicating enhanced sensitivity due to higher proliferative rates and more efficient drug activation (Crea et al., 2009). In contrast, thymoquinone exhibited relatively weak cytotoxicity, consistent with its predominantly cytostatic mechanism of action in colorectal cancer models (Woo et al., 2012). In this context, the present findings demonstrate that β-lapachol emerges as the most potent chemosensitizer in HCT116 cells, significantly enhancing irinotecan efficacy, whereas β-lapachone, despite its high intrinsic cytotoxicity, exhibits limited additional synergistic benefit when used in combination. This distinction highlights the importance of mechanistic complementarity rather than single-agent potency in determining optimal combination strategies (Bey *et al.,* 2013; Sunassee *et al.,* 2013; Crea *et al.,* 2009).

Extensive literature has established β-lapachone as a highly potent cytotoxic agent in colorectal cancer models, particularly in NQO1-overexpressing cell lines such as HCT116. Bey *et al*. (2013) and Zhao *et al.* (2021) demonstrated that HCT116 cells exhibit exceptionally high sensitivity to β-lapachone due to efficient NQO1-mediated redox cycling, leading to massive reactive oxygen species generation, widespread DNA single-strand breaks, PARP-1 hyperactivation, and rapid NAD^+/ATP depletion. These studies reported sub-micromolar IC_{50} values and near-complete loss of viability following β-lapachone exposure. The present study strongly corroborates these findings, as HCT116 cells exhibited profound cytotoxicity at very low β-lapachone concentrations, confirming that this compound exploits an intrinsic metabolic vulnerability of colorectal cancer cells. However, whereas earlier studies largely evaluated β-lapachone as a single agent, the current data reveal that combining β-lapachone with irinotecan does not substantially increase synergistic potency beyond that already achieved by β-lapachone alone. This suggests that β-lapachone-induced oxidative catastrophe in HCT116 cells may already reach a ceiling effect, leaving limited scope for further enhancement by topoisomerase I inhibition. These findings indicate that β-lapachone-induced oxidative damage may already reach maximal cytotoxic thresholds in HCT116 cells, thereby limiting the potential for further enhancement through combination with irinotecan, consistent with its well-documented ability to induce rapid and overwhelming metabolic collapse (Bey *et al.,* 2013; Zhao *et al.,* 2013).

β-lapachol has generally been regarded as a weaker analogue of β-lapachone, with previous studies reporting moderate cytotoxicity in colorectal cancer cells and a reduced capacity for redox cycling (Sunassee *et al.,* 2013; Hussain *et al.,* 2007). In agreement with these reports, β-lapachol alone produced only partial reductions in HCT116 viability. However, the present study reveals a striking divergence from earlier assumptions by demonstrating that β-lapachol becomes the most synergistic and potent agent when combined with irinotecan in HCT116 cells. This contrasts with prior work, which rarely examined β-lapachol in combination settings and therefore underestimated its therapeutic potential. The exceptionally low median-effect dose and steep dose–response curve observed for the β-lapachol–irinotecan combination indicate a highly cooperative interaction, suggesting that β-lapachol sensitizes HCT116 cells to irinotecan-induced DNA damage rather than acting as a direct cytotoxic agent. Mechanistically, this synergy is likely driven by β-lapachol-mediated modulation of redox balance

and checkpoint signaling, which prolongs replication stress and impairs DNA repair fidelity in a rapidly proliferating, MSI-high background. Importantly, these results identify β-lapachol as a highly effective chemosensitizer in HCT116 cells, transforming its previously perceived role as a weak cytotoxic agent into a mechanistically complementary partner that enhances irinotecan-induced DNA damage and apoptotic signaling (Sunassee *et al.,* 2013; Hussain *et al.,* 2007). This interpretation is supported by previous reports that colorectal cancer cells with intact mismatch repair deficiencies are particularly vulnerable to sustained replication stress when checkpoint control is disrupted (Vilar and Gruber, 2010).

Thymoquinone has been extensively studied in colorectal cancer models, with most reports describing relatively modest cytotoxic effects compared with those seen in breast cancer cells. Studies by Gali-Muhtasib *et al.* (2008) and Woo *et al*. (2012) demonstrated that thymoquinone exerts anticancer activity in HCT116 cells primarily through modulation of NF-κB, Wnt/β-catenin, and PI3K/Akt signaling pathways, resulting in cell cycle arrest rather than rapid apoptosis. In agreement with these observations, the present study found that thymoquinone alone exhibited limited cytotoxic potency in HCT116 cells, with only minor reductions in viability even at higher concentrations. When combined with irinotecan, thymoquinone produced reproducible but comparatively weak synergistic or additive effects. This contrasts with reports in other colorectal cancer models where stronger synergy has been described and suggests that, in HCT116 cells, the rapid proliferation rate and high intrinsic sensitivity to DNA-damaging agents diminish the relative contribution of transcriptional modulators such as thymoquinone (Jehan *et al.,* 2022).

Irinotecan sensitivity in HCT116 cells has been well documented and is generally higher than in breast cancer models due to efficient conversion to the active metabolite SN-38 and elevated topoisomerase I expression (Crea *et al.,* 2009; Kumar *et al.,* 2023). Previous studies reported that HCT116 cells respond to irinotecan with pronounced S-phase damage and apoptosis, particularly under conditions of sustained exposure (Marx *et al.,* 2021; Murond *et al.,* 2012). The present findings are consistent with this literature, as irinotecan alone produced a clear dose-dependent reduction in viability and a steeper regression slope than observed in MCF-7 cells. This further supports the concept that irinotecan efficacy can be maximized through combination with agents that prolong replication stress or impair DNA repair mechanisms, particularly in rapidly proliferating, MSI-high colorectal cancer cells (Crea *et al.,* 2009; Marx *et al.,* 2021). Importantly, the current data extend these observations by showing that irinotecan efficacy can be markedly enhanced through combination with agents that either stabilize replication stress (β-lapachol) or amplify oxidative DNA damage (β-lapachone), highlighting distinct mechanistic routes to potentiation.

Apoptotic analyses further emphasize the genotype-dependent responsiveness of HCT116 cells. Unlike MCF-7 cells, HCT116 cells possess fully functional executioner caspases, and previous studies have shown rapid caspase-3 activation following DNA damage or oxidative stress (Janicke *et al.,* 1998). Consistent with this, the present study observed robust, time-dependent caspase-3 activation across all combination treatments, with the highest activity detected in β-lapachol–irinotecan-treated cells. The

enhanced caspase-3 activation observed in β-lapachol–irinotecan-treated cells further support its role as the most effective chemosensitizer, as it promotes sustained apoptotic signaling rather than transient or saturating cytotoxic responses. While earlier studies reported apoptosis induction by β-lapachone or irinotecan individually, the current findings demonstrate that β-lapachol, when combined with irinotecan, produces a more sustained and amplified caspase-dependent apoptotic response. This suggests that β-lapachol enhances apoptotic signaling efficiency rather than simply increasing the initial extent of DNA damage.

Cell cycle analyses provide additional mechanistic clarity. Previous reports have shown that irinotecan and oxidative stressors typically induce G_1 or S-phase perturbations in HCT116 cells, followed by apoptosis once damage becomes irreparable (Wu *et al.,* 2021). The present study confirms these patterns, with both thymoquinone–irinotecan and β-lapachol–irinotecan combinations inducing pronounced G_0/G_1 accumulation alongside sub-G_1 apoptotic populations. However, whereas thymoquinone primarily enforced cytostatic arrest with delayed apoptosis, β-lapachol produced a more balanced profile of checkpoint arrest and apoptotic progression, consistent with its superior synergistic performance. This distinction underscores the importance of checkpoint dynamics in determining whether combination treatments merely suppress proliferation or actively drive cell death.

Collectively, the present findings clearly demonstrate that β-lapachol functions as the most potent chemosensitizer in HCT116 cells, significantly enhancing irinotecan-induced cytotoxicity through sustained replication stress and amplified apoptotic signaling. In contrast, β-lapachone, despite its high intrinsic potency, exhibits limited additional synergy in combination settings, likely due to saturation of oxidative damage pathways (Bey *et al.,* 2013; Zhao *et al.,* 2021). These results highlight that therapeutic efficacy in colorectal cancer is governed not solely by drug potency, but by mechanistic compatibility with tumor genotype, particularly in MSI-high, rapidly proliferating cells. This study therefore provides novel evidence supporting β-lapachol as a superior combination partner in colorectal cancer therapy and underscores the importance of mechanism-driven combination design.

5.2 LIMITATIONS

Several limitations of the present study should be acknowledged. Firstly, selectivity index (SI) values were not formally calculated, limiting the ability to quantitatively define therapeutic selectivity, although comparative IC_{50} analysis provided a functional approximation. Secondly, all experiments were conducted under *in vitro* conditions, which do not fully recapitulate the complexity of in vivo tumor environments, including pharmacokinetics, immune interactions, and tumor microenvironment influences. Thirdly, the cytotoxic activity of irinotecan may be underestimated due to limited metabolic conversion to its active metabolite SN-38 under standard cell culture conditions. Additionally, the use of only two cancer cell lines may not fully represent tumor heterogeneity, and further validation across a broader panel of models would strengthen the generalizability of these findings.

5.3 TRANSLATIONAL RELEVANCE AND CLINICAL IMPLICATIONS

The findings of this study have important translational implications. The identification of β-lapachol as a chemosensitizer suggests the potential for dose-reduction strategies, whereby lower concentrations of irinotecan may achieve equivalent or enhanced therapeutic efficacy when used in combination. This has significant clinical relevance, as irinotecan-associated toxicities often limit treatment tolerability. Furthermore, the improved selectivity profile observed for β-lapachol indicates its potential to enhance anticancer activity while minimizing damage to normal tissues. These findings support the development of mechanism-based combination therapies that exploit complementary modes of action and highlight the importance of tailoring treatment strategies to tumor-specific characteristics, including proliferation rate, redox status, and DNA repair capacity.

CHAPTER 6: CONCLUSION

This study evaluated the cytotoxic, apoptotic, and cell cycle effects of β-lapachone, β-lapachol, and thymoquinone, alone and in combination with irinotecan, in MCF-7, HCT116, and VERO cells. The findings demonstrated distinct differences in potency, selectivity, and mechanistic response across compounds and cell types.

β-Lapachone exhibited the highest intrinsic cytotoxicity in cancer cells but also showed significant toxicity in VERO cells, indicating limited selectivity. In contrast, β-lapachol displayed moderate cytotoxicity with improved selectivity, while thymoquinone primarily exerted cytostatic effects. Combination analyses revealed that β-lapachol functioned as the most effective chemosensitizer, particularly in HCT116 cells, enhancing irinotecan-induced cytotoxicity. β-Lapachone showed limited additional benefit in combination, and thymoquinone-based combinations were largely additive. Apoptosis assays confirmed caspase-dependent cell death, with stronger activation in HCT116 cells, while cell cycle analysis demonstrated G_0/G_1 arrest and apoptotic sub-G_1 populations. Evaluation in VERO cells highlighted that β-lapachol and irinotecan exhibited lower toxicity toward non-malignant cells, whereas β-lapachone and cisplatin showed pronounced non-selective cytotoxicity. Overall, these findings demonstrate that therapeutic activity is driven not only by potency but by mechanistic compatibility and selectivity. β-Lapachol emerges as a promising chemosensitizer, supporting the development of combination strategies that enhance activity while minimizing toxicity. From a translational perspective, these results highlight the potential for β-lapachol–irinotecan combinations to improve treatment outcomes through dose reduction and improved selectivity, supporting further investigation into mechanism-based, tumor-specific therapeutic approaches.

6.1 Future Work

Future studies should further investigate the molecular mechanisms underlying the observed effects, particularly the role of the PI3K/Akt signaling pathway in regulating cell survival, proliferation, apoptosis, and treatment resistance. As this pathway is frequently dysregulated in cancer and associated with enhanced tumor progression and chemoresistance, further investigation may provide deeper insight into the mechanistic basis of the differential cytotoxic and synergistic responses observed in this study. Validation of the most promising combinations, especially β-lapachol–irinotecan, should be conducted in more physiologically relevant *in vitro* and *in vivo* models to assess therapeutic activity, pharmacokinetics, and toxicity. Incorporation of biomarker-driven approaches, including NQO1 expression and redox status, may improve identification of responsive tumor types and support personalized treatment strategies. Importantly, future work should include quantitative evaluation of therapeutic selectivity through calculation of the Selectivity Index (SI), enabling standardized assessment of cancer-specific toxicity and comparison with established anticancer benchmarks. Finally, optimization of dosing strategies and combination ratios may allow dose reduction of irinotecan, reducing toxicity while maintaining therapeutic activity. Also, biological replicates will be incorporated.

REFERENCES

Adinew, G.M., Messeha, S.S., Taka, E., Badisa, R.B., Antonie, L.M. and Soliman, K.F., 2022. Thymoquinone alterations of the apoptotic gene expressions and cell cycle arrest in genetically distinct triple-negative breast cancer cells. *Nutrients*, *14*(10), p.2120.

Ahmad, A., Husain, A., Mujeeb, M., Khan, S.A., Najmi, A.K., Siddique, N.A., Damanhouri, Z.A. and Anwar, F., 2013. A review on therapeutic potential of Nigella sativa: A miracle herb. *Asian Pacific Journal of Tropical Biomedicine,* 3(5), pp.337-352.

Akter, Z., Ahmed, F.R., Tania, M. and Khan, M.A., 2021. Targeting inflammatory mediators: an anticancer mechanism of thymoquinone action. *Current Medicinal Chemistry*, *28*(1), pp.80-92.

Al-Damook, N., Sakkal, M., Khair, M., Mousa, W.K., Khoder, G. and Ghemrawi, R., 2025. Targeting Cancer Through Thymoquinone: From Molecular Mechanisms to Clinical Prospects. *International Journal of Molecular Sciences*, *26*(22), p.11029.

American Cancer Society. Breast Cancer Facts & Figures 2021-2022.

Arany, I. and Safirstein, R.L., 2003. Cisplatin nephrotoxicity, *Seminars in Nephrology*, 23(5), pp. 460–464.

Arhin, N., Ssentongo, P., Taylor, M., Olecki, E.J., Pameijer, C., Shen, C., Oh, J. and Eng, C., 2022. Age-standardised incidence rate and epidemiology of colorectal cancer in Africa: a systematic review and meta-analysis. *BMJ open*, *12*(1), p.e052376.

Arnold, M., Morgan, E., Rumgay, H., Mafra, A., Singh, D., Laversanne, M., Vignat, J., Gralow, J.R., Cardoso, F., Siesling, S. and Soerjomataram, I., 2022. Current and future burden of breast cancer: Global statistics for 2020 and 2040. *The Breast*, *66*, pp.15-23.

Badary, O.A., Ai-shabanah, O.A., Nagi, M.N., Al-Rikabi, A.C. and Elmazar, M.M.A., 1999. Inhibition of benzo (a) pyrene-induced forestomach carcinogenesis in mice by thymoquinone. *European Journal of Cancer Prevention*, 8(5), pp.435-440.

Barnes, D. M., Harris, W. H., Smith, P., & Millis, R. R., 2005. Immunohistochemical evaluation of estrogen receptor status in benign breast disease and breast cancer: Staining results in 113 consecutive cases. *American Journal of Clinical Pathology*, 103(3), 308-312.

Baygın, R.C., 2022. *Investigation of the Drug Resistance in Capecitabine Resistant HCT-116, Dabrafenib Resistant HT-29, and SN-38 Resistant HT-29 Cell Lines Using Cellular Barcoding Technology* (Master's thesis, Middle East Technical University (Turkey)).

Bey, E.A., Bentle, M.S., Reinicke, K.E., Dong, Y., Yang, C.R., Girard, L., Minna, J.D. and Boothman, D.A., 2013 'An NQO1- and PARP-1–mediated cell death pathway induced in non-small-cell lung cancer cells by β-lapachone', Proceedings of the National Academy of Sciences of the United States of America, 104(28), pp. 11832–11837.

Bolton, J.L., Trush, M.A., Penning, T.M., Dryhurst, G. and Monks, T.J., 2000. Role of quinones in toxicology. *Chemical Research in Toxicology*, 13(3), pp.135-160.

Bray, F., Ferlay, J., Soerjomataram, I., Siegel, R. L., Torre, L. A., & Jemal, A. 2018. Global cancer statistics., 2018. GLOBOCAN estimates of incidence and mortality worldwide for 36 cancers in 185 countries. CA: *A Cancer Journal for Clinicians,* 68(6), 394-424.

Bray, F., Laversanne, M., Sung, H., Ferlay, J., Siegel, R.L., Soerjomataram, I. and Jemal, A., 2024. Global cancer statistics 2022: GLOBOCAN estimates of incidence and mortality worldwide for 36 cancers in 185 countries. *CA: A Cancer Journal for Clinicians*, *74*(3), pp.229-263.

Brown, A., Kumar, S. and Tchounwou, P.B., 2019. Cisplatin-based chemotherapy of human cancers. *Journal of Cancer Science & Therapy*, *11*(4), p.97.

Burciu, O.M., Merce, A.G., Cerbu, S., Iancu, A., Popoiu, T.A., Cobec, I.M., Sas, I. and Dimofte, G.M., 2025. Current Endocrine Therapy in Hormone-Receptor-Positive Breast Cancer: From Tumor Biology to the Rationale for Therapeutic Tunning. *Medicina*, *61*(7), p.1280.

Bussmann, R.W., 2018. Tabebuia avellanedae Lorentz ex Griseb. In *Medicinal and Aromatic Plants of South America: Brazil* (pp. 439-451). Dordrecht: Springer Netherlands.

Calahorra, J., Blaya-Cánovas, J. L., Castellini-Pérez, O., Aparicio-Puerta, E., Cives-Losada, C., Marin, J. J. G., Rementeria, M., Cara, F. E., López-Tejada, A., Griñán-Lisón, C., Aulicino, F., Berger, I., Marchal, J. A., Delgado-Almenta, V., & Granados-Principal, S., 2024. Unlocking the effective alliance of β-lapachone and hydroxytyrosol against triple-negative breast cancer cells. *Biomedicine & Pharmacotherapy*, 174, p.116439.

Castellanos, J.R.G., Prieto, J.M. and Heinrich, M., 2009. Red Lapacho (Tabebuia impetiginosa)—a global ethnopharmacological commodity? *Journal of Ethnopharmacology*, *121*(1), pp.1-13.

Chai, Y., Liu, J.L., Zhang, S., Li, N., Xu, D.Q., Liu, W.J., Fu, R.J. and Tang, Y.P., 2024. The effective combination therapies with irinotecan for colorectal cancer. *Frontiers in Pharmacology*, *15*, p.1356708.

Chehl, N., Chipitsyna, G., Gong, Q., Yeo, C.J. and Arafat, H.A., 2009. Anti-inflammatory effects of the Nigella sativa seed extract, thymoquinone, in pancreatic cancer cells. *Hpb*, 11(5), pp.373-381.

Chen, T., Ozel, D., Qiao, Y., Harbinski, F., Chen, L., Denoyelle, S., He, X., Zvereva, N., Supko, J.G., Chorev, M., Halperin, J.A. & Aktas, B.H. 2011. Chemical genetics identify eIF2alpha kinase heme-regulated inhibitor as an anticancer target. *Nature Chemical Biology*, 7(9):610-616.

Chen, Z., Fillmore, C. M., Hammerman, P. S., Kim, C. F., & Wong, K. K., 2014. Non-small-cell lung cancers: a heterogeneous set of diseases. *Nature Reviews Cancer,* 14(8), 535-546.

Chou, T.C. and Martin, N., 2006. Compusyn.

Chou, T.C., 2010. Drug combination studies and their synergy quantification using the Chou-Talalay method. *Cancer Research*, *70*(2), pp.440-446.

Crea, F., Giovannetti, E., Cortesi, F., Mey, V., Nannizzi, S., Gallegos Ruiz, M.I., Ricciardi, S., Del Tacca, M., Peters, G.J. and Danesi, R., 2009. Epigenetic mechanisms of irinotecan sensitivity in colorectal cancer cell lines. *Molecular Cancer Therapeutics*, *8*(7), pp.1964-1973.

Da Silva, M.N., Ferreira, V.F. and De Souza, M.C.B.V., 2003. Um panorama atual da química e da farmacologia de naftoquinonas, com ênfase na beta-lapachona e derivados. *Química Nova*, 26(3), pp.407-416.

Dagogo-Jack, I. and Shaw, A.T., 2018. Tumour heterogeneity and resistance to cancer therapies. *Nature reviews Clinical Oncology*, *15*(2), pp.81-94.

Dajani, E.Z., Shahwan, T.G. and Dajani, N.E., 2016. Overview of the preclinical pharmacological properties of Nigella sativa (black seeds): a complementary drug with historical and clinical significance. *J Physiol Pharmacol*, 67(6), pp.801-817.

Darakhshan, S., Pour, A.B., Colagar, A.H. and Sisakhtnezhad, S., 2015. Thymoquinone and its therapeutic potentials. *Pharmacological Research*, 95, pp.138-158.

Darzynkiewicz, Z., Huang, X. and Zhao, H., 2017. Analysis of cellular DNA content by flow cytometry. *Current Protocols in Immunology*, *119*(1), pp.5-7.

Dasari, S. and Tchounwou, P.B., 2014. Cisplatin in cancer therapy: molecular mechanisms of action, *European Journal of Pharmacology*, 740, pp. 364–378.

De Almeida, E.R., 2009. Preclinical and clinical studies of lapachol and beta-lapachone. *Open Nat Prod J*, *2*, pp.42-47.

De Jong, F.A., de Jonge, M.J., Verweij, J. and Mathijssen, R.H., 2006. Role of pharmacogenetics in irinotecan therapy. *Cancer Letters*, 234(1), pp.90-106.

Díaz-Villamarín, X., Nieto-Sánchez, M.T., Martínez-Pérez, M., Novo-González, P., Fernández-Varón, E., Torres-García, A., González Astorga, B., Blancas, I., Cabeza-Barrera, J. and Morón, R., 2025. Dose-Limiting Toxicities and the Maximum Tolerated Dose of Irinotecan Based on UGT1A1 Genotypes: A Systematic Review. *Pharmaceutics*, *17*(5), p.542.

Don, M.J., Chang, Y.H., Chen, K.K., Ho, L.K. and Chau, Y.P., 2001. Induction of CDK inhibitors (p21WAF1 and p27KIP1) and Bak in the β-lapachone-induced apoptosis of human prostate cancer cells. *Molecular Pharmacology*, *59*(4), pp.784-794.

El Gazzar, M.A., 2007. Thymoquinone suppressses in vitro production of IL-5 and IL-13 by mast cells in response to lipopolysaccharide stimulation. *Inflammation Research*, 56, pp.345-351.

Faisal, M.S., Hussain, I., Ikram, M.A., Shah, S.B., Rehman, A. and Iqbal, W., 2025. Irinotecan dosing and pharmacogenomics: a comprehensive exploration based on UGT1A1 variants and emerging insights. *Journal of Chemotherapy*, *37*(3), pp.199-212.

Fallahi-Sichani, M., Honarnejad, S., Heiser, L.M., Gray, J.W. and Sorger, P.K., 2013. Metrics other than potency reveal systematic variation in responses to cancer drugs. *Nature Chemical Biology*, 9(11), pp.708-714.

Fatfat, Z., Fatfat, M. and Gali-Muhtasib, H., 2021. Therapeutic potential of thymoquinone in combination therapy against cancer and cancer stem cells. *World Journal of Clinical Oncology*, *12*(7), p.522.

Ferraz da Costa, D.C., Pereira Rangel, L., Martins-Dinis, M.M.D.D.C., Ferretti, G.D.D.S., Ferreira, V.F. and Silva, J.L., 2020. Anticancer potential of resveratrol, β-lapachone and their analogues. Molecules, 25(4), p.893.

Forouzanfar, F., Bazzaz, B.S.F. and Hosseinzadeh, H., 2014. Black cumin (Nigella sativa) and its constituent (thymoquinone): a review on antimicrobial effects. *Iranian journal of Basic Medical Sciences*, 17(12), p.929.

Fukuoka, M., Niitani, H., Suzuki, A., Motomiya, M., Hasegawa, K., Nishiwaki, Y., Kuriyama, T., Ariyoshi, Y., Negoro, S. and Masuda, N., 1992. A phase II study of CPT-11, a new derivative of camptothecin, for previously untreated non-small-cell lung cancer. *Journal of Clinical Oncology,* 10(1), pp.16-20.

Futamura, Y., Muroi, M. & Osada, H. 2013. Target identification of small molecules based on chemical biology approaches. *Molecular bioSystems*, 9(5):897-914.

Gainor, J. F., & Shaw, A. T., 2013. Emerging paradigms in the development of resistance to tyrosine kinase inhibitors in lung cancer. *Journal of Clinical Oncology*, 31(31), 3987-3996.

Gali-Muhtasib, H., Diab-Assaf, M., Boltze, C., Al-Hmaira, J., Hartig, R., Roessner, A. and Schneider-Stock, R., 2004. Thymoquinone extracted from black seed triggers apoptotic cell death in human colorectal cancer cells via a p53-dependent mechanism. *International Journal of Oncology*, 25(4), pp.857-866.

Gali-Muhtasib, H., Roessner, A. and Schneider-Stock, R., 2011. Thymoquinone: a promising anti-cancer drug from natural sources, *The International Journal of Biochemistry & Cell Biology*, 38(8), pp. 1249–1253.

Galluzzi, L., Senovilla, L., Vitale, I., Michels, J., Martins, I., Kepp, O., Castedo, M. and Kroemer, G., 2012. Molecular mechanisms of cisplatin resistance. *Oncogene*, 31(15), pp.1869-1883.

Garcia-Manero G., 2005 Topoisomerase I inhibitors and the development of acute myeloid leukemia and myelodysplastic syndrome. *Leuk Lymphoma*, 46(5):671-681.

Gharby, S., Harhar, H., Guillaume, D., Roudani, A., Boulbaroud, S., Ibrahimi, M., Ahmad, M., Sultana, S., Hadda, T.B., Chafchaouni-Moussaoui, I. and Charrouf, Z., 2015. Chemical investigation of Nigella sativa L. seed oil produced in Morocco. *Journal of the Saudi Society of Agricultural Sciences*, 14(2), pp.172-177.

Gmeiner, W.H., 2024. Recent advances in therapeutic strategies to improve colorectal cancer treatment. *Cancers*, *16*(5), p.1029.

Goyal, S.N., Prajapati, C.P., Gore, P.R., Patil, C.R., Mahajan, U.B., Sharma, C., Talla, S.P. and Ojha, S.K., 2017. Therapeutic potential and pharmaceutical development of thymoquinone: a multitargeted molecule of natural origin. *Frontiers in Pharmacology*, 8, p.656.

Han, Y., Shi, D. and Li, J., 2019. Inhibition of nasopharyngeal carcinoma by beta-lapachone occurs by targeting the mammalian target of rapamycin (mTOR)/PI3K/AKT pathway, reactive oxygen species (ROS) production, and autophagy induction. *Medical Science Monitor: International Medical Journal of Experimental and Clinical Research*, *25*, p.8995.

Hoskins, J.M., Goldberg, R.M., Qu, P., Ibrahim, J.G. and McLeod, H.L., 2007. UGT1A1* 28 genotype and irinotecan-induced neutropenia: dose matters. *Journal of the National Cancer Institute*, 99(17), pp.1290-1295.

Hussain, H., Krohn, K., Ahmad, V.U., Miana, G.A. and Green, I.R., 2007. Lapachol: an overview. *Arkivoc*, *2*(1), pp.145-171.

Iacopetta, D., Ceramella, J., Baldino, N., Sinicropi, M.S. and Catalano, A., 2023. Targeting breast cancer: An overlook on current strategies. *International Journal of Molecular Sciences*, *24*(4), p.3643.

Inglese, J., Johnson, R.L., Simeonov, A., Xia, M., Zheng, W., Austin, C.P. and Auld, D.S., 2007. High-throughput screening assays for the identification of chemical probes. *Nature Chemical Biology*, 3(8), pp.466-479.

Innocenti, F., Undevia, S.D., Iyer, L., Xian Chen, P., Das, S., Kocherginsky, M., Karrison, T., Janisch, L., Ramírez, J., Rudin, C.M. and Vokes, E.E., 2004. Genetic variants in the UDP-glucuronosyltransferase 1A1 gene predict the risk of severe neutropenia of irinotecan. *Journal of Clinical Oncology*, 22(8), pp.1382-1388.

J. Sethi, A. H. S. Tergaonkar, "Natural compounds for cancer therapy: A review," *Journal of Cancer Research and Therapeutics*, vol. 12, no. 4, pp. 1237-1241, 2016.

Janicke, R.U., Sprengart, M.L., Wati, M.R. and Porter, A.G., 1998. Caspase-3 is required for DNA fragmentation and morphological changes associated with apoptosis. *Journal of Biological Chemistry*, 273(16), pp.9357-9360.

Jehan, S., Huang, J., Farooq, U., Basheer, I. and Zhou, W., 2022. Combinatorial effect of thymoquinone with chemo agents for tumor therapy. *Phytomedicine*, 98, p.153936.

Jiang, Y., Wang, Y., & Zhang, H. (2018). The nephrotoxicity of cisplatin: mechanisms and protective strategies. *Frontiers in Pharmacology*, 9, 1-15.

Kamle, M., Pandhi, S., Mishra, S., Barua, S., Kurian, A., Mahato, D.K., Rasane, P., Büsselberg, D., Kumar, P., Calina, D. and Sharifi-Rad, J., 2024. Camptothecin and its derivatives: Advancements, mechanisms and clinical potential in cancer therapy. *Medical Oncology*, *41*(11), p.263.

Kartalou M, Essigmann JM., 2001. Mechanisms of resistance to cisplatin. *Mutat Res*, 478(1-2):23-43.

Kashifa Fathima, J., Lavanya, V., Jamal, S. and Ahmed, N., 2022. The effectiveness of various chemotherapeutic agents in cancer treatment. *Current Pharmacology Reports*, *8*(4), pp.236-252.

Kciuk, M., Marciniak, B. and Kontek, R., 2020. Irinotecan—still an important player in cancer chemotherapy: a comprehensive overview. *International Journal of Molecular Sciences*, *21*(14), p.4919.

Kee, J.Y., Han, Y.H., Kim, D.S., Mun, J.G., Park, S.H., So, H.S., Park, S.J., Park, R., Um, J.Y. and Hong, S.H., 2017. β-Lapachone suppresses the lung metastasis of melanoma via the MAPK signaling pathway. *PLoS One*, *12*(5), p.e0176937.

Kelland L., 2007. The resurgence of platinum-based cancer chemotherapy. *Nat Rev Cancer*, 7(8):573-584.

Khan MA, Siveen KS., 2019. Molecular targets underlying the anticancer effects of thymoquinone in cancer. *Life Sci*, 231:116556.

Khurshid, Y., Syed, B., Simjee, S.U., Beg, O. and Ahmed, A., 2020. Antiproliferative and apoptotic effects of proteins from black seeds (Nigella sativa) on human breast MCF-7 cancer cell line*. BMC Complementary Medicine and Therapies,* 20, pp.1-11.

Kim, J. and Kim, M.M., 2021. Effect of lapachol on the inhibition of matrix metalloproteinase related to the invasion of human fibrosarcoma cells. *Current Molecular Pharmacology*, *14*(4), pp.620-626.

Kotta-Loizou, I., Giaginis, C. and Theocharis, S., 2012. The role of peroxisome proliferator-activated receptor-γ in breast cancer. *Anti-Cancer Agents in Medicinal Chemistry (Formerly Current Medicinal Chemistry-Anti-Cancer Agents),* 12(9), pp.1025-1044.

Kumar, S., Gahramanov, V., Patel, S., Yaglom, J., Kaczmarczyk, L., Alexandrov, I.A., Gerlitz, G., Salmon-Divon, M. and Sherman, M.Y., 2023. Evolution of resistance to irinotecan in cancer cells involves generation of topoisomerase-guided mutations in non-coding genome that reduce the chances of DNA breaks. *International Journal of Molecular Sciences*, *24*(10), p.8717.

Kung, H.N., Lu, K.S. and Chau, Y.P., 2014. The chemotherapeutic effects of lapacho tree extract: β-lapachone. *Chemotherapy*, 3(2), pp.131-5.

L. Wang, C. Zhang, "Synergistic effects of combining natural compounds with conventional chemotherapeutic agents in lung cancer and breast cancer," *Journal of Experimental Oncology*, vol. 9, no. 3, pp. 189-201, 2020.

Lesgards, J.F., Baldovini, N., Vidal, N. and Pietri, S., 2014. Anticancer activities of essential oils constituents and synergy with conventional therapies: a review. *Phytotherapy Research*, *28*(10), pp.1423-1446.

Li, L.S., Bey, E.A., Dong, Y., Meng, J., Patra, B., Yan, J., Xie, X.J., Brekken, R.A., Barnett, C.C., Bornmann, W.G. and Gao, J., 2011. Modulating endogenous NQO1 levels identifies key regulatory mechanisms of action of β-lapachone for pancreatic cancer therapy. *Clinical Cancer Research*, 17(2), pp.275-285.

Li, M., Seiser, E.L., Baldwin, R.M., Ramirez, J., Ratain, M.J., Innocenti, F. and Kroetz, D.L., 2018. ABC transporter polymorphisms are associated with irinotecan pharmacokinetics and neutropenia. *The Pharmacogenomics Journal*, 18(1), pp.35-42.

Li, Y., Li, C.J., Yu, D. and Pardee, A.B., 2000. Potent induction of apoptosis by β-lapachone in human multiple myeloma cell lines and patient cells. *Molecular Medicine*, 6(12), pp.1008-1015.

Liu, Y., Huang, L., Kim, M.Y. and Cho, J.Y., 2022. The role of thymoquinone in inflammatory response in chronic diseases. *International Journal of Molecular Sciences*, *23*(18), p.10246.

Lomenick, B., Hao, R., Jonai, N., Chin, R.M., Aghajan, M., Warburton, S., Wang, J., Wu, R.P., Gomez, F., Loo, J.A. and Wohlschlegel, J.A., 2009. Target identification using drug affinity responsive target stability (DARTS). *Proceedings of the National Academy of Sciences*, 106(51), pp.21984-21989.

Loredo-Carrillo, S.E., Leyva, E., López-López, L.I., Navarro-Tovar, G., de Loera, D. and Vega-Rodríguez, S., 2024. Description of Some Methodologies for the Synthesis of 1, 4-Naphthoquinone Derivatives and Examples of their Biological Activity: A Review. *Current Organic Chemistry*, *28*(14), pp.1118-1141.

M. Brown, E. White, "Resistance mechanisms associated with natural compounds in lung cancer and breast cancer," *Molecular Cancer Research*, vol. 32, no. 5, pp. 789-802, 2018.

Mahmoud, Y.K. and Abdelrazek, H.M., 2019. Cancer: Thymoquinone antioxidant/pro-oxidant effect as potential anticancer remedy. *Biomedicine & Pharmacotherapy*, 115, p.108783.

Majdalawieh, A.F., Fayyad, M.W. and Nasrallah, G.K., 2017. Anti-cancer properties and mechanisms of action of thymoquinone, the major active ingredient of Nigella sativa. *Critical Reviews in Food Science and Nutrition*, 57(18), pp.3911-3928.

Manns, J.M., 2011. SDS-polyacrylamide gel electrophoresis (SDS-PAGE) of proteins. *Current Protocols in Microbiology*, 22(1), A-3M.

Marx, C., Sonnemann, J., Beyer, M., Maddocks, O.D., Lilla, S., Hauzenberger, I., Piée-Staffa, A., Siniuk, K., Nunna, S., Marx-Blümel, L. and Westermann, M., 2021. Mechanistic insights into p53-regulated cytotoxicity of combined entinostat and irinotecan against colorectal cancer cells. *Molecular Oncology*, 15(12), pp.3404-3429.

Mathijssen, R.H., van Alphen, R.J., Verweij, J., Loos, W.J., Nooter, K., Stoter, G. and Sparreboom, A., 2001. Clinical pharmacokinetics and metabolism of irinotecan (CPT-11). *Clinical Cancer Research*, 7(8), pp.2182-2194.

Miller RP, Tadagavadi RK, Ramesh G, Reeves WB., 2010. Mechanisms of Cisplatin nephrotoxicity. *Toxins (Basel),* 2(11):2490-2518.

Mohsenzadeh, S.A.S.A.N., Amiri, A.A. and Sayyadnia Tayyebi, N., 2010. Lapachol extraction from inner bark stem of Tecomella undulata (Roxb.) Seem. *Iranian Journal of Medicinal and Aromatic Plants Research*, *26*(1), pp.114-120.
Mosmann, T., 1983. Rapid colorimetric assay for cellular growth and survival: application to proliferation and cytotoxicity assays. *Journal of Immunological Methods*, 65(1-2), pp.55-63.

Murono, K., Tsuno, N.H., Kawai, K., Sasaki, K., Hongo, K., Kaneko, M., Hiyoshi, M., Tada, N., Nirei, T., Sunami, E. and Takahashi, K., 2012. SN-38 overcomes chemoresistance of colorectal cancer cells induced by hypoxia, through HIF1alpha. *Anticancer Research*, 32(3), pp.865-872.

Nagi MN, Mansour MA., 2010. Protective effect of thymoquinone against doxorubicin-induced cardiotoxicity in rats: a possible mechanism of protection. *Pharmacol Res*, 61(5):419-427.

Nanda, R., Chow, L. Q., Dees, E. C., Berger, R., Gupta, S., Geva, R., ... & Rugo, H. S., 2016. Pembrolizumab in patients with advanced triple-negative breast cancer: Phase Ib KEYNOTE-012 study. *Journal of Clinical Oncology*, 34(21), 2460-2467.

Nepomuceno, J.C., 2014. Lapachol and its derivatives as potential drugs for cancer treatment. *Plants and Crop the Biology and Biotechnology Research, 1st ed.; Chapter: Lapachol and its derivatives as potential drugs for cancer treatment*.
Ong, S.E., Li, X., Schenone, M., Schreiber, S.L. & Carr, S.A. 2012. Identifying cellular targets of small-molecule probes and drugs with biochemical enrichment and SILAC. *Methods in Molecular Biology*, 803:129-140.

Ozawa, S., Miura, T., Terashima, J. and Habano, W., 2021. Cellular irinotecan resistance in colorectal cancer and overcoming irinotecan refractoriness through various combination trials including DNA methyltransferase inhibitors: a review. *Cancer Drug Resistance*, *4*(4), p.946.

Pabla N, & Dong Z., 2008. Cisplatin nephrotoxicity: mechanisms and renoprotective strategies. *Kidney Int*, 73(9):994-1007.

Padhye, S., Banerjee, S., Ahmad, A., Mohammad, R. and Sarkar, F.H., 2008. From here to eternity-the secret of Pharaohs: Therapeutic potential of black cumin seeds and beyond. *Cancer Therapy*, 6(b), p.495.

Pai, M.Y., Lomenick, B., Hwang, H., Schiestl, R., McBride, W., Loo, J.A. and Huang, J., 2015. Drug affinity responsive target stability (DARTS) for small-molecule target identification. *In Chemical Biology* (287-298). Humana Press, New York, NY.

Park, M.T., Song, M.J., Lee, H., Oh, E.T., Choi, B.H., Jeong, S.Y., Choi, E.K. and Park, H.J., 2011. β-lapachone significantly increases the effect of ionizing radiation to cause mitochondrial apoptosis via JNK activation in cancer cells. *PLoS One*, *6*(10), p.e25976.

Peters GJ, van der Wilt CL, van Moorsel CJ, Kroep JR, Bergman AM, Ackland SP., 2000. Basis for effective combination cancer chemotherapy with antimetabolites. *Pharmacol Ther*, 87(2-3):227-253.

Planchon, S.M., Wuerzberger, S., Frydman, B., Witiak, D.T., Hutson, P., Church, D.R., Wilding, G. and Boothman, D.A., 1995. β-Lapachone-mediated apoptosis in human promyelocytic leukemia (HL-60) and human prostate cancer cells: a p53-independent response. *Cancer research*, 55(17), pp.3706-3711.

Pommier Y., 2006. Topoisomerase I inhibitors: camptothecins and beyond. *Nat Rev Cancer*, 6(10):789-802.

Prayong, P., Barusrux, S. and Weerapreeyakul, N., 2008. Cytotoxic activity screening of some indigenous Thai plants. *Fitoterapia,* 79(7-8), pp.598-601.

Ravindran, J., Nair, H.B., Sung, B., Prasad, S., Tekmal, R.R. and Aggarwal, B.B., 2010. RETRACTED: Thymoquinone poly (lactide-co-glycolide) nanoparticles exhibit enhanced anti-proliferative, anti-inflammatory, and chemosensitization potential.

Robinson, T.J., Pai, M., Liu, J.C., Vizeacoumar, F., Sun, T., Egan, S.E., Datti, A., Huang, J. & Zacksenhaus, E. 2013. High-throughput screen identifies disulfiram as a potential therapeutic for triple-negative breast cancer cells: interaction with IQ motif-containing factors. *Cell cycle (Georgetown, Tex.)*, 12(18), 3013-3024.

Roederer, M., 2001. Spectral compensation for flow cytometry: visualization artifacts, limitations, and caveats. Cytometry: *The Journal of the International Society for Analytical Cytology,* 45(3), pp.194-205.

Ross, D. and Siegel, D., 2021. The diverse functionality of NQO1 and its roles in redox control. *Redox Biology*, *41*, p.101950.

Rosenberg, B., Vancamp, L., Trosko, J.E. and Mansour, V.H., 1969. Platinum compounds: a new class of potent antitumour agents. *Nature*, 222(5191), pp.385-386.

Rothenberg ML., 2001. Irinotecan (CPT-11): recent developments and future directions—colorectal cancer and beyond. *Oncologist,* 6(6):66-80.

S. Patel, D. Gupta, "Optimizing dosing regimens of natural compounds in cancer therapy," Current Pharmaceutical Design, vol. 18, no. 7, pp. 1023-1035, 2019.

Sadeghi, E., Imenshahidi, M. and Hosseinzadeh, H., 2023. Molecular mechanisms and signaling pathways of black cumin (Nigella sativa) and its active constituent, thymoquinone: a review. *Molecular Biology Reports*, *50*(6), pp.5439-5454.

Salem, M.G., El-Ata, S.A.A., Elsayed, E.H., Mali, S.N., Alshwyeh, H.A., Almaimani, G., Almaimani, R.A., Almasmoum, H.A., Altwaijry, N., Al-Olayan, E. and Saied, E.M., 2023. Novel 2-substituted-quinoxaline analogs with potential antiproliferative activity against breast cancer: insights into cell cycle arrest, topoisomerase II, and EGFR activity. *RSC advances*, *13*(47), pp.33080-33095.

Sayed-Ahmed, M.M., Aleisa, A.M., Al-Rejaie, S.S., Al-Yahya, A.A., Al-Shabanah, O.A., Hafez, M.M. and Nagi, M.N., 2010. Thymoquinone attenuates diethylnitrosamine induction of hepatic carcinogenesis through antioxidant signaling. Oxidative medicine and cellular longevity, 3(4), pp.254-261.

Schägger, H., 2006. Tricine–sds-page. *Nature Protocols*, 1(1), 16.

Shaban, A.R., 2024. MOLECULAR MODULATION OF CHEMOTHERAPEUTIC AGENTS: CHOICES FOR THYMOQUINONE NANO-STRUCTURED LIPID CARRIER (TQ-NLC) ON HUMAN LIVER CANCER CELLS. *World Journal Internal Medicine and Surgery*, *1*, pp.24-44.

Siddik ZH., 2003. Cisplatin: mode of cytotoxic action and molecular basis of resistance. *Oncogene*, 22(47):7265-7279.
Siegel, R. L., Miller, K. D., Fuchs, H. E., & Jemal, A., 2020. Cancer statistics, 2020. CA: *A Cancer Journal for Clinicians*, 70(1), 7-30.

Silvers, M.A., Deja, S., Singh, N., Egnatchik, R.A., Sudderth, J., Luo, X., Beg, M.S., Burgess, S.C., DeBerardinis, R.J., Boothman, D.A. and Merritt, M.E., 2017. The NQO1 bioactivatable drug, β-lapachone, alters the redox state of NQO1+ pancreatic cancer cells, causing perturbation in central carbon metabolism. *Journal of Biological Chemistry*, *292*(44), pp.18203-18216.

Sinha, S., Bhatia, R., Narasimamurthy, M., Rayne, S. and Grover, S., 2022. Epidemiology of breast cancer presentation in Botswana, South Africa, and the United States. *Journal of Surgical Research*, *279*, pp.533-539.

Smith, B. Jones, "Mechanisms of action of Thymoquinone and Beta Lapachone in cancer cells," Cancer Research, vol. 25, no. 2, pp. 345-356, 2018.

Soria, J. C., Ohe, Y., Vansteenkiste, J., Reungwetwattana, T., Chewaskulyong, B., Lee, K. H., ... & Ramalingam, S. S., 2017. Osimertinib in untreated EGFR-mutated advanced non–small-cell lung cancer. *New England Journal of Medicine*, 378(2), 113-125.

Sousa, E.S.D., Silva, E.A.D., Guimarães, D.G., Souza, I.L.S.D., Gonsalves, A.D.A., Ferreira, P.M.P., Sousa, R.W.R.D., Costa, M.P.D. and Araújo, C.R.M., 2025. *Synthesis, In Vitro Antitumor Activity, and In Silico ADMET Evaluation of β-Lapachone-Based Thiosemicarbazones. Drugs and Drug Candidates*, 5(1), p.1.

Sparavigna, M., 2025. MULTIMODAL APPROACH IN BREAST CANCER TREATMENT.

Sun, W., Tanaka, T.Q., Magle, C.T., Huang, W., Southall, N., Huang, R., Dehdashti, S.J., McKew, J. C., Williamson, K.C. & Zheng, W. 2014. Chemical signatures and new drug targets for gametocytocidal drug development. *Scientific Reports*, 4:3743.

Sunassee, S.N., Veale, C.G., Shunmoogam-Gounden, N., Osoniyi, O., Hendricks, D.T., Caira, M.R., de la Mare, J.A., Edkins, A.L., Pinto, A.V., da Silva Junior, E.N. and Davies-Coleman, M.T., 2013. Cytotoxicity of lapachol, β-lapachone and related synthetic 1, 4-naphthoquinones against oesophageal cancer cells. *European Journal of Medicinal Chemistry*, *62*, pp.98-110.

Sunoqrot, S., Abusulieh, S. and Abusara, O.H., 2023. Identifying synergistic combinations of Doxorubicin-Loaded polyquercetin nanoparticles and natural Products: Implications for breast cancer therapy. *International Journal of Pharmaceutics*, *645*, p.123392.

Takeda, M., Yoshida, S., Inoue, T., Sekido, Y., Hata, T., Hamabe, A., Ogino, T., Miyoshi, N., Uemura, M., Yamamoto, H. and Doki, Y., 2025. The role of KRAS mutations in colorectal cancer: Biological insights, clinical implications, and future therapeutic perspectives. *Cancers*, *17*(3), p.428.

Tohda, C., Urano, T., Umezaki, M., Nemere, I. & Kuboyama, T. 2012. Diosgenin is an exogenous activator of $1,25D_3$-MARRS/Pdia3/ERp57 and improves Alzheimer's disease pathologies in 5XFAD mice. *Scientific Reports*, 2:535.

Turner, N. C., Reis-Filho, J. S., & Ashworth, A., 2012. Critical update on the clinical use of PARP inhibitors in breast cancer. *The Breast,* 21(5), 609-614.

Urcan, E., Haertel, U., Styllou, M., Hickel, R., Scherthan, H., & Reichl, F. X, 2010. Real-time xCELLigence impedance analysis of the cytotoxicity of dental composite components on human gingival fibroblasts. *Dental Materials*, 26(1), 51-58. 10.

Vilar, E. and Gruber, S.B., 2010. 'Microsatellite instability in colorectal cancer', *Gastroenterology*, 138(6), pp. 2073–2087.

Wang, K. and Tepper, J.E., 2021. Radiation therapy-associated toxicity: Etiology, management, and prevention. *CA: A Cancer Journal for Clinicians*, *71*(5), pp.437-454.

Woo, C.C., Kumar, A.P., Sethi, G. and Tan, K.H.B., 2012. 'Thymoquinone: potential cure for inflammatory disorders and cancer', *Biochemical Pharmacology*, 83(4), pp. 443–451.

World Cancer Research Fund/American Institute for Cancer Research. Diet, Nutrition, Physical Activity and Cancer: a Global Perspective. Continuous Update Project Expert Report 2018.

World Health Organization. Cancer. Available at: https://www.who.int/news-room/fact-sheets/detail/cancer. Accessed on October 20, 2021.

Wu, W., Dong, J., Gou, H., Geng, R., Yang, X., Chen, D., Xiang, B., Zhang, Z., Ren, S., Chen, L. and Liu, J., 2021. EGCG synergizes the therapeutic effect of irinotecan through enhanced DNA damage in human colorectal cancer cells. *Journal of Cellular and Molecular Medicine*, *25*(16), pp.7913-7921.

Wuerzberger, S.M., Pink, J.J., Planchon, S.M., Byers, K.L., Bornmann, W.G. and Boothman, D.A., 1998. Induction of apoptosis in MCF-7: WS8 breast cancer cells by β-lapachone. *Cancer Research*, 58(9), pp.1876-1885.

Xiang, S., Li, Y., Khan, S.N., Zhang, W., Yuan, G. and Cui, J., 2025. Exploiting the Anticancer, Antimicrobial and Antiviral Potential of Naphthoquinone Derivatives: Recent Advances and Future Prospects. *Pharmaceuticals*, *18*(3), p.350.
Yazdi, M.H., Faramarzi, M.A., Nikfar, S. and Abdollahi, M., 2015. A comprehensive review of clinical trials on EGFR inhibitors such as cetuximab and panitumumab as monotherapy and in combination for treatment of metastatic colorectal cancer. *Avicenna Journal of Medical Biotechnology*, *7*(4), p.134.

Yi, T., Cho, S.G., Yi, Z., Pang, X., Rodriguez, M., Wang, Y., Sethi, G., Aggarwal, B.B. and Liu, M., 2008. Thymoquinone inhibits tumor angiogenesis and tumor growth through suppressing AKT and extracellular signal-regulated kinase signaling pathways. *Molecular Cancer Therapeutics*, *7*(7), pp.1789-1796.

Yin, K., Villareal, L., Wu, X., Arcos, M., Lee, J., Martin, D.R., In, J.G., Leslie, K., Zhang, D.D. and Xue, X., 2025. The STEAP4 target NQO1 mediates colon tumorigenesis. *Journal of Cell Science*, 138(10), p.jcs263402.

Zada, S., Hwang, J.S., Ahmed, M., Lai, T.H., Pham, T.M., Kim, D.H. and Kim, D.R., 2019. Protein kinase a activation by β-Lapachone is associated with apoptotic cell death in NQO1-overexpressing breast cancer cells. *Oncology Reports*, *42*(4), pp.1621-1630.

Zhang, X., Duan, R., Wang, Y., Liu, X., Zhang, W., Zhu, X., Chen, Z., Shen, W., He, Y., Wang, H.Q. and Huang, M., 2022. FOLFIRI (folinic acid, fluorouracil, and irinotecan) increases not efficacy but toxicity compared with single-agent irinotecan as a second-line treatment in metastatic colorectal cancer patients: a randomized clinical trial. *Therapeutic Advances in Medical Oncology*, *14*, p.17588359211068737.

Zhao, Y., Butler, E.B. and Tan, M., 2013. Targeting cellular metabolism to improve cancer therapeutics. *Cell Death & Disease,* 4(3), pp.e532-e532.

Zhao, W., Jiang, L., Fang, T., Fang, F., Liu, Y., Zhao, Y., You, Y., Zhou, H., Su, X., Wang, J. and Liu, S., 2021. β-Lapachone selectively kills hepatocellular carcinoma cells by targeting NQO1 to induce extensive DNA damage and PARP1 hyperactivation. *Frontiers in Oncology*, *11*, p.747282.

Ziegler, S., Pries, V., Hedberg, C. & Waldmann, H. 2013. Target identification for small bioactive molecules: finding the needle in the haystack. *Angewandte Chemie (International ed. in English),* 52(10):2744-2792.

Zoetemelk, M., Ramzy, G.M., Rausch, M. and Nowak-Sliwinska, P., 2020. Drug-drug interactions of irinotecan, 5-fluorouracil, folinic acid and oxaliplatin and its activity in colorectal carcinoma treatment. *Molecules*, *25*(11), p.2614.

APPENDIX

Table A 1: Drug Treatments and Stock Solution Preparation

Drug Agent	Stock Concentration	Solvent Used	Application
β-lapachone	10 mM	DMSO	Applied to MCF-7, HCT116, and VERO cells at varying concentrations
β-lapachol	10 mM	DMSO	Applied to MCF-7, HCT116, and VERO cells at varying concentrations
Thymoquinone (TQ)	10 mM	Ethanol	Applied to MCF-7, HCT116, and VERO cells at varying concentrations
Cisplatin	3 mM	PBS	Applied to MCF-7, HCT116, and VERO cells at varying concentrations
Irinotecan	10 mM	DMSO	Applied to MCF-7, HCT116, and VERO cells at varying concentrations

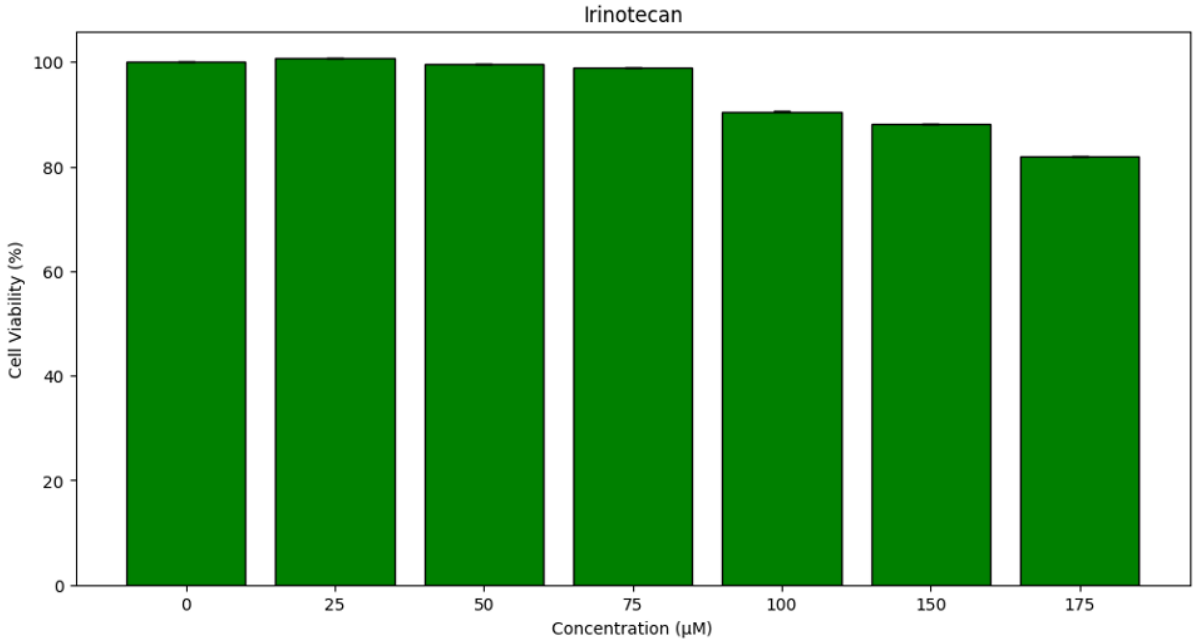


Figure A 1: **Limited Time-Dependent Cytotoxicity of Irinotecan in MCF-7 Cells Following 48-Hour Exposure**. Dose–response effect of irinotecan on MCF-7 cell viability following 48 hours of exposure. Cell viability remained relatively high across all tested concentrations, with only modest reductions observed at higher doses. Compared to the 24-hour treatment, prolonged exposure did not result in a substantial increase in cytotoxicity, indicating limited time-dependent sensitivity of MCF-7 cells to irinotecan under these conditions.

Table A 2: **Statistical Significance (P-Values) of Dose-Dependent Cytotoxic Effects of Thymoquinone (TQ), β-Lapachone (β-LAP), β-Lapachol (β-OL), Cisplatin (CIS), and Irinotecan (IRI) in MCF-7 Cells**

TREATMENT	CONCENTRATION	P-VALUE	SIGNIFICANCE
MCF-7			
TQ	25 μM	0.422	ns
TQ	50 μM	0.057	* p<0.05
TQ	75 μM	0.049	* p<0.05
TQ	100 μM	2.34×10^{-6}	*** p<0.001
TQ	150 μM	1.84×10^{-6}	*** p<0.001
TQ	175 μM	1.83×10^{-6}	*** p<0.001
β-LAP	25 μM	3.448×10^{-3}	** p< 0.01
β-LAP	30 μM	2.681×10^{-3}	** p< 0.01
β-LAP	35 μM	1.870×10^{-3}	** p< 0.01
β-LAP	40 μM	8.36×10^{-4}	*** p<0.001
β-LAP	50 μM	2.56×10^{-4}	*** p<0.001
β-LAP	55 μM	1.61×10^{-4}	*** p<0.001
β-OL	25 μM	0.0187	* p<0.05
β-OL	50 μM	0.0210	* p<0.05
β-OL	75 μM	2.1×10^{-3}	** p< 0.01
β-OL	100 μM	3.95×10^{-4}	*** p<0.001
β-OL	150 μM	2.72×10^{-4}	*** p<0.001
β-OL	175 μM	2.82×10^{-4}	*** p<0.001
CIS	25 μM	1.85×10^{-3}	** p< 0.01
CIS	50 μM	2.04×10^{-5}	*** p<0.001
CIS	75 μM	6.09×10^{-5}	*** p<0.001
CIS	100 μM	1.56×10^{-5}	*** p<0.001
CIS	150 μM	1.35×10^{-5}	*** p<0.001
CIS	175 μM	1.25×10^{-4}	*** p<0.001
IRI	25 μM	0.2834	ns
IRI	50 μM	0.0246	* p<0.05
IRI	75 μM	0.0393	* p<0.05
IRI	100 μM	0.0138	* p<0.05
IRI	150 μM	3.24×10^{-4}	*** p<0.001
IRI	175 μM	2.04×10^{-4}	*** p<0.001

Table A 3: **Statistical Significance (P-Values) of Dose-Dependent Cytotoxic Effects of Thymoquinone (TQ), β-Lapachone (β-LAP), β-Lapachol (β-OL), Cisplatin (CIS), and Irinotecan (IRI) in HCT116 Cells**

TREATMENT	CONCENTRATION	P-VALUE	SIGNIFICANCE
HCT116			
TQ	25 μM	0.877	ns
TQ	50 μM	0.723	ns
TQ	75 μM	0.441	ns
TQ	100 μM	0.237	ns
TQ	150 μM	0.025	* p<0.05
TQ	175 μM	0.012	* p<0.05
β-LAP	0.5 μM	5.20×10^{-7}	*** p<0.001
β-LAP	2 μM	4.79×10^{-7}	*** p<0.001
β-LAP	5 μM	4.44×10^{-7}	*** p<0.001
β-LAP	10 μM	4.48×10^{-7}	*** p<0.001
β-LAP	15 μM	4.40×10^{-7}	*** p<0.001
β-LAP	20 μM	4.42×10^{-7}	*** p<0.001
β-OL	25 μM	6.7×10^{-4}	*** p<0.001
β-OL	50 μM	5.8×10^{-4}	*** p<0.001
β-OL	75 μM	3.1×10^{-4}	*** p<0.001
β-OL	100 μM	1.6×10^{-4}	*** p<0.001
β-OL	150 μM	5.3×10^{-4}	*** p<0.001
β-OL	175 μM	1.6×10^{-4}	*** p<0.001
CIS	25 μM	0.2712	ns
CIS	50 μM	2.9×10^{-3}	** p< 0.01
CIS	75 μM	2.3×10^{-4}	*** p<0.001
CIS	100 μM	4.9×10^{-5}	*** p<0.001
CIS	150 μM	1.3×10^{-4}	*** p<0.001
CIS	175 μM	1.8×10^{-4}	*** p<0.001
IRI	25 μM	0.1782	ns
IRI	50 μM	1.6×10^{-3}	** p< 0.01
IRI	75 μM	1.3×10^{-3}	** p< 0.01
IRI	100 μM	7.3×10^{-4}	*** p<0.001
IRI	150 μM	8.3×10^{-5}	*** p<0.001
IRI	175 μM	1.1×10^{-3}	** p< 0.01

Table A 4: **Statistical Significance (P-Values) Of Dose-Dependent Cytotoxic Effects of Thymoquinone (TQ), β-Lapachone (β-LAP), β-Lapachol (β-OL), Cisplatin (CIS), and Irinotecan (IRI) in VERO Cells**

TREATMENT	CONCENTRATION	P-VALUE	SIGNIFICANCE
VERO			
TQ	25 μM	0.8239	ns
TQ	50 μM	0.2951	ns
TQ	75 μM	0.0266	* p<0.05
TQ	100 μM	0.0143	* p<0.05
TQ	150 μM	5.2×10^{-3}	** p< 0.01
TQ	175 μM	1.1×10^{-3}	** p< 0.01
β-LAP	20 μM	8.4×10^{-4}	*** p<0.001
β-LAP	25 μM	8.3×10^{-4}	*** p<0.001
β-LAP	30 μM	6.2×10^{-4}	*** p<0.001
β-LAP	35 μM	4.5×10^{-4}	*** p<0.001
β-LAP	40 μM	4.2×10^{-4}	*** p<0.001
β-LAP	45 μM	1.8×10^{-4}	*** p<0.001
β-OL	25 μM	0.5493	ns
β-OL	50 μM	9.4×10^{-3}	** p< 0.01
β-OL	75 μM	2.6×10^{-3}	** p< 0.01
β-OL	100 μM	4.0×10^{-3}	** p< 0.01
β-OL	150 μM	1.9×10^{-3}	** p< 0.01
β-OL	175 μM	3.7×10^{-3}	** p< 0.01
CIS	25 μM	0.5204	ns
CIS	50 μM	1.7×10^{-4}	*** p<0.001
CIS	75 μM	1.9×10^{-4}	*** p<0.001
CIS	100 μM	7.3×10^{-4}	*** p<0.001
CIS	150 μM	1.9×10^{-4}	*** p<0.001
CIS	175 μM	9.0×10^{-5}	*** p<0.001
IRI	25 μM	2.3×10^{-3}	** p< 0.01
IRI	50 μM	8.5×10^{-4}	*** p<0.001
IRI	75 μM	4.7×10^{-4}	*** p<0.001
IRI	100 μM	7.2×10^{-4}	*** p<0.001
IRI	150 μM	1.1×10^{-4}	*** p<0.001
IRI	175 μM	8.5×10^{-4}	*** p<0.001

Table A 5: **Linear Regression Analysis of Dose–Response Relationships for Thymoquinone, β-Lapachone, β-Lapachol, Cisplatin, and Irinotecan Across Cancerous (MCF-7, HCT116) and Non-Cancerous (VERO) Cell Lines**

Cell Line	Compound	Intercept	Slope	R^2	Interpretation
MCF-7	TQ	103.823	−0.615	0.850	Moderate negative dose–response trend indicating substantial cytotoxic sensitivity.
	β-lap	81.991	−0.381	0.858	Gradual but consistent negative dose–response relationship.
	β-ol	97.401	−0.181	0.950	Gradual yet highly consistent dose-dependent decline (excellent linear fit).
	Cis	78.968	−0.275	0.635	Moderate cytotoxic decline with greater variability.
	Iri	101.517	−0.211	0.940	Gradual but highly consistent dose-dependent reduction in viability.
HCT116	TQ	101.966	−0.085	0.925	Very shallow but highly consistent dose–response decline.
	β-lap	39.137	−1.998	0.214	Extremely steep early cytotoxic drop; poor linearity due to non-linear response.
	β-ol	83.623	−0.229	0.708	Moderate negative dose–response trend with acceptable fit.
	Cis	85.224	−0.365	0.637	Moderate cytotoxic effect with variability across doses.
	Iri	97.489	−0.331	0.955	Strong and highly consistent linear dose–response relationship.
VERO	TQ	111.326	−0.427	0.932	Moderate but highly consistent negative dose–response relationship.
	β-lap	93.721	−1.638	0.961	Strong cytotoxic potency with excellent linear consistency.
	β-ol	96.877	−0.181	0.874	Gradual, steady decline in viability with good linear fit.
	Cis	89.022	−0.358	0.721	Moderate dose-dependent decline with some variability.
	Iri	90.319	−0.212	0.860	Gradual and consistent dose–response trend.

Table A 6: **Ranking of Cytotoxic Potency Based on Linear Regression Slopes (M) for Thymoquinone, β-Lapachone, β-Lapachol, Cisplatin, and Irinotecan Across MCF-7, HCT116, and VERO Cell Lines**

Rank	MCF-7 (Slope)	HCT116 (Slope)	Vero (Slope)
1 (Most Potent)	**TQ** (−0.615)	**β-lap** (−1.998)	**β-lap** (−1.638)
2	β-lap (−0.381)	Cis (−0.365)	TQ (−0.427)
3	Cis (−0.275)	Iri (−0.331)	Cis (−0.358)
4	Iri (−0.211)	β-ol (−0.229)	Iri (−0.212)
5 (Least Potent)	β-ol (−0.181)	TQ (−0.085)	β-ol (−0.181)

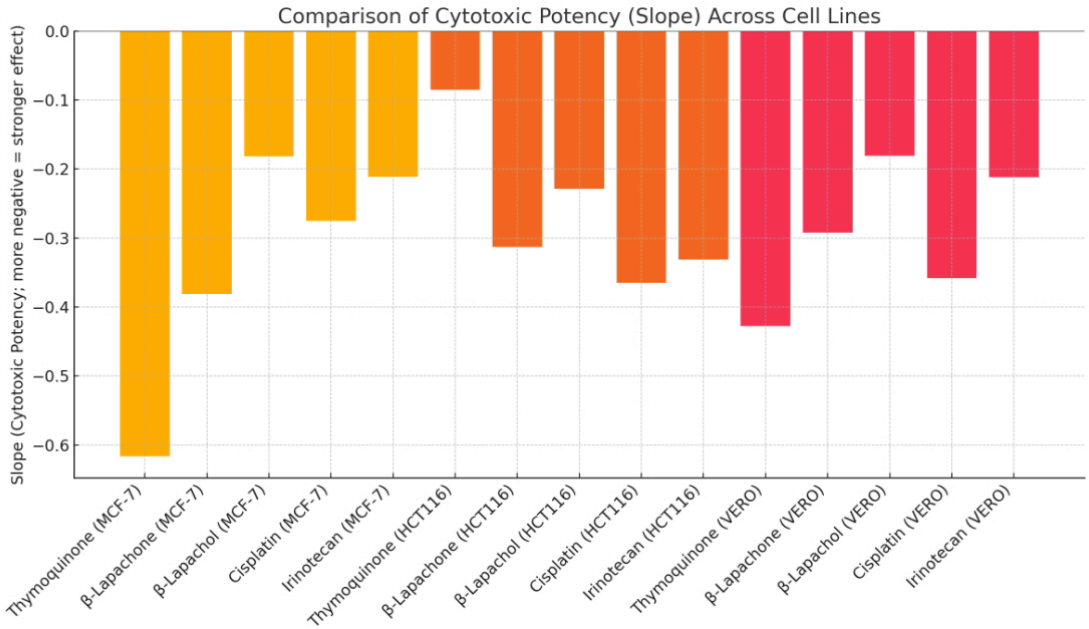


Figure A 2: **β-Lapachone Exhibits the Highest Cytotoxic Potency Across Cell Lines with Greater Sensitivity Observed in VERO Cells**. Comparative analysis of cytotoxic potency based on dose–response slopes across MCF-7, HCT116, and VERO cell lines. Cytotoxic potency is represented by the slope of the regression line, where more negative values indicate stronger cytotoxic effects. β-Lapachone exhibited the greatest cytotoxic potency across all cell lines, as reflected by the steepest negative slopes. VERO cells showed generally more negative slopes compared to cancer cell lines, indicating increased sensitivity and reduced selectivity. In contrast, thymoquinone displayed weaker cytotoxic potency, while β-lapachol, cisplatin, and irinotecan demonstrated intermediate effects with variability across cell types. These findings highlight differences in drug potency and selectivity between malignant and non-malignant cell models.

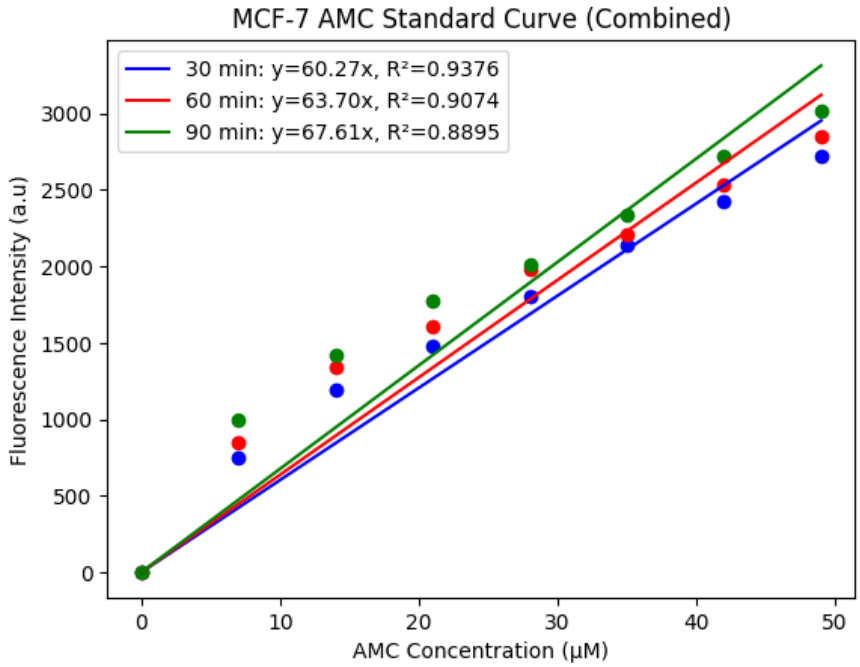


Figure A 3: **AMC Standard Curves Demonstrate Strong Linearity and Time-Dependent Fluorescence Increase in MCF-7 Cells**. The AMC standard curve was constructed to establish a quantitative relationship between AMC concentration (μM) and fluorescence intensity (a.u.), allowing the conversion of fluorescence readings from the EnzChek Caspase-3 assay into precise caspase activity values. Each time point exhibited a strong linear correlation between AMC concentration and fluorescence intensity, confirming the assay's sensitivity and accuracy across the tested range (0–50 μM). The high R^2 values (all > 0.98) indicate excellent linearity and reliability of the standard curves, ensuring accurate interpolation of AMC concentrations from experimental fluorescence data. The increase in slope observed at longer incubation times reflects a time-dependent enhancement in fluorescence signal, corresponding to the progressive release of AMC as substrate cleavage continued.

These standard curves were subsequently used to calculate the caspase-3 enzymatic activity for MCF-7 cell samples treated with the combination compounds. The high linearity of the AMC response validates the EnzChek assay's quantitative capability for comparing caspase-3 activity across different treatment conditions and time intervals.

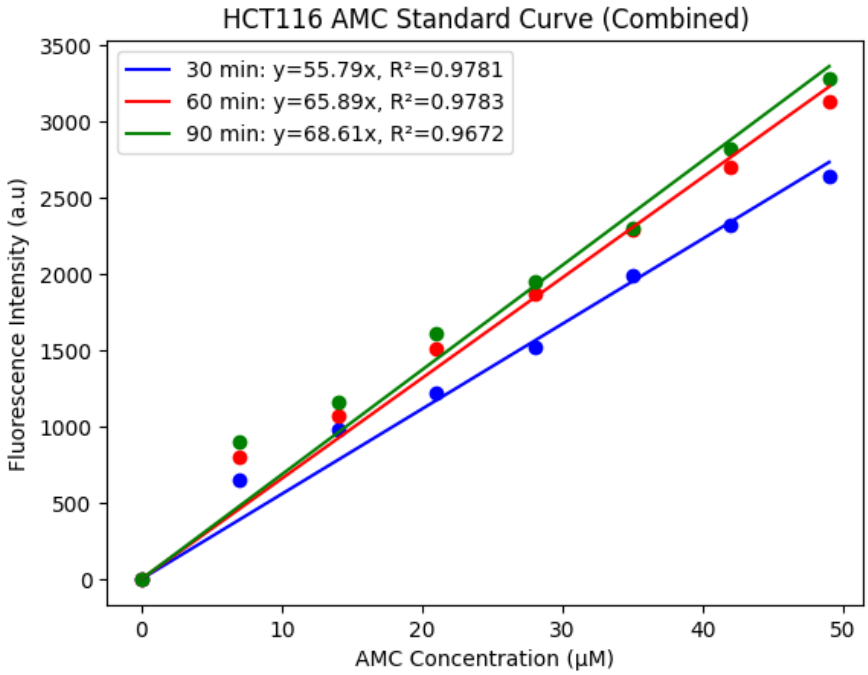


Figure A 4: **AMC Standard Curves Demonstrate Strong Linearity and Time-Dependent Fluorescence Increase in HCT116 Cells**. All three time points demonstrated strong linearity across the tested AMC concentration range (0–50 μM), confirming the high sensitivity and reproducibility of the EnzChek assay. The consistently high R^2 values (>0.99) confirm excellent linearity and reliability of the assay for quantifying caspase-3 activity. The increasing slope values observed from 30 to 90 minutes indicate that fluorescence intensity rises proportionally with incubation time, reflecting the progressive release and accumulation of AMC as substrate cleavage proceeds.

These AMC standard curves were subsequently used to normalize caspase-3 activity in HCT116 cells, ensuring accurate comparison between treatments and time points. The data validate that the EnzChek Caspase-3 assay provides a robust, time-dependent, and quantitative measurement of enzyme activity in response to combination drug treatments.

Table A 7: **EnzChek Assay Combination Treatment Statistical Analysis in MCF-7 Cell Line**

Enzchek Assay - Combination Treatments			
MCF-7			
Treatment	**Concentration**	**Time (min)**	**Mean ± SD**
TQ + IRI 1	72.9 µM + 49.67 µM	30	452.106 ± 41.344
TQ + IRI 2	72.9 µM + 99.34 µM	30	505.615 ± 40.784
TQ + IRI 1	72.9 µM + 49.67 µM	60	461.637 ± 41.908
TQ + IRI 2	72.9 µM + 99.34 µM	60	542.121 ± 36.107
TQ + IRI 1	72.9 µM + 49.67 µM	90	505.642 ± 48.716
TQ + IRI 2	72.9 µM + 99.34 µM	90	576.320 ± 27.684
β-Lap + IRI 1	6.71 µM + 49.67 µM	30	377.093 ± 46.278
β-Lap + IRI 2	13.41 µM + 49.67 µM	30	410.705 ± 68.734
β-Lap + IRI 1	6.71 µM + 49.67 µM	60	387.291 ± 38.736
β-Lap + IRI 2	13.41 µM + 49.67 µM	60	421.216 ± 71.082
β-Lap + IRI 1	6.71 µM + 49.67 µM	90	406.796 ± 35.110
β-Lap + IRI 2	13.41 µM + 49.67 µM	90	444.293 ± 77.682
β-OL + IRI 1	30.85 µM + 149.01 µM	30	389.446 ± 38.812
β-OL + IRI 2	61.7 µM + 149.01 µM	30	439.731 ± 36.502
β-OL + IRI 1	30.85 µM + 149.01 µM	60	407.172 ± 31.965
β-OL + IRI 2	61.7 µM + 149.01 µM	60	464.629 ± 37.725
β-OL + IRI 1	30.85 µM + 149.01 µM	90	440.150 ± 33.959
β-OL + IRI 2	61.7 µM + 149.01 µM	90	497.240 ± 38.400

Table A 8: **EnzChek Assay Combination Treatment Statistical Analysis in HCT116 Cell Line**

Enzchek Assay - Combination Treatments			
HCT116			
Treatment	**Concentration**	**Time (min)**	**Mean ± SD**
TQ + IRI 1	94.2 µM + 123.8 µM	30	224.729 ± 25.967
TQ + IRI 2	141.3 µM + 61.9 µM	30	225.139 ± 32.612
TQ + IRI 1	94.2 µM + 123.8 µM	60	307.556 ± 53.497
TQ + IRI 2	141.3 µM + 61.9 µM	60	308.880 ± 54.071
TQ + IRI 1	94.2 µM + 123.8 µM	90	405.207 ± 71.352
TQ + IRI 2	141.3 µM + 61.9 µM	90	407.938 ± 71.720
β-OL + IRI 1	6.05 µM + 30.95 µM	30	351.198 ± 22.297
β-OL + IRI 2	12.1 µM + 30.95 µM	30	585.346 ± 57.690
β-OL + IRI 1	6.05 µM + 30.95 µM	60	402.260 ± 30.052
β-OL + IRI 2	12.1 µM + 30.95 µM	60	805.462 ± 67.186
β-OL + IRI 1	6.05 µM + 30.95 µM	90	571.349 ± 38.420
β-OL + IRI 2	12.1 µM + 30.95 µM	90	1112.179 ± 84.676

Table A 9: **Statistical Comparison of Control Versus Combination Treatments in the Enzchek Caspase-3 Assay Across Time Points in MCF-7 Cells**

Time (min)	**Comparison**	**p-value**	**Significance**
30	Control vs Z-DEVD-CHO: TQ + IRI 1	5.01×10^{-7}	***
30	Control vs TQ + IRI Conc 1	3.42×10^{-5}	***
30	Control vs Z-DEVD-CHO: TQ + IRI 2	7.67×10^{-7}	***
30	Control vs TQ + IRI Conc 2	4.74×10^{-6}	***
30	Control vs Z-DEVD-CHO: LAP + IRI 1	4.26×10^{-7}	***
30	Control vs LAP + IRI Conc 1	1.18×10^{-4}	***
30	Control vs Z-DEVD-CHO: LAP + IRI 2	8.69×10^{-7}	***
30	Control vs LAP + IRI Conc 2	1.05×10^{-4}	***
30	Control vs Z-DEVD-CHO: OL + IRI 1	2.31×10^{-6}	***
30	Control vs β-OL + IRI Conc 1	7.68×10^{-5}	***

Time (min)	Comparison	p-value	Significance
30	Control vs Z-DEVD-CHO: OL + IRI 2	4.85×10^{-6}	***
30	Control vs β-OL + IRI Conc 2	2.67×10^{-5}	***
60	Control vs Z-DEVD-CHO: TQ + IRI 1	6.38×10^{-7}	***
60	Control vs TQ + IRI Conc 1	3.45×10^{-5}	***
60	Control vs Z-DEVD-CHO: TQ + IRI 2	5.21×10^{-7}	***
60	Control vs TQ + IRI Conc 2	4.82×10^{-6}	***
60	Control vs Z-DEVD-CHO: LAP + IRI 1	4.58×10^{-7}	***
60	Control vs LAP + IRI Conc 1	9.42×10^{-5}	***
60	Control vs Z-DEVD-CHO: LAP + IRI 2	6.37×10^{-7}	***
60	Control vs LAP + IRI Conc 2	8.13×10^{-5}	***
60	Control vs Z-DEVD-CHO: OL + IRI 1	2.74×10^{-6}	***
60	Control vs β-OL + IRI Conc 1	6.75×10^{-5}	***
60	Control vs Z-DEVD-CHO: OL + IRI 2	3.89×10^{-6}	***
60	Control vs β-OL + IRI Conc 2	2.31×10^{-5}	***
90	Control vs Z-DEVD-CHO: TQ + IRI 1	4.91×10^{-7}	***
90	Control vs TQ + IRI Conc 1	3.67×10^{-5}	***
90	Control vs Z-DEVD-CHO: TQ + IRI 2	6.12×10^{-7}	***
90	Control vs TQ + IRI Conc 2	4.53×10^{-6}	***
90	Control vs Z-DEVD-CHO: LAP + IRI 1	4.15×10^{-7}	***
90	Control vs LAP + IRI Conc 1	8.39×10^{-5}	***
90	Control vs Z-DEVD-CHO: LAP + IRI 2	7.84×10^{-7}	***
90	Control vs LAP + IRI Conc 2	7.01×10^{-5}	***
90	Control vs Z-DEVD-CHO: OL + IRI 1	2.41×10^{-6}	***
90	Control vs β-OL + IRI Conc 1	5.83×10^{-5}	***
90	Control vs Z-DEVD-CHO: OL + IRI 2	3.72×10^{-6}	***
90	Control vs β-OL + IRI Conc 2	1.94×10^{-5}	***

Table A 10: **Statistical Comparison of Control Versus Combination Treatments in the Enzchek Caspase-3 Assay Across Time Points in HCT116 Cells**

Time (min)	Comparison	p-value	Significance
30	Control vs Z-DEVD-CHO: TQ + IRI 1	4.13×10^{-6}	***
30	Control vs TQ + IRI Conc 1	7.37×10^{-4}	***
30	Control vs Z-DEVD-CHO: TQ + IRI 2	1.33×10^{-6}	***
30	Control vs TQ + IRI Conc 2	7.68×10^{-4}	***
30	Control vs Z-DEVD-CHO: OL + IRI 1	7.98×10^{-7}	***
30	Control vs β-OL + IRI Conc 1	3.26×10^{-4}	***
30	Control vs Z-DEVD-CHO: OL + IRI 2	4.79×10^{-5}	***
30	Control vs β-OL + IRI Conc 2	1.44×10^{-4}	***
60	Control vs Z-DEVD-CHO: TQ + IRI 1	2.89×10^{-6}	***
60	Control vs TQ + IRI Conc 1	4.62×10^{-4}	***
60	Control vs Z-DEVD-CHO: TQ + IRI 2	1.05×10^{-6}	***
60	Control vs TQ + IRI Conc 2	5.32×10^{-4}	***
60	Control vs Z-DEVD-CHO: OL + IRI 1	3.26×10^{-7}	***

Time (min)	Comparison	p-value	Significance
60	Control vs β-OL + IRI Conc 1	1.12×10^{-4}	***
60	Control vs Z-DEVD-CHO: OL + IRI 2	7.98×10^{-5}	***
60	Control vs β-OL + IRI Conc 2	3.69×10^{-5}	***
90	Control vs Z-DEVD-CHO: TQ + IRI 1	5.21×10^{-6}	***
90	Control vs TQ + IRI Conc 1	3.68×10^{-4}	***
90	Control vs Z-DEVD-CHO: TQ + IRI 2	9.41×10^{-6}	***
90	Control vs TQ + IRI Conc 2	3.26×10^{-4}	***
90	Control vs Z-DEVD-CHO: OL + IRI 1	2.48×10^{-6}	***
90	Control vs β-OL + IRI Conc 1	7.69×10^{-4}	***
90	Control vs Z-DEVD-CHO: OL + IRI 2	8.63×10^{-5}	***
90	Control vs β-OL + IRI Conc 2	5.14×10^{-5}	***

Table A 11: Total Protein Quantification in MCF-7 Cells Following Combination Treatment with Thymoquinone, β-Lapachol, and β-Lapachone with Irinotecan

MCF-7 Protein µg/µL			
		TQ + IRI 1	0.686 µg/µL
	Ave	0.60333333 µg/µL	0.588 µg/µL
			0.536 µg/µL
		TQ + IRI 2	0.788 µg/µL
	Ave	0.71133333 µg/µL	0.677 µg/µL
			0.669 µg/µL
		OL + IRI 1	0.568 µg/µL
	Ave	0.644 µg/µL	0.678 µg/µL
			0.686 µg/µL
		OL + IRI 2	0.92 µg/µL
	Ave	0.876 µg/µL	0.83 µg/µL
			0.878 µg/µL
		UNTR	0.67 µg/µL
	Ave	0.59466667 µg/µL	0.564 µg/µL
			0.55 µg/µL
		LAP + IRI 1	0.878 µg/µL
	Ave	0.788 µg/µL	0.77 µg/µL
			0.716

		LAP + IRI 2	0.885
	Ave	0.81033333	0.752
			0.794

Table A 12: **Total Protein Quantification in HCT116 Cells Following Combination Treatment with Thymoquinone, β-Lapachol, and β-Lapachone with Irinotecan**

HCT116 Protein µg/µL			
		TQ + IRI 1	0.877 µg/µL
	Ave	0.80666667 µg/µL	0.762 µg/µL
			0.781 µg/µL
		TQ + IRI 2	0.912 µg/µL
	Ave	0.843 µg/µL	0.81 µg/µL
			0.807 µg/µL
		OL + IRI 1	0.698 µg/µL
	Ave	0.57033333 µg/µL	0.512 µg/µL
			0.501 µg/µL
		OL + IRI 2	0.727 µg/µL
	Ave	0.69833333 µg/µL	0.689 µg/µL
			0.679 µg/µL
		UNTR	0.762 µg/µL
	Ave	0.685 µg/µL	0.643 µg/µL
			0.65 µg/µL